

**PERFORMANCE EVALUATION OF FIBER-
REINFORCED POLYMER POLES FOR
TRANSMISSION LINES**

BY

SHERIF MOHAMED IBRAHIM

A Thesis

Submitted to the Faculty of Graduate Studies
in Partial Fulfillment of the Requirements for the Degree of

Doctor of Philosophy

Department of Civil and Geological Engineering

The University of Manitoba

Winnipeg, Manitoba, Canada, March 2000

© SHERIF IBRAHIM 2000



**National Library
of Canada**

**Acquisitions and
Bibliographic Services**

**395 Wellington Street
Ottawa ON K1A 0N4
Canada**

**Bibliothèque nationale
du Canada**

**Acquisitions et
services bibliographiques**

**395, rue Wellington
Ottawa ON K1A 0N4
Canada**

Your file Votre référence

Our file Notre référence

The author has granted a non-exclusive licence allowing the National Library of Canada to reproduce, loan, distribute or sell copies of this thesis in microform, paper or electronic formats.

The author retains ownership of the copyright in this thesis. Neither the thesis nor substantial extracts from it may be printed or otherwise reproduced without the author's permission.

L'auteur a accordé une licence non exclusive permettant à la Bibliothèque nationale du Canada de reproduire, prêter, distribuer ou vendre des copies de cette thèse sous la forme de microfiche/film, de reproduction sur papier ou sur format électronique.

L'auteur conserve la propriété du droit d'auteur qui protège cette thèse. Ni la thèse ni des extraits substantiels de celle-ci ne doivent être imprimés ou autrement reproduits sans son autorisation.

0-612-51638-5

Canada

**THE UNIVERSITY OF MANITOBA
FACULTY OF GRADUATE STUDIES

COPYRIGHT PERMISSION PAGE**

**Performance Evaluation of Fiber-Reinforced Polymer Poles
for Transmission Lines**

BY

Sherif Mohamed Ibrahim

**A Thesis/Practicum submitted to the Faculty of Graduate Studies of The University
of Manitoba in partial fulfillment of the requirements of the degree
of
Doctor of Philosophy**

SHERIF IBRAHIM © 2000

Permission has been granted to the Library of The University of Manitoba to lend or sell copies of this thesis/practicum, to the National Library of Canada to microfilm this thesis/practicum and to lend or sell copies of the film, and to Dissertations Abstracts International to publish an abstract of this thesis/practicum.

The author reserves other publication rights, and neither this thesis/practicum nor extensive extracts from it may be printed or otherwise reproduced without the author's written permission.

ABSTRACT

The increasing demand for pole-type transmission structures has necessitated the utilization of innovative and environmentally friendly materials for such structures. Traditional materials such as wood, steel, and concrete are commonly used to construct electrical transmission and distribution poles. However, the shortage of wooden poles, their short life expectancy, and various environmental concerns have promoted hydro-electric utility companies to search for a cost-effective alternative. Glass Fiber-Reinforced Polymer (GFRP) poles are lightweight. The use of GFRP poles is not new. A number of companies are already involved in the production of such poles. Research in this area, however, is limited. Therefore, a research program was conducted at the University of Manitoba, Canada, to evaluate the performance of tapered GFRP poles and to develop design guidelines for the use of such poles by electric utilities. The aim of this research program was to develop an analytical model capable of predicting the performance and the strength of GFRP poles. This analytical model had to be verified through extensive experimental work.

The first phase of this research program consisted of the experimental investigation. A total of twelve 2.5 m and twelve 6.1 m GFRP poles were tested under lateral loading in accordance with current standards. The specimens were designed to cover a wide range of parameters such as wall thickness, fiber orientation, and fiber arrangement. The experimental results showed that GFRP poles can sustain a transverse load capacity similar to that of wooden, steel or concrete poles with a strength-to-weight ratio considerably higher than these traditional materials. Failure due to local buckling due to flexural was the most dominant failure mode of the specimens tested.

The second phase of the research program included an analytical investigation to predict the strength and performance of GFRP poles. The ANSYS finite element program was employed to analyze the tested specimens and to develop a numerical model to analyze GFRP poles.

Following the verification of the finite element technique through comparison with the experimental results, a parametric study was conducted to examine the effect of a number of variables including the wall thickness, the fiber orientation and arrangement, and the diameter of GFRP poles. As a result of this parametric study, design charts for various types of poles were developed. Optimum parameters, such as cross section dimensions, wall thickness, and fiber orientation were also developed.

In addition to the finite element model and the design charts, a simplified nonlinear analytical model was developed to predict the critical buckling load. This model can also be used to examine the progressive cross-sectional distortion of GFRP poles under steadily increasing loading as well as the occurrence of any local buckling in the section. The laminate stiffness and equivalent moduli used in the analysis were derived from the classical lamination theory. The current study was extended to include the dynamic behavior of GFRP poles by developing a simplified finite element model. Comparison between results from this model and results from the ANSYS finite element program showed an excellent correlation.

ACKNOWLEDGEMENT

The author wishes to express his gratitude and appreciation to his supervisor Prof. D. Polyzois, Department of Civil and Geological Engineering, for his guidance, advice and encouragement throughout this research program.

The author also wishes to thank the members of his committee, Drs. S. Rizkalla, N. Rajapakse, and G. Wang for their comments and suggestions.

The author is deeply grateful to Dr. G. Bhuyan, Adjunct Professor, University of British Columbia, Senior Researcher, POWERTECH labs Inc., for his constructive criticism and valuable suggestions after reviewing the first draft of this thesis.

The experimental program of this study was conducted at the Structural Engineering and Construction and Research and Development Facility of the Department of Civil and Geological Engineering at the University of Manitoba, Canada. The author wishes to express his appreciation for the technical assistance provided by its staff.

This research was funded by ISIS-Canada, the Province of Manitoba, and Faroex Ltd., Gimli, Manitoba.

TABLE OF CONTENTS

| | |
|------------------------|------|
| ABSTRACT..... | ii |
| ACKNOWLEDGEMENT..... | iv |
| TABLE OF CONTENTS..... | v |
| LIST OF TABLES..... | xi |
| LIST OF FIGURES..... | xiii |

CHAPTER 1: INTRODUCTION

| | |
|--|---|
| 1.1 GENERAL..... | 1 |
| 1.2 POLES AS TRANSMISSION AND DISTRIBUTION STRUCTURES..... | 3 |
| 1.3 HISTORICAL DEVELOPMENT OF GFRP POLES AND FILAMENT WINDING PROCESS..... | 4 |
| 1.4 SCOPE..... | 6 |

CHAPTER 2: LITERATURE SURVEY

| | |
|---|----|
| 2.1 POLE DESIGN SPECIFICATIONS AND STANDARDS..... | 11 |
| 2.2 EXPERIMENTAL INVESTIGATIONS OF GFRP POLES..... | 17 |
| 2.3 THEORETICAL INVESTIGATIONS OF GFRP POLES..... | 19 |
| 2.3.1 ANALYTICAL ANALYSIS OF LAMINATED SHELLS..... | 19 |
| 2.3.2 FINITE ELEMENT ANALYSIS PROGRAMS..... | 21 |
| 2.3.3 OVALIZATION ANALYSIS OF TUBULAR SECTIONS UNDER BENDING..... | 23 |

| | | |
|-------|--|----|
| 2.3.4 | EFFECT OF OVALIZATION ON LOCAL BUCKLING..... | 26 |
| 2.3.5 | MATERIAL FAILURE CRITERIA..... | 28 |

CHAPTER 3: EXPERIMENTAL PROGRAM

| | | |
|-------|-------------------------------------|----|
| 3.1 | INTRODUCTION | 34 |
| 3.2 | MANDREL CONSTRUCTION..... | 35 |
| 3.2.1 | FABRICATION OF GFRP POLES..... | 37 |
| 3.3 | SCALED TEST SPECIMENS | 38 |
| 3.3.1 | TEST SET-UP | 40 |
| 3.3.2 | INSTRUMENTATION..... | 41 |
| 3.3.3 | TEST PROCEDURE..... | 42 |
| 3.4 | FULL-SCALE TEST SPECIMENS..... | 42 |
| 3.4.1 | TEST SET-UP | 45 |
| 3.4.2 | INSTRUMENTATION..... | 46 |
| 3.4.3 | TEST PROCEDURE..... | 48 |
| 3.5 | MATERIAL MECHANICAL PROPERTIES..... | 48 |

CHAPTER 4: EXPERIMENTAL RESULTS

| | | |
|-------|--------------------------------|----|
| 4.1 | INTRODUCTION | 64 |
| 4.2 | SCALED SPECIMENS..... | 64 |
| 4.2.1 | PERFORMANCE OF SPECIMENS | 65 |
| 4.2.2 | FAILURE MODES..... | 69 |

| | | |
|-------|---|----|
| 4.2.3 | LOAD-DEFLECTION RELATIONSHIP | 70 |
| 4.2.4 | LOAD-OVALIZATION RELATIONSHIP | 71 |
| 4.2.5 | LOAD-STRAIN RELATIONSHIP | 72 |
| 4.3 | FULL-SCALE SPECIMENS | 74 |
| 4.3.1 | PERFORMANCE OF FULL-SCALE SPECIMENS | 74 |
| 4.3.2 | OPTIMUM CONFIGURATION OF GFRP POLE..... | 76 |
| 4.3.3 | FAILURE MODES..... | 77 |
| 4.3.4 | LOAD-DEFLECTION RELATIONSHIP | 78 |
| 4.3.5 | LOAD-OVALIZATION RELATIONSHIP | 79 |
| 4.3.6 | STRAINS | 81 |

CHAPTER 5: RATIONAL ANALYSIS

| | | |
|-------|---|-----|
| 5.1 | INTRODUCTION | 94 |
| 5.2 | MATERIAL PROPERTIES | 94 |
| 5.3 | MATERIAL STRENGTH..... | 96 |
| 5.4 | VERIFICATION OF MATERIAL PROPERTIES | 100 |
| 5.5 | FAILURE CRITERION | 101 |
| 5.6 | EQUIVALENT LAMINATE PROPERTIES..... | 102 |
| 5.7 | NONLINEAR OVALIZATION ANALYSIS | 105 |
| 5.7.1 | BASIC ASSUMPTIONS | 106 |
| 5.7.2 | FORMULATION..... | 107 |

| | | |
|---------|---|-----|
| 5.7.2.1 | STAGE 1: STRAIN ENERGY CALCULATION DUE TO OVALIZATION | 108 |
| 5.7.2.2 | STAGE 2: STRAIN ENERGY CALCULATION DUE TO APPLIED BENDING | 111 |
| 5.7.2.3 | MOMENT-OVALIZATION RELATIONSHIP | 114 |
| 5.7.2.4 | STRESS CALCULATIONS | 115 |
| 5.7.2.5 | CRITICAL BUCKLING STRESS | 117 |
| 5.7.2.6 | APPLICATION | 118 |

CHAPTER 6: NUMERICAL ANALYSIS AND DESIGN CHARTS

| | | |
|---------|---|-----|
| 6.1 | INTRODUCTION | 125 |
| 6.2 | FINITE ELEMENT ANALYSIS | 126 |
| 6.2.1 | ELEMENT TYPE | 126 |
| 6.2.2 | STRESS-STRAIN RELATIONSHIP | 127 |
| 6.2.3 | GEOMETRIC NONLINEARITY | 128 |
| 6.3 | ANALYSIS OF THE TESTED GFRP POLES | 130 |
| 6.3.1 | MODELING OF THE GFRP POLES | 130 |
| 6.3.1.1 | MODELING OF THE SCALED SPECIMENS | 130 |
| 6.3.1.2 | MODELING OF THE FULL-SCALE SPECIMENS | 131 |
| 6.3.1.3 | SOLUTION AND DETERMINATION OF FAILURE LOADS | 132 |
| 6.3.2 | RESULTS AND DISCUSSION | 133 |

| | | |
|---------|---|-----|
| 6.3.2.1 | SCALED SPECIMENS..... | 133 |
| 6.3.2.2 | FULL-SCALE SPECIMENS | 136 |
| 6.4 | PARAMETRIC STUDY AND DESIGN CHARTS..... | 139 |
| 6.4.1 | CASE 1: EFFECT OF CIRCUMFERENCIAL LAYERS ON ULTIMATE STRENGTH OF GFRP POLES | 140 |
| 6.4.2 | CASE 2: EFFECT OF LONGITUDINAL FIBER ORIENTATION | 145 |
| 6.4.3 | CASE 3: EFFECT OF CROSS-SECTION DIMENSIONS..... | 149 |
| 6.4.3.1 | SERIES 1 | 152 |
| 6.4.3.2 | SERIES 2..... | 154 |
| 6.4.3.3 | SERIES 3 | 155 |

CHAPTER 7: SIMPLIFIED FINITE ELEMENT METHOD FOR DYNAMIC ANALYSIS OF TAPERED GFRP POLES

| | | |
|-----|--|-----|
| 7.1 | INTRODUCTION | 194 |
| 7.2 | EQUIVALENT MATERIAL PROPERTIES..... | 195 |
| 7.3 | FINITE ELEMENT FORMULATION | 198 |
| 7.4 | NUMERICAL RESULTS AND DISCUSSION | 207 |
| 7.5 | CONCLUSIONS..... | 211 |

| | |
|---|-----|
| CHAPTER 8: SUMMARY, CONCLUSIONS AND RECOMMENDATION FOR FUTURE WORK | 215 |
| REFERENCES | 221 |
| APPENDIX A: ANSYS INPUT FILES | 230 |
| A.1 INPUT FILE FOR SCALED SPECIMEN A25 | 230 |
| A.2 INPUT FILE FOR FULL-SCALE SPECIMEN 3..... | 234 |
| APPENDIX B: STIFFNESS AND MASS MATRIX FOR PRISMATIC ELEMENT | 240 |

LIST OF TABLES

| Table | Page |
|--|-------------|
| 2-1 Strength factors for standard method (NESC 1997)..... | 12 |
| 2-2 Overload factors for standard method (NESC 1997)..... | 12 |
| 2-3 Strength factor for the alternate method (NESC 1997) | 13 |
| 2-4 Overload factors for the alternate method (NESC 1997)..... | 13 |
| 2-5 Transverse load capacity of wooden poles according to ANSI 05.1 | 15 |
| 3-1 Properties of E-Glass and Polyester resin | 39 |
| 3-2 Configuration and fiber volume fraction for scaled-specimens | 40 |
| 3-3 Configuration and fiber volume fraction of full-scale specimens..... | 45 |
| 3-4 Dimensions of the tested coupons..... | 49 |
| 3-5 Mechanical properties of the tested coupons | 50 |
| 4-1 Performance of scaled GFRP poles | 67 |
| 4-2 Load capacity-to-mass ratio of scaled GFRP poles..... | 68 |
| 4-3 Performance of full-scale GFRP poles..... | 75 |
| 5-1 Experimental and theoretical materials properties..... | 100 |
| 6-1 Comparison between experimental and finite element failure load for scaled specimens | 135 |
| 6-2 Comparison between experimental and finite element failure load for full-scale specimens | 138 |

| | | |
|-----|---|-----|
| 6-3 | Material properties and ultimate strength of GFRP | 139 |
| 6-4 | Parametric variations for Case 1 | 141 |
| 6-5 | Parametric variations for Case 2 | 146 |
| 6-6 | Parametric variations for Case 3 | 151 |
| 7-1 | Stiffness components \overline{Q}_{ij} as function of $\pm\theta$ | 196 |
| 7-2 | Effective modulus E_{eff} (GPa) for various number of layers (N) | 198 |
| 7-3 | Convergence study for tapered and prismatic element models | 208 |
| 7-4 | Natural frequency and period for various taper ratios and $\pm\theta$ | 209 |

LIST OF FIGURES

| Figure | | Page |
|---------------|---|-------------|
| 2-1 | Ovalization of cylindrical tube under bending moment | 32 |
| 2-2 | Typical moment–curvature relationship for cylindrical tubes | 32 |
| 2-3 | Maximum stress, Maximum Strain, and Tsai–Hill failure surfaces in $\sigma_1 - \sigma_2$ space | 33 |
| 3-1 | Schematic drawing different components of full–scale mandrel | 52 |
| 3-2 | Three–axis filament winding machine | 53 |
| 3-3 | Schematic of three axis motion of filament winding machine | 54 |
| 3-4 | Schematic drawing of the scaled test setup | 55 |
| 3-5 | Test setup for scaled specimens | 56 |
| 3-6 | Targeted dimensions of full–scale FRP pole | 57 |
| 3-7 | Schematic drawing of the full–scale test setup | 58 |
| 3-8 | Connection between concrete base and structure wall | 59 |
| 3-9 | Load cell connection for full–scale specimens | 59 |
| 3-10 | Measurement of ovalization by two LMTs installed at opposite side of the specimen | 60 |
| 3-11 | Unidirectional flat coupons | 61 |
| 3-12 | Test setup for unidirectional coupon | 62 |
| 3-13 | Failure mode unidirectional GFRP coupons | 62 |

| | | |
|------|---|----|
| 3-14 | Typical stress-strain relationship for unidirectional coupons..... | 63 |
| 4-1 | Load capacity to weight ratio for scaled specimens..... | 82 |
| 4-2 | Local buckling failure mode for specimens A25 | 82 |
| 4-3 | Diagonal fracture failure mode for specimen B25 | 83 |
| 4-4 | Tension failure associated with necking and transverse fiber pull-out | 83 |
| 4-5 | Load-deflection curves for fiber angle 25 degrees | 84 |
| 4-6 | Load-deflection curves for fiber angle 30 degrees | 84 |
| 4-7 | Load-deflection curves for fiber angle 35 degrees | 85 |
| 4-8 | Effect of fiber volume fraction and fiber orientation on performance of FRP pole..... | 85 |
| 4-9 | Load-ovalization relationship for scaled specimens | 86 |
| 4-10 | Load-strain relationship for specimen A30..... | 86 |
| 4-11 | Load-strain relationship for specimen B30 | 87 |
| 4-12 | Load-strain relationship for specimen D30..... | 87 |
| 4-13 | Load Capacity to weight ratio for full-scale specimens..... | 88 |
| 4-14 | Local buckling failure mode for full-scale specimens | 88 |
| 4-15 | Local buckling failure mode for specimen 1 | 89 |
| 4-16 | Diagonal fracture failure mode for specimen 6 | 89 |
| 4-17 | Load-deflection relationship for specimens with 10 ⁰ longitudinal fibers | 90 |
| 4-18 | Load-deflection relationship for specimens with 20 ⁰ longitudinal fibers | 90 |

| | | |
|------|--|-----|
| 4-19 | Load–deflection for specimens with 5 ⁰ longitudinal fibers | 91 |
| 4-20 | Load–ovalization relationship for specimens with 10 ⁰ longitudinal fibers | 91 |
| 4-21 | Load–ovalization relationship for specimens with 20 ⁰ longitudinal fibers | 92 |
| 4-22 | Load–ovalization relationship for specimens with 5 ⁰ longitudinal fibers | 92 |
| 4-23 | Strain distribution along the height for specimen 1 | 93 |
| 5-1 | Laminate geometry and layer numbering system | 121 |
| 5-2 | Ovalization of GFRP poles and ovalization distribution along the height | 121 |
| 5-3 | Displacement variables for ovalization analysis of GFRP poles | 122 |
| 5-4 | Curvature of GFRP pole under applied load..... | 122 |
| 5-5 | Schematic for Moment and stress-ovalization relationship | 123 |
| 5-6 | Moment and stress–ovalization relationship for specimen 7 | 124 |
| 5-7 | Comparison between experimental and proposed model failure load | 124 |
| 6-1 | Layered quadrilateral eight–node shell element | 158 |
| 6-2 | The coordinate system of layered shell element..... | 158 |
| 6-3 | Increment Newton–Raphson procedure..... | 159 |
| 6-4 | Dimensions of the scaled specimens..... | 159 |
| 6-5 | Finite element mesh for scaled specimen A25 | 160 |
| 6-6 | Finite element mesh and applied load for full–scale specimens..... | 161 |
| 6-7 | Distribution of lateral displacement along the concrete base | 162 |
| 6-8 | Deformed shape for specimen A25..... | 162 |

| | | |
|------|--|-----|
| 6-9 | Values of the Tsai-Wu failure criterion along specimen A25 | 163 |
| 6-10 | Values of the Tsai-Wu failure criterion along specimen C25..... | 164 |
| 6-11 | Comparison between finite element model and experimental failure load..... | 165 |
| 6-12 | Comparison of load-deflection curves between experimental and finite element method..... | 165 |
| 6-13 | Deformed shape for full-scale Specimen 5 | 166 |
| 6-14 | Values of the Tsai-Wu failure criterion along full-scale Specimen 5..... | 167 |
| 6-15 | Values of the Tsai-Wu failure criterion value full-scale specimen 6..... | 168 |
| 6-16 | Comparison between experimental and finite element load-deflection relationship for 10° full-scale specimens | 169 |
| 6-17 | Comparison between experimental and finite element load-ovalization relationship for 10° full-scale specimens | 169 |
| 6-18 | Effect of circumferencial layers on the thickness of GFRP poles | 170 |
| 6-19 | Effect of circumferencial layers on the mass of GFRP poles | 171 |
| 6-20 | Effect of circumferencial layers on the lateral deflection of GFRP poles | 172 |
| 6-21 | Values of the Tsai-Wu failure criterion for a 12.2 m class1 GFRP poles without circumferencial fibers..... | 173 |
| 6-22 | Local buckling a 6.1 m class 1 GFRP pole with circumferencial fibers..... | 174 |
| 6-23 | Distribution of stresses in the fiber direction for a 12.2 m class1 GFRP pole without circumferencial fibers | 175 |
| 6-24 | Distribution of stresses in the transverse to fiber direction for a 12.2 m class1 GFRP pole without circumferencial fibers | 176 |

| | | |
|------|--|-----|
| 6-25 | Distribution of shear stresses in the fiber direction and transverse to fiber direction for a 12.2 m class1 GFRP pole without circumferencial fibers | 177 |
| 6-26 | Effect of longitudinal fiber angle on the thickness of GFRP poles..... | 178 |
| 6-27 | Effect of longitudinal fiber angle on the mass of GFRP poles | 179 |
| 6-28 | Effect of longitudinal fiber angle on the lateral deflection of GFRP poles | 180 |
| 6-29 | Compression side failure mode of a 12.2 m class1 GFRP poles with 15° longitudinal fiber angle | 181 |
| 6-30 | Tension side failure mode of a 18.3 m GFRP pole with 45° longitudinal fiber angle | 181 |
| 6-31 | Distribution of stresses in the fiber direction for a 12.2 m class1 GFRP pole with 15° longitudinal fiber angle..... | 182 |
| 6-32 | Distribution of stresses in the transverse to fiber direction for a 12.2 m class1 GFRP pole with15° longitudinal fiber angle..... | 182 |
| 6-33 | Distribution of shear stresses in the fiber and transverse to fiber plane for a 12.2 m class1 GFRP pole with15° longitudinal fiber angle..... | 183 |
| 6-34 | Distribution of stresses in the transverse to fiber direction for a 18.3 m class1 GFRP pole with 45° longitudinal fiber angle..... | 183 |
| 6-35 | Distribution of shear stresses in the fiber direction and transverse to fiber direction for a 18.3 m class1 GFRP pole with 45° longitudinal fiber angle..... | 184 |
| 6-36 | Design charts for 6.1 m GFRP poles (strength criterion)..... | 185 |
| 6-37 | Local buckling of a 6.1 m class 3 GFRP pole..... | 186 |
| 6-38 | Compression side failure mode for a 6.1 m class 1 GFRP pole..... | 186 |
| 6-39 | Design charts for 6.1 m GFRP poles (strength and deflection criteria)..... | 187 |

| | | |
|------|--|-----|
| 6-40 | Design charts for 12.2 m GFRP poles (strength criterion)..... | 188 |
| 6-41 | Design charts for 12.2 m GFRP poles (strength and deflection criteria)..... | 189 |
| 6-42 | Compression side failure mode for a 12.2 m class 1 GFRP pole with bottom diameter 225 mm..... | 190 |
| 6-43 | Design charts for 18.3 m GFRP poles (strength criterion)..... | 191 |
| 6-44 | Design charts for 18.3 m GFRP poles (strength and deflection criteria)..... | 192 |
| 6-45 | Compression side failure mode for a 18.3 m class H1 GFRP pole with bottom diameter 300 mm..... | 193 |
| 7-1 | Geometry and lay-up of composite tapered pole | 212 |
| 7-2 | (a) Coordinate system, (b) Tapered element and degrees-of-freedom..... | 212 |
| 7-3 | Convergence study for the tapered and prismatic beam elements | 213 |
| 7-4 | Natural frequency for various taper ratios and lamination angles | 213 |
| 7-5 | Natural frequency for various mass ratios and lamination angles | 214 |
| 7-6 | Natural frequency as a function of the mass ratio for $d_2/d_1 = 0.5$ | 214 |

CHAPTER 1

INTRODUCTION

1.1 GENERAL

When two or more distinct materials are combined in a macroscopic scale, the resulting material is referred to as a composite material. The basic constituents of such a material are usually combined in order that the composite exploits their best qualities. Therefore, the composite material exhibits overall properties that are superior to those of the individual constituents. The particular type of composite material that was investigated in this research project was a fibrous composite material referred to in the industry as Fiber-Reinforced Polymers (FRP). This material is obtained when fibers of relative high strength, such as carbon, aramid, or glass, are impregnated with lightweight resin which forms the matrix or the binder material of the composite whose main function is to support and protect the load carrying fibers. The main reinforcement of the matrix is provided by the fibers which are characterized by very high length-to-diameter ratios.

One of the major attributes that has made FRP an attractive alternative to traditional materials in a variety of civil engineering applications is their high strength-to-weight ratio (Labossiere and Turkkan 1992).

Military aircraft designers were among the first to realize the tremendous potential of composites with high specific strength and high specific stiffness since performance and maneuverability of those vehicles depend so heavily on weight (Gibson

1995). Fiber-reinforced polymer technology gained its roots during World War II with the development of the B-17 bomber program. Composite structural elements are now used in a variety of components for automotive, aerospace, marine, architectural structures, and sports equipment.

The use of FRP in civil engineering applications has also increased in recent years following extensive laboratory research. Bridges and structures using FRP as tensile elements for prestressed concrete have been built in Europe, Japan, USA, and Canada (Mufti et al 1991). Oil companies utilize FRP products in a number of applications ranging from simple roof trusses to very sophisticated structures such as offshore oil drilling platforms. The lightweight characteristic of FRP makes handling and installation easier resulting in lower costs of assembly. The fact that FRP are lightweight, also makes them very attractive as a rehabilitation material. Chimneys, columns, slabs and girders have been strengthened to accommodate overloads from earthquakes or changes in code requirements using carbon FRP products (Muffti et al 1992). These products are most often unidirectional fiber tapes or fiber winding strands and fabrics. Flexural and shear strengthening are also possible using these products. Another application involves retrofitting of highway bridges to increase seismic resistance of existing bridge columns. Recent studies (Saadatmanesh and Eshani 1994) have shown that composite overwraps or jackets can be effectively used to strengthen bridge support columns.

1.2 POLES AS TRANSMISSION AND DISTRIBUTION STRUCTURES

Traditional materials such as wood, steel, and concrete are commonly used to construct electrical transmission and distribution poles. However, the shortage of wooden poles, their short life expectancy, and various environmental concerns have promoted electric utility companies to search for a cost-effective alternative. Wooden poles are continuously exposed to weather, fungi, woodpeckers, etc., which result in a very significant deterioration of their load bearing capacity with time. The service life of wooden poles is approximately 30 to 40 years (Vanderbuilt and Criswell 1988). Any extension of this service life requires continuous inspection and follow-up care. In a number of European countries, concrete poles are used. The main disadvantage of concrete poles is their weight, which drastically increases transportation and erection costs. Chemical influences on the concrete surfaces due to environmental impact can also affect their long term performance. As in the case of other concrete structures, concrete poles are subject to corrosion of the steel reinforcement, resulting in further strength deterioration and expensive maintenance. Steel is the most common material for the construction of transmission poles in North America. These poles, however, are very expensive. Corrosion protection is of primary concern in steel poles, which must be painted or galvanized, a process which does not always guarantee long term protection. Generally, traditional poles made of wood, concrete, or steel are subject to deterioration under environmental attacks. Regular maintenance is essential to prolonging serviceability of these poles.

On the other hand, FRP, and more specifically Glass Fiber–Reinforced Polymer (GFRP), poles are lightweight and corrosion resistant. Being lightweight is a major advantage of GFRP poles making them suitable for transportation and installation in mountain terrains and marshes. Although the initial cost of GFRP poles may be higher than traditional poles, the long term benefits these poles provide, make their selection attractive. The use of GFRP poles is not new. A number of companies are already involved in the production of such poles. Research in this area, however, is limited.

1.3 HISTORICAL DEVELOPMENT OF GFRP POLES AND FILAMENT WINDING PROCESS

The earliest known GFRP distribution poles were manufactured by Gar Wood Industries in 1954 (Derrick 1996). During this period, there was considerable interest in fiberglass pole technology. One of the original installations of GFRP poles was in Hawaii by Hawaii Electric which installed a series of GFRP poles in 1960. Although these poles are almost 30 years old and in an area subjected to high winds by hurricanes Iwa and Iniki, they are still in use and performing their function well.

In 1981, the city of Alameda, California, replaced secondary distribution poles to reach back yard areas with GFRP poles (Derrick 1996). Using the technology available at this time, over 800 GFRP poles were installed and included an early form of climbing steps. These poles were well accepted by the city and are still performing well.

The Canadian Electric Association (CEA) and ABCO plastics conducted a joint market research on the application of GFRP for utility and lighting poles in 1982 and

issues related to the design and manufacturing of GFRP poles were discussed in a subsequent report (Escher 1982). Through the market study, the report concluded that there was an interest in GFRP poles for street lighting in main street urban renewal projects where appearance is a consideration and where higher priced concrete poles are used.

The first true wide usage of GFRP poles came with the construction of a primary line through the rugged mountainous terrain in Montana, USA (Miller 1994). The Montana Power Company installed 75 GFRP poles manufactured by Shakespeare in the U.S., at the Mystic Lake power plant. Since this installation, a wide array of installations has been completed using class 2 through class 5^{*} poles in lengths 20 to 60 feet (6.1 to 18.3 m).

A number of advanced processes are available which can be used to produce high performance FRP structures. These processes are generally automated such as pultrusion, braiding, and filament winding. Filament winding is an attractive process for a number of reasons such as low production cost, flexibility of design, controlled fiber orientation, and high fiber volume. The process of filament winding of FRP member consists of placing resin impregnated bands of fibers under controlled tension through a payout eye on a rotating mandrel in a prescribed geometric path and pattern. For axisymmetric components, the pattern must be repeated to provide complete coverage of the mandrel.

Filament winding was first introduced by the M. W. Kellogg Co. in 1947 when it built the first dedicated filament winding machine (Munro 1988). The first filament

* classification method of wooden poles is discussed in details in section 2.1

wound product was the nozzle for the X248 rocket motor unit, produced in 1948, using E-glass with epoxy resin for higher temperature capability (Murphy 1998). The first recorded commercial use of filament winding was for the production of lightweight FRP hoops for the Manhattan Project in 1954, which later became the basis for Naval Ordnance Laboratory rings used in tension and shear tests (Murphy 1998). The first commercial filament winding machines were designed and produced by McClean Anderson in the 1960s. Goldworthy Engineering designed and built the first six-axis machine for the United States Army Aviation Systems Command in 1965.

Filament winding is now being used in a variety of industrial and structural applications. Helically wound tube-type components composed of either fiberglass or graphite fiber are used for MX missile and solid rocket booster casings. Filament wound composite automotive and helicopter drive shafts are already in service. Both spherical and elongated filament wound fiber composite pressure vessels are utilized in different applications such as for the storage of compressed natural gas (CNG). Other axisymmetric yet more complex structures include rectangular and square box sections, tapered poles, and ellipsoid shapes. Non-axisymmetric structures included pipe tees, elbows, T-shaped air ducts, leaf springs, and bumper frames. Other non-axisymmetric structures have been built included helicopter blades and boom sections, windmill blades, and aircraft fuselage.

1.4 SCOPE

One of the main characteristics of GFRP sections is their low stiffness, which leads to excessive deformation and instability. Thus, in the case of GFRP poles, the

classical linear beam–column theory may not be adequate for their analysis and design. Furthermore, the relatively small thickness–to–radius ratio of GFRP poles and the high stress near ground level result in distortion of the cross section which, in turn, may significantly reduce the load carrying capacity of these poles. A typical distortion of hollow cross sections is the so–called ovalization, which may not be accounted for by the beam–column theory. Ovalization is the leading factor in determining the ultimate load of GFRP poles and must be included in the analysis.

The main objectives of research reported in this thesis are as follows:

- a) to develop both rational and numerical models that account for the nonlinear behavior and cross section distortion of GFRP poles;
- b) to verify the developed theoretical models through experimental program conducted on filament wound GFRP poles;
- c) to use the experimental and the theoretical results to define optimum configurations of GFRP poles for use in the construction of utility lines; and,
- d) to develop design charts and guidelines for GFRP utility poles based on a realistic model of member behavior.

In this research program, the effect of fiber orientation, layer sequence, and wall thickness on the behavior and load carrying capacity of GFRP poles were investigated.

In the experimental investigation, twelve scaled specimens and twelve full–scale pole specimens were tested as cantilever in bending. The scaled specimens had a total

height of 2.5 m. The bottom and top diameters were 100 mm and 75 mm respectively. The wall thickness for the scaled specimens was varied from 0.88 mm to 2.2 mm. The fiber orientation with respect to the longitudinal direction was varied from 25° to 35° in 5° increments. The specimens were fixed to a concrete base with free length of 2.07 m. The load was applied laterally at 1.94 m above the fixed base (Polyzois et al. 1999). The full-scale specimens had a total height of 6.25 m. The bottom and top diameters were 416 and 305 mm, respectively. Both circumferential and longitudinal fibers were implemented in the manufacturing. Three fiber orientations with respect to the longitudinal axis were investigated: 5°, 10°, and 20° (Ibrahim et al. 1999a and Ibrahim. et al. 1999b). The specimens were fixed at the base in a segmented concrete block. The load was applied horizontally 600 mm below the top, as required by the ANSI standard (1992).

In the theoretical investigation, a nonlinear analytical model was developed to predict the critical buckling load (Ibrahim and Polyzois 1999). In this model, the progressive ovalization of GFRP poles under steadily increasing bending moment and the occurrence of local buckling were investigated. The developed model accounts for the cross section distortion (ovalization) of the section. The laminate stiffness and equivalent moduli were derived from the classical lamination theory.

The finite element (FE) method was utilized to perform a numerical analysis for GFRP poles (Ibrahim et al. 1999b). More specifically, the ANSYS finite element program (1995) was employed to analyze the tested specimens and to predict the failure loading. A comparison between the experimental results and the results obtained from both the theoretical and the numerical analysis showed very good correlation. Once the

results from the FE analysis were verified through comparison with the experimental results, it was used to conduct an extensive parametric study to determine the influence of other parameters, such as fiber lay-up and cross-section dimensions, on the behavior of a series of GFRP poles.

The current research program was extended to include the dynamic behavior of GFRP poles by developing a simplified finite element model (Polyzois et al. 1998). Modal analysis was performed to calculate the natural frequency of GFRP poles with various configurations.

This thesis consists of eight chapters. In Chapter one an introduction of the topic and a summary of the scope and objectives of this study are presented.

Chapter two presents a survey of the related literature. This survey reviews the history of GFRP poles, the theoretical investigations, and the failure criteria of composite materials.

Chapter three describes the experimental program. This includes a description of the specimens, the test setup, the test preparation, the dimensions and variables of the tested GFRP poles.

Chapter four presents the results from the experimental program. The observed behavior and failure modes are also discussed in this chapter.

Chapter five presents a rational method for estimating the material properties, the strength and the equivalent laminate properties of GFRP poles. A nonlinear model for the ovalization analysis is also formulated in this chapter.

Chapter six covers the numerical analysis of GFRP poles. The finite element method is adopted as a method of analysis in this chapter. The analysis includes the effect of large deformation and cross section distortion. An extensive parametric study and design charts are also presented in this chapter.

Chapter seven presents a simple finite element formulation for the dynamic analysis of GFRP poles. Modal analysis is presented in this chapter to obtain the natural frequency and period of poles with various lengths and geometry.

Chapter eight summarizes the results obtained from the experimental and the theoretical analysis. It also contains conclusions and suggestions for future work.

CHAPTER 2

LITERATURE SURVEY

2.1 POLE DESIGN SPECIFICATIONS AND STANDARDS

The unguyed single-pole structure is commonly used to support transmission and distribution lines whose design must be based on a reliability-based methodology. To accomplish this, the variable nature of the resistance of the pole and the loads acting on it must first be defined. The basic concept of reliability-based design is expressed by the following expression:

$$\alpha R_n \geq \beta Q_n \quad (2-1)$$

where R_n and Q_n are the nominal values of the resistance and the load effect respectively, and α and β are the strength and the overload factors, respectively. The values of the strength and the overload factors are specified by the National Electrical Safety Code (NESC 1997) on the basis of the grade of construction of the transmission and distribution lines. Grades of construction are required to differentiate between the relative degree of strength and expected performance. Differences in voltage classifications of facilities also affect the required grades of construction. According to NESC (1997), the current grades of construction applicable to supply lines are designated as B, C, and N; for grades B and C, specific strength and overload factors are provided. Grade B represents the strongest construction. For wood and reinforced concrete poles, two methods for determining the strength and the overload factor are given by NESC (1997):

the standard method and the alternate method. Both methods meet the basic requirements of safety. For steel and prestressed concrete poles, only the standard method can be used. The strength and overload factors for the standard method are given in Tables (2-1) and (2-2). The strength and the overload factor for the alternate method are given in Tables (2-3), (2-4).

Table (2-1): Strength factors for the standard method (NESC 1997)

| Grade of construction | Grade B | Grade C |
|---|---------|---------|
| Strength factors for the case of combined wind and ice | | |
| Metal and prestressed concrete | 1.00 | 1.00 |
| Wood and reinforced concrete | 0.65 | 0.85 |
| Guy wire | 0.90 | 0.90 |
| Guy anchor and foundations | 1.00 | 1.00 |
| Strength factors for the case of extreme wind | | |
| Metal and prestressed concrete | 1.00 | 1.00 |
| Wood and reinforced concrete | 0.75 | 0.75 |
| Guy wire | 0.90 | 0.90 |
| Guy anchor and foundations | 1.00 | 1.00 |

Table (2-2): Overload factors for the standard method (NESC 1997)

| Overload factors | | |
|--|---------|---------|
| Loading type | Grade B | Grade C |
| Vertical loads | 1.50 | 1.50 |
| Transverse loads | | |
| a) Wind | 2.50 | 2.20 |
| b) Wire tension | 1.65 | 1.30 |
| 1) Longitudinal loads at crossing | | |
| a) In general | 1.10 | N. R.* |
| b) At deadends | 1.65 | 1.30 |
| 2) Longitudinal loads elsewhere | | |
| a) In general | 1.00 | N.R.* |
| b) At deadends | 1.65 | 1.30 |
| Extreme wind case | 1.00 | 1.00 |

* N.R= No requirement is specified

Table (2-3): Strength factor for the alternate method (NESC 1997)

| | Grade B | Grade C |
|---|---------|---------|
| Strength factors for use with case of combined wind and ice and extreme wind | | |
| Wood and reinforced concrete | 1.00 | 1.00 |

Table (2-4): Overload factors for the alternate method (NESC 1997)

| Loading type | Overload factors | | | |
|---------------------|------------------|----------------|----------------|----------------|
| | Grade B | | Grade C | |
| | When installed | At replacement | When installed | At replacement |
| Vertical loads | 2.20 | 1.50 | 2.20 | 1.50 |
| Transverse loads | | | | |
| a) Wind at crossing | 4.00 | 2.67 | 2.67 | 1.33 |
| b) Wind elsewhere | 4.00 | 2.67 | 2.00 | 1.33 |
| c) Wire tension | 2.00 | 1.33 | 1.33 | 1.00 |
| Longitudinal loads | | | | |
| a) In general | 1.33 | 1.00 | N. R.* | N. R.* |
| b) At deadends | 2.00 | 1.33 | 1.33 | 1.00 |
| Extreme wind | 1.33 | 1.00 | 1.33 | 1.00 |

* N.R = No requirement is specified

As it is evident of Tables (2-1) and (2-2), the standard method recognizes both the uncertainty of the applied loads and the relative degradability and nonhomogeneity of the materials. The standard method separate these effects by setting an appropriate strength factor for each material, while keeping the overload factor independent of the material used for construction. On the other hand, the alternate method accounts for both the uncertainties in the material strength and the loading by setting higher values for the overload factor and assuming a strength factor equal to 1.0. According to NESC (1997), only one method may be used in the design of each component of the transmission line. For example, the designer can not use the standard method to check the case of extreme wind and the alternate method to check the case of combined wind and ice. However, one

method could be used for the design of the pole and another method could be used for the design of the crossarm.

The resistance or load carrying capacity of a pole structure depends on the material used in the construction. The load carrying capacity can be determined experimentally, through testing of pole structures under various loading conditions, or it can be determined theoretically through the well-known strength of materials rules described in various specifications and standards. For wooden poles, ANSI Standard O5.1 (1992) categorizes poles by classes according to their load carrying capacity. The class of a pole of a given diameter and length is obtained by assuming the pole has uniform taper and it is loaded by a single transverse load placed two feet from the tip. By assuming a value for the modulus of flexural for a given wood species, the value of the transverse load can be computed. This transverse load can then be used to determine the moment resistance of a wooden pole. ANSI O5.1 (1992) gives the pole size as a function of the class load and wood species. The transverse load for the fifteen classes defined in ANSI O5.1 (1992) is shown in Table (2-5). Thus, a class 1 pole can carry 20 kN (4500 lb) regardless of species. The transverse loads listed in Table (2-5) are the mean ultimate loads that the various corresponding poles can carry. There are no safety factors included in these values. The Canadian Standard for Wood Utility Poles and Reinforcing Stubs (CAN/CSA-O15-90) has adopted the same method for classification of wooden poles. However, this standard only defines the transverse load for the first thirteen classes (class H6 to class 7). The value of the transverse load placed 600 mm (2 ft) from the tip described by CAN/CSA-O15-90 is identical to that given by ANSI O5.1 (1992).

Table (2-5): Transverse load capacity of wooden poles according to ANSI O5.1

| Class | Transverse load (lb) | Transverse load (kN) |
|-------|----------------------|----------------------|
| H6 | 11400 | 50.7 |
| H5 | 10000 | 44.5 |
| H4 | 8700 | 38.7 |
| H3 | 7500 | 33.4 |
| H2 | 6400 | 28.5 |
| H1 | 5400 | 24.0 |
| 1 | 4500 | 20.0 |
| 2 | 3700 | 16.5 |
| 3 | 3000 | 13.3 |
| 4 | 2400 | 10.7 |
| 5 | 1900 | 8.5 |
| 6 | 1500 | 6.7 |
| 7 | 1200 | 5.3 |
| 9 | 740 | 3.3 |
| 10 | 370 | 1.6 |

According to the ASCE Manual for Design of Steel Transmission Pole Structures (1990), the design approach used to determine the load carrying capacity of steel poles is based on the ultimate strength method. For instance, the bending resistance of a steel pole with a circular cross section satisfying the local buckling condition is based on the yield strength of the steel.

A method to calculate the various loads acting on transmission and distribution poles for grade B and C constructions is given in NESC (1997) which specifies that three loading conditions have to be checked:

- a) combined ice and wind loading;

- b) extreme wind loading; and
- c) longitudinal loading due to tension in conductors that are not balanced.

It is recognized that transmission line failures usually involve complicated combinations of these and other types of loads, such as torsional loads set up by wire breaks, loads due to conductor oscillations and swaying of supporting structures, and many others. However, according to NESC (1997), experience has shown that the strength requirements included in the simple assumption of the three types of load will provide adequate overall safety.

For case of combined ice and wind, the amount of radial thickness of ice accumulated on the conductor depends on the weather conditions where the line is constructed. Three degrees of loading conditions are recognized: heavy, medium, and light loading. For instance, in heavy loading conditions the radial thickness of ice on the conductor should be taken as 12.5 mm and the wind pressure calculated on the projected area of the ice-coated conductors and on pole without ice-coating should be taken as 190 Pa.

Extreme wind loading conditions are taken into account in poles exceeding 18 m (60 ft). In this case, the horizontal wind speed is based on five-minute period averages. The horizontal load is determined as follows NESC (1997):

$$\text{Load (in Newtons)} = 0.613 V^2 \times \text{shape factor} \times \text{projected area (in m}^2\text{)} \quad (2-2)$$

where, V is the wind speed in m/sec.

If along a transmission line, there is a change in the grade of construction, a failure on the weaker side of the line will affect the stronger side. Therefore, the longitudinal load at such point is based upon the assumption that a certain number of wires will break. Where wires smaller than AWG No. 2 are used, it is assumed that two-thirds of these wires will break. However, to ensure protection in cases where there are also a number of larger wires on the pole, a minimum unbalanced load equal to the loaded tension in two of the largest wires is assumed in design. The actual tension in the conductors corresponding to the existing sag is used in the computation of longitudinal load. The poles in a transmission line should also be capable of supporting the unbalanced longitudinal load created by the difference in tensions in the wires in adjacent spans caused by unequal vertical loads or unequal spans. Consideration should be given to longitudinal loads that may occur during wire stringing operations.

2.2 EXPERIMENTAL INVESTIGATIONS OF GFRP POLES

The results of a market research conducted by Martin and Richter (1974) for the possible application of GFRP poles for lighting standards showed that GFRP poles can be widely used in the utility pole market. The technical phase of this market research included the testing of two aluminum poles and seven GFRP poles. Test results showed that the load-deflection behavior of the fiber glass poles was near linear up to failure which was due to local section collapse. Martin and Richter also concluded that fiber glass poles could be designed so that their stiffness and strength are equal to those of their aluminum counterparts with little weight penalties. However, this level of performance,

the authors concluded can only be attained through proper reinforcement orientation and effective pole size design.

In 1988, Bell initiated its own investigation of GFRP poles. The experimental program was conducted at the Centre de Recherche du Reseau Exterior (CERRE) (McClure et al 1992). The tested specimens were tapered with a hollow cross section and were manufactured by centrifugal casting. The tests indicated that GFRP poles could safely resist transverse loads comparable to those of wooden poles under same conditions. The behavior of the GFRP poles was found to be truly elastic even for large deflections.

A similar experimental investigation was conducted by Shakespeare Inc., on filament wound GFRP poles in 1993 (Derrick 1996). Class 4 GFRP poles were tested at the National Test Labs of Engineering Data Management (EDM) in Colorado, USA. The tests were successful as each pole met or exceeded the strength requirement specified for wooden poles.

A limited experimental program was also conducted in the Department of Civil and Geological Engineering, University of Manitoba in 1993 (Lin 1995). The objective of this program was to investigate theoretically the behavior of GFRP under cantilever loading conditions. Four scaled specimens were also tested. These were prismatic and had a circular hollow cross section with wall thickness of 6 mm. According to the test results, a linear behavior of the specimens was observed till failure.

2.3 THEORETICAL INVESTIGATIONS OF GFRP POLES

The theoretical analysis of GFRP poles requires complete understanding of the behavior of composite materials. Fiber-reinforced poles can be considered as shells of revolution. Both rational analyses and finite element methods may be used for the analysis of such structures. Thin-walled GFRP poles are subjected to considerable cross section distortion which may significantly affect their behavior. To account for this distortion, a special nonlinear analysis known as ovalization analysis is required to predict the behavior. The choice of appropriate failure criteria is essential in determining the ultimate load carrying capacity of GFRP poles.

2.3.1 ANALYTICAL ANALYSIS OF LAMINATED SHELLS

Most of the analyses of fiber reinforced laminated shells employ the classical lamination theory based on the Love-Kirchoff hypothesis. The general theory of anisotropic composite shells was developed by Dong et al (1962). Complete analysis of the stability of anisotropic cylindrical shells under combined loads has been given by Cheng and Ho (1963). Ugural and Cheng (1968) investigated the buckling of composite cylindrical shells under pure bending. The problem was solved by assuming suitable expressions for midplane surface displacements, and solving Flugge's differential equation. Based on their research results, Ugural and Cheng indicated that the coupling effect is very important in determining the buckling load of composite cylinders.

Holston (1968) investigated the buckling load of filament wound cylinders under axial compression. Jones and Morgan (1975) studied the buckling and vibration behavior

of cross ply laminated circular cylindrical shells by applying the classical laminated theory and solving the Donnell-type differential equations. They showed that for both buckling and vibration of antisymmetric cross ply shells, the effect of coupling between bending and extension vanishes rapidly as the number of layers increases.

Although the laminate analysis, performed using the classical lamination theory, provides a simple and direct procedure, it does not include the transverse shear deformation. Application of such theories could lead to significant errors, especially, in the case of small radius-to-thickness ratio. Whitney and Sun (1973) developed a shear deformation theory for laminated cylindrical shells that includes both transverse shear deformation and transverse normal strain as well as expansional strains. Waltz and Vinson (1976) investigated the interlaminar stresses in laminated composite cylindrical shells. They utilized the elastic shell theory and included in their formulation transverse shear deformations. By treating each lamina individually and imposing stress and displacement boundary conditions between laminae, the governing equations of each individual laminae are combined yielding the interlaminar shear.

Reddy (1984) developed closed form solutions for computing deflections and natural frequencies of simply supported cross ply laminated and quasi-isotropic shells. These closed-form solutions were derived using the shear deformation version of the Sanders shell theory to account for transverse shear strains and rotations about the normal of the shell.

A comparison between different models used to analyze laminated composite shells has been reported by Noor et al (1991). The models used in that study are classified

into three groups: in the first group are the three dimensional and quasi three dimensional elasticity models; in the other two groups are the first order shear deformation shell theories based on linear displacement or strain variation through the entire shell thickness and the higher order shear deformation shell theories based on nonlinear variation of displacements or stresses through the shell thickness. The results of this study showed that for most practical problems, transverse shear deformation has much more pronounced effect on the response of multilayered composite cylinders than transverse normal strain and stress. In addition, it has been indicated that an accurate prediction of the stress and displacement distribution through the thickness of multilayered cylinders requires the use of three dimensional equilibrium and constitutive relations. These equations can be used in an inexpensive, postprocessing mode with any of the modeling approaches based on two dimensional theories.

2.3.2 FINITE ELEMENT ANALYSIS PROGRAMS

The finite element analysis is considered one of the most powerful numerical analysis tools in structural engineering. It has been used in the analysis of complex civil engineering problems for which an exact or a closed-form solution is unattainable. The finite element method can be coupled with the laminated shell theory for computing the state of stress and deformation in GFRP poles.

Navaratna et al (1968) were among the early researchers to use the finite element method to analyze the stability of shells of revolution. The approach used by Navaratna et al to develop the geometric stiffness matrix was also followed by Gould and Basu (1977) for the linear buckling analysis and incremental deformation analysis of rational shells.

Noor and Mathers (1974) applied the finite element analysis to study the geometrically nonlinear behavior of laminated shells using eight noded and twelve noded shear flexible quadrilateral shell elements. Reddy (1981) performed the large deflection analysis of layered anisotropic shells using several shell theories and a doubly curved shear deformable shell element. Cho and Reddy (1984) analyzed laminated composite shells using a three dimensional degenerated finite element. This formulation allowed the study of a wide variety of multilayered solid elements and moderately thick and thin laminated shells. Saigal et al (1986) presented computational procedures for the finite element analysis of laminated anisotropic composite thin shells including imperfections. The derivation of the nonlinear geometric element stiffness matrices was based on total Lagrangian description.

Jun and Hong (1988) used the nonlinear finite element procedure to study the buckling behavior of laminated composite cylindrical shells. They also conducted a parametric study on the effect of fiber angle on the buckling load of the shells. Yunus et al (1989) presented an efficient numerical integration scheme for calculating the stiffness matrix of doubly curved, multilayered composite shell finite element. This formulation was based on an explicit separation of the thickness variable from the shell surface parallel variables. The results of this research indicated that the proposed formulation is an order of magnitude more economical than the conventional scheme.

Pre- and postbuckling behaviors of curved composite shells were studied by Jeusette and Laschet (1990) using the finite element analysis. Three dimensional multilayered finite element analysis coupled with an automatic incremental iterative method was used to find the nonlinear response laminated composite shells.

2.3.3 OVALIZATION OF TUBULAR SECTIONS UNDER BENDING

When a long thin-walled circular tube is subjected to bending, it is found that the cross section of the entire tube becomes progressively more oval as the bending curvature increases. The first investigation of the ovalization behavior of long tubes was made by Brazier (1927). He showed that when an initially straight tube is bent uniformly, the longitudinal tension and compression which resist the applied bending moment tend to flatten or ovalize the cross section, as shown in Figure (2-1). This distortion in turn reduces the flexural stiffness (EI) of the tube as the curvature increases. Brazier showed that under steadily increasing curvature the bending moment reaches a maximum value. The tube becomes unstable and buckles after the maximum bending moment is reached. Brazier's solution for infinitely long isotropic cylindrical shells subjected to pure bending was based on the assumption that the radial deformation is small in comparison to the section radius and that the shell is inextensional in the circumferential direction. With these assumptions, Brazier was able to derive an expression for the total strain energy per unit length of the tube in terms of the change in curvature. By minimizing this expression with respect to the change in curvature, Brazier found the critical bending moment to be:

$$M_{cr} = \frac{2\sqrt{2}}{9} \frac{E\pi r t^2}{\sqrt{1-\nu^2}} \quad (2-3)$$

where, E is the material elastic modulus, r is the original radius of the tube, t is the wall thickness, and ν is the Poisson's ratio.

A more general formulation of the ovalization problem was derived by Reissner (1959), who also dealt with the case of thin-walled, cylindrical tubes of arbitrary cross section subjected to bending. Fabian (1977), derived a numerical solution to Reissner's equation and compared his results to those obtained through Brazier's solution. He concluded that Brazier's solution overestimates the critical moment by approximately 3%. This indicates that the gains in Brazier's analytical simplicity and computational efficiency for the approximate solution are well worth the small difference in the results.

The first investigation on the ovalization of infinitely long composite cylindrical tubes subjected to pure bending was presented by Keward (1978). Keward applied a similar treatment and assumptions as Brazier to deduce an expression of the critical bending moment of composite tubes in the following form:

$$M_{cr} = \frac{4\sqrt{2}}{3\sqrt{3}} \sqrt{\frac{D_{22}}{E_x t}} E_x \pi r t \quad (2-4)$$

where, E_x is the effective modulus in the longitudinal direction of the composite laminate, D_{22} is the circumferential bending stiffness, r is the original radius of the tube, and t is the tube wall thickness.

Libai and Bert (1994) presented a new approach based on a mixed variational functional to predict the nonlinear ovalization behavior of orthotropic cylindrical tubes. Their analysis accounted for both infinitely long tubes and tubes of finite length subjected to pure moment or moment gradient. They adopted the semi-membrane approximation and assumed symmetry of the cross section distortion. They also showed that their

solution could be reduced to that of Brazier's and Keward's solution given by Equations (2-3) and (2-4), respectively.

Li (1995) investigated the ovalization of composite tubes subjected to both static and dynamic applied loads. Li showed that the dynamic instability of composite tubes occurs at a moment equal to 71% of the corresponding critical static moment but deformations of the longitudinal bending curvature and ovalization at the critical instability state are much larger than those corresponding to the static instability.

Tatting et al (1996) developed a new approach for the ovalization analysis of orthotropic infinitely long tubes based on the classical nonlinear shell theory along with semi-membrane constitutive relations. They showed that the traditional cylindrical shell equations are not sufficient to model accurately the nonlinearity of the ovalization problem and they derived suitable corrections. The formulation resulted in a highly nonlinear fourth order differential equation which was solved numerically using the finite difference technique. The results of Tatting et al (1996) agree exactly with the numerical solution of Fabian (1977) who used similar techniques but who also introduced the loading through ad hoc methods. In addition, Tatting et al (1996) showed that Brazier's Equation (2-3) gives excellent results despite its simplicity. Tatting et al (1997) extended their nonlinear shell theory to predict the limit bending moment of finite length composite tubes. They showed that their solution agrees with the rigorous nonlinear finite element results performed by Stephens et al (1975).

2.3.4 EFFECT OF OVALIZATION ON LOCAL BUCKLING

As discussed in the previous section, the relationship between the applied bending moment on a tube and the curvature is a nonlinear one as shown in Figure (2-2). According to Tatting et al (1996), the highest point on the nonlinear load path corresponds to the collapse moment for long tubes under bending. Once the maximum bending moment is reached, the ability of the tube to carry additional load is gone and failure occurs. The value of this maximum bending moment for an infinitely long composite tube is given by Equation (2-4). Though this maximum moment is theoretically true for some tubes with very large length-to-radius ratios, most tubes collapse before the maximum moment is reached. This collapse is due to the formation of a kink at the point of maximum stress. The mechanism that produces this kink is local buckling on the compressive side of the tube. However, the ovalization effect still plays a significant role in this failure mode. The development of local buckling depends, substantially, on the local curvature of the cross section.

Siede and Weingaten (1961) predicted the bifurcation buckling load by using a linear membrane prebuckling state over a limited length of simply supported cylinders in pure bending. They showed that under pure bending, local buckling occurs when the extreme fiber compressive stress reaches the classical buckling stress of a shell under pure axial compression. This stress is given by:

$$\sigma_{cr} = \frac{1}{\sqrt{3}} \frac{Et}{\sqrt{(1-\nu^2)} r} \quad (2-5)$$

However, due to ovalization, the cross section of the tube deforms into an oval and the radius of curvature at the critical location increases, thus, lowering the critical buckling stress. Hutchinson (1968) showed that the critical stress formula (2-5) is still, approximately, correct for tubes having smooth non-circular cross sections provided that the local radius of curvature is used in place of the original radius, r , of the circular tube. The modified critical stress, which can be used as a criterion for local buckling, is given as follows:

$$\sigma_{cr} = \frac{1}{\sqrt{3}} \frac{Et}{\sqrt{(1-\nu^2)} \rho} \quad (2-6)$$

where, ρ is the new radius of cross section after being ovalized.

Tatting et al (1996) showed that the corresponding critical buckling stress for composite materials is:

$$\sigma_{cr} = \frac{2\sqrt{D_{11}E_y t}}{t\rho} \quad (2-7)$$

where, D_{11} is the longitudinal bending stiffness and E_y is the elastic modulus in the circumferencial direction.

A good estimate of the collapse moment may be obtained by determining the axial stress corresponding to the compressive side of the tube given by the critical value in Equation (2-7).

Almorth and Starnes (1975) also performed a stability analysis from the nonlinear prebuckled state and examined the ovalization and local buckling of limited length

cylindrical shells using the energy method and the finite difference technique. The STAG code (Structural Analysis of General Shell) was used to analyze five isotropic tubes whose radius-to-thickness ratio was equal to 100 and whose length-to-radius ratios varied. Their results indicated that for tubes with length-to-radius ratio equal to 20, local buckling occurs very close to the maximum critical moment. However, for shorter tubes local buckling occurs before the maximum ovalization moment is reached.

Tatting et al (1997) applied Equation (2-7) to determine the failure load of tubes with various length-to-radius ratios. Their results showed excellent agreement with those presented by Stephens et al (1975) who used a nonlinear finite element analysis.

2.3.5 MATERIAL FAILURE CRITERIA

The limit state design criteria of a structure require that the stresses and strains resulting from factored loads do not exceed the factored resistance of the material at failure. While the loading conditions are determined through observations and measurements, the material resistance is determined through testing. In case of multi-axial stress fields, a suitable failure theory should be used. Failure is assumed to have taken place in the material when a loading condition has exceeded the limit defined by the particular failure criterion chosen. In the case of isotropic materials, for example, that exhibit yielding, either the shear stress theory (Tresca criterion) or the distortional energy theory (von Mises criterion) is commonly used to define failure. Unlike isotropic materials, the strength properties of FRP are strongly dependent on the direction of loading. In other words, FRP are classified as orthotropic materials.

Several failure criteria have been developed for orthotropic composite materials. All these criteria are phenomenological in nature, having evolved from attempts to develop analytical models to describe experimental observations of failure under combined stresses (Gibson 1995). As pointed out by Wu (1974), a large experimental data base alone could form the basis of an empirical failure criterion, but the semiempirical mathematical model is preferable because it can reduce the number of required experiments and provide a more systematic approach for design.

The maximum stress criterion for orthotropic composites was first suggested by Jenkins (1920) as an extension to the maximum normal stress theory (Rankin theory) for isotropic materials. This criterion predicts failure when any principle axis stress component is exceeded. The failure surface for the maximum stress criterion in $\sigma_1 - \sigma_2$ space is a rectangle, as shown in Figure (2-3). It can be noted from this figure, that this failure surface is independent of the shear stress τ_{12} , and that the criterion does not account for possible interaction between stress components.

Waddopus (1967) proposed the maximum strain criterion of failure for orthotropic composite materials as an extension to the maximum normal strain theory (St. Venant's theory) for isotropic materials. According to this failure criterion, failure occurs when the principal strain component is reached. In $\sigma_1 - \sigma_2$ space, the maximum strain failure criterion surface is a skewed parallelogram, as shown in Figure (2-3).

In 1948, Hill suggested that the von Mises criterion could be modified to include the effects of induced anisotropic behavior in initially isotropic metals during large plastic deformations. Hill used the, so-called, quadratic interaction criteria to account for

the interaction of the stress components. An extension to the Hill's criterion failure to orthotropic, transversely isotropic lamina was suggested by Azzi and Tsai (1965). This failure criterion is often referred to as the Tsai-Hill criterion. The failure surface generated by this criterion is an ellipse, as shown Figure (2-3). This ellipse is symmetric about the axes because of the assumption of equal strengths in tension and compression. One way to account for different strengths in tension and compression is to include terms that are linear in the normal stresses σ_1 , σ_2 , and σ_3 , as suggested by Hoffman (1967).

Tsai and Wu (1971) proposed an improved and simplified version of a tensor polynomial failure theory for anisotropic materials that had been suggested earlier by Gol'denblat and Koponov. This failure criterion included linear terms that characterize the different strength in tension and compression and quadratic terms that provide an ellipsoid shaped failure envelope in the stress space. The strength parameters needed to define the failure criterion could be obtained from uniaxial and biaxial tests, as reported by Tsai and Wu.

Tennyon et al (1978) extended the tensor polynomial criterion to include cubic terms. Obviously, the evaluation of the strength parameters in such an equation is a formidable task. However, Tennyon et al indicated that in the practical case of failure in laminated tubes under internal pressure loading, the cubic criterion is more accurate than the quadratic one. Hashin (1980) presented three dimensional failure criteria in terms of quadratic stress polynomial that are expressed in terms of the transversely isotropic invariant of the applied average stress state. Hashin modeled separately different distinct

failure modes (tensile, compressive fiber, and matrix modes) resulting in a piecewise smooth failure surface.

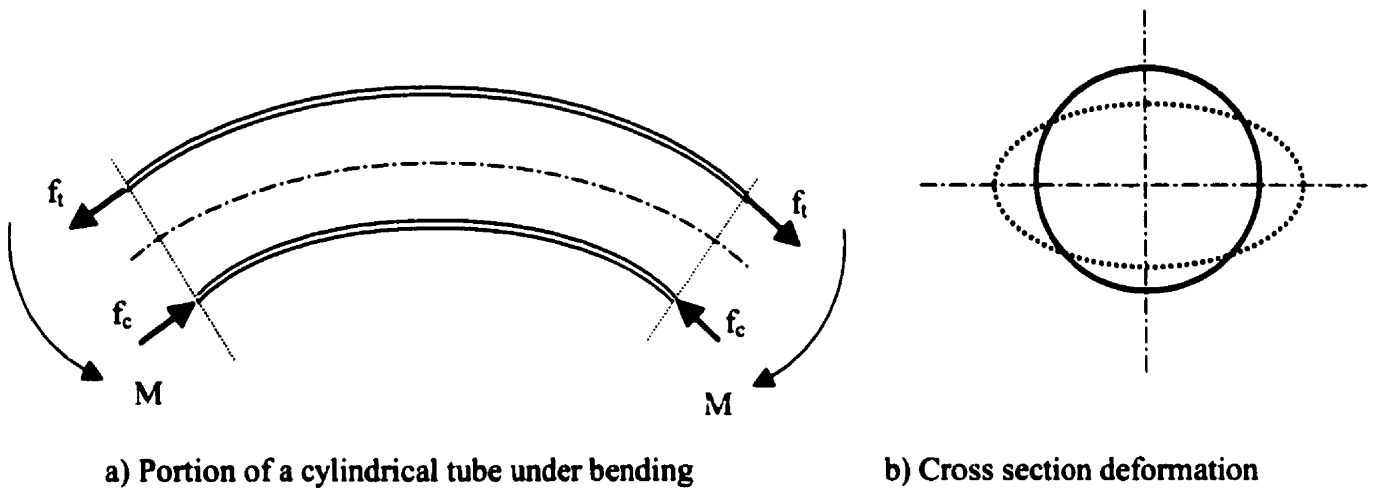


Figure (2-1) Ovalization of cylindrical tube under bending moment

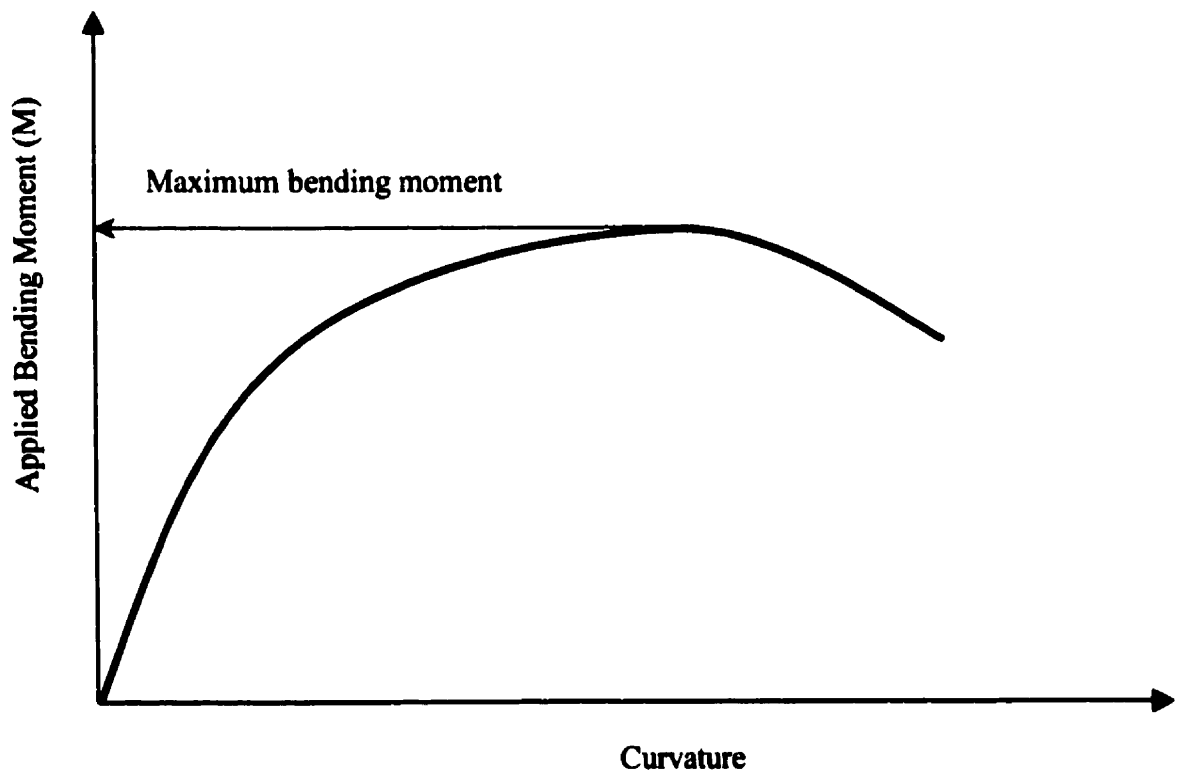


Figure (2-2): Typical moment-curvature relationship for cylindrical tubes

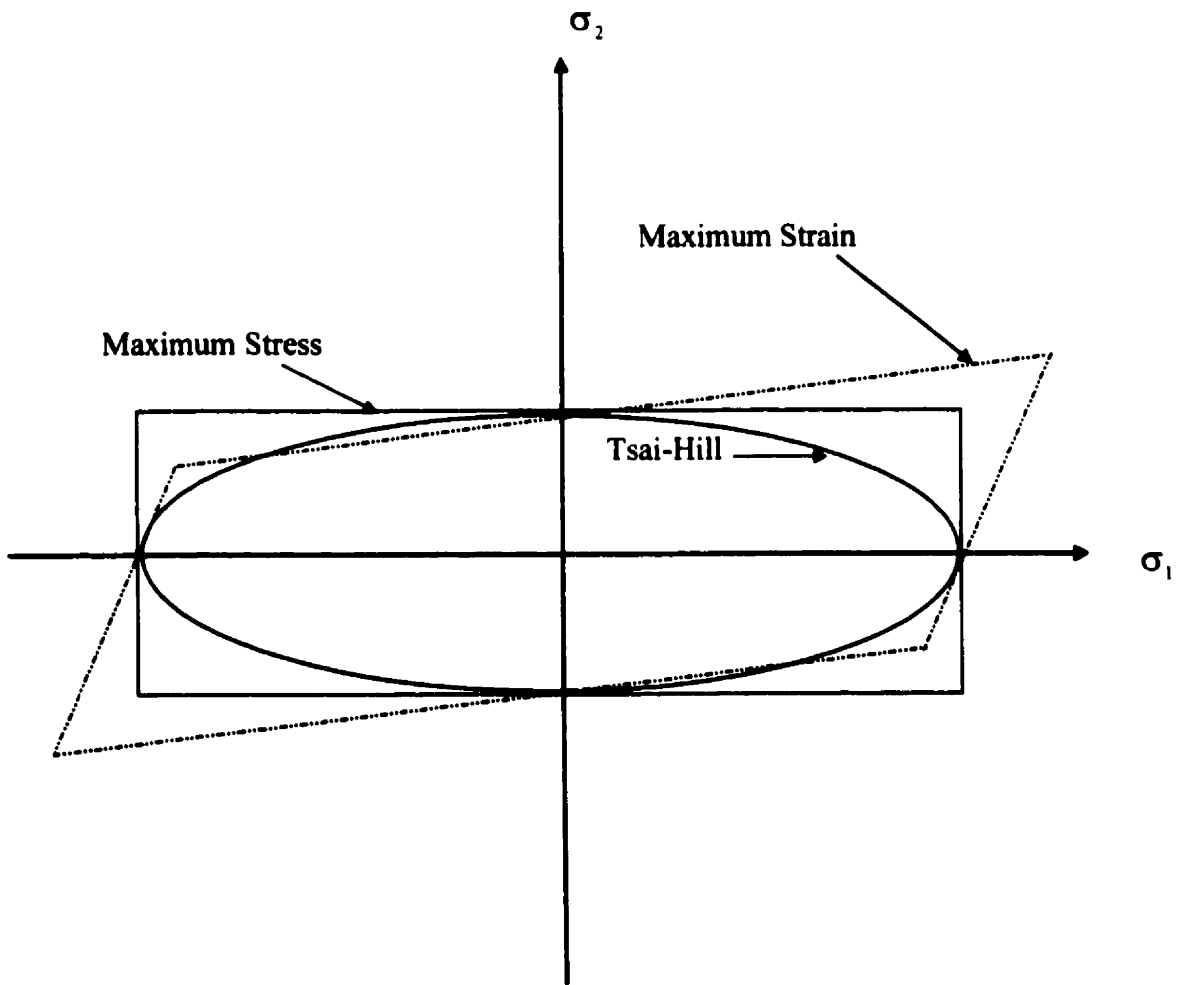


Figure (2-3): Maximum Stress, Maximum Strain, and Tsai-Hill failure surfaces in $\sigma_1 - \sigma_2$ space.

CHAPTER 3

EXPERIMENTAL PROGRAM

3.1 INTRODUCTION

As discussed in Chapter 1, one of the objectives of this research program was to develop a theoretical model to predict the structural behavior and strength of GFRP poles. This theoretical model, however, has to be verified through comparison with experimental results. This verification was accomplished through a comprehensive experimental program that was conducted at the Structural Engineering and Construction Research and Development Facility of the University of Manitoba. Twelve scaled (2500 mm long) and twelve full-scale (6250 mm long) specimens were tested to failure. All specimens were tapered. The scaled specimens had diameter at the base of 100 mm and a diameter at the top of 75 mm. The full-scale specimens had a diameter at the base of 416 mm and a diameter at the top of 305 mm. The parameters examined in this experimental investigation included the wall thickness, the fiber volume ratio, and the fiber angle orientation. The specimens were tested as cantilevers under a concentrated lateral load at the free end. The reasons for testing scaled specimens can be summarized as follows:

- a) It was more economical to verify the theoretical analysis using scaled specimens instead of using costly full-scale specimens; and,

b) testing of scaled poles was part of the technology development which included the establishment of the best winding path, the resin formulation, the curing process, and removal of specimens from the mandrels.

Once the theoretical model was verified through the experimental results of the scaled specimens, it was used to design the full-scale specimens. The dimensions of the full-scale specimens were selected so that the poles would be able to sustain a transverse load equivalent to that of commonly used wooden poles. These specimens were designed in such a way that they could be used as single 6.1 m (20 ft) poles or they could be used as the top segments of 12.2 m or 18.3 m long poles. To expand the scope of the verification procedure of the theoretical model, it was important to produce full-scale specimens with fiber orientations and fiber lay-up that were different from those of the scaled specimens.

The specimens were fabricated using the filament winding process at the ISIS-Faroex Filament Winding Facility located in Gimli, Manitoba. A description of the filament winding process, the test specimens, the test setup, the instrumentation, and the various parameters considered in this program are presented in detail in this chapter. A brief description of the manufacturing process is also provided.

3.2 MANDREL CONSTRUCTION

Composite mandrels were fabricated to wind the full-scale specimens. The composite construction provided an economical, lightweight and re-usable mandrel. The core of the full-scale mandrel was constructed using a 6100 mm long hollow aluminum tube as a core. It had an outer diameter of 152 mm. Wooden ring disks of variable outer

diameter were bonded on the aluminum tube, as shown in Figure (3-1), using epoxy thickened with colloidal silica. The outer circumference of each ring was designed to provide the required taper ratio of the final mandrel. Longitudinal stiffeners were placed between the rings to resist any longitudinal forces during the extraction of the pole from the mandrel. Longitudinal wooden sheets were mounted on the ring disks to provide a closed surface of the mandrel, as shown in Figure (3-1). The dome end of the mandrel was fabricated from wood with the required geometry. At the middle of the dome end, a drive nut system with a thrust plate was installed. A drive screw was welded at each end of the mandrel. This drive screw and nut system was used to move the domes – a technique which facilitated the removal of the specimens from the mandrel.

After installing the longitudinal wooden sheets on the ring disks and the surface machined to precise taper, the mandrel was mounted onto the filament winding machine and was wrapped with various layers of fiber glass and resin. The surface layers were wound at several orientations to provide support in the both longitudinal and the hoop directions. Layers of fibers at 10, 45, and 90 degrees were used. The surface of the mandrel was machined ensure a smooth surface finish which was manually sanded to remove any residue and coated to approximately 50 mm with polyester tooling resin. After the resin was cured completely the surface was sanded again and surface defects were filled by applying tooling resin. The weight of the finished mandrel was approximately 280 kg (630 lb).

3.2.1 FABRICATION OF GFRP POLES

Prior to filament winding, the mandrel surface was prepared by applying honeybee wax, a release agent, uniformly while the mandrel was rotating. The surface was then polished to remove any wax residue from the surface. This process resulted in a low coefficient of friction between the mandrel and the specimen and facilitated the removal of the specimens. To protect the mandrel surface, a plastic sheet was wrapped tightly around the mandrel. A three-axis filament winding computer-controlled machine was used to deploy the resin impregnated E-glass fibers, as shown in Figure (3-2). The three-axis motion included: the rotation of the mandrel, the longitudinal motion of the carriage, and the transverse motion of the payout eye, as shown schematically in Figure (3-3). Fabrication of GFRP poles over a mandrel with appropriate dome contours requires that the filament winding machine rotates the mandrel and advances the carriage at a precise speed. For wet winding it is crucial that the fibers follow the geodesic path of the surface being wound. The geodesic path is the path which describes the shortest distance between points on the surface so that, if tension is applied, the band of fibers will not slip. Once the winding path is selected, the machine computer generates the required velocity and acceleration in each direction. At high wind angles the carriage motion relative to the mandrel rotation is low allowing for the mandrel rotations to dominate the winding speed. At low wind angles the carriage motion is large compared to mandrel rotation. The computer motion files for a specific winding path were evaluated during dry runs at low speeds in order to eliminate any acceleration "bumps" which could cause damage at higher speeds.

Twenty-line band of fiber glass roving of brand 1100 TEX were utilized to wind the GFRP pole specimens. The fiber glass bales were mounted separately in a stationary rack. Access to bales was important for replacement during the winding process or repair of broken lines. The carriage speed was approximately 1.0 meter per second. The resin was loaded into baths in batches each weighing 3.0 kg. Between the resin bath and the mandrel are numerous control structures which squeeze the excess resin, guide the fibers, eliminate the catenary twist and basically control the band width of the multiple rovings. For each individual layer, the fiber glass bales were weighed to determine the amount of fiber used.

After winding, the GFRP pole was cured for approximately 24 hours at room temperature. The big dome end was then cut to allow the removal of the pole from the mandrel. The drive screw at the small dome end was used to push the specimen away from the mandrel. In some specimens air pressure was applied through a tiny hole drilled at the end of the specimen to overcome the friction forces between the mandrel and the pole. The following section describe in detail the test procedure of the specimens fabricated.

3.3 SCALED TEST SPECIMENS

Twelve scaled specimens were fabricated at the ISIS-Faroex Filament Winding facility using the filament winding technique. E-glass fiber and polyester resin (DERAKANE 470-300) were used for manufacturing these poles. The material properties and strength for both the fiber and the resin presented in Table (3-1) were provided by the supplier.

Table (3-1) Properties of E-Glass and Polyester resin

| Properties | E-Glass | Polyester resin (DERAKANE 470-300) |
|-------------------------------|---------|---------------------------------------|
| Tensile modulus (GPa) | 72.4 | 3.58 |
| Poisson's ratio | 0.2 | 0.3 |
| Tensile Strength (MPa) | 2100 | 85 |
| Shear Modulus (GPa) | 30 | 1.38 |
| Density (gm/cm ³) | 2.54 | 1.08 |

(Source: Dow Plastics Company)

The specimens were tapered hollow sections 2500 mm in length. The inner diameters at the base and the top were 100 mm and 74 mm, respectively. The wall thickness varied depending on the number of layers. The thickness of an individual layer was limited to 0.22 mm due to the use of 4 roving in the filament winding process. The number of layers varied from 4 to 10, placed in two layer increments, giving a total thickness of between 0.88 mm and 2.2 mm. For each wall thickness, three different fiber orientations were studied. The fiber orientation with respect to the longitudinal axis of the pole in this study was taken as 25/-25, 30/-30, and 35/-35. The fiber volume fraction was measured during the manufacturing process by determining the weight of the fibers and

the resin used and transforming those weights into volume fractions. The configurations as well as the fiber volume fraction for the tested specimens are listed in Table (3-2).

Table (3-2) Configuration and fiber volume fraction of scaled-specimens

| SPECIMEN | Number of layers | Fiber angle | Total thickness at base (mm) | Fiber volume fraction (%) |
|----------|------------------|-------------|------------------------------|---------------------------|
| A25 | 4 | 25/-25 | 0.88 | 0.58 |
| A30 | | 30/-30 | 0.88 | 0.53 |
| A35 | | 35/-35 | 0.88 | 0.72 |
| B25 | 6 | 25/-25 | 1.32 | 0.57 |
| B30 | | 30/-30 | 1.32 | 0.56 |
| B35 | | 35/-35 | 1.32 | 0.71 |
| C25 | 8 | 25/-25 | 1.76 | 0.55 |
| C30 | | 30/-30 | 1.76 | 0.56 |
| C35 | | 35/-35 | 1.76 | 0.57 |
| D25 | 10 | 25/-25 | 2.2 | 0.58 |
| D30 | | 30/-30 | 2.2 | 0.59 |
| D35 | | 35/-35 | 2.2 | 0.49 |

3.3.1 TEST SET-UP

A concrete plug 230 mm in diameter and 430 mm in height was cast for each specimen. This plug was placed vertically into a reinforced concrete block which was fixed to the rigid floor of the structural laboratory.

All specimens were tested using the set-up shown schematically in Figure (3-4). The load was applied horizontally, 140 mm below the top end, through a loading sleeve

which was attached to a tension bar equipped with an electronic load cell to monitor applied load. The other end of the tension bar was connected to a lever arm. The load was applied through a hydraulic jack with a capacity of 250 kN and a stroke range of 168 mm, as shown in Figure (3-5). The hydraulic jack was connected to Enerpac hydraulic pump PAM1022.

3.3.2 INSTRUMENTATION

The instrumentation used in this experimental investigation was designed to measure:

- a) the applied load at the top of the GFRP pole;
- b) the horizontal displacement of the tip of specimen;
- c) the change in diameter above the fixed base of the specimens; and
- d) the strains in the horizontal, the vertical, and 45 degrees directions at various location.

The load was measured with pre-calibrated electronic load cell with a capacity of 4500 N. The lateral deflection at the loading position was monitored by two electronic linear measurement transducers (LMT) mounted on a fixed steel column 1000 mm away from the specimen. The stroke range for each LMT was 350 mm. Therefore, the first LMT was used to measure the deflection up to 300 mm. The second LMT was then connected to continue the deflection measurement beyond this point.

The change in diameter for specimens A25, B25, B25, and D25 was monitored by measuring the diameter with a digital caliber at locations 200, 300, and 400 mm above the concrete base at different load levels.

Twelve electrical resistance strain gauges were mounted in each specimen. The strain gauges which had 5 mm gauge length and 120 ohm electrical resistance were mounted at four different locations. At each of these locations, three strain gauges were mounted to measure the strains in the longitudinal, circumferential and 45 degrees off-axis directions. Two sets of strain gauges were located on the tension side and the compression side of the specimen at heights 30 mm, and 250 mm above the concrete base.

3.3.3 TEST PROCEDURE

Each test began by placing the specimen in the concrete block and connecting it to the loading fixture. Then, the load cell, LMTs, and strain gauges were connected to a 32 channel Data Acquisition System to monitor and record all data onto a hard drive of a 486 PC computer. Initial readings of all instruments were set to zero. The specimens were loaded using a loading rate 25 mm/min. Readings of the change in diameter at different locations of the specimen were taken and visual observations were made during testing. The loading was applied till a complete failure of the specimen occurred.

3.4 FULL SCALE TEST SPECIMENS

Theoretical model developed for evaluating the structural performance and strength of GFRP poles was verified through testing on full-scale specimens. The typical

pole targeted for testing was an 18.3 m (60 ft) tapered section, as shown in Figure (3-6a). The fabrication of 18.3 m (60 ft) single piece, however, was deemed undesirable for the following reasons:

- a) a single mandrel of this length would be too heavy for the machine to hold and its excessive deflection would cause problems during winding;**
- b) it was difficult for the winding software to keep the fiber angle and the wall thickness constant along the whole length of the pole; and**
- c) it would be too difficult and costly to transport poles of this length.**

A decision was made to design a segmented GFRP pole made of three parts as shown in Figure (3-6b) and test the upper segment for strength and performance. A separate research study was initiated to investigate the connection between the segments.

In this phase of the experimental investigation, twelve full-scale specimens were fabricated and tested as cantilever. E-glass fiber and polyester resin (DERAKANE 470-300) were used for manufacturing these poles. The material properties and strength for both the fibers and the resin were provided by the manufacturer and are presented in Table (3-1).

The specimens were 6250 mm in length and had a tapered hollow section. The inner diameters at the base and the top were 416 mm and 305 mm, respectively. The wall thickness varied depending on the number of layers. The average thickness of an individual layer with longitudinal fibers was 0.75 mm while the average thickness of a layer with circumferencial fibers was 0.5 mm. The difference in layer thickness was due

to the use of different number of roving and different band width in those two direction during the filament winding process. The number of layers varied from 4 to 8, in two layer increments, giving a total thickness of between 2.75 mm and 5.5 mm. Three different fiber orientations with respect to the longitudinal axis of the pole were investigated in this study: 5/-5, 10/-10, and 20/-20. Hoop winding was also employed in 10 of the specimens, while two of the specimens were wound without hoop fibers. The fiber volume fraction was measured during the manufacturing process by determining the weight of fibers and resin used and transforming those weights into volume fractions. The configurations as well as the fiber volume fraction for the tested specimens are listed in Table (3-3). In that table, the numerical values in fiber orientation column indicate the wind angle while the subscripts indicate the number of layers by each fiber orientation. For example, specimen #1 had 8 layers, four with 10° and four at -10° . No circumferential winding was used in this case. Specimens #8 also had 8 layers, two layers with circumferential fibers followed by four layers of longitudinal fibers (two at 20° and two at -20°) followed by two layers with circumferential fibers.

Table (3-3) Configuration and fiber volume fraction of full-scale specimens

| Specimen Number | Fiber orientation | Number of layers | Base thickness (mm) | Fiber Volume (%) | Weight (kg) |
|-----------------|---|------------------|---------------------|------------------|-------------|
| 1 | (10/-10) ₄ | 8 | 5.5 | 49 | 99.40 |
| 2 | 90,(10/-10) ₃ ,90 | 8 | 5.0 | 60 | 80.25 |
| 3 | (90) ₂ ,(10/-10) ₂ ,(90) ₂ | 8 | 4.5 | 60 | 68.15 |
| 4 | 90,(10/-10) ₂ ,90 | 6 | 4.0 | 54 | 60.85 |
| 5 | 90,(10/-10),90 | 4 | 2.4 | 60 | 39.00 |
| 6 | (20/-20) ₄ | 8 | 5.5 | 53 | 94.30 |
| 7 | 90,(20/-20) ₃ ,90 | 8 | 5.0 | 60 | 81.00 |
| 8 | (90) ₂ ,(20/-20) ₂ ,(90) ₂ | 8 | 4.9 | 58 | 72.05 |
| 9 | 90,(20/-20) ₂ ,90 | 6 | 4.0 | 57 | 59.40 |
| 10 | 90,(20/-20),90 | 4 | 2.75 | 51 | 38.20 |
| 11 | 90,(5/-5) ₂ ,90 | 6 | 4.6 | 50 | 62.5 |
| 12 | 90,(5/-5),90 | 4 | 2.8 | 52 | 38 |

3.4.1 TEST SET-UP

To provide foundation support for the specimens, a segmented reinforced concrete base approximately 800 mm wide and 1000 mm high was cast. The base had a tapered circular hole in the middle and the dimensions of this hole matched the outer diameter of the specimens. The base consisted of two segments that could be clamped

together using four dwyidag bars. To ensure the stability of the portion of the specimen within the base, a 1000 mm long GFRP tapered sleeve approximately 25 mm thick, was used as internal stiffener for the specimens. Once the specimen was placed vertically inside the concrete base, the concrete was clamped to a rigid structural wall using four hollow structural steel (HSS) sections (250 x 250x 6 mm), as shown schematically in Figure (3-7). The HSS steel sections were placed at two levels 250 mm and 750 mm above the floor. Four high strength dwyidag bars were used to clamp the HSS steel sections and the concrete base to the structural wall, as shown in Figure (3-8).

The load was applied horizontally, through two slings located 600 mm below the top of the specimens and attached to a steel cable. The slings were used to avoid local deformations at the point of the concentrated load. Load was monitored through an electronic load cell, as shown in Figure (3-9). The end of the steel cable was connected to an electrically operated overhead crane with a capacity of 120 kN through a series of pulleys, as shown in Figure (3-7). The load was applied incrementally by the overhead crane at a rate of approximately 0.25 mm/second.

3.4.2 INSTRUMENTATION

The instrumentation used in the experimental investigation was designed to measure:

- a) the applied load at the top of the GFRP pole specimens;
- b) the horizontal displacement of the point of application of the load;
- c) the change in diameter above the fixed base of the specimens; and

- d) the strains in the horizontal, the vertical, and at 45 degree directions at various locations above the base.

The load was measured using a pre-calibrated electronic load cell with a capacity of 44 kN. The lateral deflection at the loading position was monitored through an electronic linear measurement transducers (LMT). The LMT was mounted on a fixed steel column located 10000 mm away from the specimen. The stroke range of the LMT was 2500 mm.

The change in the specimen's diameter was monitored by attaching two LMTs with a range of 350 mm to measure the lateral displacement of two points at opposite sides of the specimen at a height of 1000 mm from the base, as shown in Figure (3-10). The difference between the readings of the two LMTs represented the change of the specimen's diameter at that height. This method allowed continuous monitoring of the change in diameter during loading.

Twenty four electrical resistance strain gauges were mounted in each specimen. The strain gauges had a 5 mm gauge length and 120 ohm electrical resistance. The strain gauges were mounted at eight different locations. At each of these locations, three strain gauges were mounted to measure the strains in the longitudinal, circumferential and 45 degrees off-axis directions. Four of the strain gauges were placed on the tension side and the other four on the compression side of the specimens at heights 30, 400, 800, and 1200 mm above the concrete base.

3.4.3 TEST PROCEDURE

The load cell, the LMTs, and strain gauges were connected to a 32 channel Data Acquisition System to monitor and record all data onto a hard drive of a 486 PC computer. Initial readings of all instruments were set to zero. Visual observations were also made during the test and the load was applied till a complete failure of the specimen occurred.

3.5 MATERIAL MECHANICAL PROPERTIES

To verify the material properties for the glass fiber and the polyester resin provided by the manufacturer, twelve unidirectional coupons were tested. The coupons were manufactured using filament winding procedure. A square mandrel was used to produce flat coupons. Circumferencial winding was employed to achieve unidirectional specimens. Glass fiber (TEX 1100) and polyester resin were used to manufacture the coupons. These materials were similar to those used in the manufacturing of the scaled and full-scale poles. After curing, the manufactured square-shaped was cut into four sides. Each side provided a GFRP panel 305 mm (12") wide. Two strips of GFRP were bonded at the ends of the flat panel to provide end tabs for the coupons, as shown in Figure (3-11a). Twelve coupons were cut from this flat panel. The dimensions of the coupons satisfy current ASTM standard D 3039-76 (1990). Figure (3-11b) shows typical dimensions of the tested coupons. The average fiber volume of the coupons was determined based the weight of the fiber and the resin used in producing the square-shaped part. The average fiber volume was 0.45. The width and the thickness of each coupon were measured using a digital caliber of accuracy 0.01 mm. Three separate

readings for the width and three for the thickness were recorded for each coupon and the average values are shown in Table (3-4).

Table (3-4): Dimensions of the tested coupons

| Coupon number | Average width (mm) | Average thickness (mm) |
|---------------|--------------------|------------------------|
| C1 | 24.76 | 1.28 |
| C2 | 24.70 | 1.22 |
| C3 | 24.62 | 1.22 |
| C4 | 24.58 | 1.20 |
| C5 | 24.81 | 1.21 |
| C6 | 24.98 | 1.25 |
| C7 | 24.89 | 1.24 |
| C8 | 24.73 | 1.26 |
| C9 | 24.64 | 1.22 |
| C10 | 24.71 | 1.21 |
| C11 | 24.74 | 1.25 |
| C12 | 24.92 | 1.20 |

All coupons were tested using a Baldwin testing machine. A load range of 26.67 kN (6000 lb) was selected to test all coupons. Two 100 mm Pi-gauge were placed on both sides of the coupon to monitor the longitudinal strains, as shown in Figure (3-12). The average readings of the two Pi-gauges were used to determine the longitudinal strains and to eliminate any affect due to loading eccentricity. The coupons were properly aligned in the machine to avoid bending. The rate of loading was 0.9 kN/min. Data were recorded by a Data Acquisition System. All coupons were tested to failure. Figure (3-13) shows a typical failure of one of the tested coupons. The Pi-gauges were removed from the coupons at, approximately, a 90% of the ultimate load to prevent damage. Therefore, the

actual strains at failure were not recorded. However, load recording was continued till a complete failure was observed.

A typical stress-strain curve of a GFRP coupon is presented in Figure (3-14). This behavior is typical of all tested coupons which showed a linear stress-strain relationship. The Young's modulus for the tested coupons was calculated from the slope of the stress-strain curve. On the other hand, the ultimate strength was calculated from the maximum value of the load achieved. The elastic modulus and the ultimate strength, as well as the averages and the standard deviation of all tested coupons, are summarized in Table (3-5).

Table (3-5): Mechanical properties of the tested coupons

| Coupon number | Elastic Modulus (GPa) | Ultimate strength (MPa) |
|---------------------------|-----------------------|-------------------------|
| C1 | 39.9 | 968.5 |
| C2 | 35.04 | 915.4 |
| C3 | 36.6 | 940.8 |
| C4 | 34.9 | 922.2 |
| C5 | 36.2 | 904.1 |
| C6 | 35.6 | 932.2 |
| C7 | 37.5 | 899.1 |
| C8 | 37.1 | 920.5 |
| C9 | 35.9 | 926.3 |
| C10 | 36.2 | 919.2 |
| C11 | 36.6 | 922.6 |
| C12 | 36.4 | 927.3 |
| Average value | 36.5 | 924.9 |
| Standard deviation | 1.91 | 17.76 |

The test results shown above were be used to verify of the materials properties that were provided by the manufacturer. Comparison between the mechanical properties calculated from the information provided by the manufacturer and the test results is presented in Chapter 5.

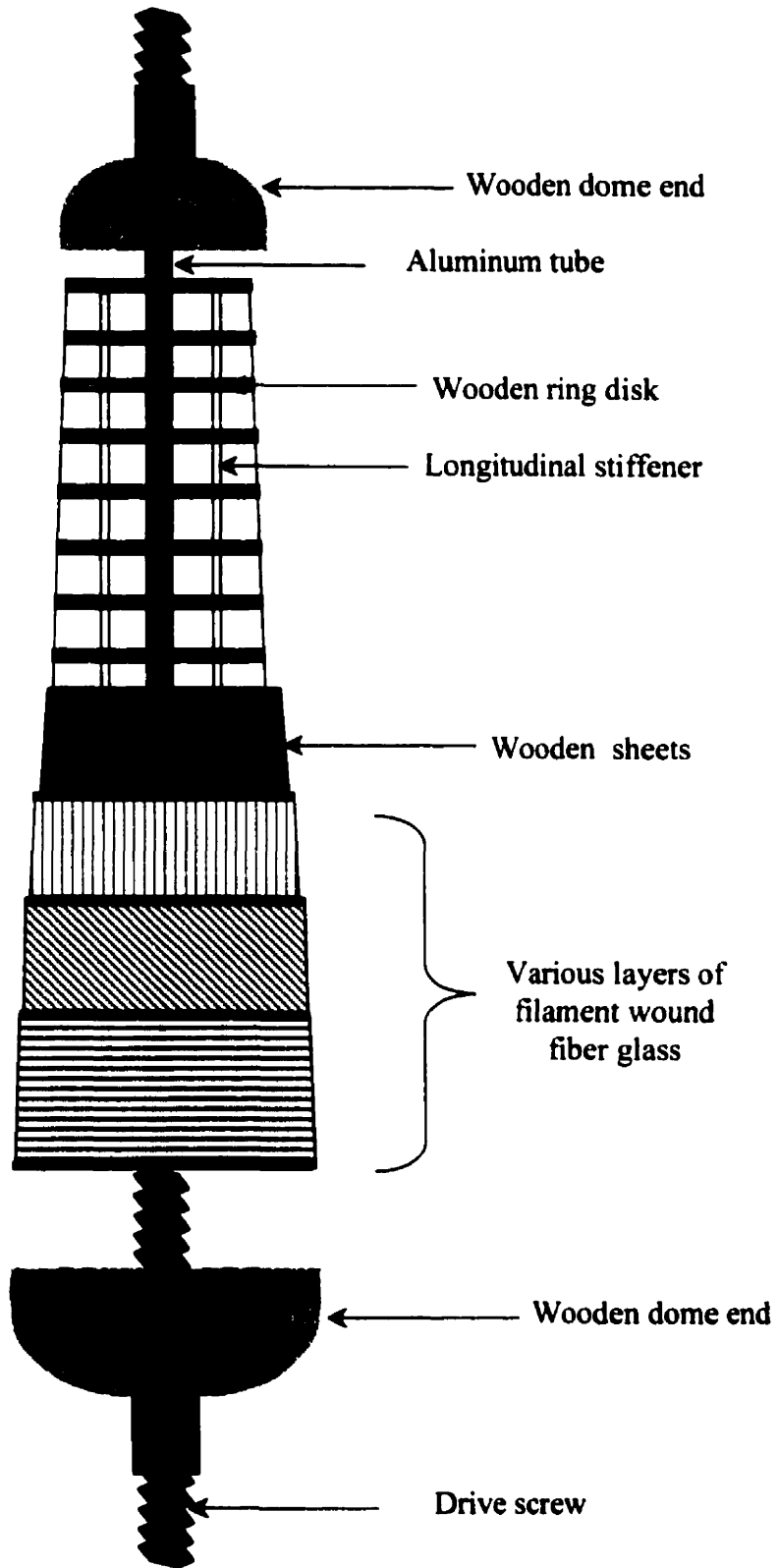


Figure (3-1): Schematic drawing of different components of full-scale mandrel

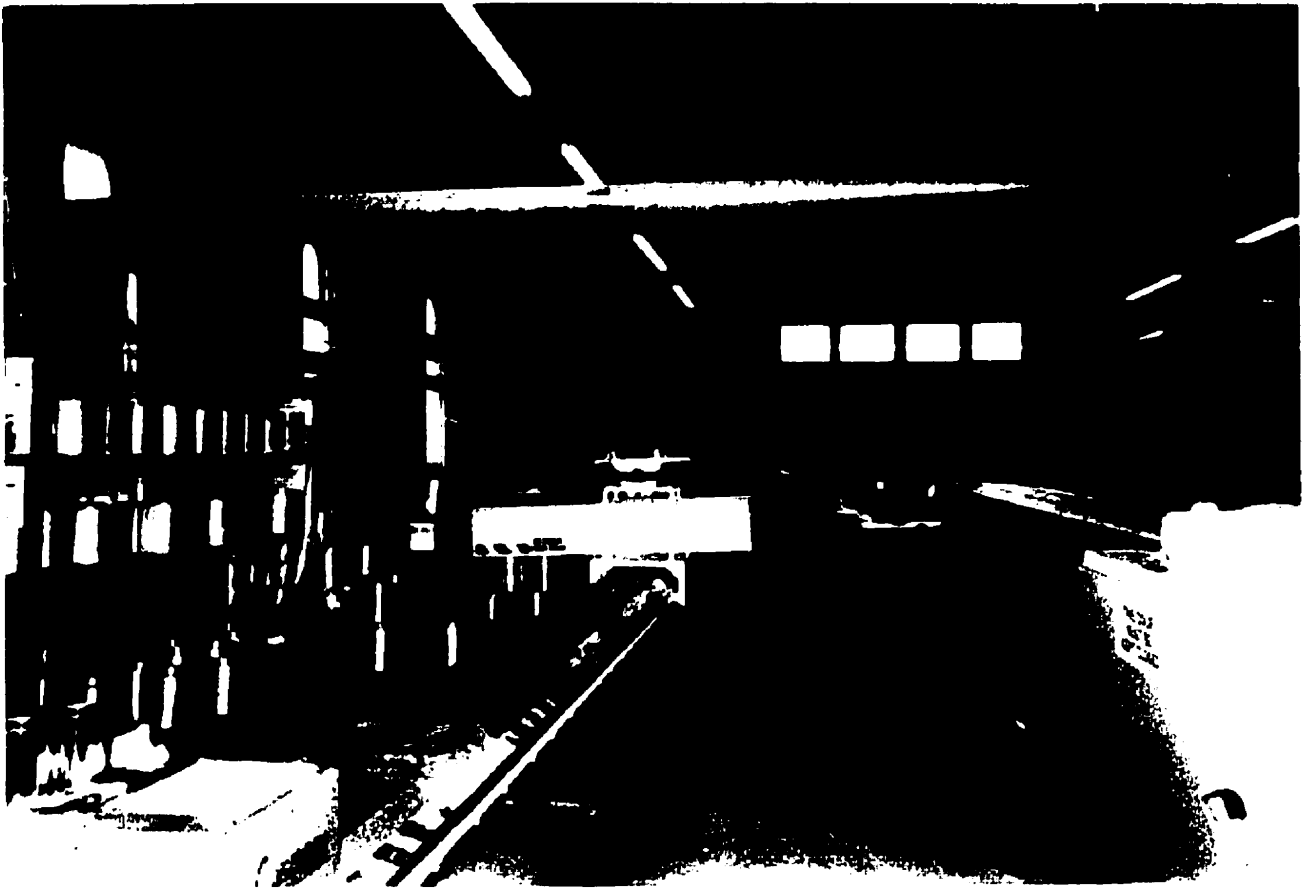


Figure (3-2): Three-axis filament winding machine

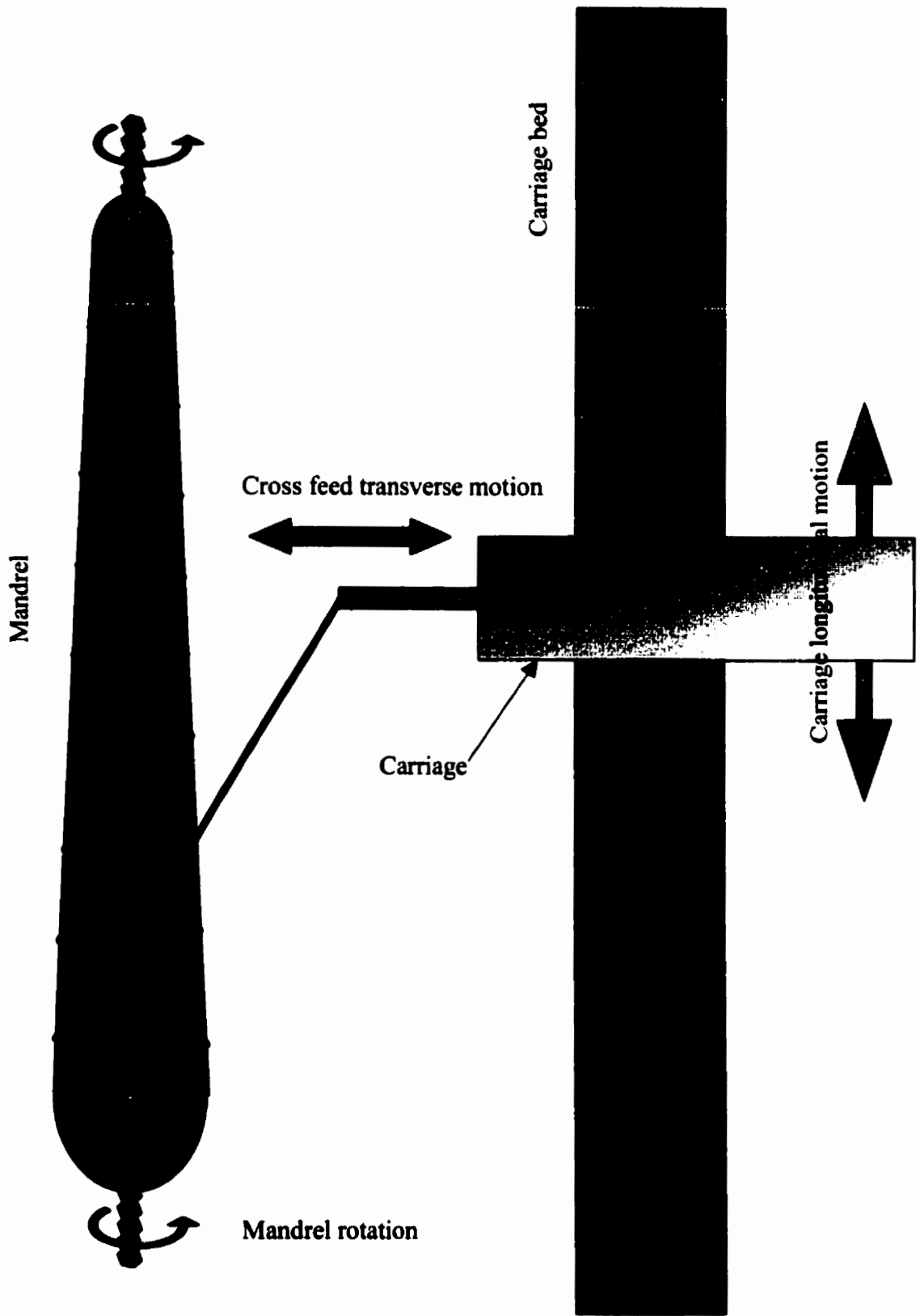


Figure (3-3): Schematic of three axis motion of filament winding machine

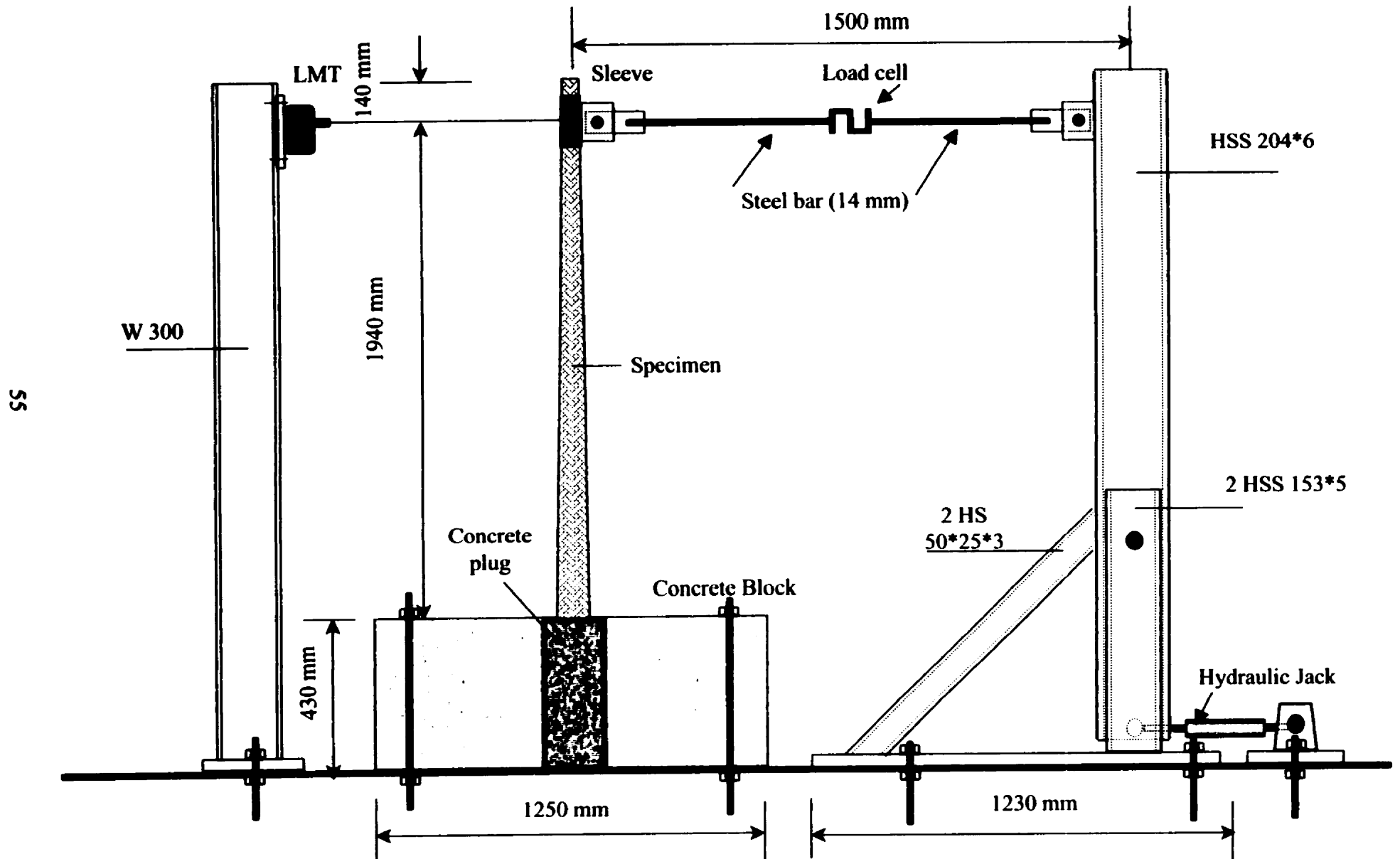


Figure (3-4): Schematic drawing of the scaled test setup

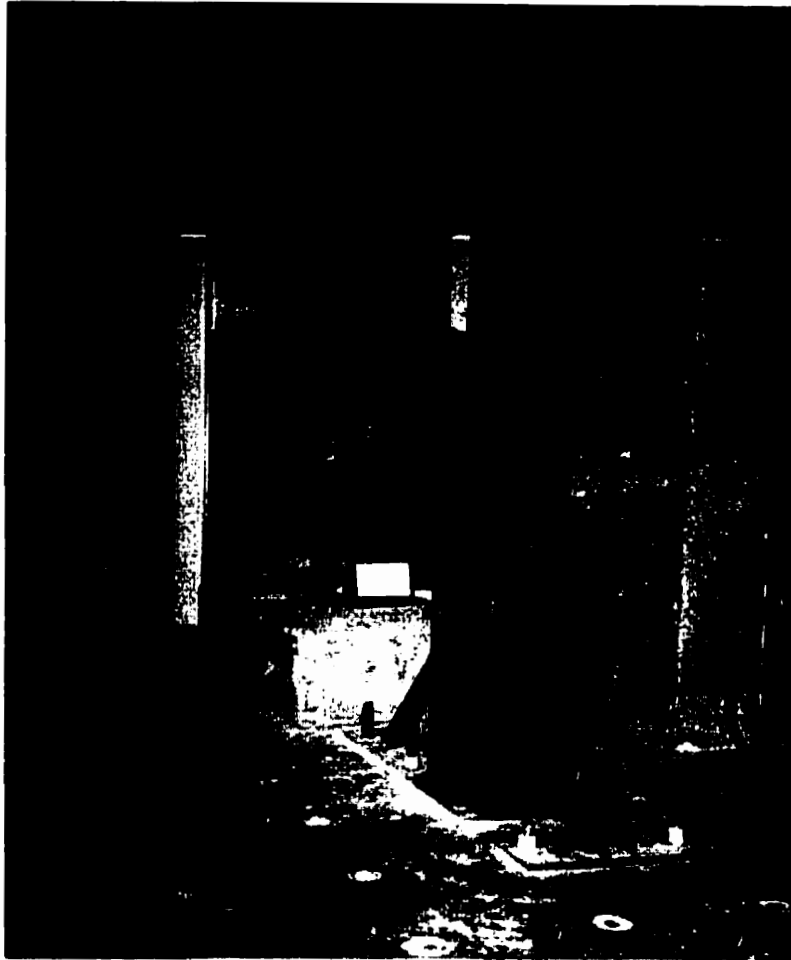
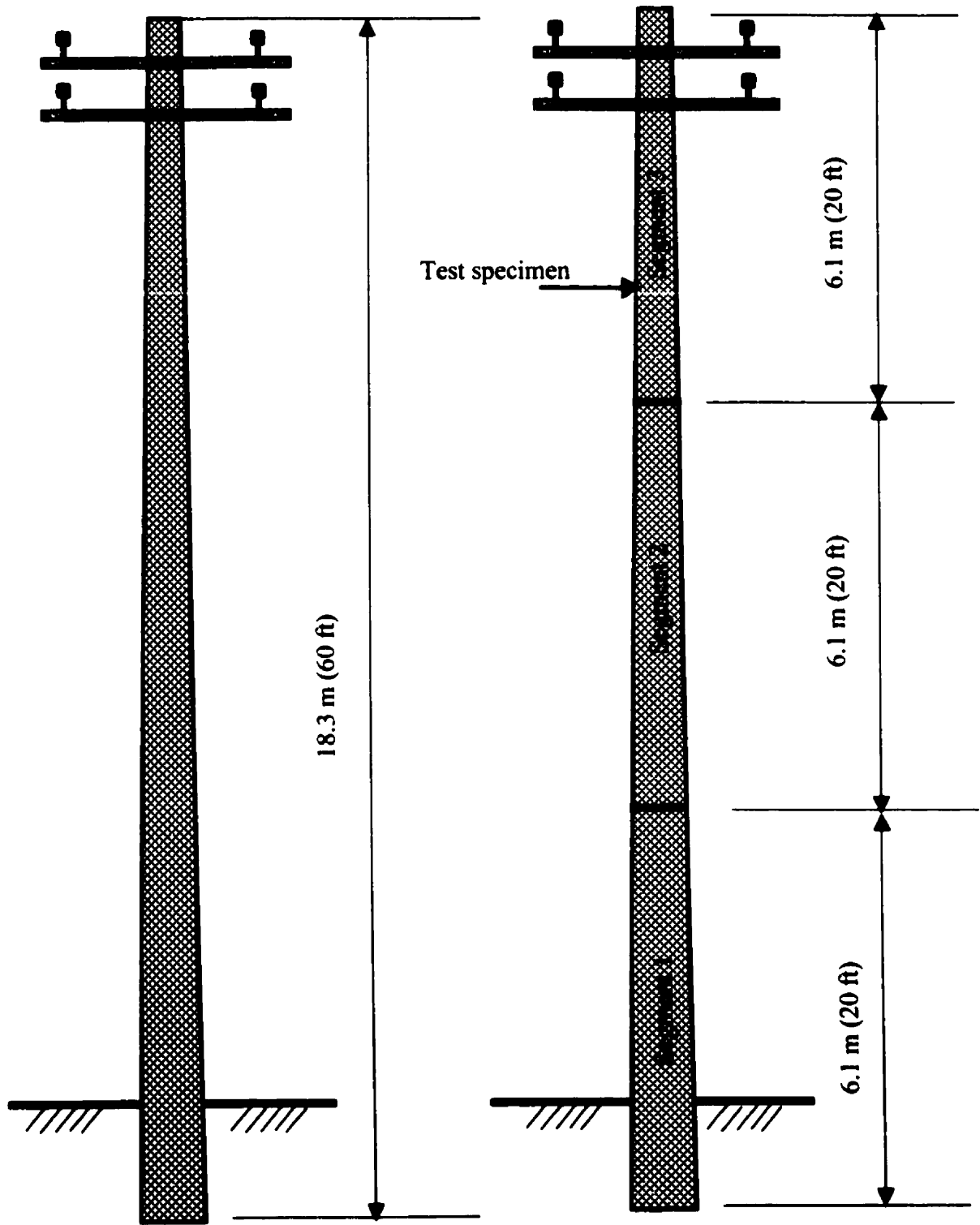


Figure (3-5): Test setup for scaled specimens



a) One- segment 18.3 m FRP pole

b) Three-segment 18.3 m FRP pole

Figure (3-6): Targeted dimensions of full-scale FRP pole

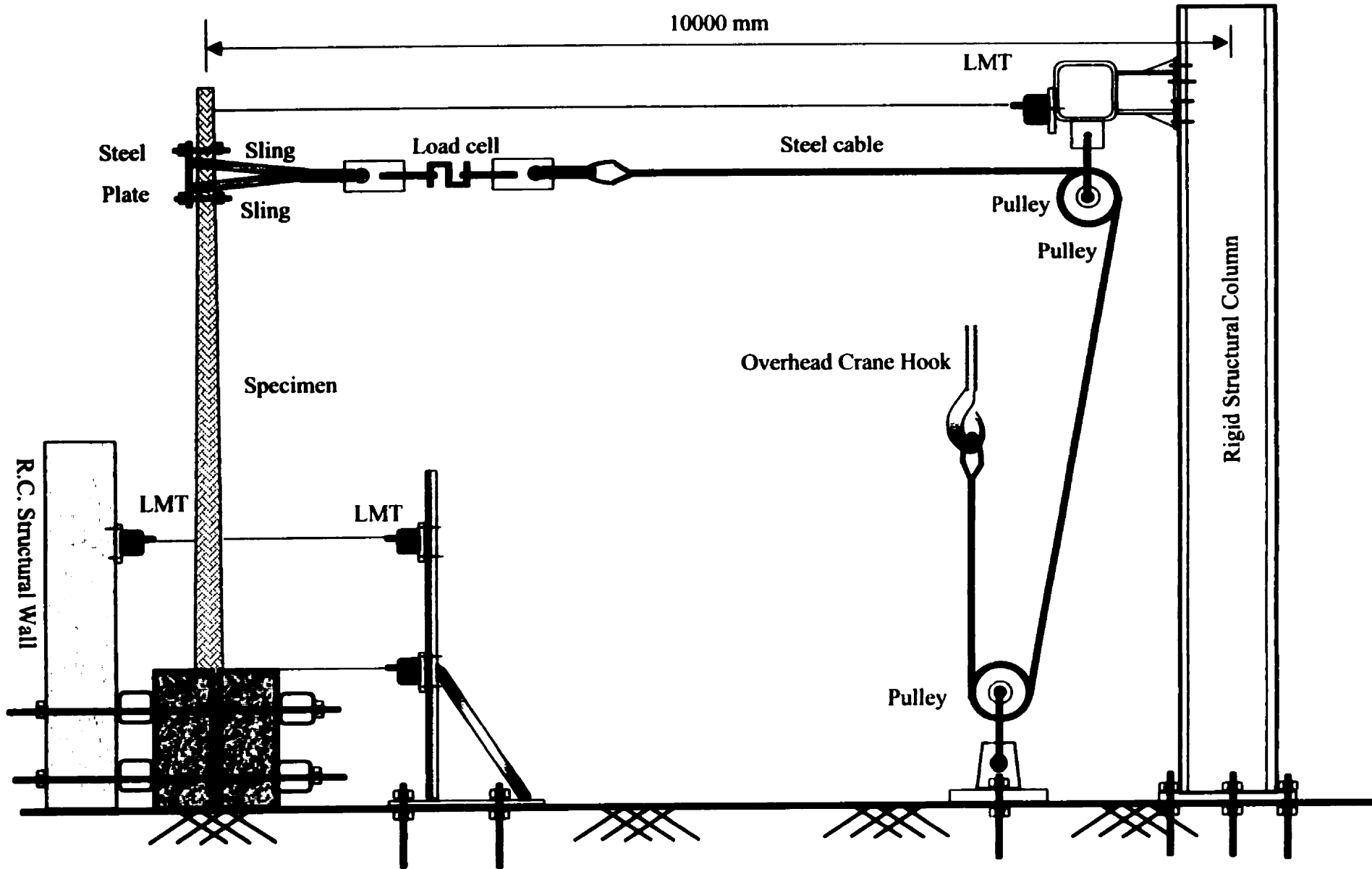


Figure (3-7): Schematic drawing of the full-scale test setup

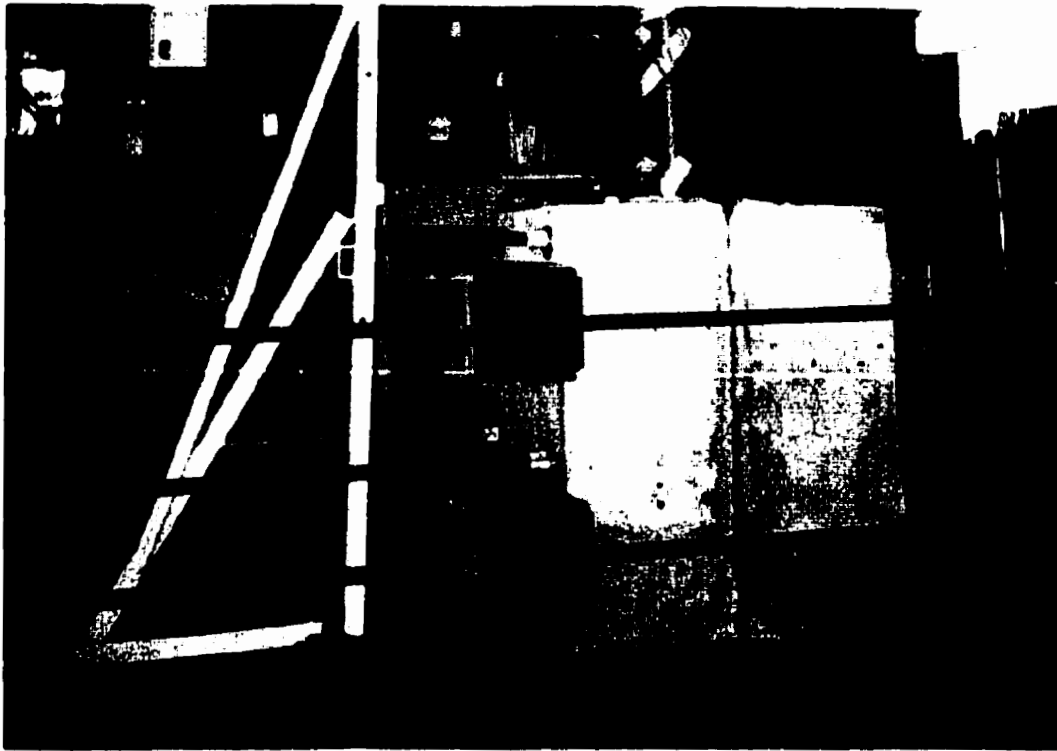


Figure (3-8): Connection between concrete base and structural wall



Figure (3-9): Load cell connection for full-scale specimens

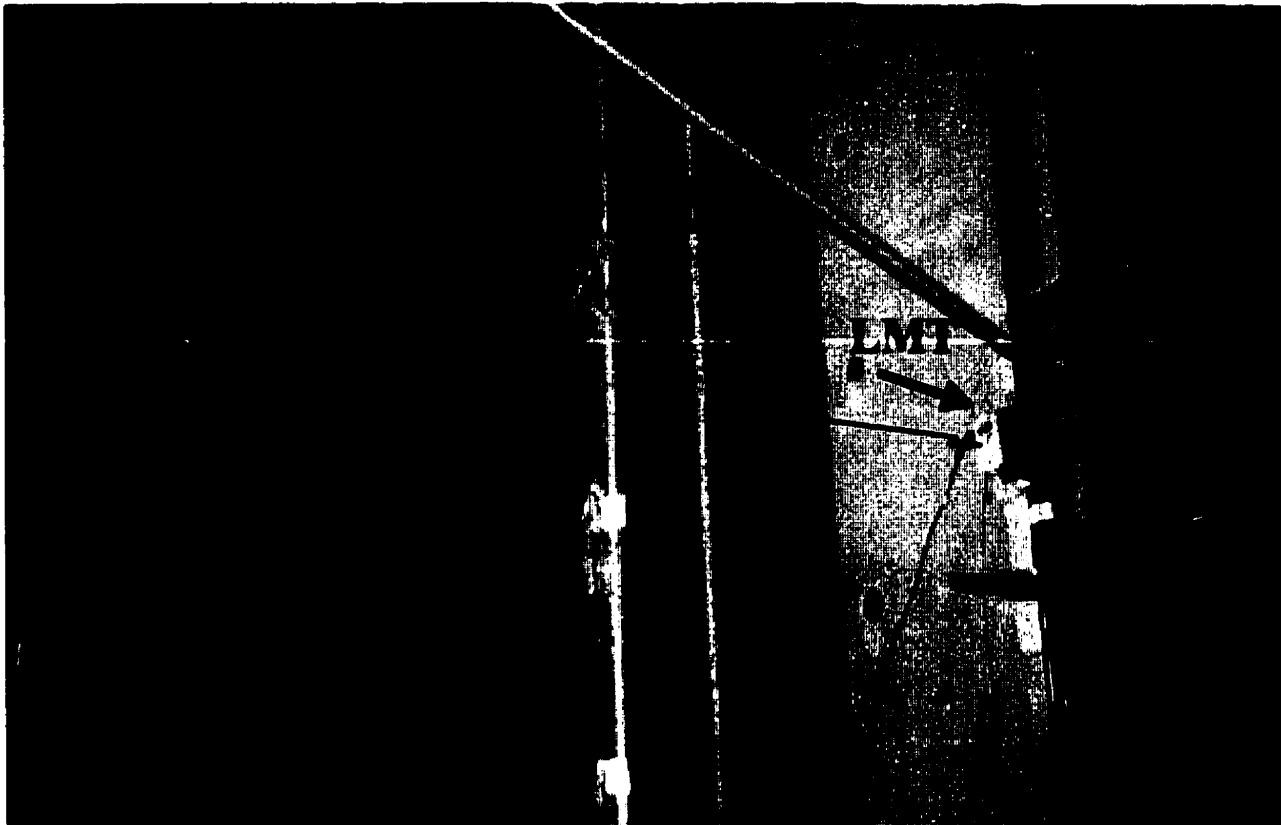
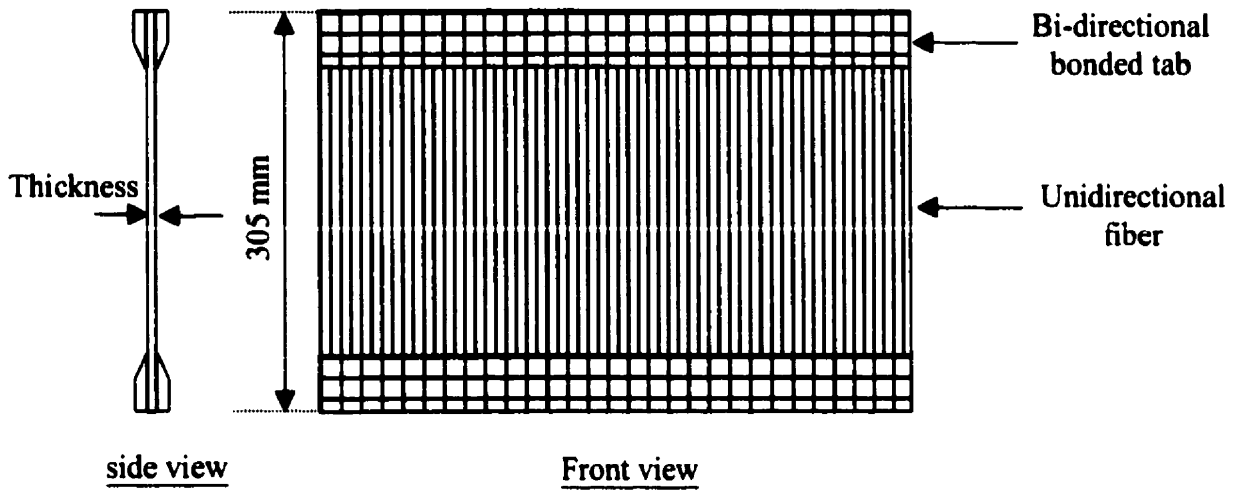
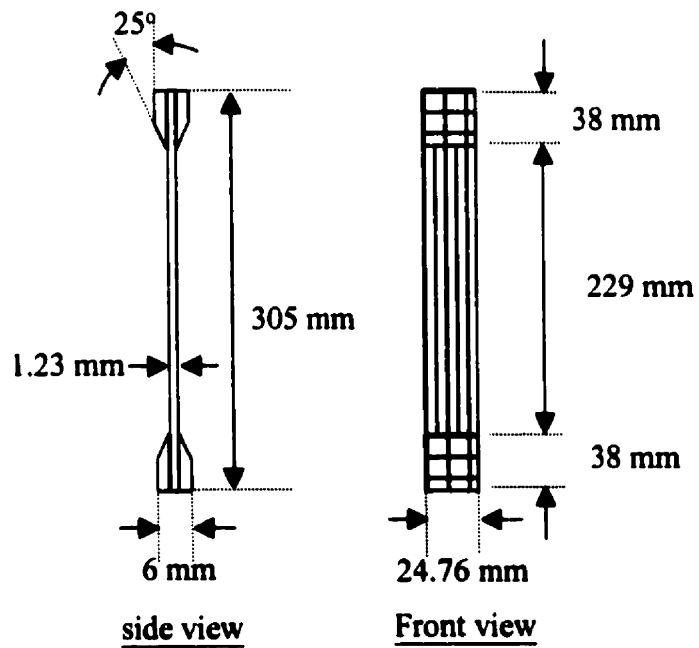


Figure (3-10): Measurement of ovalization by two LMTs installed at opposite side of the specimen



a) Flat panel with unidirectional fiber



b) Dimensions of unidirectional coupons

Figure (3-11): Unidirectional flat coupons

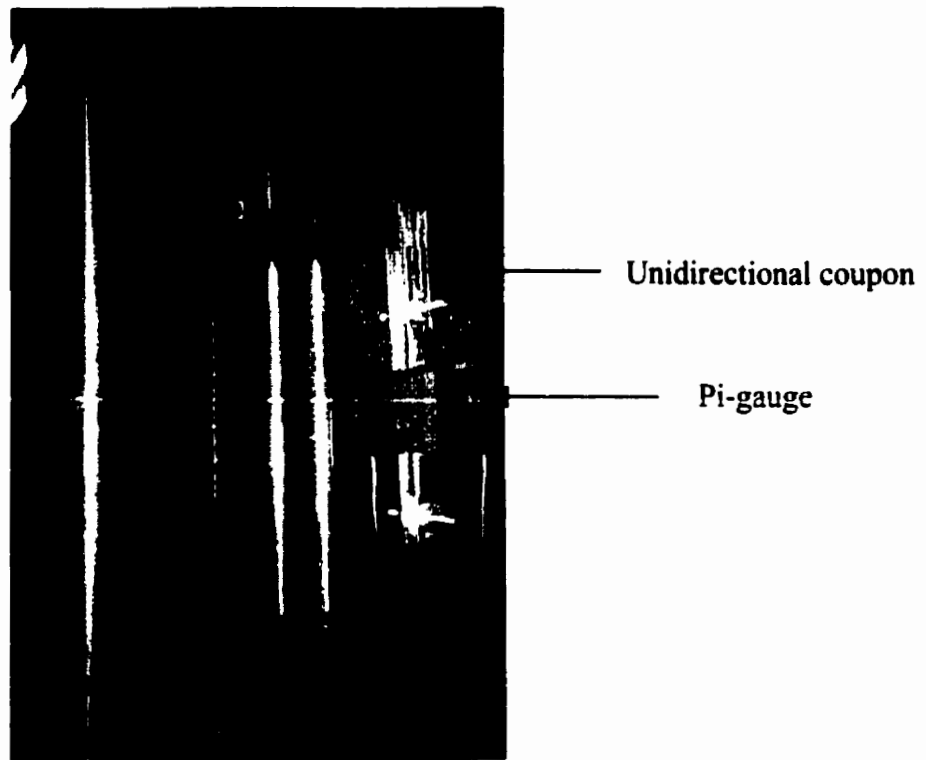


Figure (3-12): Test setup for unidirectional coupon



a) Tension coupon after failure in the testing machine



b) Tension coupons after removal from testing machine

Figure (3-13): Failure mode of unidirectional GFRP coupons

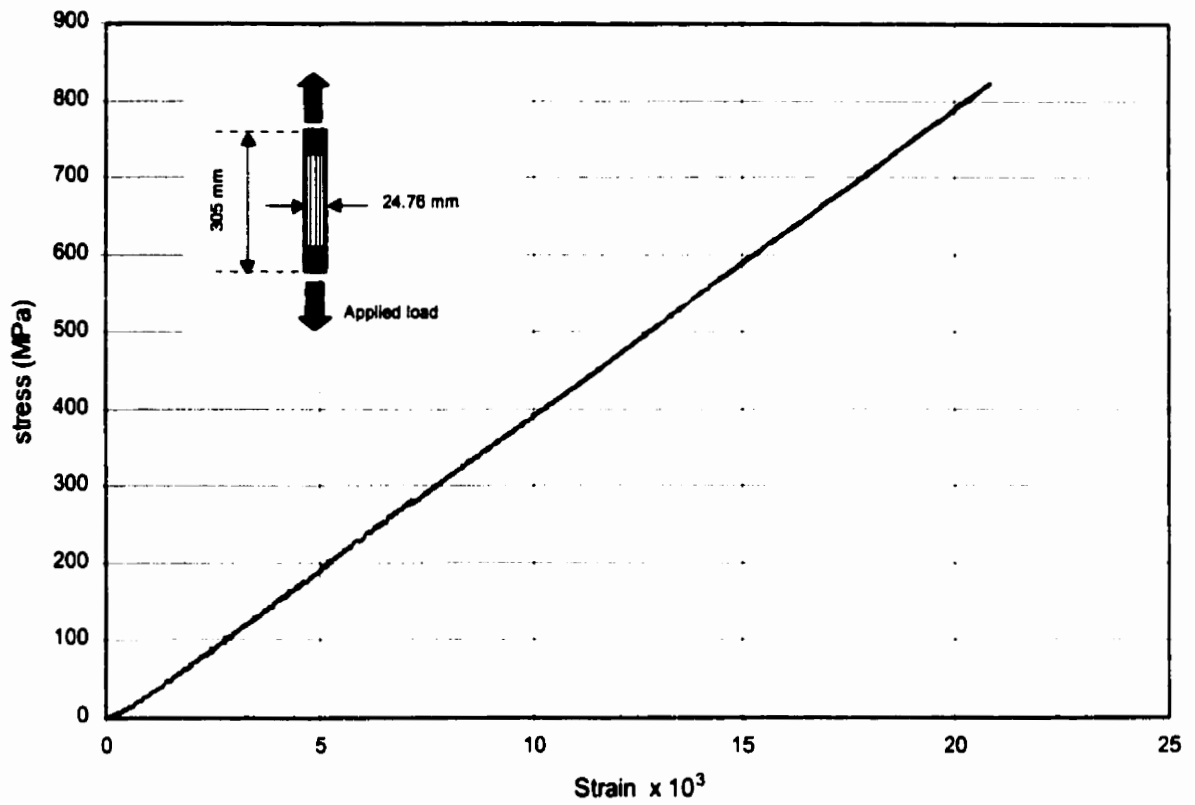


Figure (3-14): Typical stress-strain relationship for unidirectional coupons

CHAPTER 4

EXPERIMENTAL RESULTS

4.1 INTRODUCTION

In this chapter, experimental results and failure modes are discussed for both scaled and full-scale fiber reinforced plastic pole specimens and the behavior of the tested specimens is analyzed. A total of twelve scaled and twelve full-scale specimens were tested under cantilever bending. The data obtained included:

- a) the ultimate load capacity;
- b) the load–displacement relationship;
- c) the strain distribution along the height;
- d) the cross section ovalization as function of the load; and
- e) the failure mechanism.

4.2 SCALED SPECIMENS

In this section, the performance of the twelve scaled specimens will be discussed.

4.2.1 PERFORMANCE OF SPECIMENS

The ultimate transverse load capacity and the corresponding maximum lateral displacement, along with the corresponding modes of failure of all the tested scaled specimens are summarized in Table (4-1). The performance of these poles was evaluated on the basis of their ultimate transverse load capacity and their corresponding lateral displacement. As shown in Table (4-1), the transverse load carrying capacity of the pole specimens was increased with the number of layers. The average load for the four layer specimens was 327 N while for ten layer specimens the average load was 961 N. The average load carried by each layer is also shown in Table (4-1). The minimum average load capacity per layer was 82 N/layer carried by the four layer specimens, while the maximum load per layer was 96 N/layer carried by the ten layer specimens. The maximum lateral displacement of the specimens at the free end varied from approximately 11% of the free length for specimen A25 to approximately 19% for specimen D30.

Since each specimen had a different mass, the transverse load capacity-to-mass ratio (kN/kg) was used to evaluate the performance of the various specimens. The load capacity-to mass ratios of the scaled specimens are listed in Table (4-2) and are plotted in Figure (4-1). As shown in Figure (4-1), the load capacity-to-mass ratio varied from 0.12 kN/kg for specimen A35 to 0.17 kN/kg for specimen D25. The average transverse load capacity-to-mass for all specimens was 0.145 kN/kg. For a class 1 Douglas Fir wooden pole, 6.1 m (20 ft) in length, the transverse load capacity-to-mass ratio is 0.095 kN/kg. Thus, GFRP poles are more efficient than wooden poles. The efficiency, as

measured by the transverse load capacity-to-mass ratio, can be improved by optimizing the cross section dimensions of the pole. This was done in the design of the full-scale specimens whose test results are analyzed later in this chapter.

Table (4-1) Performance of scaled GFRP poles

| Specimen | Number of Layers | Ultimate Load (N) | Average Load (N) | Average Load/Layer (N) | Max. Lateral Displacement (mm) | Max. Lateral Displacement/Free height | Failure Mode |
|----------|------------------|-------------------|------------------|------------------------|--------------------------------|---------------------------------------|--------------|
| A25 | 4 | 353 | 327 | 82 | 224 | 0.112 | Mode-A |
| A30 | | 327 | | | 273 | 0.137 | Mode-A |
| A35 | | 300 | | | 237 | 0.119 | Mode-A |
| B25 | 6 | 490 | 534 | 89 | 223 | 0.112 | Mode-B |
| B30 | | 613 | | | 276 | 0.138 | Mode-B |
| B35 | | 499 | | | 295 | 0.148 | Mode-B |
| C25 | 8 | 851 | 743 | 93 | 347 | 0.174 | Mode-B |
| C30 | | 752 | | | 309 | 0.155 | Mode-B |
| C35 | | 625 | | | 297 | 0.149 | Mode-B |
| D25 | 10 | 981 | 961 | 96 | 359 | 0.180 | Mode-C |
| D30 | | 1026 | | | 379 | 0.190 | Mode-C |
| D35 | | 876 | | | 343 | 0.172 | Mode-C |

Failure Mode A: Local buckling on the compression side.

B: Diagonal fracture on the compression side.

C: Transverse fiber pull-out forming necking on the tension side.

Table (4-2) Load capacity-to-mass ratio of scaled GFRP poles

| Specimen | Number of Layers | Fiber Orientation | Load-to-Mass Ratio (kN/kg) |
|-----------------|-------------------------|--------------------------|-----------------------------------|
| A25 | 4 | 25/-25 | 0.147 |
| A30 | 4 | 30/-30 | 0.131 |
| A35 | 4 | 35/-35 | 0.120 |
| B25 | 6 | 25/-25 | 0.136 |
| B30 | 6 | 30/-30 | 0.166 |
| B35 | 6 | 35/-35 | 0.128 |
| C25 | 8 | 25/-25 | 0.172 |
| C30 | 8 | 30/-30 | 0.150 |
| C35 | 8 | 35/-35 | 0.125 |
| D25 | 10 | 25/-25 | 0.160 |
| D30 | 10 | 30/-30 | 0.166 |
| D35 | 10 | 35/-35 | 0.141 |

4.2.2 FAILURE MODES

Three different modes of failure were observed in the testing of the scaled specimens. Mode A was a local buckling failure on the compression area near the fixed support; Mode B was a material failure in the area of maximum shear stress characterized by shear fracture of the roving; Mode C was also a material failure characterized by matrix failure and stiffness degradation and associated with necking formation on the tension side of the cross-section near the fixed support. There was no other signs of failure at any part of the specimens, such as cracking or crushing of the resin or fibers during these tests.

Mode A failure was observed in all 4-layer specimens. These specimens had a diameter-to-thickness ratio of 115. A typical Mode A failure is shown in Figure (4-2). Mode A failure occurred at the critical local buckling load and was characterized by brittle collapse of the member.

Mode B failure was observed in the 6, and 8-layer specimens where diagonal fracture on the compression side near the base occurred, as shown in Figure (4-3). This mode of failure is associated with shear failure of fibers. Compressive stresses in the direction of the fibers produce a shear stress at an angle to the fibers resulting in diagonal fracture of the fibers.

Mode C failure was observed in the 10-layer specimens, as shown in Figure (4-4), and was preceded by a ductile behavior of the members. When the fibers reached their ultimate capacity and failure began, a stiffness degradation occurred locally accompanied by large deformations. Since the fibers are wound helically around the pole, a force

component normal to the pole surface was developed. This force tended to push the fibers towards the center of the tube causing delamination of the layers. This mode of failure also involved the formation of a necking on the tension side of the poles due to the reduction in the cross section dimensions. It is a well-known mode of failure for filament wound tubes under tension and is known as fiber transverse pull-out. Failure in this case was not sudden and the member retained some stiffness till it reached its ultimate load.

4.2.3 LOAD-DEFLECTION RELATIONSHIP

Typical load-deflection curves obtained from the testing of the scaled poles are shown in Figures (4-5), (4-6), and (4-7). The load-deflection relationship was non-linear especially at loads greater than 70 % of the ultimate load due to damage accumulation and progressive failure on the micro level. The 4-layer specimens (A25, A30, and A35) exhibited a sudden drop in the load once local buckling occurred. The rest of the specimens, however, exhibited a ductile behavior with a more gradual drop in load after the maximum load was attained.

The stiffness and strength of GFRP poles depend mainly on the fiber volume fraction and the fiber orientation. Increasing the fiber volume fraction, as in specimens A35 and B35, increased the elastic moduli and strength in the principal material axes. However, the material properties in the longitudinal direction were affected by the fiber angle. Figure (4-8) shows the load-deflection curves for specimen A35, B35, A25, and B25. As indicated in this figure, the stiffness and the strength of specimen B25 was similar to that of B35. Similarly, the stiffness and strength of specimen A25 was similar to that of A35. As shown in Table (3-2), the fiber volume of specimens A25 and B25

was less than that of specimens A35 and B35. These results indicate that the desired performance of GFRP poles can be achieved through the use of less fiber volume but with lower fiber angle. A comprehensive analytical parametric study was conducted to determine the optimum values of fiber angle and fiber volume fraction.

4.2.4 LOAD-OVALIZATION RELATIONSHIP

The change in the diameter of specimens A25, B25, C25, and D25 was measured using digital a caliber at levels, 200 mm, 300, 400, and 500 mm above the concrete base. The amount of cross sectional distortion is usually expressed as the ovalization ratio which equal to the ratio between the change in diameter and the original diameter. Ovalization of a circular cross section causes a reduction in the cross section resistance and consequently a reduction in the ultimate load capacity of GFRP poles. The maximum ovalization ratio for the four specimens (A25, B25, C25, and D25) was observed at level 300 mm above the concrete base. The results are given in Figure (4-9). A highly nonlinear load-ovalization relationship can be observed in Figure (4-9). Specimen A25, which failed by local buckling, had the highest ovalization ratio of 8% at the ultimate load. This specimen had the highest radius to thickness ratio, approximately 115. The load-ovalization relationship for shows that the behavior of specimen A25 was initially linear up to a load of 50% of the ultimate load. However, at higher loads the behavior was highly nonlinear. The large change in the cross section diameter reduced the cross section modulus and accelerated the occurrence of local buckling. Specimen B25, which had a radius-to-thickness ratio of 90, had maximum ovalization ratio of 6%. The nonlinear behavior for this specimen began at a load level equal to 40% of the ultimate

load. Specimens C25 and D25 had a maximum ovalization ratio equal to 1.5% and 0.6%, respectively. The ovalization ratios of specimens C25 and D25 were much smaller compared to the other specimens. This was due to a lower radius-to-thickness ratios in specimens C25 and D25 which equal to 57 and 45, respectively. As a result the low radius-to-thickness ratio, less cross sectional distortion to take place and thus the specimens did not to fail by local buckling.

4.2.5 LOAD-STRAIN RELATIONSHIP

The load-strain relationships for three of the specimens tested are discussed in this section. Each of the presented specimen failed in different mode. Typical load-strain diagrams for specimens A30, B30, and D30 are shown in Figures (4-10), (4-11), and (4-12), respectively.

In specimen A30, which failed due to local buckling, strains were monitored at the base level and at 500 mm above the base on both the tension and the compression sides. As shown in Figure (4-10), the relationship between load and both tensile and compression strains at the 500 mm level above the base was fairly linear. However, the relationship between load and the compressive strain at the base was only linear up to load of 60% of the ultimate load. Above this load, the load-compressive strain relationship was non-linear. The maximum compressive strain at failure was, approximately, $7000 \mu\epsilon$ (0.7%). This limited value of the maximum compressive strain was due to the occurrence of local buckling. A similar behavior was observed on the tension side of the pole. However, the load-strain relationship was non-linear throughout. The maximum recorded tensile strain was, approximately, $14000 \mu\epsilon$. At this

strain level, the strain gauge debonded from the surface because of failure of the adhesive material. Therefore, the maximum tensile strain at failure was not recorded.

The load–strain relationship for specimen B30, which failed due to diagonal fracture on the compression side, is shown in Figure (4-11). Strains were monitored at the base level and at 400 mm above the base on both the tension and the compression side. As shown in Figure (4-11), the relationship between load and strain at the 400 mm level above the base was fairly linear. Since this specimen failed due to shear fracture on the compression side, the maximum compressive strain at the base reached a value of 10000 $\mu\epsilon$. The load–compressive strain relationship at the base was linear up to a load equal to, approximately, 70% of the ultimate load. A nonlinear relationship was observed beyond this load level. The maximum recorded tensile strain at the base was, approximately, 19000 $\mu\epsilon$ at a load level equal to 95% of the ultimate load when the strain gauge was damaged due to adhesive debonding.

Figure (4-12) shows the strains at the base level and at a level 300 mm above the base for specimen D30. This specimen exhibited the most ductile behavior due to the transverse fiber pull-out failure mode. The strains on both of the tension and the compression sides were higher than all the other specimens. The maximum compressive strain at ultimate load reached a value of 14000 $\mu\epsilon$ while the maximum recorded tensile strain was 16000 $\mu\epsilon$. At this strain level, the strain gauge was damaged due to adhesive debonding.

4.3 FULL-SCALE SPECIMENS

The experimental results of the full-scale specimens are presented and discussed in this section.

4.3.1 PERFORMANCE OF FULL-SCALE GFRP POLES

A summary of all test results is given in Table (4-3) which shows the ultimate capacity and the maximum displacement of the poles at failure. The equivalent wooden pole class is also shown in this table. It should be noted that specimen 2 failed prematurely inside the concrete base because the internal stiffener was accidentally left out in that specimen. Two specimens (4, and 11) satisfied the requirement of class 1 pole by carrying an ultimate transverse load exceeding 20 kN (4500 lb). The maximum displacement in those two specimens was less than 10% of the free height of the pole. Specimens 4, and 11 consisted of only 6 layers and had a mass, approximately, 60 kg. Specimen 9, which also consisted of 6 layers but had fiber angle of 20°, failed at 18.9 kN. This is less by 5% of the required ultimate load for class 1. However, this specimen was classified as class 2 pole. Five specimens (1, 3, 6, 7, and 8) exceeded the class 1 limit and were classified in the heavier categories (H2 and H3). The maximum lateral displacement recorded in specimen 7 was 12.7% of the free length.

Table (4-3): Performance of Full-Scale GFRP Poles

| Specimen Number | Fiber Orientation | Ultimate Capacity (kN) | Top Displacement (mm) | Equivalent Wooden Pole Class | Displacement % of Free Height |
|-----------------|---|---|-----------------------|------------------------------|-------------------------------|
| 1 | (10/-10) ₄ | 34.2 | 486 | H3 | 9.7 |
| 2 | 90,(10/-10) ₃ ,90 | Specimen failed prematurely inside the concrete base due to a setup error | | | |
| 3 | (90) ₂ ,(10/-10) ₂ ,(90) ₂ | 30.1 | 608 | H2 | 12 |
| 4 | 90,(10/-10) ₂ ,90 | 20.8 | 430 | 1 | 8.6 |
| 5 | 90,(10/-10),90 | 7.55 | 240 | 6 | 4.8 |
| 6 | (20/-20) ₄ | 30.4 | 431 | H2 | 8.6 |
| 7 | 90,(20/-20) ₃ ,90 | 36.4 | 634 | H3 | 12.7 |
| 8 | (90) ₂ ,(20/-20) ₂ ,(90) ₂ | 28.1 | 593 | H2 | 11.9 |
| 9 | 90,(20/-20) ₂ ,90 | 18.9 | 416 | 2 | 8.3 |
| 10 | 90,(20/-20),90 | 6.9 | 252 | 6 | 5.0 |
| 11 | 90,(5/-5) ₂ ,90 | 20 | 403 | 1 | 8.1 |
| 12 | 90,(5/-5),90 | 8.8 | 278 | 5 | 5.6 |

4.3.2 OPTIMUM CONFIGURATION OF GFRP POLES

Since each specimen had a different mass and carrying capacity, the transverse load capacity-to-mass ratio (kN/kg) was used to compare the performance of the specimens tested. The results are shown in Figure (4-13). Specimen 7, which consisted of 8 layers (6 longitudinal layers and 2 circumferencial layers) had the highest performance ratio of, approximately, 0.47 kN/kg. Specimens 3, and 8, which consisted of 8 layers (4 longitudinal layers and 4 circumferencial layers) had a load-to-mass ratio of 0.4 kN/kg. This is a lower ratio than that of specimen 7 which had only two circumferencial layers. Specimens 1 and 6, which consisted of 8 longitudinal layers without any circumferencial ones, had the least performance among the 8-layered pole group with a value of 0.32 kN/kg. This shows that the optimum layer up sequence for the 8-layered poles consists of 6 longitudinal layers and 2 circumferencial layers, the inner most and the outer most layers of the pole.

A significant reduction in the performance ratio occurred when the number of layers was reduced to 6 or 4 layers. This drop was attributed to the reduction in the wall thickness which reduced the buckling load significantly. As shown in Figure (4-13), 6-layered pole (2 circumferencial and 4 longitudinal) had a load-to-mass ratio of approximately 0.32 kN/kg. This ratio is almost the same as the 8-layered pole (without circumferencial layers). This indicated that the addition of circumferencial layers resulted in excellent performance with fewer longitudinal fibers. The least performance ratio was observed in specimens 5, 10, and 12 which consisted of 4 layers (2 longitudinal layers, and 2 circumferencial layers), with a ratio of, approximately, 0.2 kN/kg.

Based on the dimensions of a class 1 Douglas Fir wooden pole with a total height of 6.1 m (20 ft), the transverse load capacity-to-mass ratio is 0.095 kN/kg. The transverse load-to-mass ratio for the equivalent class 1 GFRP pole (specimen 4, or 11) was 0.3 kN/kg or three times as efficient as the wooden poles.

4.3.3 FAILURE MODES

Three different modes of failure were observed during the testing of the full-scale specimens. The first mode was a local buckling on the compression side near the fixed base. The second mode was a failure within the foundation when the specimen was placed in the foundation without an internal stiffener and without completely filling the gap between the specimen and the concrete base. The third mode was a material failure at a section of maximum compressive stress and was characterized by shear fracture of the fibers.

All specimens with circumferential layers (with the exception of specimen 2), failed due to local buckling at a height which varied from 200 mm to 800 mm above the concrete base, as shown in Figure (4-14). Specimen 1, which had no circumferential winding, also failed by local buckling on the compression side 200 m above the base. This failure also involved splitting, delamination and buckling of the fibers, as shown in Figure (4-15).

Specimen 2 failed prematurely inside the concrete base because no internal stiffener was used to support this specimen inside the concrete base. The results from this test are not included in the analysis.

Specimen 6, was composed of 8 layers with the fibers at 20 degrees with the longitudinal axis. It fractured in diagonal direction and parallel to the fibers on the compression side, as shown in Figure (4-16). This diagonal crack extended from a height, approximately, 200 mm above the concrete base to a height of 1200 mm. This failure is similar to mode B of the scaled specimens where the compressive stresses in the fiber direction produces shear stress at an angle with the compressive stress direction and causes diagonal fracture of the fibers.

4.3.4 LOAD-DEFLECTION RELATIONSHIP

The lateral displacement at the top of the specimens was monitored using a linear measurement transducer (LMT) with a range of 2500 mm. The load-deflection graphs for all the tested specimens is presented in Figures (4-17), (4-18), and (4-19). The specimens were categorized on the basis of the fiber angle (10° , 20° , and 5°). The load-deflection relationship was almost linear for all the tested specimens until failure. The small deviation from linearity in the behavior could be attributed to the loss of stiffness in some parts in the specimens due to matrix cracking in the circumferencial layers.

Figure (4-17) shows the load-deflection graphs for the specimens with a fiber angle of 10° . Specimen 1, which had only longitudinal fibers exhibited a linear load-deflection relationship. On the other hand, with the addition of circumferencial layers, the load-deflection relationship tended to deviate, somewhat, from the linear behavior. This could be attributed to the loss of stiffness due the matrix break up in the circumferencial layers. Specimen 1 had the highest stiffness, 70.4 N/mm. Although specimen 3 had two extra circumferencial layers, its stiffness was (49 N/mm) almost identical to that of

specimen 4 which had the type of longitudinal fibers. This indicates that the circumferencial layers did not enhance the longitudinal stiffness of the GFRP poles. However, circumferencial layers increased the ultimate load capacity of specimen 3 which failed at a load approximately 44% higher than the failure load of specimen 4. Specimen 5 had the lowest stiffness with a value of 31.5 N/mm since only 4 layers were used in this specimen and two of these were circumferencial.

Figure (4-18) shows the load–deflection results for specimens with a fiber angle of 20°. As expected, specimen 6 had the highest stiffness, 70.5 N/mm. Specimen 7 had the same total number of layers as specimen 6, but with two extra circumferencial layers. This caused a drop in the pole stiffness from 70.5 N/mm to 57.4 N/mm. However, specimen 7 had an ultimate load of 36.4 kN, which was, approximately, 20% higher than the failure load of specimen 6. Specimens 8 and 9 had almost identical stiffness although specimen 8 has two extra circumferencial layers. There was a significant drop in stiffness in specimen 10, which had two less longitudinal layers than specimen 9. This result stresses the importance of longitudinal fibers in the pole stiffness.

The load–deflection graphs for the two specimens with fiber angle 5° are shown in Figure (4-19). The load–deflection relationship for these two specimens was almost linear. Specimen 11 had a higher capacity and stiffness than specimen 12.

4.3.5 LOAD-OVALIZATION RELATIONSHIP

The change in diameter of all specimens (except specimen # 6) was monitored at 1000 mm above the concrete base. Two LMT's were placed 1000 mm above the concrete base one on the compression side and the other one at the tension side. The difference

between the two LMT readings gave the amount of change in the cross section diameter at that location. The amount of cross section distortion is usually expressed as the ovalization ratio defined as the change in diameter with respect to the original diameter. Ovalization in circular cross sections causes a reduction in the cross sectional properties and, consequently, result in a reduction in the ultimate capacity. A highly nonlinear load-ovalization relationship was observed for all specimens, as shown in Figures (4-20), (4-21), and (4-22).

Figure (4-20) shows the load-ovalization relationship for specimens with fiber angle 10° . The highest ovalization ratio was 5.5% for specimen 1, which had no circumferencial winding compared to 4% for specimen 4. This shows that including circumferencial layers result in a reduction in the amount of cross section distortion. It should be noted that the ovalization ratio was measured at 1000 mm above the base and the maximum ovalization might have occurred at a different location.

Figure (4-21) shows the load-ovalization relationship for specimens with 20° fiber angle. The maximum ovalization ratio for specimen 7 was 6.2%. Both specimens 7 and 8, had 8 layers but specimen 8 had two more circumferencial layers and two less longitudinal layers. This caused a reduction in the amount of the maximum ovalization to 5.8%. The least amount of ovalization ratio was recorded in specimen 10, which had a maximum ovalization of 2%.

Figure (4-22) shows the load-ovalization relationship for the two specimens with a fiber angle of 5° . The maximum ovalization ratios for specimens 11 and 12 were 2.4% and 3.4%, respectively.

4.3.6 STRAINS

The distribution of the longitudinal strains along the height on both the compression and tension sides is shown in Figure (4-23), for specimen 1. This figure represents a typical strain distribution for the tested specimens. The maximum tensile strains always occurred at the base level and reached a maximum value at failure of 8000 $\mu\epsilon$. On the compression side, the strain distribution became more nonlinear with the increase in the applied load. The maximum compressive strain always occurred at the failure location.

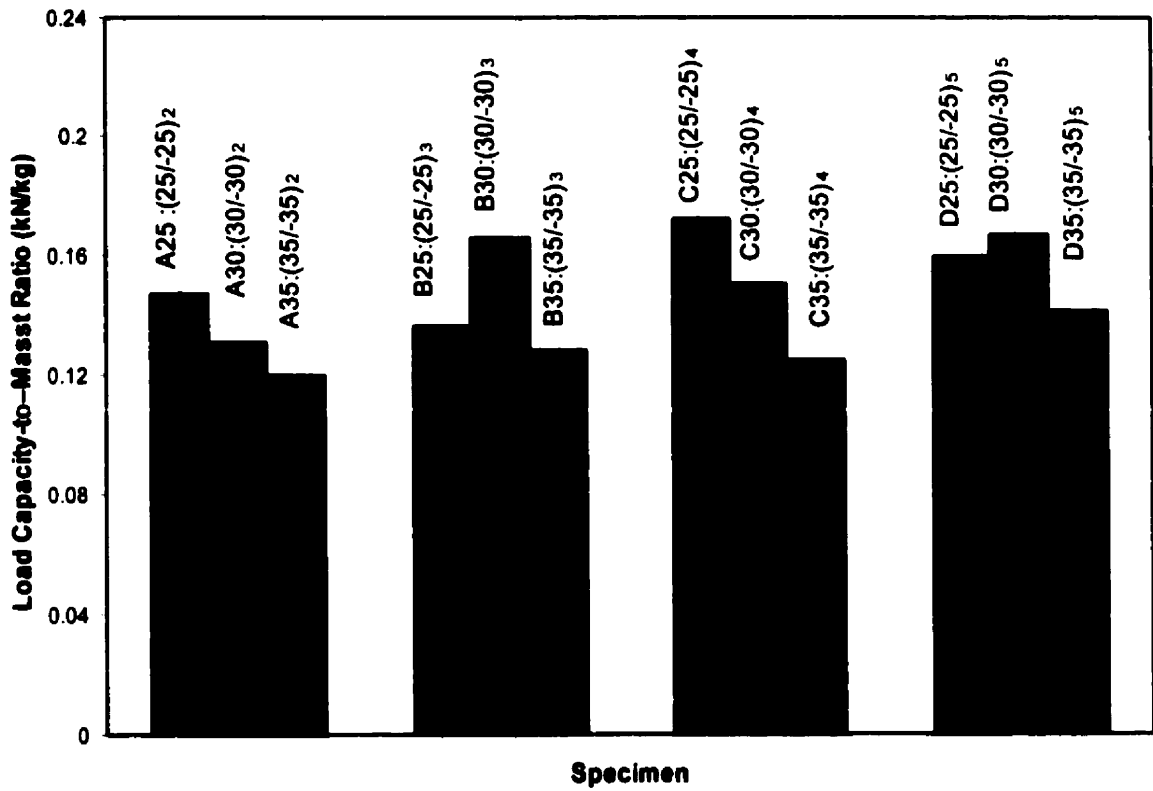


Figure (4-1): load capacity-to-mass ratio for scaled specimens

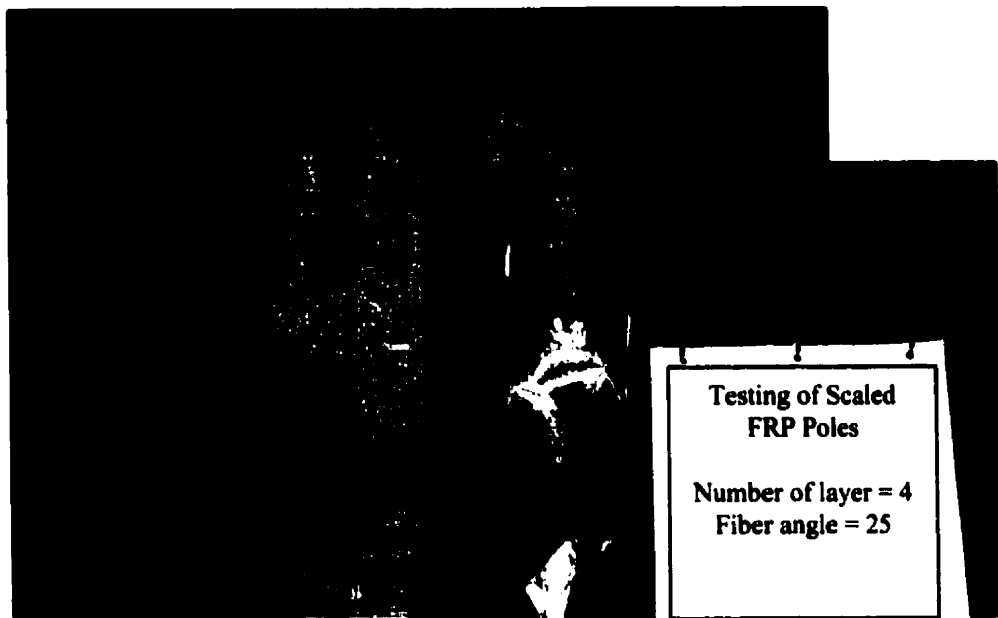


Figure (4-2): Local buckling failure mode for specimen A25

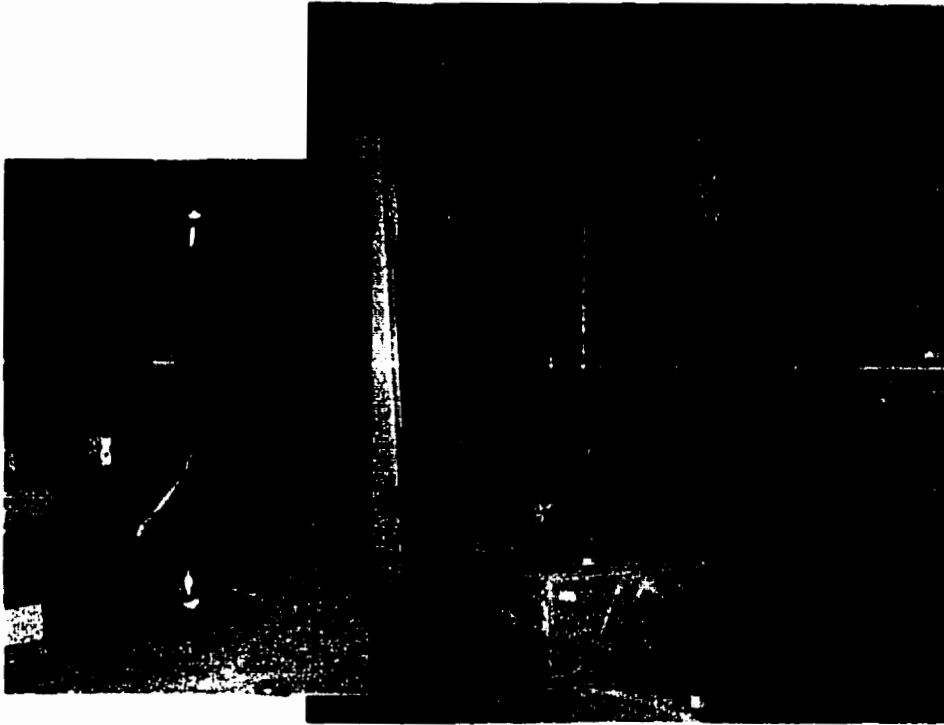


Figure (4-3): Diagonal fracture failure mode for specimen B25

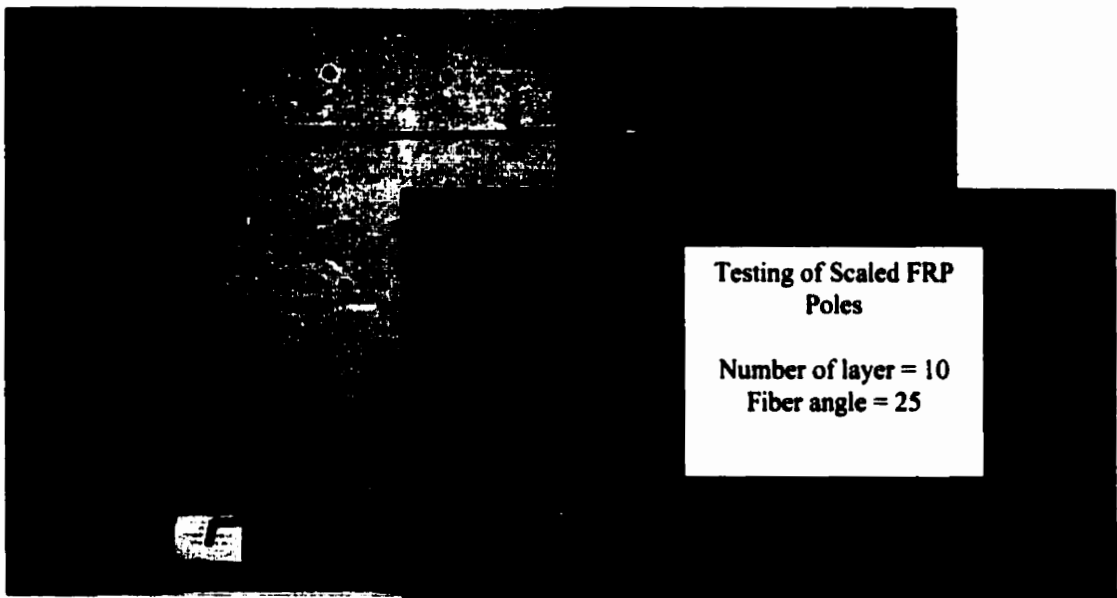


Figure (4-4): Tension failure associated with necking and transverse fiber pull-out

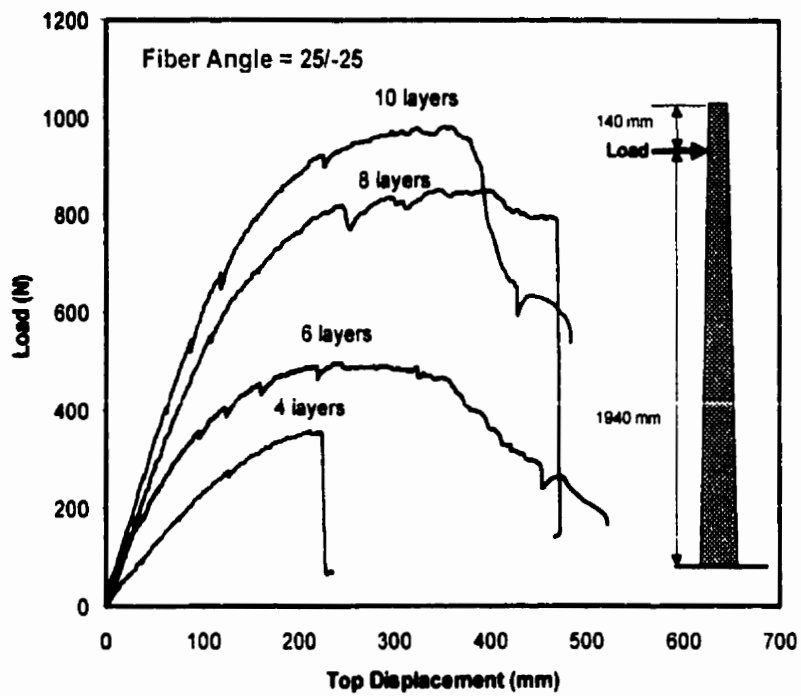


Figure (4-5): Load-deflection curves for fiber angle 25 degrees

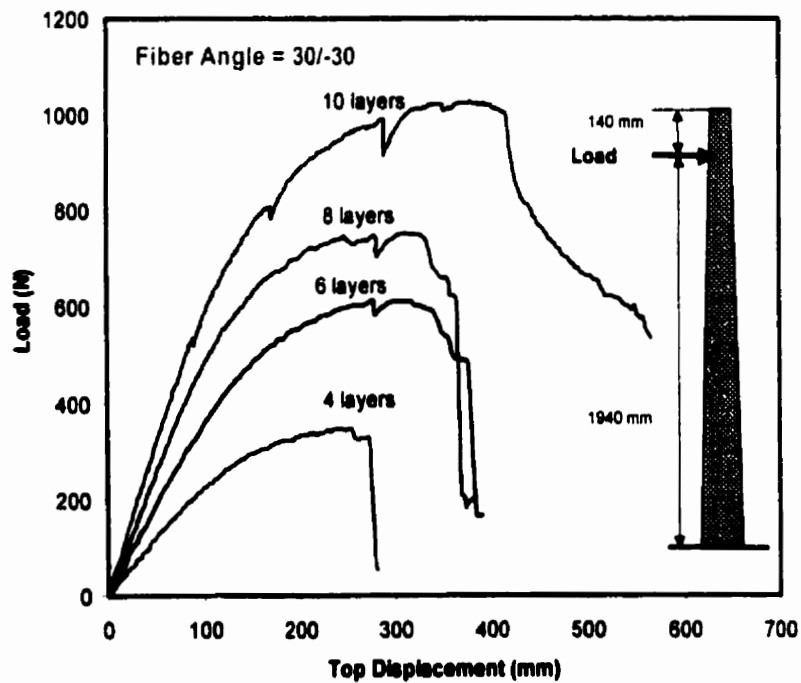


Figure (4-6): Load-deflection curves for fiber angle 30 degrees

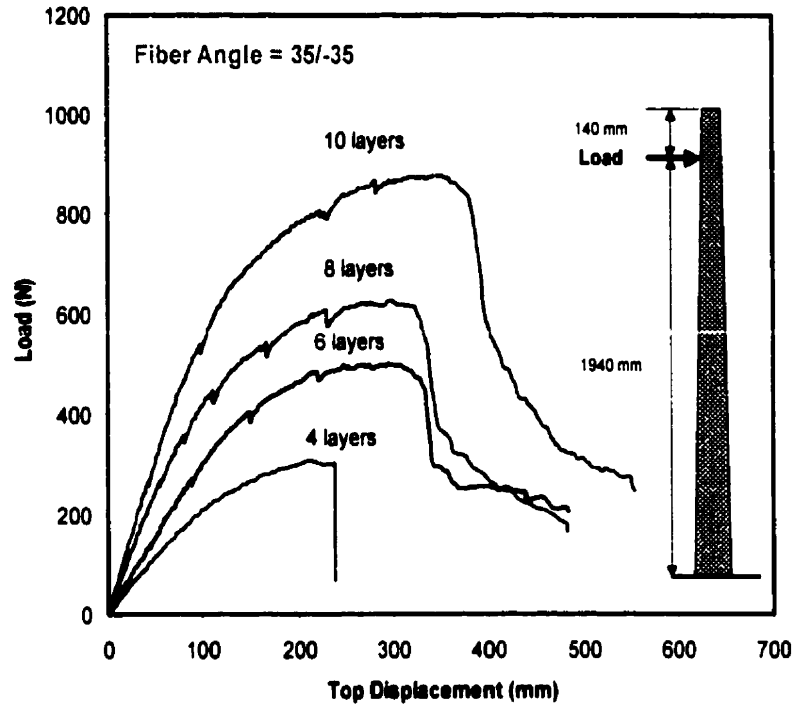


Figure (4-7): Load-deflection curves for fiber angle 35 degrees

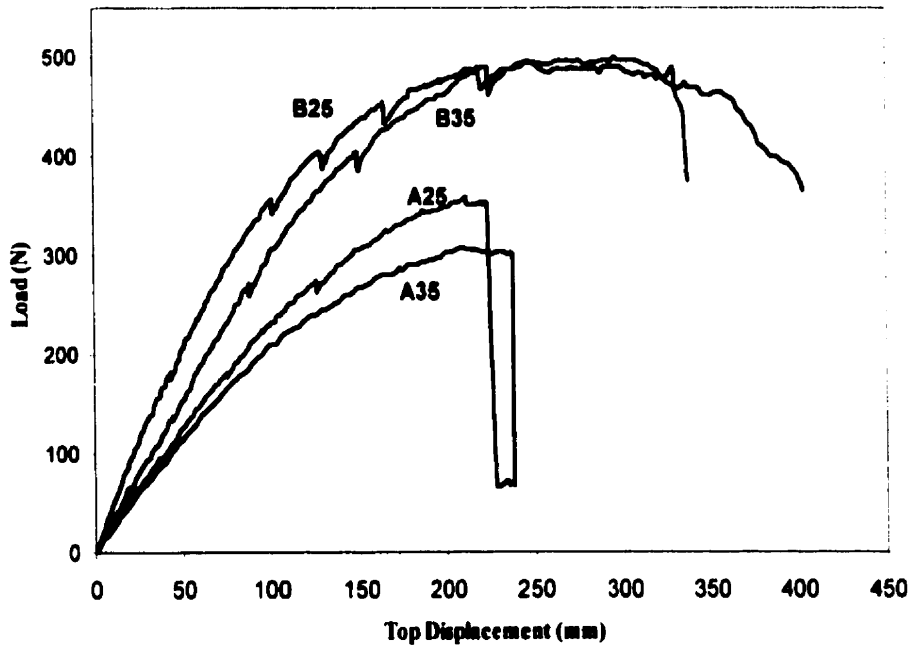


Figure (4-8): Effect of fiber volume fraction and fiber orientation on performance of FRP

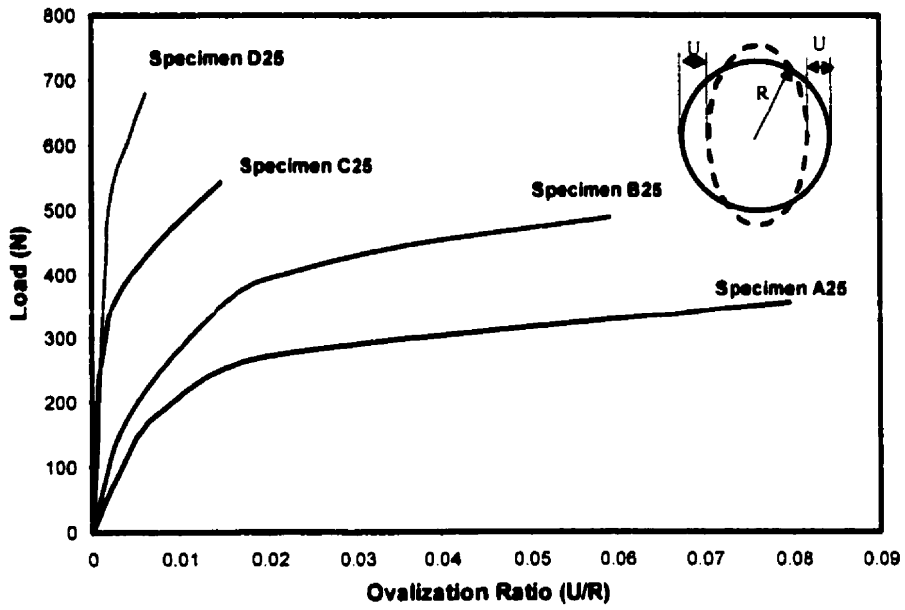


Figure (4-9): Load-ovalization relationship for scaled specimens

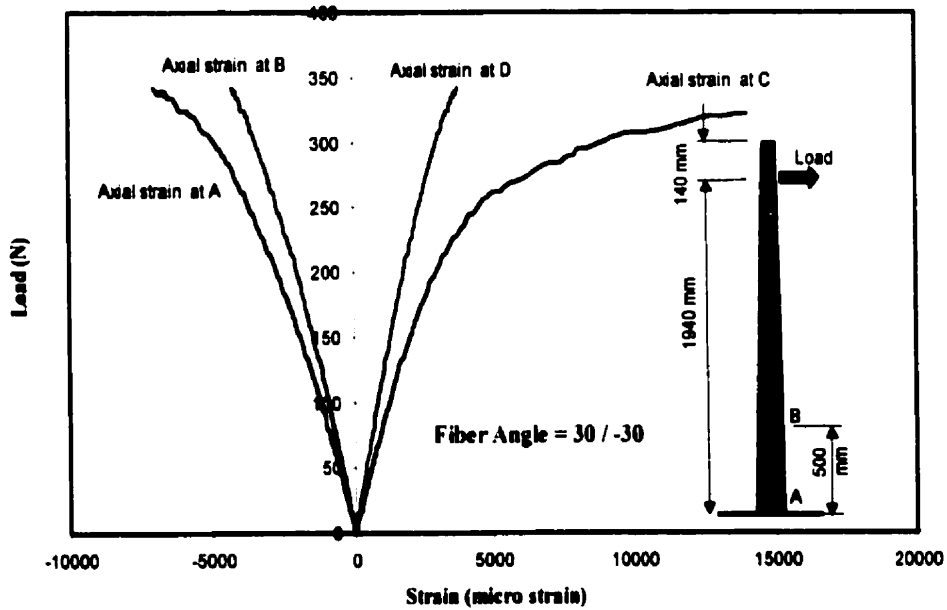


Figure (4-10): Load-strain relationship for specimen A30

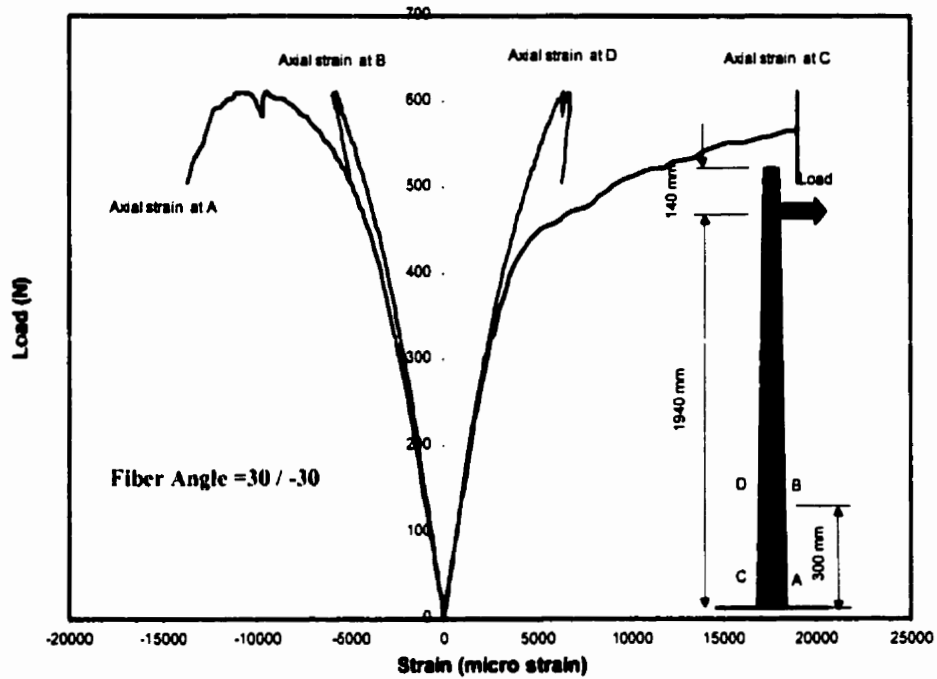


Figure (4-11): Load-strain relationship for specimen B30

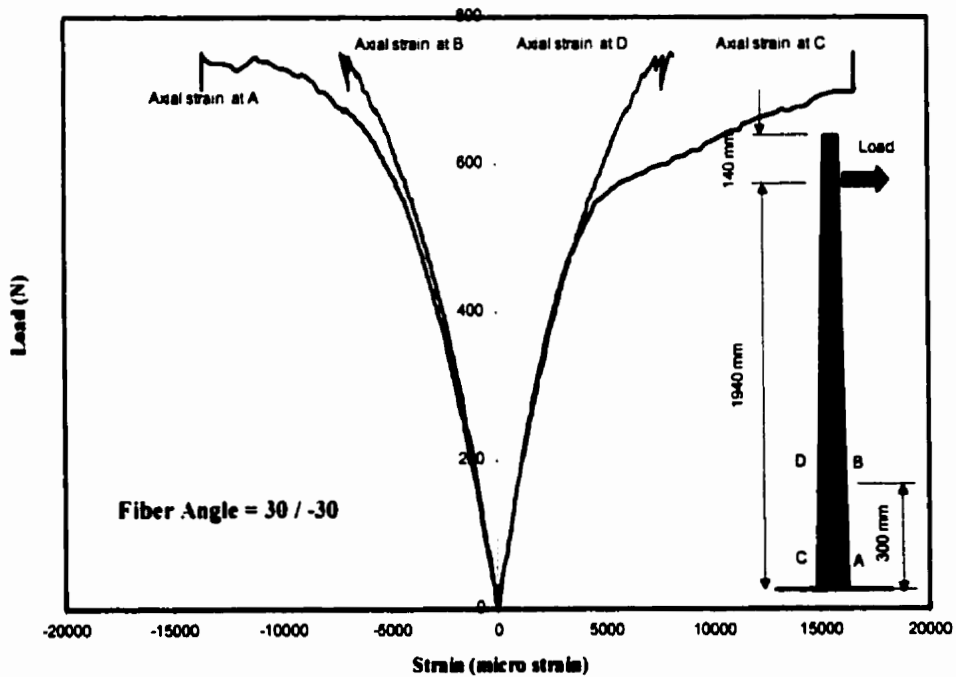


Figure (4-12): Load-strain relationship for specimen D30

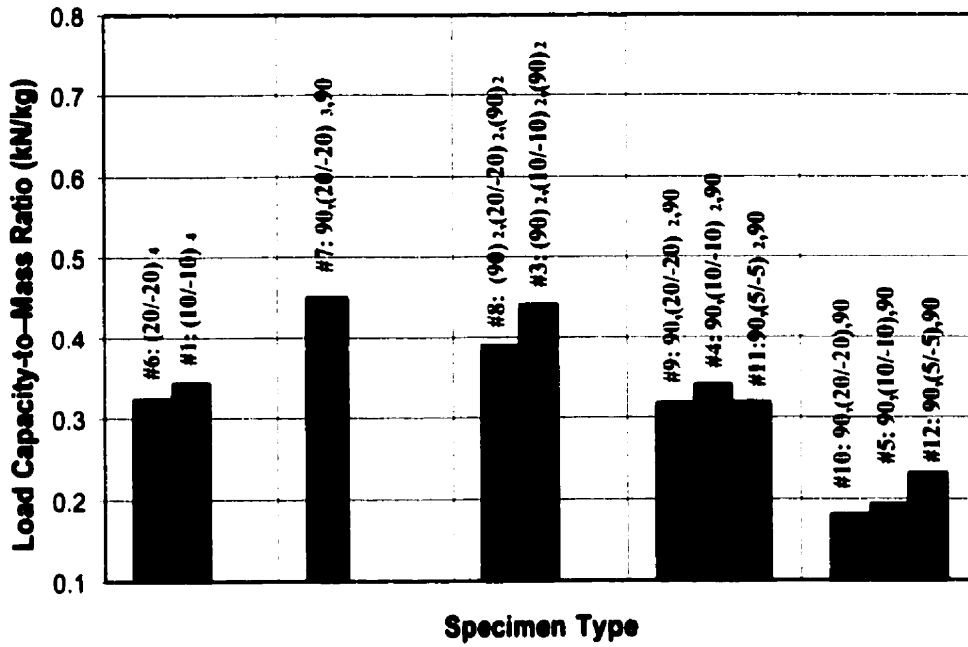


Figure (4-13): load capacity-to-mass ratio for full-scale specimens

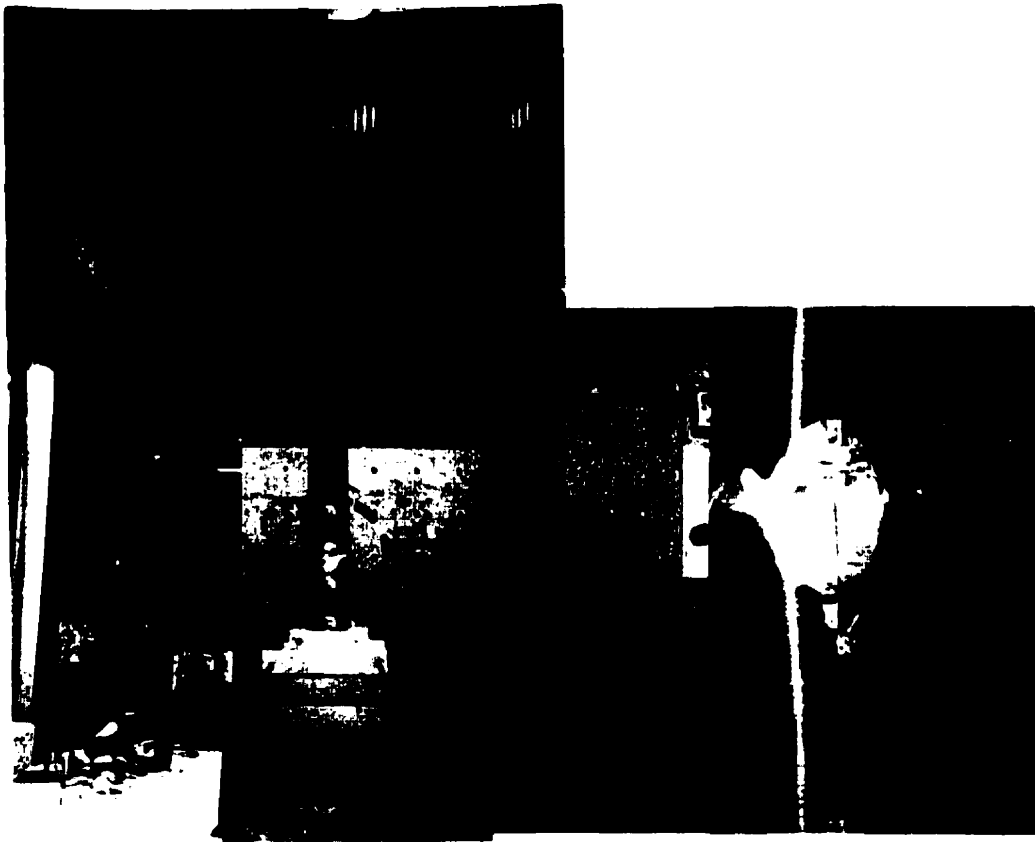


Figure (4-14): Local buckling failure mode for full-scale specimens

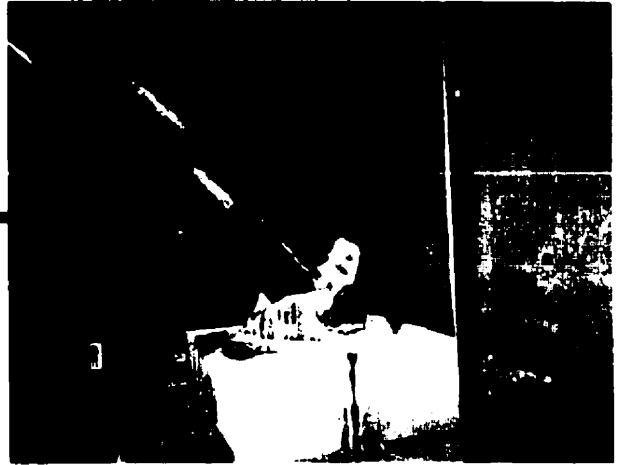


Figure (4-15): Local buckling failure mode for specimen 1



Figure (4-16): Diagonal fracture failure mode for specimen 6

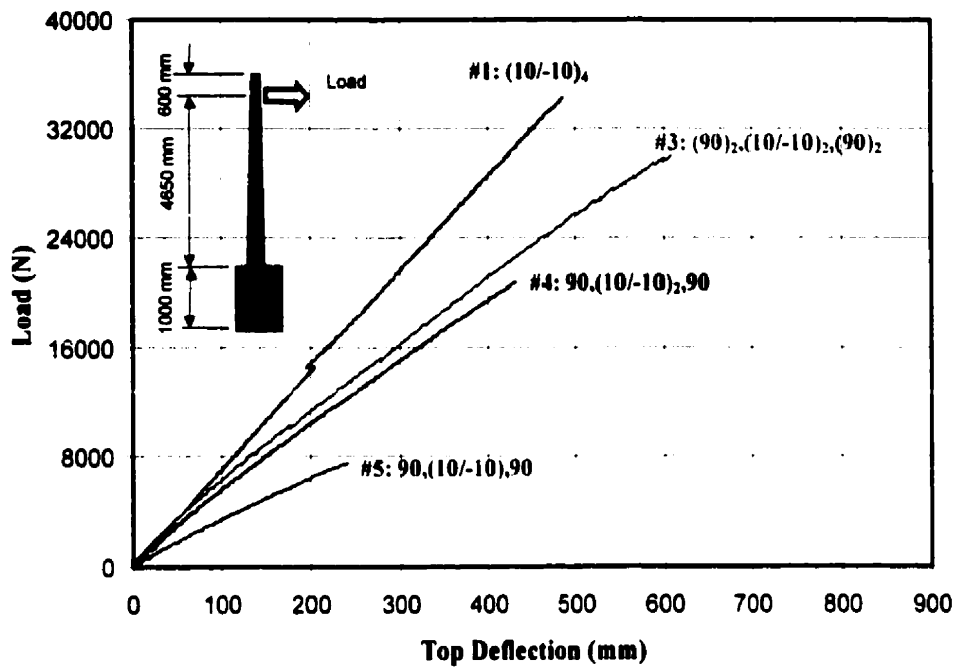


Figure (4-17): Load–deflection relationship for specimens with 10° longitudinal fibers

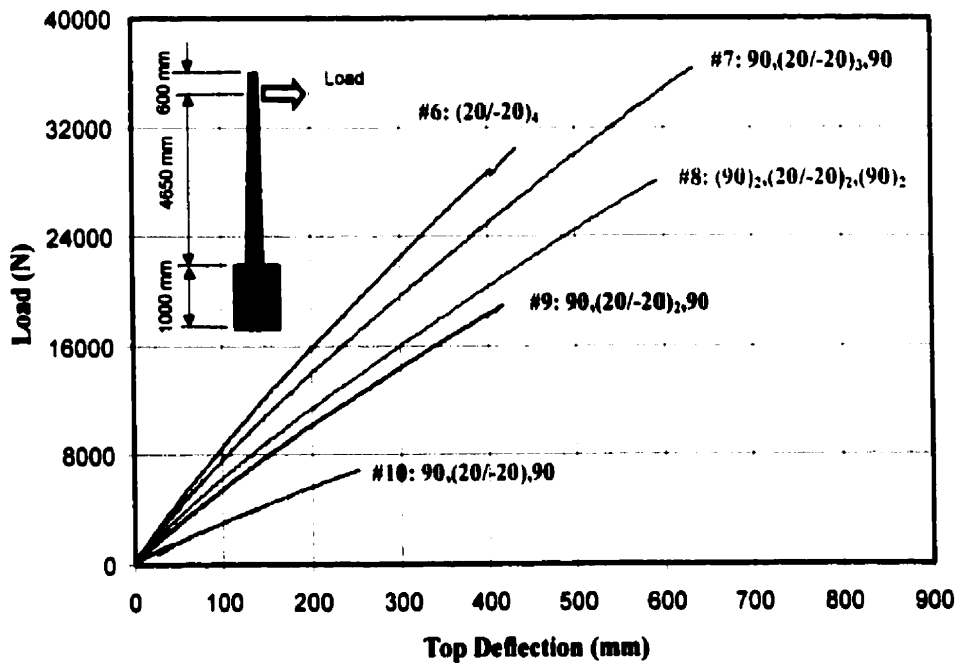


Figure (4-18): Load–deflection relationship for specimens with 20° longitudinal fibers

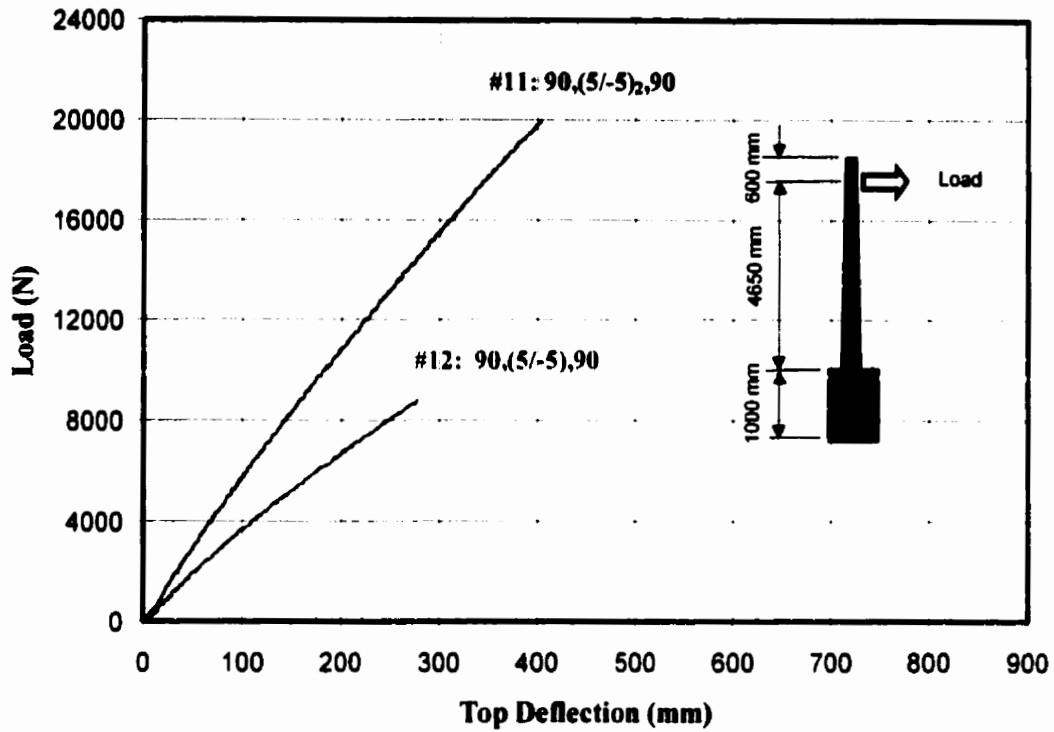


Figure (4-19): Load-deflection relationship for specimens with 5⁰ longitudinal fibers

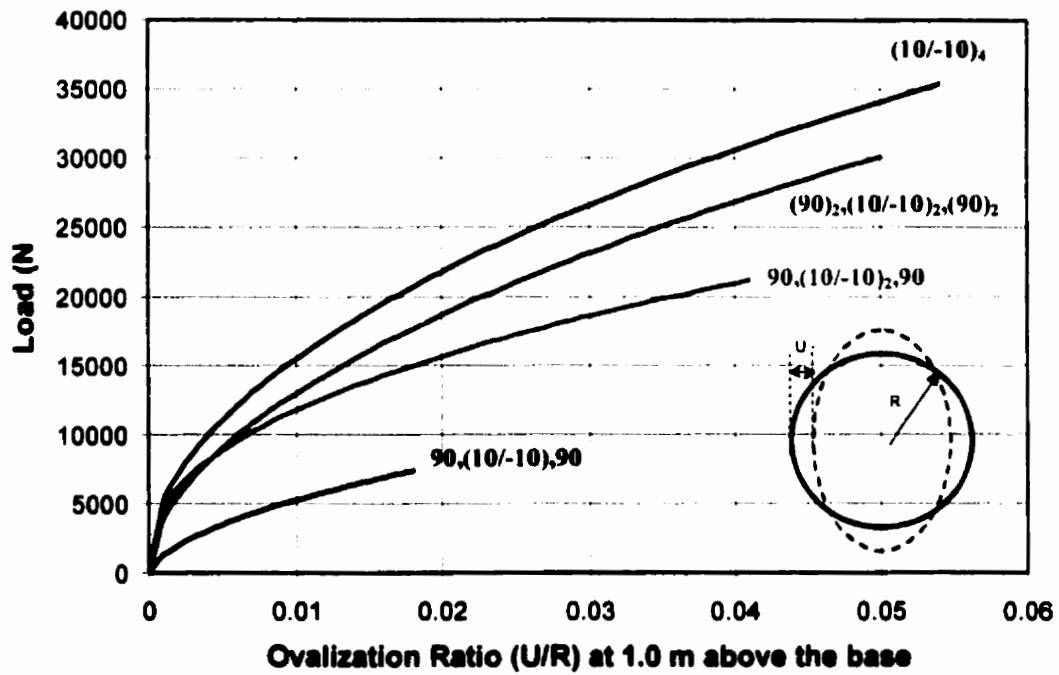


Figure (4-20): Load-ovalization relationship for specimens with 10⁰ longitudinal fibers

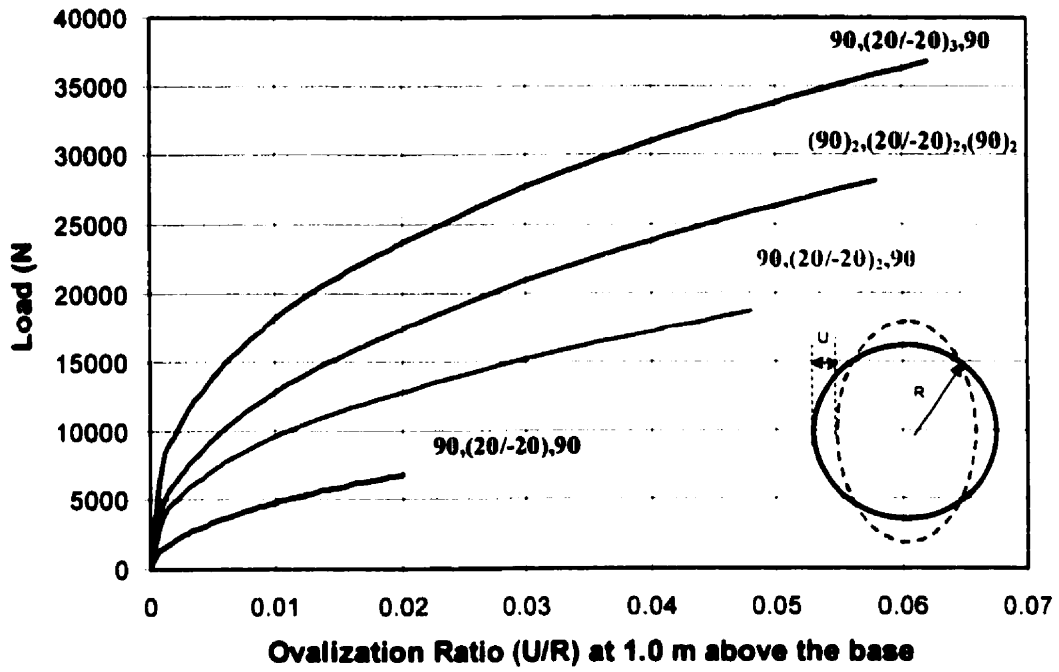


Figure (4-21): Load-ovalization relationship for specimens with 20° longitudinal fibers

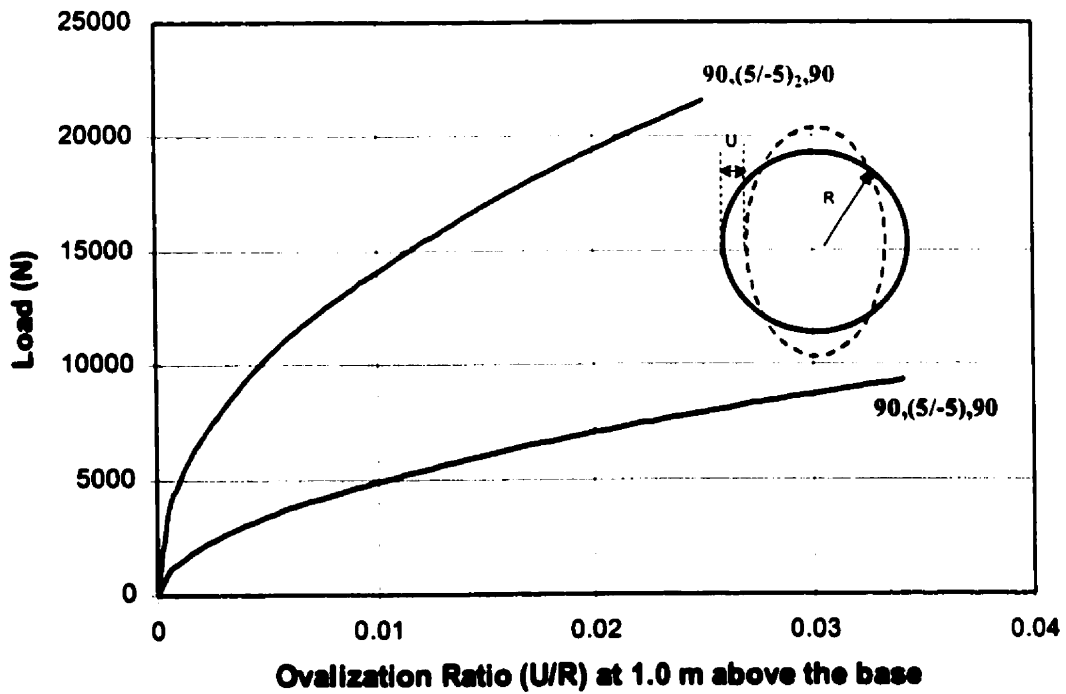


Figure (4-22): Load-ovalization relationship for specimens with 5° longitudinal fibers

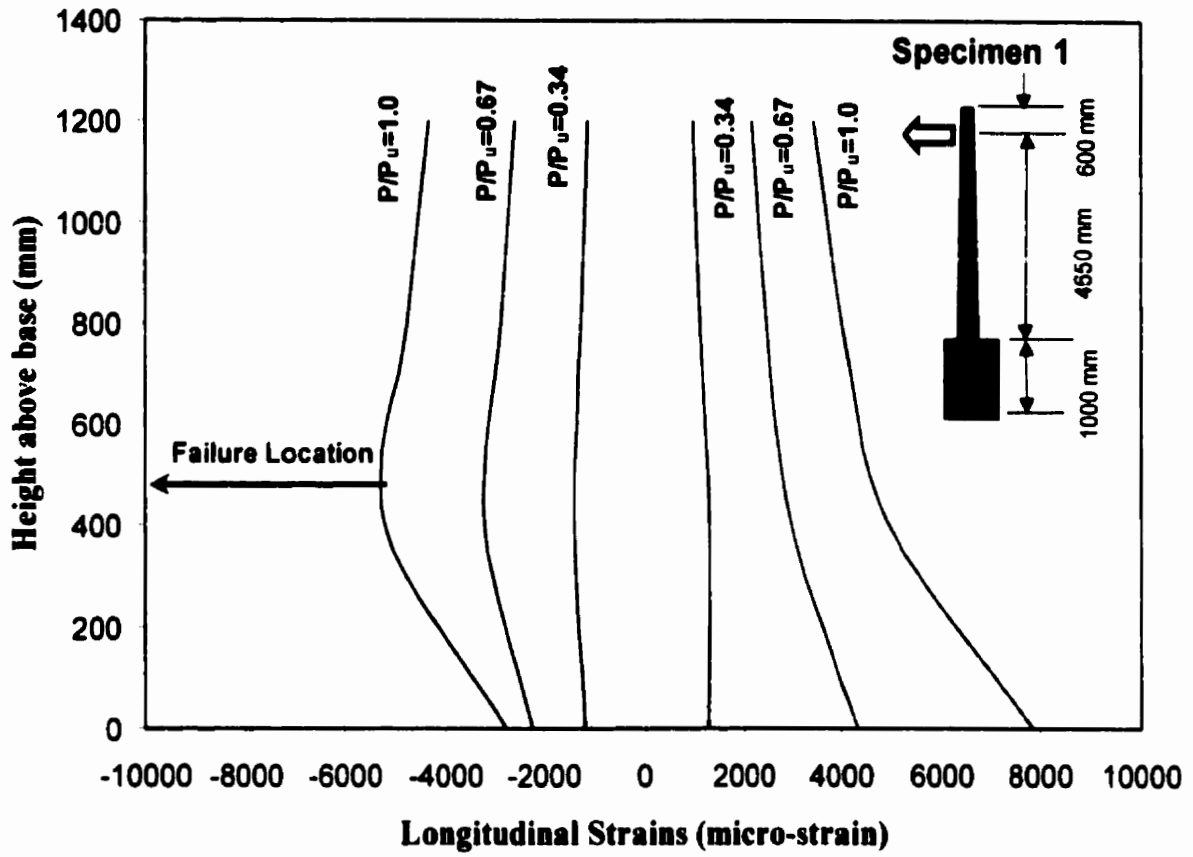


Figure (4-23): Strain distribution along the height for specimen 1

CHAPTER 5

RATIONAL ANALYSIS

5.1 INTRODUCTION

A theoretical method for evaluating material properties, material strengths, and failure criteria is presented in this chapter. The classical lamination theory was implemented to determine the equivalent laminate properties. These properties were included in the analytical model used in this investigation.

A simplified nonlinear analytical model was also developed to predict the ultimate load corresponding to the local buckling failure mode is presented in this chapter. This model accounts for the cross sectional distortion (ovalization) and its effect on the bending capacity. It is an extension of the original notable work by Brazier (1927), who was the first to study the ovalization of isotropic shells under pure bending. A comparison between the experimental results and those obtained through the model is also given in this chapter.

5.2 MATERIAL PROPERTIES

The lamina properties of the GFRP were derived from the material properties of the E-glass fiber and the polyester resin. They used to derive the effective moduli of elasticity of the composite material based on micromechanical models. The Rule of

Mixture, reported by Adams (1987), was used to evaluate the modulus of elasticity in the fiber direction (E_1), and the major Poisson's ratio (μ_{12}) as follows:

$$E_1 = E_f v_f + E_m v_m \quad (5-1)$$

$$\mu_{12} = \mu_f v_f + \mu_m v_m \quad (5-2)$$

where,

v_f and v_m are the fiber and the matrix volume ratios, respectively;

E_f and E_m are the fiber and the matrix Young's moduli, respectively; and

μ_f and μ_m are the fiber and the matrix Poisson's ratios respectively.

For calculating the effective Young's modulus in the transverse direction (E_2) and the shear modulus (G_{12}), the Tsai-Hahn (1980) approach was used. This approach was based on the fact that the stresses in both fibers and matrix are not equal under the corresponding loading conditions. The Tsai-Hahn equations were expressed in terms of the fiber and matrix properties as follows:

$$E_2 = \frac{(v_f + \psi v_m)}{\left[\frac{v_f}{E_f} + \frac{\psi v_m}{E_m} \right]} \quad (5-3)$$

$$G_{12} = \frac{(v_f + \psi v_m)}{\left[\frac{v_f}{G_f} + \frac{\psi v_m}{G_m} \right]} \quad (5-4)$$

where,

G_f and G_m are the fiber and the matrix shear moduli, respectively; and,

ψ is the stress partitioning parameter. It was found that a value of $\psi = 0.5$ yields accurate predictions based on comparison with experimental data for glass epoxy (Tsai and Hahn 1980).

Equations (5-1) to (5-4) were used to determine the effective materials properties for the composite lamina in this study. The fiber volume ratio v_f and the matrix volume ratio v_m were measured during the manufacture process. The fiber and the matrix properties were provided by the manufacturer and the supplier, respectively.

5.3 MATERIAL STRENGTH

The strength of a composite material can be determined in a similar manner using a micromechanical model and advanced elasticity methods. It depends on the relative properties of the fibers and the matrix and their corresponding volume fractions.

Longitudinal tensile strength

The tensile strength of the composite in the fiber direction (S_1^+) can be determined when the fiber stress reaches its ultimate value (S_f^+). The corresponding strain in both the fiber and the matrix (ϵ_f^+ , and ϵ_m) can be determined as follows:

$$\epsilon_f^+ = \epsilon_m = \frac{S_f^+}{E_f} \quad (5-5)$$

The corresponding matrix stress (S_m) reaches a value:

$$S_m = E_m \varepsilon_m = E_m \frac{S_f^+}{E_f} \quad (5-6)$$

The tensile strength in the fiber direction can be computed using the rule of mixtures as follows:

$$S_1^+ = S_f^+ \nu_f + E_m \frac{S_f^+}{E_f} \nu_m \quad (5-7)$$

Longitudinal compressive strength

A model for calculating the longitudinal compressive strength (S_1^-) of composite materials has been presented by Agarwal and Broutman (1990). This model was based on the maximum strain criterion applied to tensile transverse Poisson strain (ε_2) under longitudinal compressive loading, computed as follows:

$$\varepsilon_2 = \varepsilon_1 \mu_{12} = \frac{S_1^-}{E_1} \mu_{12} \quad (5-8)$$

The ultimate longitudinal compressive strength is reached when the transverse strain (ε_2) of composite reaches its maximum value. Nielsen (1974) presented a semi-empirical model for calculating the ultimate value of the composite transverse strain as follows:

$$\varepsilon_2 = \varepsilon_m^+ (1 - \sqrt[3]{\nu_f}) \quad (5-9)$$

where, ε_m^+ is the ultimate tensile strain of the matrix.

Equations (5-8), and (5-9) can be combined to evaluate the longitudinal compressive strength as follows:

$$S_1^- = \frac{E_1}{\mu_{12}} (1 - \sqrt[3]{\nu_f}) \epsilon_m^+ = \frac{E_1}{\mu_{12}} (1 - \sqrt[3]{\nu_f}) \frac{S_m^+}{E_m} \quad (5-10)$$

where, S_m^+ is the matrix tensile strength.

Tensile transverse strength

Failure of a composite lamina under transverse tension occurs at very low stress (Gibson, 1995). The low values of the transverse tensile strength (S_2^+) and the corresponding transverse ultimate strain (ϵ_2) are due to strain concentration in the matrix around the fibers. The Model developed by Neilsen (1974) to compute for the ultimate transverse strain in a composite, can be used to derive the transverse tensile strength as follows:

$$S_2^+ = E_2 \epsilon_2 = E_2 (1 - \sqrt[3]{\nu_f}) \epsilon_m^+ = E_2 (1 - \sqrt[3]{\nu_f}) \frac{S_m^+}{E_m} \quad (5-11)$$

Compressive transverse strength

The same method outlined above can also be used to estimate the transverse compressive strength (S_2^-) by replacing the tensile strains or strengths with the corresponding compressive strains or strengths. Therefore, the compressive transverse strength can be expressed as follows:

$$S_2^- = E_2 \varepsilon_2 = E_2 (1 - \sqrt[3]{V_f}) \varepsilon_m^- = E_2 (1 - \sqrt[3]{V_f}) \frac{S_m^-}{E_m} \quad (5-12)$$

where, S_m^- is the matrix compressive strength.

In-plane shear strength

In-plane shear failure could take place if there is matrix shear failure (Agarwal, 1990). The in-plane shear strength (S_{12}) can be determined when the ultimate in-plane shear strain (γ_{12}) for the composite is reached. Therefore, the in-plane shear strength can be expressed as follows:

$$S_{12} = G_{12} \gamma_{12} \quad (5-13)$$

The in-plane shear strain of composites is always lower than the matrix in-plane shear strain because of the strain concentrations around the interface between the fiber and the matrix. In-plane shear strain can be expressed in terms of the matrix in-plane shear strain as follows:

$$\gamma_{12} = \gamma_m (1 - \sqrt[3]{V_f}) = \frac{S_{12m}}{G_m} (1 - \sqrt[3]{V_f}) \quad (5-14)$$

where, S_{12m} is the matrix in-plane shear strength.

Equations (5-13), and (5-14) can be used to estimate the in-plane shear strength as follows:

$$S_{12} = \frac{G_{12}}{G_m} S_{12m} (1 - \sqrt[3]{V_f}) \quad (5-15)$$

5.4 VERIFICATION OF MATERIAL PROPERTIES

In this section, the mechanical properties calculated on the basis of the information provided by the manufacturer are compared to those obtained experimentally and discussed in Chapter 3. Equations (5-1) and (5-7) were used to calculate the mechanical properties using the material properties for the glass fiber and the polyester resin shown in Table (3-1) provided by the manufacturer in. The average values of the longitudinal elastic modulus and the longitudinal tensile strength shown in Table (3-5) were used here. Table (5-1) shows the experimental results for the elastic modulus and the tensile strength as well as calculated from Equations (5-1) and (5-7).

Table (5-1): Experimental and theoretical material properties

| Mechanical properties | Average of experimental data | Theoretical values based on manufacturer data | Theoretical / experimental |
|-------------------------------------|------------------------------|---|----------------------------|
| Longitudinal modulus (GPa) | 36.5 | 34.4 | 0.94 |
| Longitudinal tensile strength (MPa) | 924.9 | 1002.4 | 1.08 |

As shown in Table (5-1), the mechanical properties calculated from the manufacturer's information are very close to the experimental results. This indicates that the material properties provided by the manufacturer for the glass fiber and the polyester resin was used with confidence to develop the lamina mechanical properties.

5.5 FAILURE CRITERION

A failure criterion can be incorporated in the theoretical analysis to predict the ultimate capacity of GFRP poles by using the ply stresses obtained through a finite element analysis and comparing them to the material strengths. The Tsai-Wu (1971) failure criterion was adopted for this purpose. This failure criterion was chosen because it accounts for the interaction between different stress components. In the Tsai-Wu general quadratic interaction criterion, the failure surface in stress space is described by the following equation:

$$\zeta = \left(\frac{1}{\sigma_{xt}^f} + \frac{1}{\sigma_{xc}^f} \right) \sigma_x + \left(\frac{1}{\sigma_{yt}^f} + \frac{1}{\sigma_{yc}^f} \right) \sigma_y + \left(\frac{1}{\sigma_{zt}^f} + \frac{1}{\sigma_{zc}^f} \right) \sigma_z - \frac{\sigma_x^2}{\sigma_{xt}^f \sigma_{xc}^f} - \frac{\sigma_y^2}{\sigma_{yt}^f \sigma_{yc}^f} - \frac{\sigma_z^2}{\sigma_{zt}^f \sigma_{zc}^f} + \frac{\sigma_{xy}^2}{(\sigma_{xy}^f)^2} + \frac{\sigma_{yz}^2}{(\sigma_{yz}^f)^2} + \frac{\sigma_{xz}^2}{(\sigma_{xz}^f)^2} + \frac{2C_{xy}\sigma_x\sigma_y}{\sqrt{\sigma_{xt}^f \sigma_{xc}^f \sigma_{yt}^f \sigma_{yc}^f}} + \frac{2C_{yz}\sigma_y\sigma_z}{\sqrt{\sigma_{yt}^f \sigma_{yc}^f \sigma_{zt}^f \sigma_{zc}^f}} + \frac{2C_{xz}\sigma_x\sigma_z}{\sqrt{\sigma_{xt}^f \sigma_{xc}^f \sigma_{zt}^f \sigma_{zc}^f}} \quad (5-16)$$

In order to avoid failure, the value of ζ must be less than unity, and failure is predicted when ζ is greater or equal to unity. The terms in equation (5-16) are defined as follows:

$\sigma_x, \sigma_y, \sigma_z$ are stresses obtained from the analysis of any layer in x, y, and z directions, respectively;

$\sigma_{xy}, \sigma_{yz}, \sigma_{xz}$ are the shear stresses for any layer in the xy, yz, and xz planes, respectively;

$\sigma_{xt}^f, \sigma_{xc}^f$ are the tension, and compression failure stresses of the material in the x direction, respectively;

$\sigma_{yt}^f, \sigma_{yc}^f$ are the tension, and compression failure stresses of the material in the y direction, respectively;

$\sigma_{zt}^f, \sigma_{zc}^f$ are the tension, and compression failure stresses of the material in the z direction, respectively;

$\sigma_{xy}^f, \sigma_{yz}^f, \sigma_{xz}^f$ are the failure shear stresses in the xy, yz, and xz planes respectively, and,

C_{xy}, C_{yz}, C_{xz} are the coupling coefficients used in the Tsai-Wu theory in the xy, yz, and xz planes, respectively.

The Tsai-Wu coupling coefficients must be between -1.0 and 1.0. This requirement is necessary to ensure that the failure surface intercepts each stress axis and the shape of the surface is a closed one and not open-ended like a hyperboloid.

5.6 EQUIVALENT LAMINATE PROPERTIES

The stiffness components of a generally orthotropic plate can be determined using the classical lamination theory (Tsai, 1989). The constitutive equations for the laminate are

$$\begin{Bmatrix} N \\ M \end{Bmatrix} = \begin{bmatrix} A & B \\ B & D \end{bmatrix} \begin{Bmatrix} \epsilon \\ \kappa \end{Bmatrix} \quad (5-17)$$

or, in a more expanded format:

$$\begin{Bmatrix} N_x \\ N_y \\ N_{xy} \\ M_x \\ M_y \\ M_{xy} \end{Bmatrix} = \begin{bmatrix} A_{11} & A_{12} & A_{13} & B_{11} & B_{12} & B_{13} \\ A_{21} & A_{22} & A_{23} & B_{21} & B_{22} & B_{23} \\ A_{31} & A_{32} & A_{33} & B_{31} & B_{32} & B_{33} \\ B_{11} & B_{12} & B_{13} & D_{11} & D_{12} & D_{13} \\ B_{21} & B_{22} & B_{23} & D_{21} & D_{22} & D_{23} \\ B_{31} & B_{32} & B_{33} & D_{31} & D_{32} & D_{33} \end{bmatrix} \begin{Bmatrix} \varepsilon_x \\ \varepsilon_y \\ \varepsilon_{xy} \\ \kappa_x \\ \kappa_y \\ \kappa_{xy} \end{Bmatrix} \quad (5-18)$$

where, $\{N\}$ and $\{M\}$ are the stress resultants and stress couples, respectively; and, $\{\varepsilon\}$ and $\{\kappa\}$ are the strains and curvatures, respectively. The stiffness coefficients A_{ij} , B_{ij} , and D_{ij} correspond to membrane, coupling, and bending stiffness coefficient and are defined as follows:

$$A_{ij} = \int_{-t/2}^{t/2} \bar{Q}_{ij} dz = \sum_{k=1}^n (\bar{Q}_{ij})_k (h_k - h_{k-1}) \quad (5-19)$$

$$B_{ij} = \int_{-t/2}^{t/2} z \bar{Q}_{ij} dz = \frac{1}{2} \sum_{k=1}^n (\bar{Q}_{ij})_k (h_k^2 - h_{k-1}^2) \quad (5-20)$$

$$D_{ij} = \int_{-t/2}^{t/2} z^2 \bar{Q}_{ij} dz = \frac{1}{3} \sum_{k=1}^n (\bar{Q}_{ij})_k (h_k^3 - h_{k-1}^3) \quad (5-21)$$

where, t is the laminate thickness, z is the distance between the laminate mid-plane to any point within the laminate; \bar{Q}_{ij} are the transformed layer stiffness components; n is the total number of layers within the laminate; and, h_k , and h_{k-1} are the distances between the laminate mid-plane and the two boundaries of layer k , respectively, as shown in Figure (5-1).

The transformed stiffness matrix depends on the lamina fiber orientation and the stiffness matrix in the lamina local axes. The transformed stiffness matrix can be expressed as follows:

$$[\bar{Q}_{ij}] = [T_{ij}]^{-1} [Q_{ij}] [T_{ij}] \quad (5-22)$$

where, $[T]$, and $[Q_{ij}]$ are the transformation matrix and the stiffness matrix in lamina local axes, respectively. These are defined as follows:

$$[T_{ij}] = \begin{bmatrix} \cos^2 \theta & \sin^2 \theta & 2 \sin \theta \cos \theta \\ \sin^2 \theta & \cos^2 \theta & -2 \sin \theta \cos \theta \\ -\sin \theta \cos \theta & \sin \theta \cos \theta & \cos^2 \theta - \sin^2 \theta \end{bmatrix} \quad (5-23)$$

$$[Q_{ij}] = \begin{bmatrix} \frac{E_1}{1 - \mu_{12}^2 E_2 / E_1} & \frac{\mu_{12} E_1}{1 - \mu_{12}^2 E_2 / E_1} & 0 \\ \frac{\mu_{12} E_1}{1 - \mu_{12}^2 E_2 / E_1} & \frac{E_2}{1 - \mu_{12}^2 E_2 / E_1} & 0 \\ 0 & 0 & G_{12} \end{bmatrix} \quad (5-24)$$

where, θ is the fiber angle with respect to the x-axis.

Equation (5-17) can be inverted to establish a relationship between the strain components and the stress resultants, as follows:

$$\begin{Bmatrix} \varepsilon \\ \kappa \end{Bmatrix} = \begin{bmatrix} A & B \\ B & D \end{bmatrix}^{-1} \begin{Bmatrix} N \\ M \end{Bmatrix} \quad (5-25)$$

or, in a more expanded format:

$$\begin{Bmatrix} \epsilon_x \\ \epsilon_y \\ \epsilon_{xy} \\ \kappa_x \\ \kappa_y \\ \kappa_{xy} \end{Bmatrix} = \begin{bmatrix} a_{11} & a_{12} & a_{13} & b_{11} & b_{12} & b_{13} \\ a_{21} & a_{22} & a_{23} & b_{21} & b_{22} & b_{23} \\ a_{31} & a_{32} & a_{33} & b_{31} & b_{32} & b_{33} \\ b_{11} & b_{12} & b_{13} & d_{11} & d_{12} & d_{13} \\ b_{21} & b_{22} & b_{23} & d_{21} & d_{22} & d_{23} \\ b_{31} & b_{32} & b_{33} & d_{31} & d_{32} & d_{33} \end{bmatrix} \begin{Bmatrix} N_x \\ N_y \\ N_{xy} \\ M_x \\ M_y \\ M_{xy} \end{Bmatrix} \quad (5-26)$$

It is, however, more convenient to use the effective laminate engineering constants in the theoretical analysis of composite structures. The effective moduli in both x and y directions, which govern the response of the laminate in those direction, can be determined from the following equations:

$$E_{x\text{eff}} = \frac{\sigma_x}{\epsilon_x} = \frac{N_x / t}{a_{11} N_x} = \frac{1}{a_{11} t} \quad (5-27)$$

$$E_{y\text{eff}} = \frac{\sigma_y}{\epsilon_y} = \frac{N_y / t}{a_{22} N_y} = \frac{1}{a_{22} t} \quad (5-28)$$

The effective laminate Poisson's ratio is defined as:

$$\mu_{xy} = \frac{a_{12}}{a_{11}} \quad (5-29)$$

5.7 NONLINEAR OVALIZATION ANALYSIS

When a thin-walled tube of a circular cross section, and originally straight, is subjected to a bending moment M, the tensile and compressive longitudinal stresses on opposite sides of the neutral plane combine with the curvature of the axis of the tube to flatten the cross section into an oval section. The ovalization, in turn, decreases the

moment of inertia of the cross section about the axis of bending leading to a nonlinear load-displacement relationship. Additionally, the deformation of the cross section increases the axial bending stresses and lowers the structure's buckling load. As mentioned in Chapter 2, this problem was first formulated by Brazier (1927) for isotropic tubes under pure bending moment.

The main objective of this section is to establish a relationship between the applied bending moment and the cross sectional deformation of a composite tube. The corresponding stresses due to the applied bending and the cross section distortion (ovalization) will be checked for local buckling conditions.

5.7.1 BASIC ASSUMPTIONS AND LIMITATIONS

A discussion of the assumptions and limitations imposed on the analysis is presented in this section. These assumptions can be summarized as follows:

- 1) Deformation of the cross section with respect to the shell circumference is inextensional. This implies that the circumferential strains are zero.
- 2) Displacement components in the radial and tangential direction of the shell are always small compared to the radius of the shell.
- 3) Effective orthotropic laminate properties will be used to represent the composite material in the analysis.
- 4) Radial displacements at the bottom and at the top of GFRP poles are prevented. In this present study, this was accomplished through the use of an internal stiffener

(GFRP sleeve) and through the existence of thick dome end at the top which prevented radial deformation.

- 5) The distribution of the ovalization along the height the GFRP poles is assumed to follow a sinusoidal variation. The same assumption was adopted by Calladine (1983) in his analysis of isotropic tubes.
- 6) The average radius of the tapered GFRP poles was used in the analysis. The tapering ratio, defined as the ratio of the difference between the bottom and the top radii to the total height, of GFRP poles is usually very small. For the tested full-scale specimens, the tapering ratio was only 0.0083. Ibrahim and Polyzois (1999) showed that the use of the average radius in the ovalization analysis resulted in excellent agreement with nonlinear finite analysis.

5.7.2 FORMULATION

When GFRP poles are subjected to a horizontal loading at the top, the resulting bending moment will tend to distort the cross section into an oval shape as shown in Figure (5-2). The distribution of the ovalization along the height is also shown in this figure. Formulation of a theoretical model for the member behavior starts by expressing the total strain energy of a GFRP pole in terms of the maximum ovalization ratio and the average longitudinal curvature of the GFRP pole. The total strain energy is the sum of the strain energies due to the circumferential bending and the longitudinal stretching. Thus, the strain energy can be computed at two distinct stages of deformed configuration. The first stage involves the ovalization of a straight tube restrained at both ends. The second

stage involves the GFRP pole with ovalized cross section subjected to the applied bending moment.

5.7.2.1 Stage 1: Strain energy calculation due ovalization

In this stage, the GFRP pole being analyzed is considered as a straight tube with an ovalized cross section and restrained against radial displacements at both ends. The derivation of the necessary displacements at this stage will be presented before the strain energy expression is evaluated.

Based on an assumed sinusoidal distribution of the ovalization along the height of the GFRP pole, the ovalization at any location can be determined as follows:

$$\xi = \xi_0 \sin \frac{\pi x}{L} \quad (5-30)$$

where, ξ is the ovalization at distance x from the loaded end, ξ_0 is the maximum ovalization at the mid height cross section, and L is the length of the GFRP pole, as shown in Figure (5-2).

Assuming that the deformed shape is an oval, the distribution of radial displacement along the cross section can be described as follows:

$$w = a \xi_0 \sin \frac{\pi x}{L} \cos 2\phi \quad (5-31)$$

where, w is the radial displacement as shown in Figure (5-3), a is the average radius of the pole, and ϕ is the angular coordinate measured from the neutral plane in the original configuration.

According to the assumption of inextensional deformation of the cross section, the circumferential displacement, v , is given by:

$$\frac{dv}{d\phi} + w = 0 \quad (5-32)$$

The solution of the above differential equation yields the following expression for the circumferential displacement:

$$v = -\frac{1}{2} a \xi_0 \sin \frac{\pi x}{L} \sin 2\phi \quad (5-33)$$

It should be noted that in the above solution, the integration constant was set to zero, since there is no net rotation of the cross section of the tube.

Since the radial deformation of the tube is restrained at both ends, longitudinal strains (ϵ_x) and longitudinal stresses (N_x) will be developed in the GFRP pole. The longitudinal stresses can be computed from basic cylindrical shell theory (Calladine 1983) as follows:

$$\frac{\partial w}{\partial x} = \frac{1}{a} \frac{\partial^2 u}{\partial \phi^2} \quad (5-34)$$

where, u is the longitudinal displacement.

Using Equation (5-31), the solution of the above differential equation can be expressed as follows:

$$u = -\frac{a^2 \pi}{4L} \xi_0 \cos \frac{\pi x}{L} \cos 2\phi \quad (5-35)$$

$$\varepsilon_x = \frac{\partial u}{\partial x} = \frac{a^2 \pi^2}{4L^2} \xi_0 \sin \frac{\pi x}{L} \cos 2\phi \quad (5-36)$$

$$N_x = E_{\text{eff}} \varepsilon_x t = \frac{\pi^2 a^2 E_{\text{eff}} t}{4L^2} \xi_0 \sin \frac{\pi x}{L} \cos 2\phi \quad (5-37)$$

The last required displacement component required for the strain energy calculations at this stage is the change in the circumferential curvature (κ_2), which is defined as follows:

$$\kappa_2 = -\frac{1}{a^2} \left(\frac{\partial^2 w}{\partial \phi^2} + w \right) \quad (5-38)$$

Substituting in Equation (5.38) the expression for w given by Equation (5-31), the change in the circumferential curvature can be rewritten as follows:

$$\kappa_2 = \frac{3}{a} \xi_0 \sin \frac{\pi x}{L} \cos 2\phi \quad (5-39)$$

The strain energy at any given location x, due to the first stage of deformation (U_{1x}), can be calculated as follows:

$$U_{1x} = \frac{1}{2} \int_0^{2\pi} \kappa_2 D_{22} a d\phi + \frac{1}{2} \int_0^{2\pi} \frac{N_x^2}{E_{\text{eff}} t} a d\phi \quad (5-40)$$

where, D_{22} is the circumferencial bending stiffness component determined from Equation (5-21). Performing the above integration, the strain energy can be expressed in the following form:

$$U_{1x} = \frac{9\pi}{2a} \xi_0^2 D_{22} \left[1 + \frac{\pi^4}{12\Omega^4} \right] \sin^2 \frac{\pi x}{L} \quad (5-41)$$

where,

$$\Omega = \frac{L}{a} \sqrt[4]{\frac{12D_{22}}{a^2 E_{xeff} t}} \quad (5-42)$$

The total strain energy of the GFRP pole (U_1) can be calculated as follows:

$$U_1 = \int_0^L U_{1x} dx = \frac{9\pi}{4a} \xi_0^2 D_{22} \left[1 + \frac{\pi^4}{12\Omega^4} \right] L \quad (5-43)$$

5.7.2.2 Stage 2: Strain energy calculation due to applied bending

In this stage, the strain energy is calculated due the bending of GFRP pole under the applied moment gradient with the cross section already ovalized. The first step in the calculations is to determine the moment of inertia of the oval cross section as a function of the ovalization ratio. The displacement in direction normal to the neutral axis (η), can be expressed as follows:

$$\eta = w \sin \phi + v \cos \phi \quad (5-44)$$

From Equations (5-31), and (5-33), η can be rewritten as follows:

$$\eta = \frac{1}{4} a \xi (-3 \sin \phi + \sin 3\phi) = -a \xi \sin^3 \phi \quad (5-45)$$

Now by definition, the cross section moment of inertia can be calculated as follows:

$$I = \int_0^{2\pi} (a \sin \phi + \eta)^2 a t d\phi \quad (5-46)$$

On performing the above integration, the moment of inertia can be expressed as follows:

$$I = I_0 (1 - 1.5\xi) = I_0 \left(1 - 1.5\xi_0 \sin \frac{\pi x}{L}\right) \quad (5-47)$$

where,

$$I_0 = \pi a^3 t \quad (5-48)$$

It should be noted that in the above expression for the moment of inertia I , the term that include (ξ^2) has been omitted, as indicated by Brazier (1927) and Calladine (1983), by truncating second order effects.

Applying the beam theory, the curvature of the GFRP pole at a given location C_x , can be related to the applied bending moment as follows:

$$C_x = \frac{M_x}{E_{\text{eff}} I} = \frac{M_0(x/L)}{E_{\text{eff}} I_0 \left(1 - 1.5\xi_0 \sin \frac{\pi x}{L}\right)} \quad (5-49)$$

where, M_0 is the bending moment at the base. Using the binomial theorem and truncating the resulting power series, the curvature can be rewritten as follows:

$$C_x = \frac{M_0(x/L)}{E_{\text{eff}} I_0} \left(1 + 1.5\xi_0 \sin \frac{\pi x}{L} \right) \quad (5-50)$$

As shown in Figure (5-4), the free end rotation of the GFRP pole is $(L \times C)$ where, L is the length of the pole and C is the average curvature. The end rotation can be expressed in terms of the curvature at any given location as follows:

$$L \times C = \int_0^L C_x dx = \frac{M_0}{E_{\text{eff}} I_0} \int_0^L \left(\frac{x}{L} + 1.5\xi_0 \frac{x}{L} \sin \frac{\pi x}{L} \right) dx \quad (5-51)$$

On performing the above integration the average curvature can be expressed as:

$$C = \frac{M_0}{2 E_{\text{eff}} I_0} \left(1 + \frac{3\xi_0}{\pi} \right) \quad (5-52)$$

Using Equations (5-50) and (5-52) and eliminating M_0 , the curvature C_x can be rewritten as follows:

$$C_x = \frac{2C}{(1 + 3\xi_0/\pi)} \left(\frac{x}{L} \right) \left(1 + 1.5\xi_0 \sin \frac{\pi x}{L} \right) \quad (5-53)$$

The strain energy due to bending of an GFRP pole at any given location x , can be calculated from the following expression:

$$U_{2x} = \frac{1}{2} M_x C_x = \frac{1}{2} E_{\text{eff}} I_0 \left(1 - 1.5\xi_0 \sin \frac{\pi x}{L} \right) C_x^2 \quad (5-54)$$

Substituting the expression for C_x from Equation (5-53), and performing integration of U_{2x} over the whole length, the total strain energy for bending of an GFRP pole can be expressed in the following form:

$$U_2 = \int_0^L U_{2x} dx = \frac{2}{3} \frac{E_{\text{eff}} I_0 C^2}{(1 + 0.955\xi_{50})^2} (1 + 0.852\xi_{50}) L \quad (5-55)$$

5.7.2.3 Moment-ovalization relationship

The total strain energy of the GFRP pole (U) is the summation of the strain energies from the two stages mentioned in previous sections. Therefore, it can be written as follows:

$$U = U_1 + U_2 = \frac{9\pi}{4a} \xi_{50}^2 D_{22} \left[1 + \frac{\pi^4}{12\Omega^4} \right] L + \frac{2}{3} \frac{E_{\text{eff}} I_0 C^2}{(1 + 0.955\xi_{50})^2} (1 + 0.852\xi_{50}) L \quad (5-56)$$

Using the theorem of minimum strain energy, the equilibrium conditions will be determined by the condition

$$\frac{\partial U}{\partial \xi_{50}} = 0 \quad (5-57)$$

This gives a relationship between the maximum ovalization ratio, and the average curvature as follows:

$$C = 1.425 \sqrt{\frac{\pi D_{22} (1 + \pi^4 / 12\Omega^4) \xi_{50}}{E_{\text{eff}} t a^4}} \quad (5-58)$$

The bending moment at any location x , is determined from the following relation:

$$M_x = \frac{\partial}{\partial C_x} (U_{1x} + U_{2x}) = C_x E_{\text{eff}} I_0 (1 - 1.5 \xi_0 \sin \frac{\pi x}{L}) \quad (5-59)$$

Equations (5-53) and (5-58) can be used to express M_x in terms of the ovalization ratio ξ_0 , as follows:

$$M_x = 2.85 \pi a \frac{x}{L} \sqrt{\pi E_{\text{eff}} D_{22} t \left(1 + \frac{\pi^4}{12 \Omega^4}\right)} \left(1 - \frac{3}{\pi} \xi_0\right) \sqrt{\xi_0} \quad (5-60)$$

The bending moment at the base of the GFRP pole can be simply calculated when $x=L$, as follows:

$$M_0 = 2.85 \pi a \sqrt{\pi E_{\text{eff}} D_{22} t \left(1 + \frac{\pi^4}{12 \Omega^4}\right)} \left(1 - \frac{3}{\pi} \xi_0\right) \sqrt{\xi_0} \quad (5-61)$$

5.7.2.4 Stress calculations

The total stress at any point in the GFRP pole is the summation of two stresses: the stress due to the ovalization of the straight GFRP pole and the stress due to the applied bending moment on the ovalized cross section. The two stress components can be expressed in terms of the maximum ovalization at any given location. The stress due the ovalization of the straight GFRP pole (σ_1) can be derived from the axial stress resultant N_x , which was deduced for calculation of the strain energy in the first stage. Therefore, σ_1 can be written as follows:

$$\sigma_1 = \frac{N_x}{t} = \frac{\pi^2 E_{\text{eff}} a^2}{4L^2} \xi_0 \sin \frac{\pi x}{L} \cos 2\phi \quad (5-62)$$

The maximum stresses will be developed on the extreme surface of the shell at $\phi = \pi / 2$. Thus the maximum stress σ_1 is,

$$\sigma_1 = \frac{\pi^2 E_{\text{eff}} a^2}{4L^2} \xi_0 \sin \frac{\pi x}{L} \quad (5-63)$$

The stresses due the bending can be derived from the beam theory. The longitudinal strain at the extreme surface of the shell can be expressed in terms of the curvature as follows:

$$\varepsilon_x = C_x a \left(1 - \xi_0 \sin \frac{\pi x}{L}\right) \quad (5-64)$$

The effective longitudinal modulus can be used to evaluate the longitudinal stresses due the bending of the ovalized GFRP pole as follows:

$$\sigma_2 = E_{\text{eff}} \varepsilon_x = E_{\text{eff}} C_x a \left(1 - \xi_0 \sin \frac{\pi x}{L}\right) \quad (5-65)$$

Using Equations (5-53) and (5-58), to eliminate C_x and express σ_2 in terms of the ovalization ratio as follows:

$$\sigma_2 = 2.85 \sqrt{\frac{\pi D_{22} E_{\text{eff}} (1 + \pi^4 / 12 \Omega^4)}{a^2 t}} \frac{(1 - \xi_0 \sin \frac{\pi x}{L}) \sqrt{\xi_0}}{(1 + \frac{3\xi_0}{\pi})(1 - 1.5\xi_0 \sin \frac{\pi x}{L})} \left(\frac{x}{L}\right) \quad (5-66)$$

The total stress (σ) at any location x , is simply the summations of the two stresses σ_1 and σ_2 . Therefore, the total stress can be expressed in terms of the ovalization ratio as follows:

$$\sigma = \frac{\pi^2 E_{\text{eff}} a^2}{4L^2} \xi_0 \sin \frac{\pi x}{L} + 2.85 \sqrt{\frac{\pi D_{22} E_{\text{eff}} (1 + \pi^4 / 12 \Omega^4)}{a^2 t}} \frac{(1 - \xi_0 \sin \frac{\pi x}{L}) \sqrt{\xi_0}}{(1 + \frac{3\xi_0}{\pi})(1 - 1.5\xi_0 \sin \frac{\pi x}{L})} \left(\frac{x}{L} \right) \quad (5-67)$$

5.7.2.5 Critical buckling stress

The critical local buckling stress, as indicated by Hutchinson (1968), depends on the local radius of curvature of the cross section. Therefore, when GFRP pole ovalizes progressively under the action of bending moment, the local radius of curvature increases. This causes a reduction in the compressive stress required to form the local buckling. Tating, et al. (1996), showed that the critical buckling stress (σ_{cr}) for an orthotropic composite shell can be computed as follows:

$$\sigma_{cr} = \frac{2 \sqrt{D_{11} E_{\text{yeff}} t}}{\rho t} \quad (5-68)$$

where, D_{11} is the laminate bending stiffness in the longitudinal direction computed from Equation (5-21); E_{yeff} is the effective circumferencial modulus calculated in Equation (5-28); and, ρ is the local radius of curvature of the cross section. The local radius of curvature of the ovalized cross section can be calculated as follows:

$$\frac{1}{\rho} = \frac{1}{a} + \kappa_2 \quad (5-69)$$

where, $\frac{1}{\rho}$ is the new cross section curvature; $\frac{1}{a}$ is the original cross section curvature;

and, κ_2 is the change in circumferencial curvature.

Equation (5-38) was used to replace the change in circumferencial curvature and express the critical buckling stress in terms of the ovalization ratio. Therefore, the local radius of curvature of the cross section can be rewritten as:

$$\rho = \frac{a}{\left(1 - 3\xi_0 \sin \frac{\pi x}{L}\right)} \quad (5-70)$$

Using the above equation, the critical stress can be expressed in terms of the ovalization ratio as follows:

$$\sigma_{cr} = \frac{2 \sqrt{D_{11} E_{yeff} t}}{a t} \left(1 - 3\xi_0 \sin \frac{\pi x}{L}\right) \quad (5-71)$$

It is evident from the above equation that the critical buckling stress decreases under progressively increasing ovalization.

5.7.2.6 Application

Under progressively increasing bending moment, the cross-section ovalization ratio and the longitudinal stresses in the GFRP poles increase. On the other hand, the critical buckling stress decreases with the increase in the cross section ovalization. Failure would occur when the value of the longitudinal stress is equal to the critical buckling stress. The critical failure load may be obtained by equating the longitudinal

stress σ , computed from Equation (5-67), and the critical buckling stress σ_{cr} , computed from Equation (5-71), and solving for the value of the ovalization ratio ξ_0 at different values of x/L . Failure would occur at the minimum value of ξ_0 obtained at different values of x/L . Once the ovalization ratio ξ_0 is determined, the critical bending at the base can be determined from Equation (5-61). The critical buckling load that can be applied at the top of the GFRP pole is simply the base bending moment divided by the cantilever length of the pole.

For simplicity, the above procedure can be implemented graphically as illustrated in Figure (5-5). The longitudinal stress σ , the critical buckling stress σ_{cr} at different values of x/L , and the bending moment at the base are plotted versus the ovalization ratio, ξ_0 . The intersection points between the curves corresponding to the longitudinal and critical stresses determine the occurrence of failure at the particular value of x/L . For example, in Figure (5-5) failure at location 1 and 2 would occur at values of ovalization ratio ξ_0 corresponding to the intersection points P and Q respectively. However, member failure first occurs at the intersection point, which has the lowest value of ξ_0 . This indicates that for the shown case, member failure would occur first at location 2. From the intersection point Q, and using the bending moment-ovalization ratio relationship, the critical value of the bending moment can be determined, as shown in Figure (5-5).

The above graphical method was implemented to determine the critical bending moment as well as the critical load for all the tested full-scale GFRP poles. Figure (5-6) shows the relationship between the maximum ovalization ratio, and the longitudinal

stress, critical buckling stress, and the base bending moment, for specimen 7. As evident of this figure, the intersection point between the longitudinal and critical stress has a minimum value of ovalization ratio at location $x/L=0.9$. The corresponding value of the ovalization ratio is approximately 0.09. The value of the bending moment can be easily read from the graph at this point, as shown in Figure (5-6).

This procedure was repeated for all specimens which failed by local buckling and the critical failure load was evaluated. To evaluate the theoretical results, the ratio of the failure load P_{exp} , to the theoretical critical load P_{model} was computed for the specimens tested. These results are shown in Figure (5-7). The average ratio was 0.85 and the standard deviation was less than 10%.

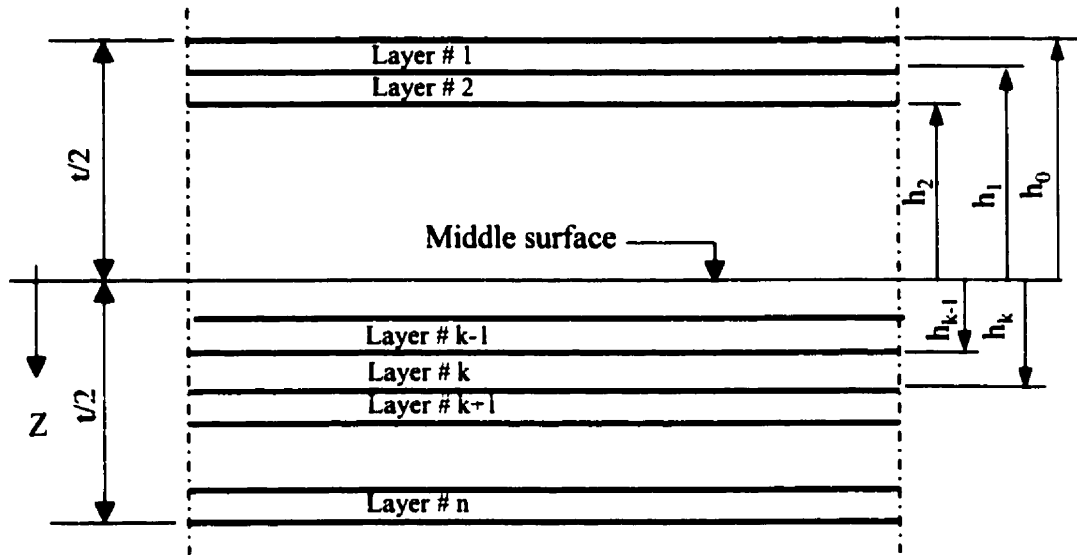


Figure (5-1): Laminate geometry and layer numbering system

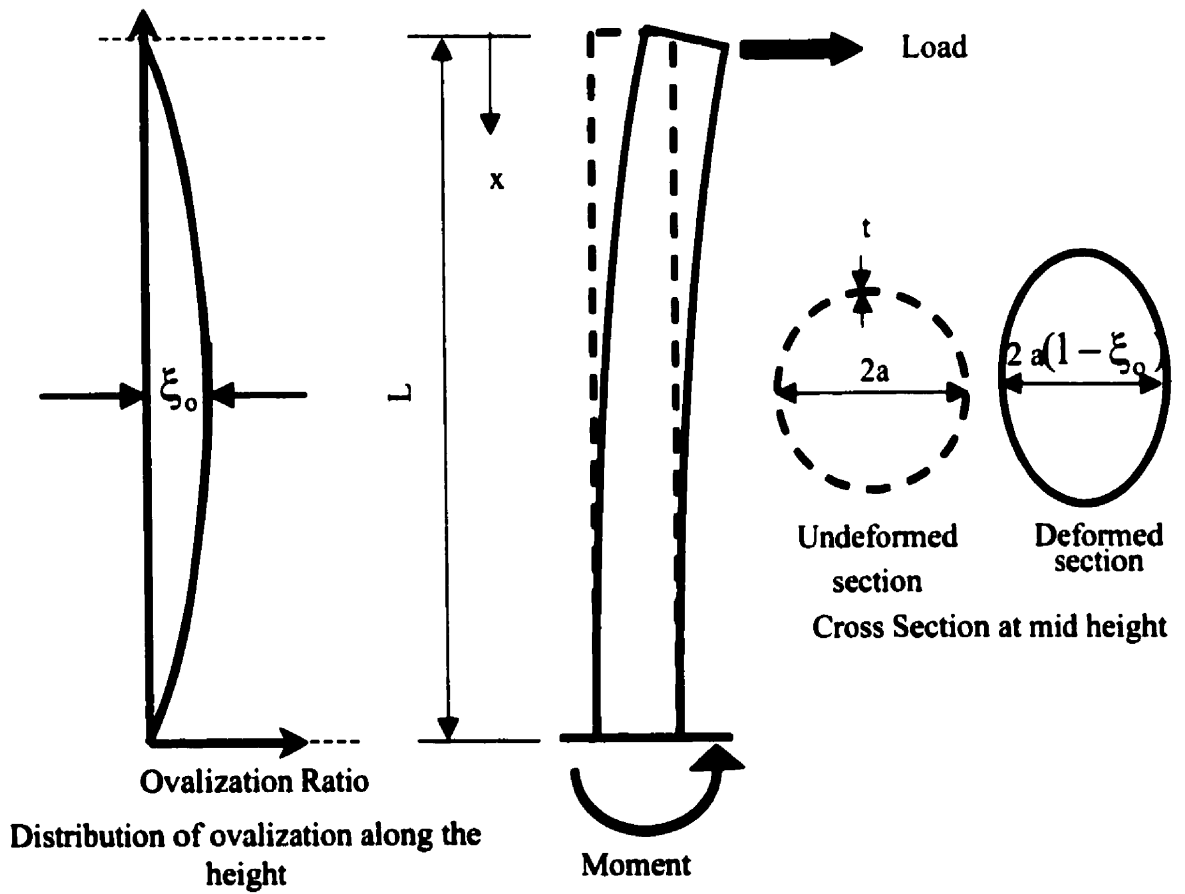


Figure (5-2): Ovalization of GFRP poles and assumed ovalization distribution along the height

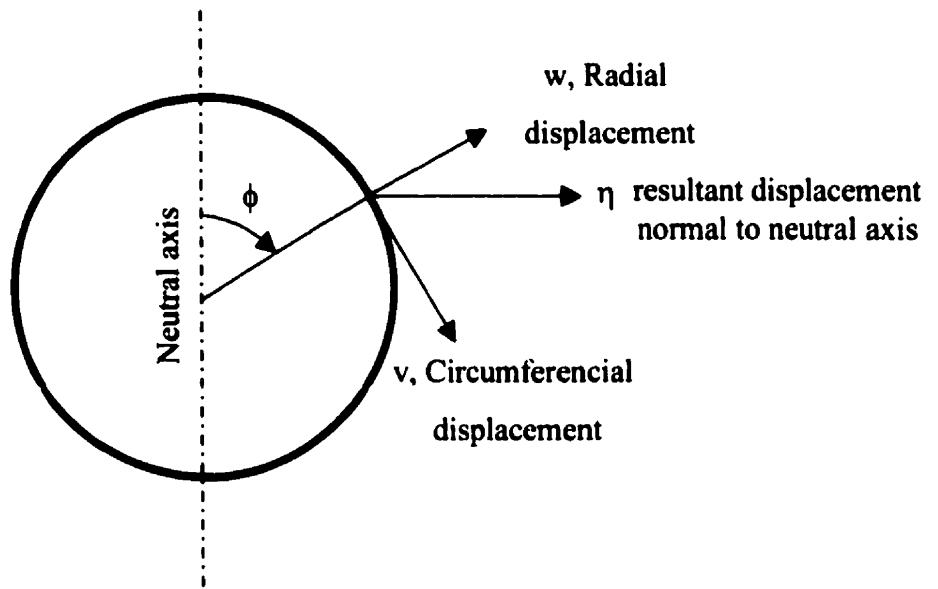


Figure (5-3): Displacement variables for ovalization analysis of GFRP poles

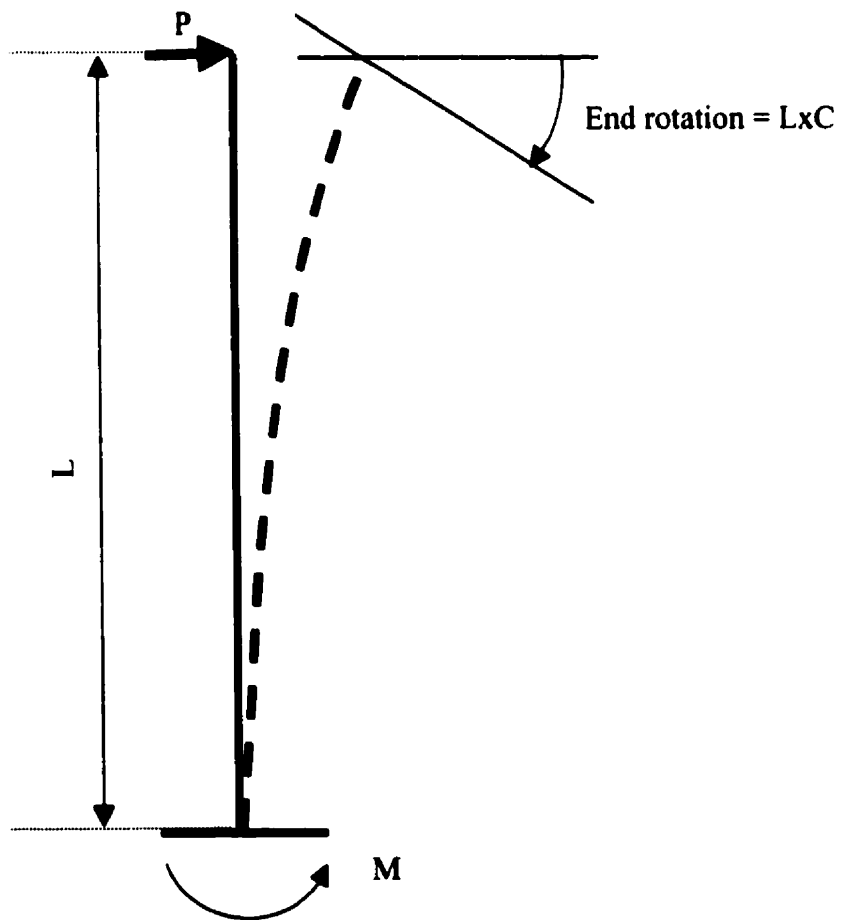


Figure (5-4): Curvature of GFRP pole under applied load

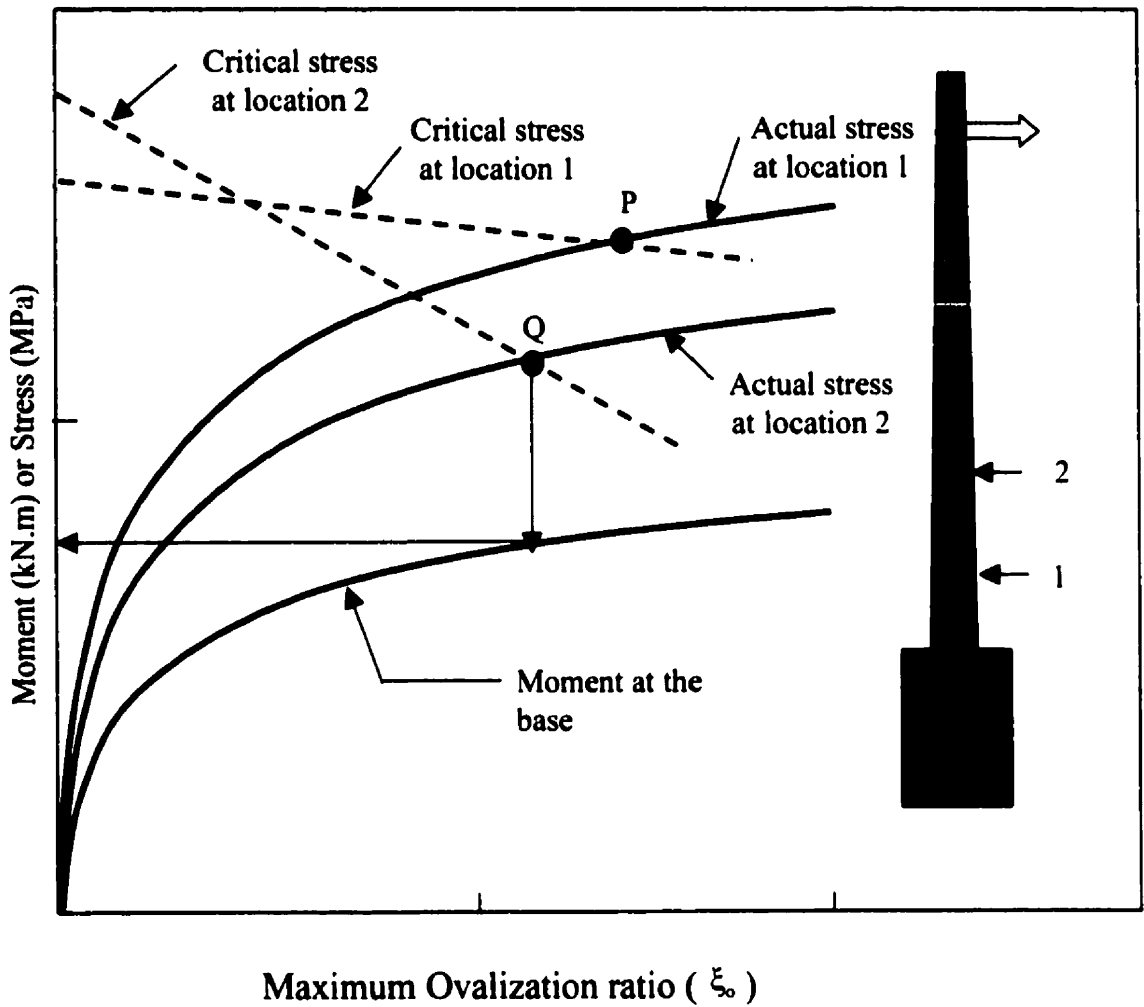


Figure (5-5): Schematic for Moment and stress-ovalization relationship

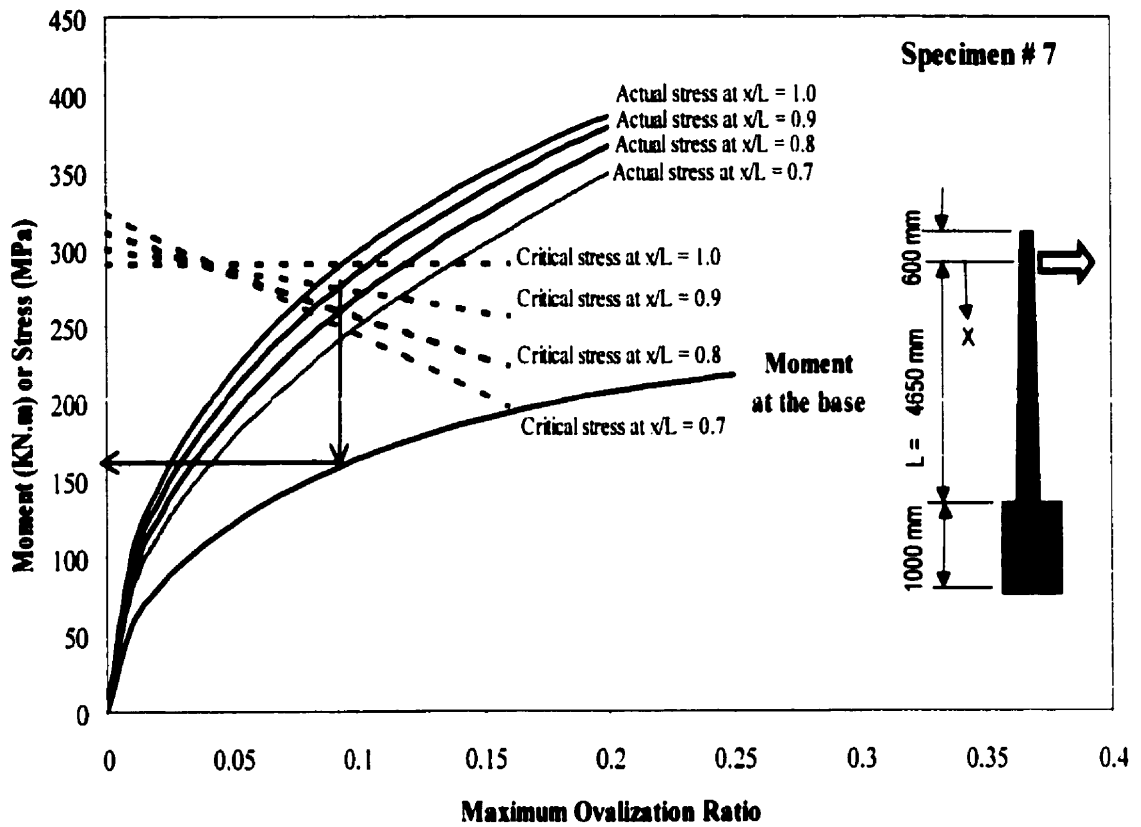


Figure (5-6): Moment and stress-ovalization relationship for specimen 7

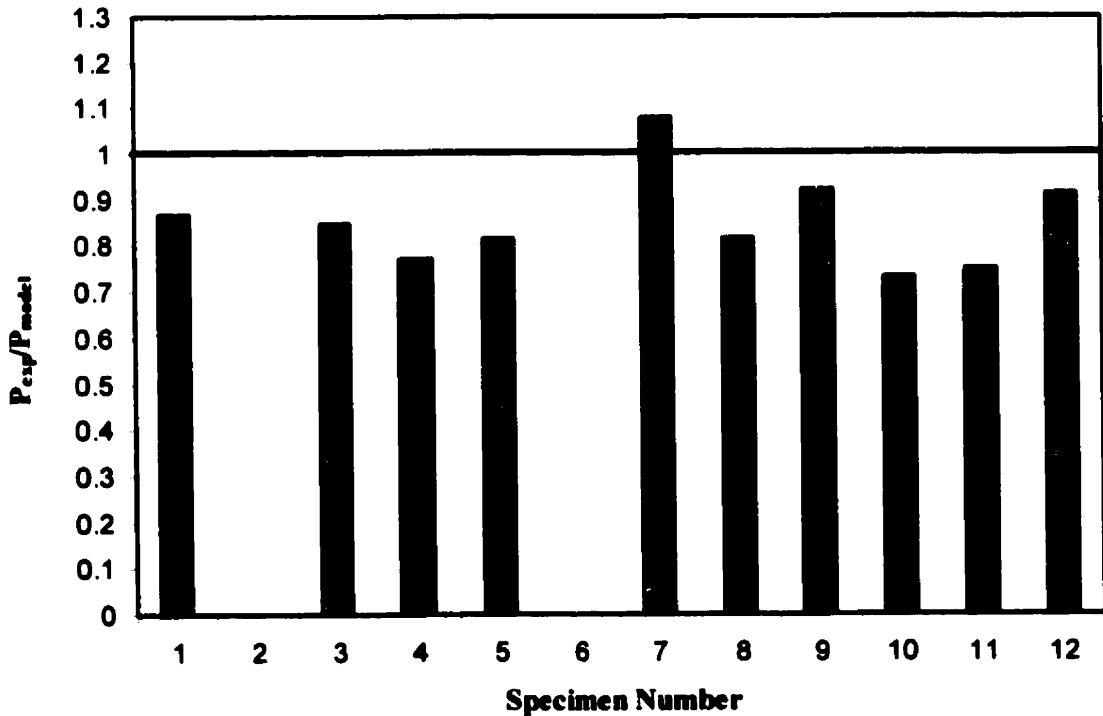


Figure (5-7): Comparison between experimental and proposed model failure load

CHAPTER 6

NUMERICAL ANALYSIS AND DESIGN CHARTS

6.1 INTRODUCTION

Since GFRP poles have been proposed as a replacement for traditional poles, an understanding of their behavior is needed before design guidelines are developed. Knowledge of this behavior could be derived from testing GFRP poles interpreting the results. However, it is impractical, and costly, to base the design entirely upon test results. Therefore, it is essential to develop analytical models capable of predicting the behavior of GFRP poles without the need of extensive testing. A prerequisite for reliable design guidelines, of course is the evaluation of the analytical models through comparison with experimental results.

In the current study, the finite element method was used to analyze and simulate the behavior of GFRP poles. Large deflections and cross-section distortion were included in the analysis and appropriate failure criteria were used in determining the failure load. This finite element analysis was verified through comparison with experimental results obtained from the static testing of both scaled and full-scale specimens. An extensive parametric study was conducted using the ANSYS finite element program and the results are presented in this chapter. Through the parametric study, a series of design charts covering a wide range of parameters, such as fiber orientation and lay-up, and cross-section dimensions for various classes of distribution and transmission lines were produced.

6.2 FINITE ELEMENT ANALYSIS

The basic concept of a finite element method is that the total structure can be modeled analytically using a finite number of elements whose displacement behavior is described by a number of displacement parameters known as the degrees of freedom. The objective of utilizing a finite element analysis in this study was to simulate the actual behavior of GFRP poles by incorporating all the nodes, elements, material properties, dimensions, boundary conditions, and loading in an efficient method of analysis. The following sections present the major features of the finite element method used in this study.

6.2.1 ELEMENT TYPE

Selection of the typed element to be used, depends on the characteristics of the continuum and the idealization methodology. In this study, eight-node quadrilateral layered shell elements were used to model the GFRP poles, as shown in Figure (6-1). Each node had six degrees of freedom: three translations U_x , U_y , and U_z in the nodal X, Y, and Z directions, respectively and three rotations Rot_x , Rot_y , and Rot_z about the nodal X, Y, and Z axes, respectively.

This layered shell element which discussed by Yunus et al (1989) was chosen because of its ability to:

- a) account for large deflections and cross-section distortion,
- b) handle membrane as well as bending stresses and strains in the process,

- c) handle unlimited number of layers with constant or variable thickness; and
- d) predict failure by the means of three different failure criteria.

Local and global coordinate systems of the layered shell element are shown in Figure (6-2). The shell is composed of n layers in its thickness direction r. The fiber orientation of each layer is described by defining the fiber angle (θ) with respect to the element local coordinate as shown in Figure (6-2).

6.2.2 STRESS-STRAIN RELATIONSHIP

The relationship between stress and strain for layer number (j) is given as:

$$[\sigma] = [D]_j [\varepsilon] \quad (6-1)$$

Where $[D]_j$ is the elasticity matrix can be expressed in terms of the material properties as follows:

$$[D]_j = \begin{bmatrix} AE_{x,j} & A\mu_{xy}E_{x,j} & 0 & 0 & 0 & 0 \\ A\mu_{xy,j}E_{x,j} & AE_{y,j} & 0 & 0 & 0 & 0 \\ 0 & 0 & E_{z,j}10^{-6} & 0 & 0 & 0 \\ 0 & 0 & 0 & G_{xy,j} & 0 & 0 \\ 0 & 0 & 0 & 0 & fG_{yz,j} & 0 \\ 0 & 0 & 0 & 0 & 0 & fG_{xz,j} \end{bmatrix} \quad (6-2)$$

where,

$$A = \frac{E_{y,j}}{(E_{y,j} - \mu_{xy,j} \mu_{xy,j} E_{x,j})} \quad (6-3)$$

E_{xj} , E_{yj} and G_{xyj} are the Young's modulus in the X-direction, Y-direction and the shear modulus in X-Y plane, respectively, for layer j; and $\mu_{xy,j}$ is the Poisson's ratio in X-Y plane. Those material constants have to be defined for each layer in the ANSYS input file.

The value of f in (6-2) was derived by Fried (1973) from numerical experimentation to prevent shear locking in thin shells. It is given by

$$\frac{1}{f} = 1.2 \text{ or } \frac{1}{f} = \left(1 + \frac{0.2(\text{AREA})}{25h^2} \right), \text{ whichever is greater.} \quad (6-4)$$

AREA is the area of the element in the s-t plane and h is the average thickness of the element.

6.2.3 GEOMETRIC NONLINEARITY

The geometric nonlinearity was also taken into account in the analysis since displacement constitutes an important parameter in the behavior of GFRP poles. Large deflections in GFRP poles result in a change in the element orientation and, consequently, in a change in the element stiffness matrix. To deal with the large deflection problem, the element stiffness matrix was continuously updated using the Newton-Raphson iterative procedure. The Newton-Raphson method is based on an incremental procedure in which a series of linear iterations converge to the actual nonlinear solution, as shown in Figure (6-3). In this procedure, the tangent stiffness matrix is updated as follows:

$$[K_e] = \int_{-1}^1 \int_{-1}^1 \sum_{j=1}^n \int_{r_{j1}}^{r_{j2}} [T_n]^T [B]^T [D]_j [B] [T_n] |J| dr ds dt \quad (6-5)$$

where, $[T_n]$ is the orthogonal transformation relating the original element coordinates to the deformed element coordinates. It is computed by separating the rigid body rotation from the total deformation.

The element restoring force can be expressed as:

$$\{F_e\} = \int_{vol} [T_n]^T [B]^T [D] \{\epsilon_n^{el}\} d(vol) \quad (6-6)$$

where,

$$\{\epsilon_n^{el}\} = [B] \{u_n^d\} \quad (6-7)$$

and $\{u_n^d\}$ is the element deformation.

The process used to account for the large deflections can be summarized in a three-step process for each element:

- a) First, the updated transformation matrix $[T_n]$ for the element is determined;
- b) the deformation displacement $\{u_n^d\}$ is extracted from the total element displacement $\{u_n\}$ used to compute the stresses as well as the restoring force $\{F_e\}$; and,

- c) after the rotational increments $\{\Delta u\}$ are computed, the node rotations are updated appropriately.

6.3 ANALYSIS OF THE TESTED GFRP POLES

The ANSYS general purpose finite element program was used to analyze the tested specimens. The main objective of this analysis was to determine the ultimate load carrying capacity of the GFRP poles and compare it to the experimental results. The deflection curve as well as the cross-section ovalization were also obtained through the analysis and the results were compared to the experimental values.

6.3.1 MODELING OF THE GFRP POLES

The geometric boundaries of the GFRP poles were defined as the first step in the modeling process. To simulate these boundaries, key points were used to define the axis of rotation and one line along the length of the pole. The surface area of the pole was generated by the ANSYS program through rotating this line around the axis of rotation. The meshing process and boundary conditions were entered differently for the scaled and the full-scale specimens. This is discussed in the following sections for each type of specimens.

6.3.1.1 MODELING OF THE SCALED SPECIMENS

Only the part of the specimens above the concrete base was modeled assuming fixed support condition, as shown in Figure (6-4). Once the geometric shape of the pole was set, the discretization process was performed subdividing the pole into equivalent finite element systems. It is well known that refining the finite element mesh leads to

more accurate results. Thus, a fine mesh was used in the bottom part of the pole where failure was expected to take place. A coarser finite element mesh was used in the top portion of the pole. This was accomplished by using the automatic meshing capability of the ANSYS program. Eight hundreds elements were used to model the scaled specimens, as shown in Figure (6-5). Sixteen elements were used in the circumferencial direction. The element size was 25 mm at the base in the longitudinal direction. This increased to 40 mm, gradually, towards the top of the pole. The element used in this analysis had the capability of modeling composite materials with an unlimited number of layers each having its own fiber orientation, as shown in Figure (6-5). All the degrees of freedom (U_x , U_y , U_z , Rot_x , Rot_y , and Rot_z) along the bottom base of the pole were restrained simulating the fixed end condition of the pole at the concrete foundation. To simulates the concentrated load was applied laterally at a point located 140 mm below the top of the pole, a load was applied at, as shown in Figure (6-5).

6.3.1.2 MODELING OF THE FULL-SCALE SPECIMENS

In the case of full-scale specimen, the whole specimen was modeled including the part embedded within the concrete foundation. The specimens were discretized into 784 elements, as shown in Figure (6-6). The circumference was divided into 16 elements. In the longitudinal direction, the element length was 100 mm at the base of the pole and, gradually, increased to 185 mm at the top. This variation in element size was employed to provide a fine mesh near the area of maximum stress and the anticipated failure zone. The portion of the specimen which was embedded inside the concrete base was also included in the model. All the degrees of freedom (except the displacement component U_x) along the embedded portion of the pole were restrained to simulate the fixed end

conditions of the pole in those directions. During the experimental investigation, the rigid body movement of the concrete foundation was monitored at the top. This movement would only affect the rigid top displacement of the specimen and has no effect on the developed stresses or the failure load. To simulate the rigid body movement of the concrete foundation, the horizontal displacement component (U_x) was set to the recorded experimental value for all the nodes at the top of the concrete foundation. Linear variation of the displacement U_x , was assumed for the portion of the pole embedded within the concrete base as shown in Figure (6-7).

Point loads were applied at the nodes 600 mm below the tip of the pole along half of the circumference to simulate the horizontal applied load, as shown in Figure (6-6).

6.3.1.3 SOLUTION AND DETERMINATION OF FAILURE LOADS

In the current study, a geometric nonlinear analysis was used to account for the cross-section distortion and the large deflection. The wavefront (frontal solution) procedure, as discussed by Irons (1970), was used in the ANSYS program to solve the system of simultaneous linear equations.

To determine the ultimate load of the modeled GFRP poles, the load step was specified. This load step was automatically divided into unequal substeps whose range depended on the behavior of the pole analyzed during from the previous substep. At the end of each substep, the ANSYS program adjusted the stiffness matrix to reflect the nonlinear changes in the pole stiffness. Ultimate loads were determined according to Tsai-Wu (1971) failure criterion unless divergence occurred prior to reaching this failure

criterion. Divergence of the solution indicates the occurrence of local buckling failure within the specimen.

A typical input file for the analysis of GFRP poles using the ANSYS program is given in Appendix A of this thesis. This input file can easily be modified to handle different configurations of GFRP poles.

6.3.2 RESULTS AND DISCUSSION

The main objective of this section was to discuss the results of the finite element analysis and to compare these results to the results obtained through testing to ascertain the validity of the finite element analysis. Once the finite element was verified, it was extended to perform a more comprehensive parametric study, which was then used to develop a design model for GFRP poles. The comparison between the finite element results and the results obtained from testing of for the scaled and full-scale specimens is presented in the following sections.

6.3.2.1 SCALED SPECIMENS

The finite element analysis was used to predict the ultimate failure load due to both instability (local buckling) as in Mode A, and due to material failure as in Mode B and Mode C. Figure (6-8) shows the deformed shape of specimen A25 at the ultimate load. The Tsai-Wu failure criterion values for this specimen at ultimate load is shown in Figure (6-9). Failure in specimen A25 was due to local buckling while the value of the failure criterion is less than unity. Figure (6-10) shows the distribution of Tsai-Wu failure

criteria values for specimen C25. As shown in this figure, failure occurred on the compression side at a location that matches the experimental results.

Figure (6-11) shows both the experimental and the predicted ultimate loads as function of the diameter-to-thickness ratio for specimens with 25° fiber angle. It is evident from this figure clear that there is a strong correlation between the results obtained from the finite element analysis and the experimental results. The failure loads obtained experimentally and the failure loads obtained from the finite element analysis for the scaled specimens are given in Table (6-1). The ratio between the experimental failure load and the finite element failure load also given in Table (6-1), varies between 0.9 to 1.12. The average ratio is 0.975 and the standard deviation is 0.06.

Table (6-1): Comparison between experimental and finite element failure load for scaled specimens

| Specimen Number | P_{exp} (N) | $P_{F.E.}$ (N) | $P_{exp} / P_{F.E.}$ |
|-----------------|------------------|-------------------|----------------------|
| A25 | 358 | 365 | 0.98 |
| A30 | 347 | 341 | 1.02 |
| A35 | 308 | 320 | 0.96 |
| B25 | 494 | 550 | 0.90 |
| B30 | 610 | 670 | 0.91 |
| B35 | 494 | 440 | 1.12 |
| C25 | 846 | 896 | 0.94 |
| C30 | 752 | 768 | 0.98 |
| C35 | 622 | 860 | 0.94 |
| D25 | 980 | 1024 | 0.96 |
| D30 | 1023 | 991 | 1.03 |
| D35 | 876 | 912 | 0.96 |
| Average | | | 0.975 |

The load–deflection curves obtained through the finite element analysis along with the experimental results for fiber angle 30/-30 are shown in Figure (6–12). Failure of

the four-layer pole was determined when divergence of the solution was achieved. This divergence occurred before the Tsai-Wu failure criterion value reached unity. This indicated that the failure mode, in this case, was due to instability and not due to material failure. On the other hand, failure of the other poles was determined when the Tsai-Wu failure criterion value was equal to unity at the most stressed element. The load-deflection curves obtained from the finite element method for those poles were linear because no progressive failure was considered after the first-ply failure (FPF). Both the experimental and the finite element results were linear up to, approximately, 70% of the ultimate load. For loads greater than 70 % of the ultimate load, the experimental load-deflection curves began to diverge from the finite element curves due to the damage accumulation and progressive failure on the micro level.

6.3.2.2 FULL-SCALE SPECIMENS

Figure (6-13) shows the deformed shape obtained from the finite element analysis for Specimen 5. The distribution of Tsai-Wu failure criterion value along specimen at the ultimate load is shown in Figure (6-14). As indicated in Figure (6-14), the Tsai-Wu failure criterion value is less than unity at the ultimate load signifying failure by local buckling. This specimen, indeed, failed by local buckling. On the other hand, the distribution of Tsai-Wu failure criterion value for Specimen 6, shown in Figure (6-15), is exactly equal to one at the failure load, implying material failure rather than local buckling. Specimen 6 failed due to material failure on the compression side.

A comparison between the experimental failure loads and the failure loads predicted by the finite element method for the full-scale specimens is shown in Table (6-

2). The ratio between the experimental and finite element failure loads varied from 0.91 to 1.27. The average value was 0.99 and the standard deviation was 0.12. This indicates that there was a very good correlation between the failure loads predicted by the finite element analysis and the experimental results. A comparison between the load–deflection behavior obtained from both the experimental program and the finite element analysis is shown in Figure (6-16) for specimens with a 10^0 longitudinal fiber angle. The results shown in this figure indicate that the poles analyzed by the finite element method were stiffer than actual poles. The load–deflection relationships according to the finite element analysis were linear because this analysis does not account for the progressive failure of the fibers.

The load-ovalization relationships, at 1 m above the concrete base for specimens with a 10^0 fiber orientation are shown in Figure (6–17). Results from both the finite element analysis and the experimental investigation are shown in Figure (6-17). The load–ovalization results obtained from the finite element analysis indicate nonlinear trend similar to that exhibited by the experimental results. In this case, the finite element analysis accounted for the nonlinear distortion of cross–section (geometric non–linearity). In general, the ovalization ratio U/R corresponding to the finite element analysis at a specific load level is slightly lower than that corresponding to experimental results.

Table (6-2): Comparison between experimental and finite element failure load for full-scale specimens

| Specimen Number | P _{EXP} (kN) | P _{F.E.} (kN) | P _{exp} /P _{F.E.} |
|-----------------|--------------------------|---------------------------|-------------------------------------|
| 1 | 34.2 | 36.6 | 0.93 |
| 3 | 30.1 | 25.8 | 1.17 |
| 4 | 20.8 | 22.3 | 0.93 |
| 5 | 7.55 | 7.9 | 0.96 |
| 6 | 30.4 | 34.9 | 0.87 |
| 7 | 36.4 | 28.7 | 1.27 |
| 8 | 28.1 | 28.7 | 0.98 |
| 9 | 18.9 | 20.6 | 0.92 |
| 10 | 6.9 | 7.4 | 0.93 |
| 11 | 20 | 21.9 | 0.91 |
| 12 | 8.8 | 8.2 | 1.07 |
| Average | | | 0.99 |

6.4 PARAMETRIC STUDY AND DESIGN CHARTS

The discussion in the previous section indicated a good agreement between the results from of the finite element analysis and the experimental results. Because of this agreement, the same finite element analysis was used to extend the study and examine the effect of other parameters on the behavior of GFRP poles. More specifically three cases were examined: Case 1: The effect of the ratio of circumferencial layers–to–total number of layers; Case 2: The effect of longitudinal fiber orientation; and Case 3: The effect of cross section dimensions on the behavior of GFRP poles. This study was conducted on different types of distribution and transmission poles, covering a wide range of classes. The results from this parametric study are presented in the form of design charts which can be used to select the appropriate GFRP pole for a specific application. It should be noted that those design charts were developed based on the equivalent transverse loads of wooden poles. The different configurations of GFRP pole obtained from those design charts have to be checked for various load combinations such as the combined effect of axial and lateral loads. A constant fiber volume ratio of 0.6 was assumed. The material elastic properties used and the ultimate strengths of GFRP are shown in Table (6-3).

Table (6-3): Material properties and ultimate strength of GFRP

| Fiber Volume | Materials elastic properties (GPa) | | | Poisson's ratio | Ultimate strength (MPa) | | | | |
|--------------|------------------------------------|-------|----------|-----------------|-------------------------|---------|---------|---------|---------|
| | E_1 | E_2 | G_{12} | | μ_{12} | S_1^+ | S_1^- | S_2^+ | S_2^- |
| 0.60 | 44.60 | 12.46 | 4.85 | 0.24 | 1300 | 691 | 47 | 130 | 44 |

where, E_1 and E_2 , are the elastic modulus in the fiber direction, transverse fiber direction, respectively; G_{12} is the shear modulus; S_1^+ , and S_1^- are the tensile and compressive strength in the fiber direction, respectively; S_2^+ , and S_2^- are the tensile and compressive strength in the transverse to fiber direction, respectively; and S_{12} is the shear strength.

6.4.1 CASE 1: EFFECT OF CIRCUMFERENTIAL LAYERS ON ULTIMATE STRENGTH OF GFRP POLES:

Three series of GFRP poles were considered in this investigation. Each series represented a distinct configuration of external dimensions. The geometric properties and the fiber arrangement for the three series are given in Table (6-4). All poles had 8 equal thickness layers. Within each series, the ratio of the number of circumferential layers to the total number of layers was varied from zero to 6/8. The longitudinal fibers had a fiber orientation of $\pm 5^\circ$ with respect to the vertical axis of the pole. This orientation represented the closest possible arrangement of fibers to a purely longitudinal orientation that can be produced by wet filament winding machines.

Table (6-4): Parametric variations for Case 1

| Pole Series | Geometric Properties | | | | Fiber Arrangement | | | | | |
|-------------|----------------------|----------------------|----------------------|-------------------|----------------------------------|--|----------------------------------|-----------------|-------------------------|--------------|
| | Total Length (mm) | Embedded Length (mm) | Bottom Diameter (mm) | Top Diameter (mm) | Number of Long. Layers (N_L) | Number of Circumferential Layers (N_c) | Total Number of Layers (N_T) | $R_N = N_c/N_T$ | Long. Fiber orientation | Fiber Volume |
| 1 | 6100 | 1220 | 300 | 200 | 8 | 0 | 8 | 0/8 | +/- 5° | 0.6 |
| | | | | | 6 | 2 | 8 | 2/8 | | |
| | | | | | 4 | 4 | 8 | 4/8 | | |
| | | | | | 2 | 6 | 8 | 6/8 | | |
| 2 | 12200 | 1838 | 375 | 225 | 8 | 0 | 8 | 0/8 | +/- 5° | 0.6 |
| | | | | | 6 | 2 | 8 | 2/8 | | |
| | | | | | 4 | 4 | 8 | 4/8 | | |
| | | | | | 2 | 6 | 8 | 6/8 | | |
| 3 | 18300 | 2440 | 500 | 300 | 8 | 0 | 8 | 0/8 | +/- 5° | 0.6 |
| | | | | | 6 | 2 | 8 | 2/8 | | |
| | | | | | 4 | 4 | 8 | 4/8 | | |
| | | | | | 2 | 6 | 8 | 6/8 | | |

All GFRP poles were analyzed using the developed finite element analysis. The thickness of each pole was computed using load limit of 20 kN (class 1 pole) applied laterally at 600 mm below the top. This approach required that for each pole several trial sections were analyzed until the right thickness was achieved. Failure was defined either by material failure according to Tsai-Wu criterion or by local buckling.

Figure (6-18) shows the required thickness for the pole to satisfy class 1 requirements for the three different lengths. The results in this figure indicate that a minimum thickness for a GFRP pole is achieved when the ratio between the circumferential layers and the total number of layers is $2/8$. To achieve the same strength but with no circumferential layers in the laminate lay-up, the thickness of the GFRP pole must be between 13% and 22% higher than the one with $2/8$ fiber arrangement. This implies that additional mass is required. On the other hand, when half of the laminate lay-up is composed of circumferential layers the wall-thickness of GFRP poles is increased by approximately 8% over the minimum thickness. Thus, when the ratio of circumferential-layers-to-the total numbers of layers exceeded $2/8$, thicker sections of GFRP were required to achieve the same strength.

The mass of the GFRP poles in the three investigated series are shown in Figure (6-19). The pole with the minimum mass was the one with $2/8$ circumferential winding. From a design point of view, this would represent an optimum design. In tapered filament wound poles, the wall-thickness of the poles varies linearly with the diameter when only longitudinal fibers are used with the largest thickness near the top of the pole. On the other hand, the wall-thickness is uniform along the whole length when only

circumferential fibers are used. Thus, the effect of circumferential fibers is to reduce the thickness and the mass of the poles. In general, the mass (m) of GFRP poles with different amounts of circumferential fibers is:

$$m = \pi L \gamma [D_{\text{bottom}} t_{\text{base}} (1-R) + D_{\text{av}} t_{\text{base}} R_N] \quad (6-8)$$

where,

L is the total length of the pole; γ is the density of GFRP; D_{bottom} is the bottom diameter of the GFRP pole; t_{base} is the thickness of the pole at the base; D_{av} is the average diameter defined as $0.8 D_{\text{bottom}}$; and R_N is the ratio of the circumferential layers to the total number of layers.

For the cases studied above, Equation (6-8) can be rewritten as follows:

$$\text{for } R_N = 0: \quad m = \pi L \gamma D_{\text{bottom}} t_{\text{base}} \quad (6-8-a)$$

$$\text{for } R_N = 2/8: \quad m = 0.95 \pi L \gamma D_{\text{bottom}} t_{\text{base}} \quad (6-8-b)$$

$$\text{for } R_N = 4/8: \quad m = 0.9 \pi L \gamma D_{\text{bottom}} t_{\text{base}} \quad (6-8-c)$$

$$\text{for } R_N = 6/8: \quad m = 0.85 \pi L \gamma D_{\text{bottom}} t_{\text{base}} \quad (6-8-d)$$

The lateral displacement of the poles at the free end due to a service load equal to 40% of the ultimate capacity is shown in Figure (6-20) for various ratios of R_N . Since the pole stiffness is directly affected by the number of circumferential layers, the minimum lateral displacement was attained when all the layers are oriented in the longitudinal direction. Increasing the number of circumferential layers results in a reduction in the pole stiffness and, consequently, in an increase in the lateral displacement. For example, for a pole with a ratio $R_N=6/8$, the lateral displacement was more than twice the lateral displacement of a pole with R_N equal to $0/8$ (i.e. pole without circumferential layers), though both have, approximately, equal thicknesses.

Two typical modes of failure were observed in Case1: Material failure on the compression side and local buckling. Material failure at the compression side was observed when no circumferencial fibers were incorporated in the laminate lay-up. Figure (6-21) shows the distribution of the value of Tsai–Wu failure criterion for a 12.2 m long GFRP pole with no circumferencial fibers ($R_N = 0/8$). On the other hand, failure by local buckling was observed when circumferencial layers were utilized in the laminate lay-up. Figure (6-22) shows the local buckling failure mode in a 6.1 m long GFRP pole with $R_N = 2/8$. The effect of the circumferencial fibers on the mode of failure can be explained as follows:

When no circumferencial fibers are incorporated in the laminate lay-up, the circumferencial and shear stresses were resisted only by the longitudinal fibers. Because of the low shear and transverse strength of these longitudinal fibers, failure of the poles usually occurs on the compression where the combination of longitudinal, transverse, and shear stresses caused material failure before a local buckling. Figures (6-23), (6-24), and (6-25) show the distribution of the stresses in the fiber direction, the transversely to the fiber direction, and the in-plane shear stresses for a 12.2m GFRP pole, respectively. The maximum compressive stress in the fiber direction is only 231 MPa, as shown in Figure (6-23). When this compressive stress is combined with the transverse to fiber stress of 32.4 MPa, shown in Figure (6–24), and the in-plane shear stress of 14.7 MPa, shown in Figures (6-25), failure as defined by the Tsai-Wu failure criterion takes place at this location. In the case where circumferencial fibers were incorporated in the laminate lay-up, these fibers tended to resist the transverse and shear stress components.

Consequently, there was no material failure in the compression side. Instead, local buckling failure was the dominant mode.

6.4.2 CASE 2: EFFECT OF LONGITUDINAL FIBER

ORIENTATION:

As in Case 1, three series of GFRP poles were considered in the investigation on the effect of longitudinal fibers on the behavior of the poles. Each series represented a distinct configuration of external dimensions. The total length of the GFRP poles was 6.1 m (20 ft) in the first series, 12.2 m (40 ft) in the second series, and 18.3 m (60 ft) in the third series. The bottom diameter of the poles was 300 mm for series 1, 375 mm for series 2, and 500 mm for series 3. The top diameter was 200 mm, 225 mm, and 300 mm, respectively. The wall-thickness of all poles consisted of 8 equal thickness layers with the fibers in the inner and the outer layers were oriented in the circumferential direction giving a ratio $R_N = 2/8$. The orientation of other six layers was varied in the different specimens from $\pm 5^\circ$ to $\pm 45^\circ$ in 10° increments. The choice of $R_N = 2/8$ as the ratio of circumferential layers to the total number of layers was based on the optimum ratio obtained from Case 1. The parametric variation for these series are listed in Table (6-5).

Table (6-5): Parametric variations for Case 2

| Pole Series | Geometric Properties | | | | Fiber Arrangement | | | | | |
|-------------|----------------------|----------------------|----------------------|-------------------|----------------------------------|--|----------------------------------|-----------------|-------------------------|--------------|
| | Total Length (mm) | Embedded Length (mm) | Bottom Diameter (mm) | Top Diameter (mm) | Number of Long. Layers (N_L) | Number of Circumferential Layers (N_C) | Total Number of Layers (N_T) | $R_N = N_C/N_T$ | Long. Fiber orientation | Fiber Volume |
| 1 | 6100 | 1220 | 300 | 200 | 6 | 2 | 8 | 2/8 | +/- 5° | 0.6 |
| | | | | | | | | | +/- 15° | |
| | | | | | | | | | +/- 25° | |
| | | | | | | | | | +/- 35° | |
| | | | | | | | | | +/- 45° | |
| 2 | 12200 | 1838 | 375 | 225 | 6 | 2 | 8 | 2/8 | +/- 5° | 0.6 |
| | | | | | | | | | +/- 15° | |
| | | | | | | | | | +/- 25° | |
| | | | | | | | | | +/- 35° | |
| | | | | | | | | | +/- 45° | |
| 3 | 18300 | 2440 | 500 | 300 | 6 | 2 | 8 | 2/8 | +/- 5° | 0.6 |
| | | | | | | | | | +/- 15° | |
| | | | | | | | | | +/- 25° | |
| | | | | | | | | | +/- 35° | |
| | | | | | | | | | +/- 45° | |

All GFRP poles were analyzed using the finite element method. The thickness of each pole was selected such that the pole can sustain an ultimate load of 20 kN (class 1 pole) applied laterally at 600 mm below the top. This means that for each pole, several trial sections were analyzed until the right thickness was achieved. Failure at 20 kN load was defined according to the Tsai-Wu failure criterion, or local buckling, whichever occurred first.

Figure (6-26) shows the required thickness of different lengths for a pole to satisfy class 1 requirements. The results indicated that the minimum thickness of a GFRP pole was achieved when the longitudinal fiber angle was 5° with respect to the axis of the pole. There was a slight increase in the required thickness when the longitudinal fiber angle was between 5° and 15° . The average thickness for the three series investigated with longitudinal fiber angle equal to 15° was only 6% higher than the minimum thickness. On the other hand, the required thickness increased substantially when the longitudinal fiber angle was more than 15° . For instance, the average required thickness for the three series investigated was 240% greater than the minimum thickness when the longitudinal fiber angle was 35° .

The mass of each GFRP pole in the three series investigated is shown in Figure (6-27). Since all the investigated GFRP poles had the same ratio $R_N = 2/8$, their mass was directly proportional to the designed thickness. Consequently, the pole with the minimum mass, which in design would be considered as optimum, was the one with the longitudinal fibers orientated at an angle of 5° . Generally, a range of longitudinal fiber angles between 5° and 15° can be considered to be an optimum range which leads to the

minimization of the required material resulting in substantial saving in the cost of manufacturing, as well as the cost of transportation are.

The lateral displacement at the free end of the GFRP poles examined under a service load equal to 40% of the ultimate capacity is shown in Figure (6-28). The stiffness of the GFRP poles did not change much when the longitudinal fiber angle increased from 5° and 25° . On the other hand, there was large increase in the stiffness when the fiber angle increased more than 25° . This increase in stiffness was basically due to the large variation in the thickness. The smallest lateral deflection was attained when the longitudinal fiber angle was 45° . On the average, for the three series investigated, the lateral deflection of poles with a longitudinal fiber angle of 5° was approximately 50% larger than the deflection of poles with a fiber angle of 45° .

Three typical failure modes were observed in Case 2. Failure by local buckling was observed when the longitudinal fiber angle was equal to 5° . A local buckling failure of a 6.1 m long GFRP pole with a longitudinal fiber angle equal to 5° is shown in Figure (6-22). Material failure on the compression side was observed when the fiber angle was between 15° and 25° . Figure (6-29) shows the distribution the value of the Tsai–Wu failure criterion for the 12.2 m long GFRP pole with a longitudinal fiber angle equal to 15° . On the other hand, all the GFRP poles that had a longitudinal fiber angle between 35° and 45° failed on the tension side at the ground level. The distribution of the value of the Tsai–Wu failure criterion for the 18.3 m long GFRP pole with a longitudinal fiber angle of 45° is shown in Figure (6-30). An explanation on the reasons why the longitudinal fiber angle affects the mode of failure is given below.

- Because of the very small thickness required when the longitudinal fiber angles is 5° , all the GFRP poles investigated with that lay-up failed by local buckling.
- When longitudinal fiber angle was between 15° and 25° , components of the longitudinal bending stresses in the transversely to fiber direction, combined with the in-plane shear stresses and stresses in the fiber direction caused failure to occur on the compression side before local buckling. Figures (6-31), (6-32), and (6-33) show the distribution of the stresses in the fiber direction, the transverse to fiber direction, and the in-plane shear stresses, respectively. As shown in these figures failure take place at a compressive stress in the fiber direction of 324 MPa, tensile stress in the transverse to fiber direction of 22 MPa, and an in-plane shear stress of 30 MPa.
- when a longitudinal fiber angle of 35° to 45° was used, the longitudinal bending stresses had substantial components in the transverse to the fiber direction on the tension side of the GFRP poles as shown in Figure (6-34). Consequently, failure occurred on the tension side of the poles near the ground level. Figure (6-34), and (6-35) show the distribution of the transverse to fiber stresses for a 18.3 m long GFRP pole with a longitudinal fiber angle equal to 45° . The maximum tensile stress in the transverse to fiber direction at the failure was equal to 27.2 MPa, as shown in Figure (6-34), while the maximum in-plane shear stress was equal to 31.2 MPa, as shown in Figure (6-35).

6.4.3 CASE 3: EFFECT OF CROSS-SECTION DIMENSIONS:

As in Case 1 and Case 2, three series of GFRP poles were considered in this investigation each with distinct configuration of external dimensions. The total length of the poles was 6.1 m (20 ft) in the first series, 12.2 m (40 ft) in the second series, and 18.3

m (60 ft) in the third series. The ratio of the top-to-bottom diameter was kept constant at 0.6. The bottom diameter varied from 150 mm to 450 mm in Series 1; 150 mm to 600 mm in Series 2; and 200 mm to 800 mm in Series 3. All poles had 8 equal thickness layers with the fibers in the inner and the outer layers oriented in the circumferencial direction. The orientation of the fibers in the intermediate six layers was $\pm 5^\circ$ with respect to the axis of the poles. The choice of $R_N = 2/8$, and fiber angle of ± 5 was based on the optimum results obtained form Case 1 and Case 2. The parametric variation used in the in this case are listed Table (6-6). All the GFRP poles were analyzed using the finite element method. The applied lateral load was located 600 mm below the top of the poles. The thickness of each pole was selected so that the pole would be classified in any category from class H1 to class 4 for the first and second series and from class H3 to class 2 in the third series.

Table (6-6): Parametric variations for Case 3

| Pole Series | Geometric Properties | | | | Fiber Arrangement | | | | | | Pole Class |
|-------------|----------------------|----------------------|----------------------|--------------------------------------|--|--|--|---|-------------------------|--------------|--------------------------|
| | Total Length (mm) | Embedded Length (mm) | Bottom Diameter (mm) | Top Diameter / bottom diameter ratio | Number of Long. Layers (N _L) | Number of Circumferential Layers (N _C) | Total Number of Layers (N _T) | R _N = N _C /N _T | Long. Fiber orientation | Fiber Volume | |
| 1 | | | 150 | | | | | | | | HI 1 2 3 4 |
| | | | 200 | | | | | | | | |
| | | | 250 | | | | | | | | |
| | 6100 | 1220 | 300 | 0.6 | 6 | 2 | 8 | 2/8 | +/- 5° | 0.6 | |
| | | | 350 | | | | | | | | |
| 2 | | | 150 | | | | | | | | HI 1 2 3 4 |
| | | | 225 | | | | | | | | |
| | | | 300 | | | | | | | | |
| | 12200 | 1838 | 375 | 0.6 | 6 | 2 | 8 | 2/8 | +/- 5° | 0.6 | |
| | | | 450 | | | | | | | | |
| 3 | | | 200 | | | | | | | | H3 H2 HI 1 2 |
| | | | 300 | | | | | | | | |
| | | | 400 | | | | | | | | |
| | 18300 | 2440 | 500 | 0.6 | 6 | 2 | 8 | 2/8 | +/- 5° | 0.6 | |
| | | | 600 | | | | | | | | |
| | | 700 | | | | | | | | | |
| | | 800 | | | | | | | | | |

Because of the large number of GFRP poles investigated in each series of this case, the results from each series will be discussed separately in the following sections.

6.4.3.1 SERIES 1

Figures (6-36-a) shows the required thickness for the 6.1 m GFRP poles that meet the strength requirements of class H1 and class 1 to 4. The analysis showed that the required thickness of these poles decreased in a nonlinear manner as the diameter increased. Therefore, there should be an optimum bottom diameter that could yield a minimum mass for a pole. Based on the designed thickness, the mass of the GFRP poles examined was computed and is shown in Figure (6-36-b). The optimum bottom diameter depended on the pole classification, or, more specifically, on the ultimate load requirements. The optimum diameter for class H1 and class 1 was 300 mm, 250 mm for class 2 and class 3; and 200 mm for class 4.

The lateral deflection at the free end of the GFRP poles under a service load equal to 40% of the ultimate capacity was also computed and plotted in Figure (6-36-c) for various diameters and classes. Since the design was based on strength criterion, lateral deflection of the GFRP poles can be very large. For example, the lateral deflection of the poles with bottom diameter of 150 mm was as high as 16% of the free length. Although the National Electrical Safety Code (1997) does not set a specific limit on the lateral displacement of pole-type structures, hydro-utility companies as Manitoba Hydro, specify a maximum deflection of 10% of the free length under the load class limit or 4% under service load. There is no evidence, however, to support the significance of this limit.

Two typical failure modes were observed in this series. A local buckling failure was observed when the bottom diameter was equal to or greater than the optimum diameter computed for each class. For example, the optimum diameter for a 6.1 m class 3 GFRP pole was 400 mm. This pole failed by local buckling as shown in Figure (6-37). On the other hand, material failure on the compression side was observed when the bottom diameter was less than the optimum diameter. Figure (6-38) shows the distribution of the value of the Tsai–Wu failure criterion for a 6.1 m long GFRP pole with a bottom diameter equal to 150 mm.

Serviceability limits for the lateral deflection can be combined with the strength criterion to redesign the GFRP poles. A serviceability limit for lateral deflection equal to 4% of the free length was selected in this investigation based on the most common practice in distribution line design. This limit was selected to demonstrate the ability of designing GFRP poles based on both strength and serviceability criteria. The GFRP poles investigated in this first series had a lateral deflection greater than the 4% limit. These were redesigned to satisfy the serviceability limit of 4%. As anticipated, the required thickness of those redesigned GFRP was significantly higher than that required to satisfy the strength criterion only. Figure (6-39-a) shows the required thickness for 6.1 m GFRP poles based on a combined strength and serviceability criteria. The increase in the GFRP pole thickness affected the pole mass, as shown in Figure (6-39-b). The optimum diameter was 350 mm for class H1 and class 1 sections; and 300 mm for classes 2, 3 and 4. Those optimum diameters are larger than those based on the strength criterion only. The lateral deflection of the GFRP poles examined is shown in Figure (6-39-c). The upper limit for lateral deflection in this case was set at 4% of the free length.

6.4.3.2 SERIES 2

The required thickness for the 12.2 m GFRP poles that meet the strength requirements of classes H1, 1, 2, 3, and 4 are shown in Figure (6-40-a). As in the previous series, the required thickness of the GFRP poles decreased as the diameter increased. The optimum bottom diameter was determined on the basis of minimum mass. Based on the thickness obtained through the analysis, the masses of the poles were determined and are shown in Figure (6-40-b). These were determined on the basis of the strength criterion. The optimum bottom diameter depended on the pole classification, or, more specifically, on the ultimate load requirements. The optimum diameter for this series was 375 mm for classes H1 and 1, and 300 mm for class 2. On the other hand, the curve corresponding to classes 3 and 4 did not have a distinct point of global minimum. Thus, the smallest diameter of 150 mm may be considered as the optimum diameter because it leads to a pole with minimum mass. However, at this diameter, the designed GFRP poles experience excessive lateral deflection, as shown in Figure (6-40-c). For example, the lateral deflection of a class 4 section with a base diameter of 150 mm was 38% of the free length. This deflection would be unacceptable to the hydro-utility company. It was, thus, important to include a serviceability limit as a second criterion for designing GFRP poles since design on strength only would lead to excessive deflections. As in the previous series, a serviceability limit for lateral deflection equal to 4% of the free length was selected. All the GFRP poles in this series, which had lateral deflection greater than 4% of the free length, were redesigned to satisfy the serviceability limit. As anticipated, the required thickness of those redesigned GFRP was significantly higher than that required to satisfy the strength criterion alone. Figure (6-41-a) shows the

required thickness for the 12.2 m GFRP poles based on a combined strength and serviceability criteria. The mass of these poles was also computed for various diameters and load classifications and is shown in Figure (6-41-b). When both strength and serviceability criteria were used in the design, a distinct global minimum mass was noticed for each pole class. The optimum diameter for classes H1, 1, and 2 was 525 mm, while for classes 3, and 4 was 450 mm. The lateral deflection of the poles in this series is shown in Figure (6-41-c).

When the design was based on the strength criterion, two typical failure modes were observed. Failure by local buckling failure mode was observed when the bottom diameter was equal to or greater than 375 mm for classes H1, 1, and 2; and greater than 300 mm for classes 3 and 4. On the other hand, material failure on the compression side was observed when the bottom diameter was less than these values. The distribution of the value of the Tsai–Wu failure criterion for a 12.2 m class1 GFRP pole with a bottom diameter equal to 225 mm is shown in Figure (6-42). When the serviceability limit was imposed on the design, all poles with diameter equal to or greater than the optimum value failed by local buckling. The poles with diameter less than the optimum value were designed to meet the serviceability limit only and were not affected by the strength criterion.

6.4.3.3 SERIES 3

The required thickness for 18.3 m GFRP poles that meet the strength requirements of classes H3, H2, H1, 1, and 2 is shown in Figure (6-43-a). The optimum bottom diameter based on the minimum mass is shown in Figure (6-43-b). The required thickness were obtained on the basis of the strength criterion. As in series 2, the mass

curves did not have distinct point of global minimum. Therefore, the smallest diameter of 200 mm was considered as the optimum diameter since it leads to minimum mass. However, as in previous series, there was excessive lateral deflection as shown in Figure (6-43-c). For instance, the lateral deflection of a class H3 pole with diameter equal to 150 mm was 44% of the free length. As in the previous series, a serviceability limit for the lateral deflection of 4% of the free length was selected. All the GFRP poles in this series, which had lateral deflection greater than 4% of the free length were redesigned to satisfy the serviceability limit. As anticipated, the required thickness of those redesigned GFRP was significantly higher than that required to satisfy the strength criterion alone. Figure (6-44-a) shows the required thickness for the 18.3 m GFRP poles based on either strength or the serviceability criterion depending on which one governed. The mass of 18.3 m GFRP poles for various diameters and load classifications are shown in Figure (6-44-b). When both strength and serviceability criteria were accounted for in the design, a distinct global minimum mass was obtained for each pole class. The optimum diameter was 800 mm for class H3, and 700 mm for classes H2, H1, 1 and 2. The lateral deflection of the poles investigated is shown in Figure (6-44-c).

When the strength criterion was used to design the GFRP poles in this series, two typical failure modes were observed. Failure by local buckling was observed when the bottom diameter was equal to or greater than 500 mm for classes H3, H2, and H1 and greater than 400 mm for classes 1, and 2. On the other hand, material failure on the compression side was observed when the bottom diameter was less than these values. Figure (6-45) shows the distribution of the value of the Tsai–Wu failure criterion for the 18.3 m class H1 pole with a bottom diameter equal to 300 mm. When the serviceability

criterion was incorporated in the design, all poles with diameter equal to or greater than the optimum value failed by local buckling. Those with diameters less than the optimum value were governed by the serviceability limit.

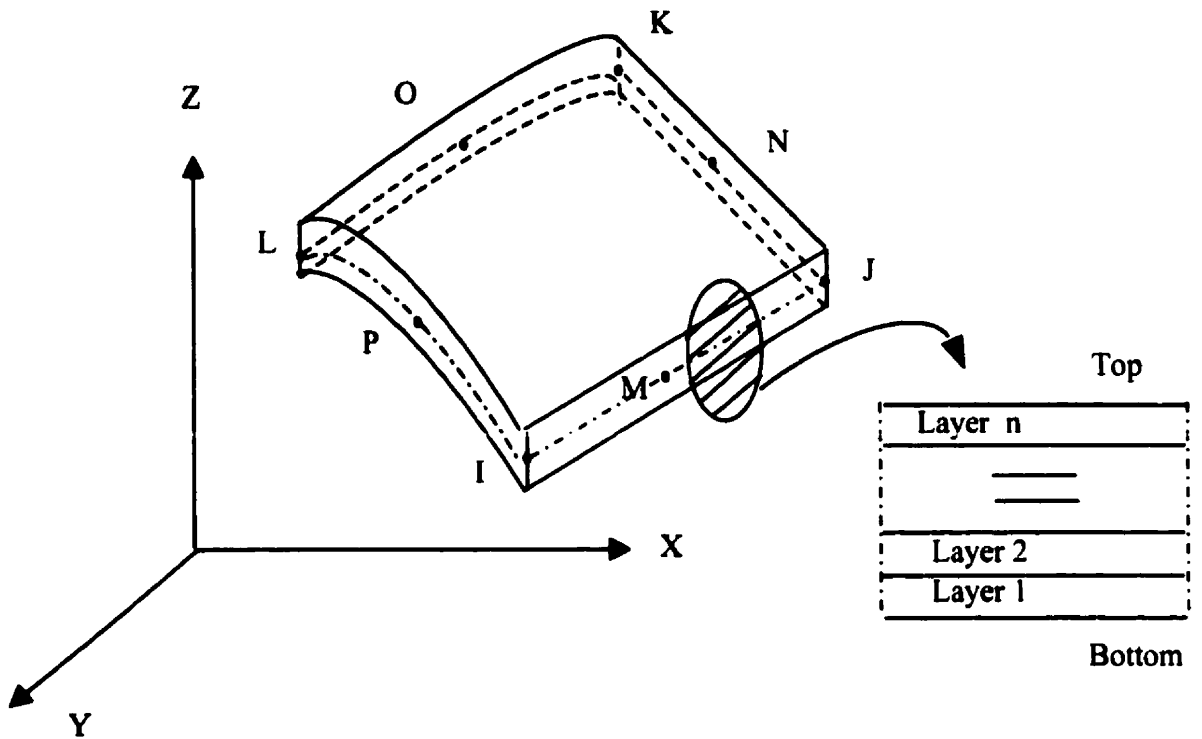


Figure (6-1) : Layered quadrilateral eight-node shell element

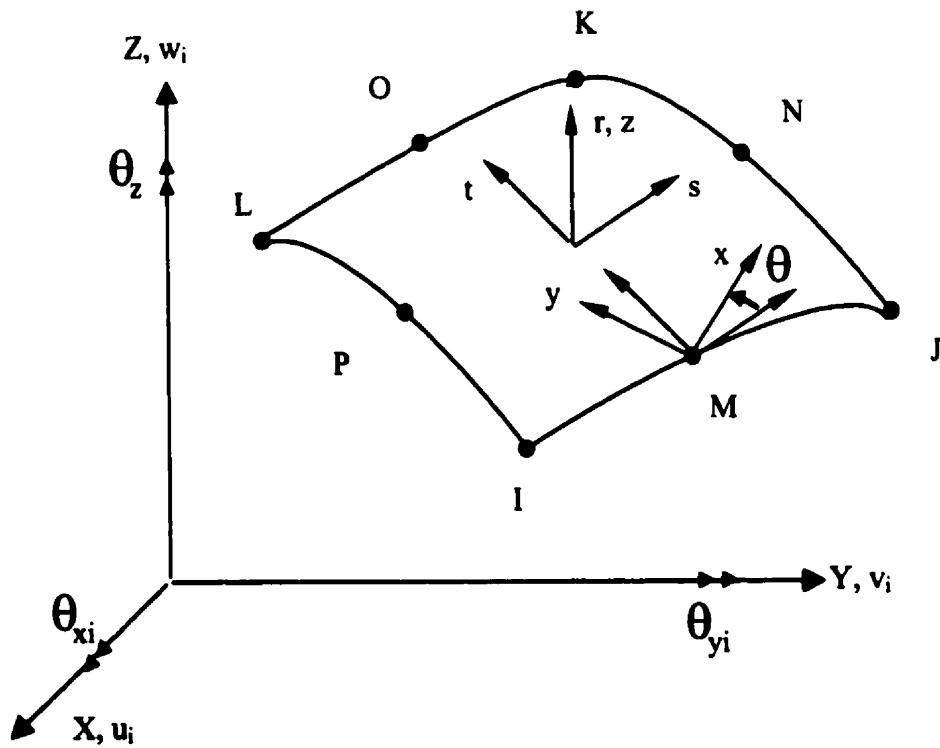


Figure (6-2) : The coordinate system of the layered shell element

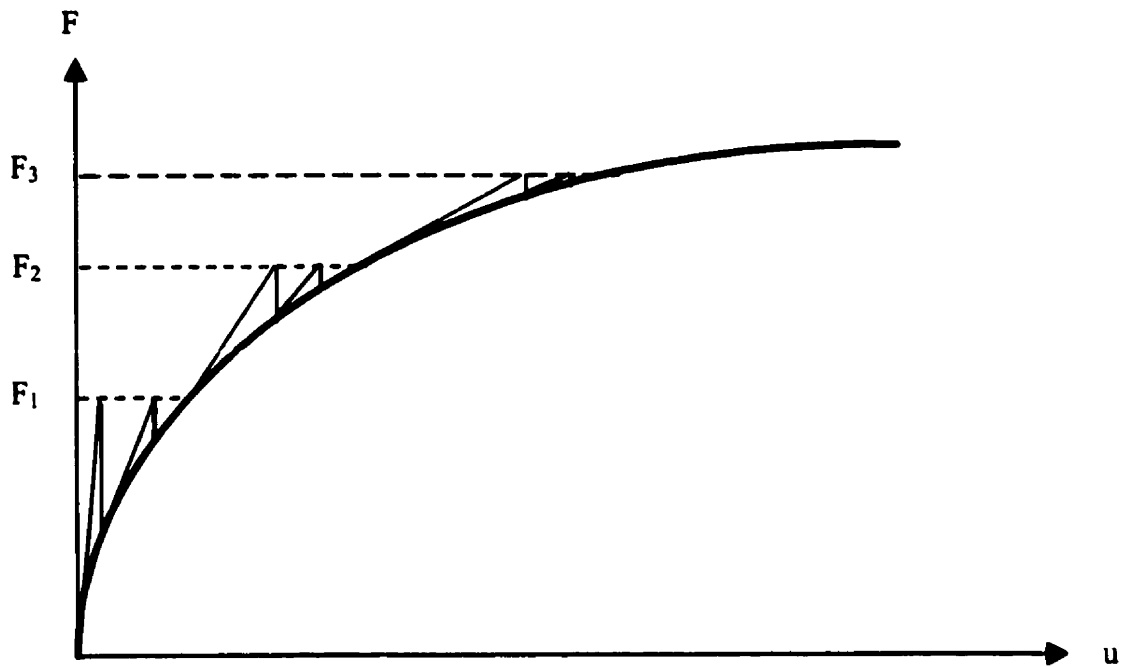


Figure (6-3): Incremental Newton-Raphson procedure

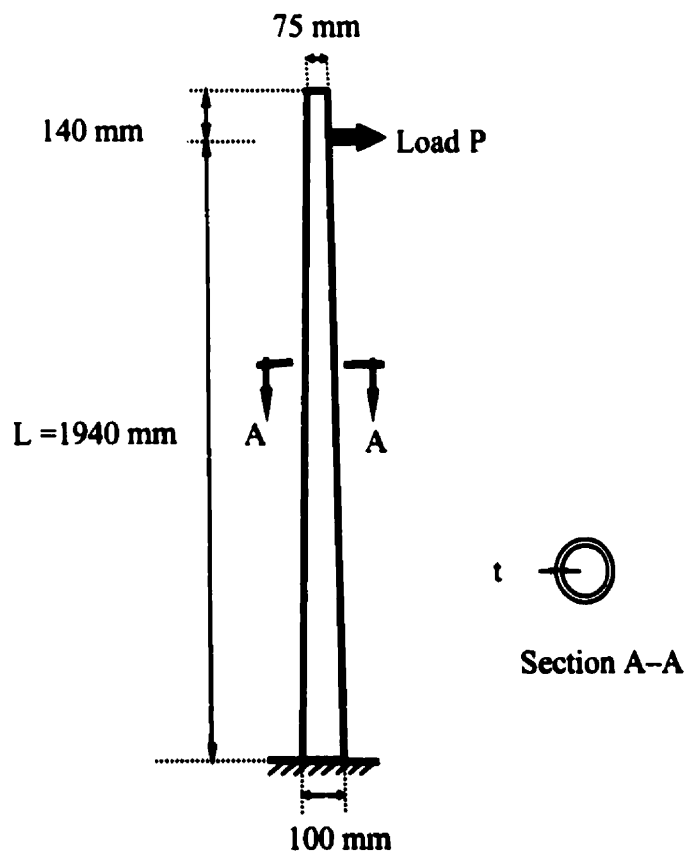


Figure (6-4): Dimensions of the scaled specimens

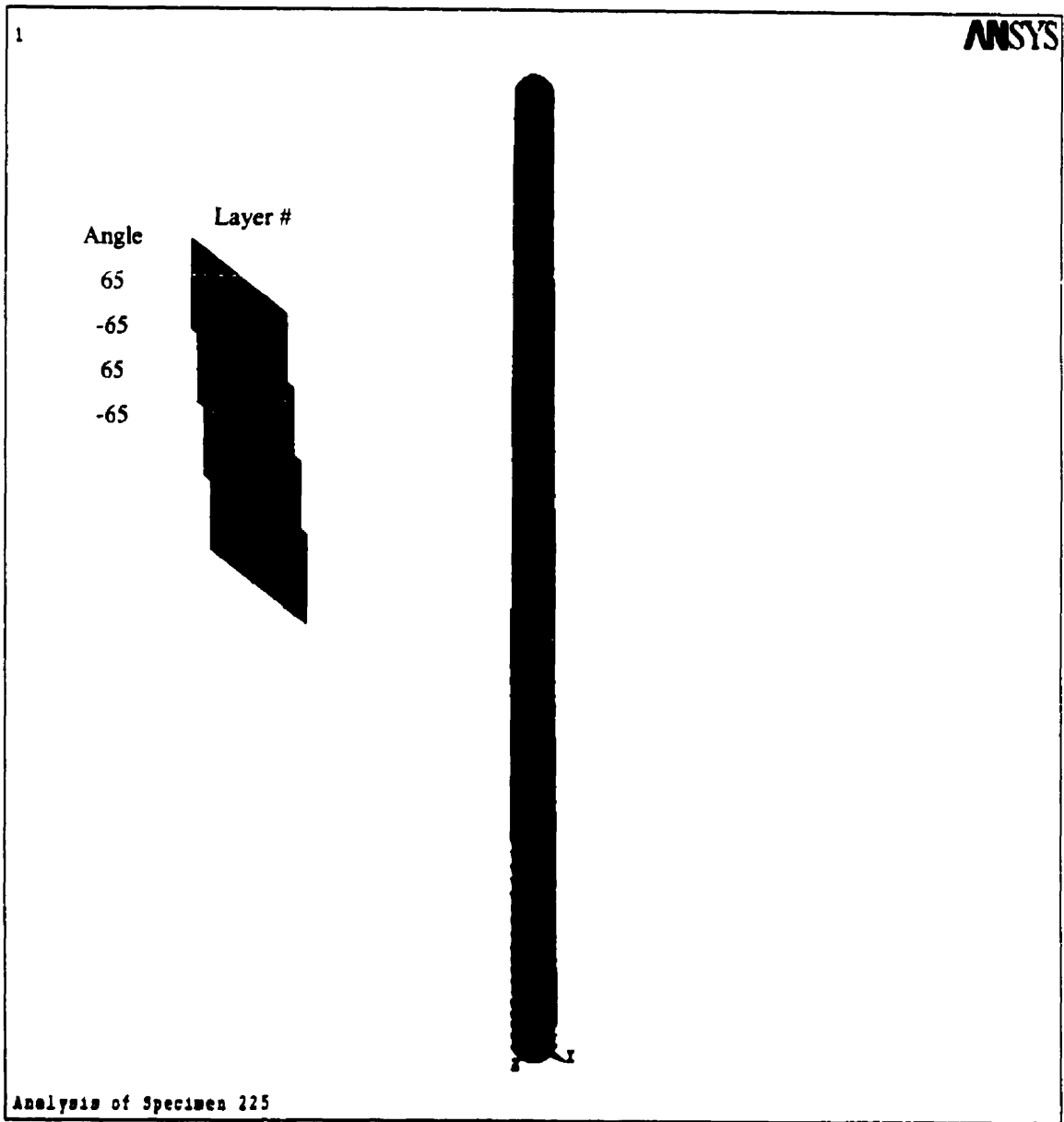


Figure (6-5): Finite element mesh for scaled specimen A25

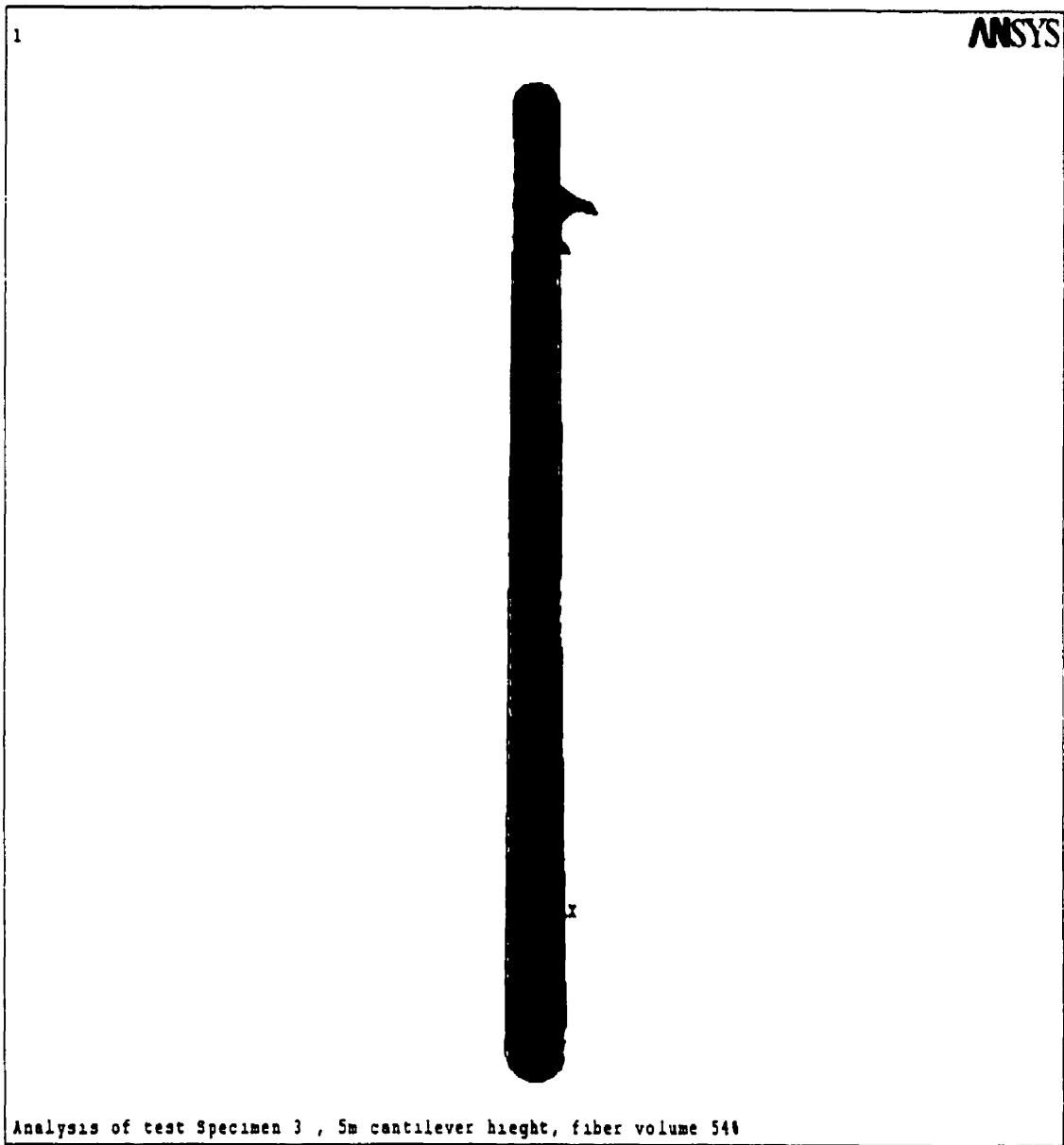


Figure (6-6): Finite element mesh and applied load for full-scale specimens

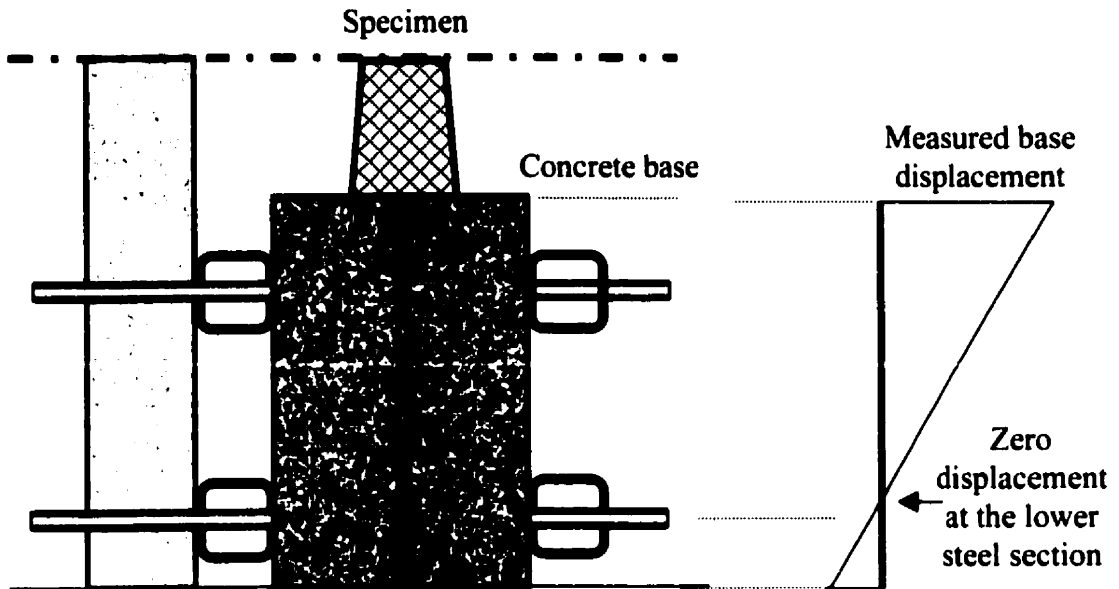


Figure (6-7): Distribution of lateral displacement along the concrete base

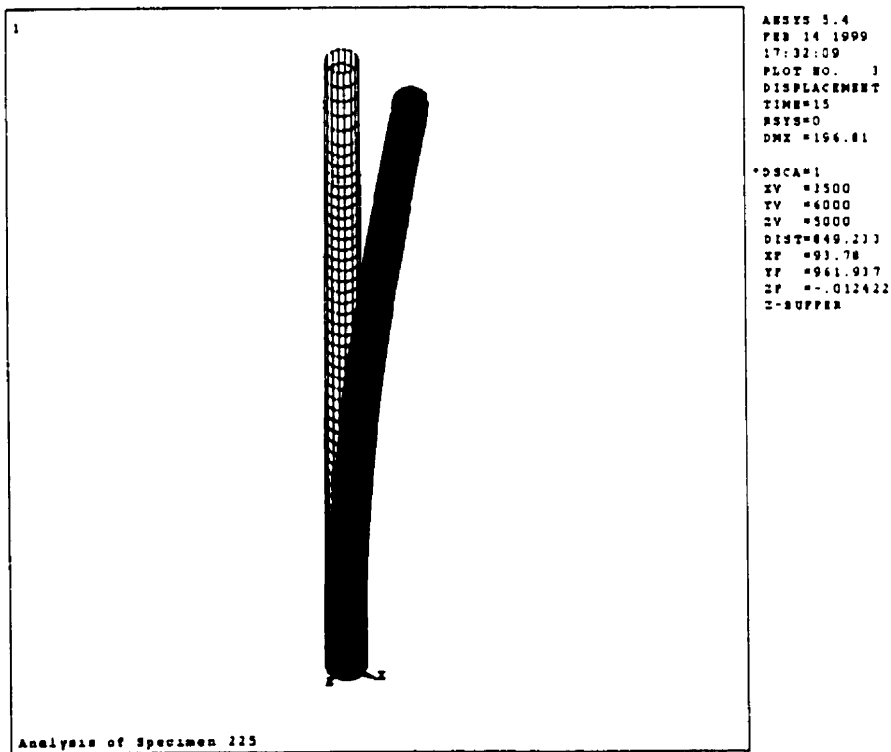


Figure (6-8): Deformed shape for specimen A25

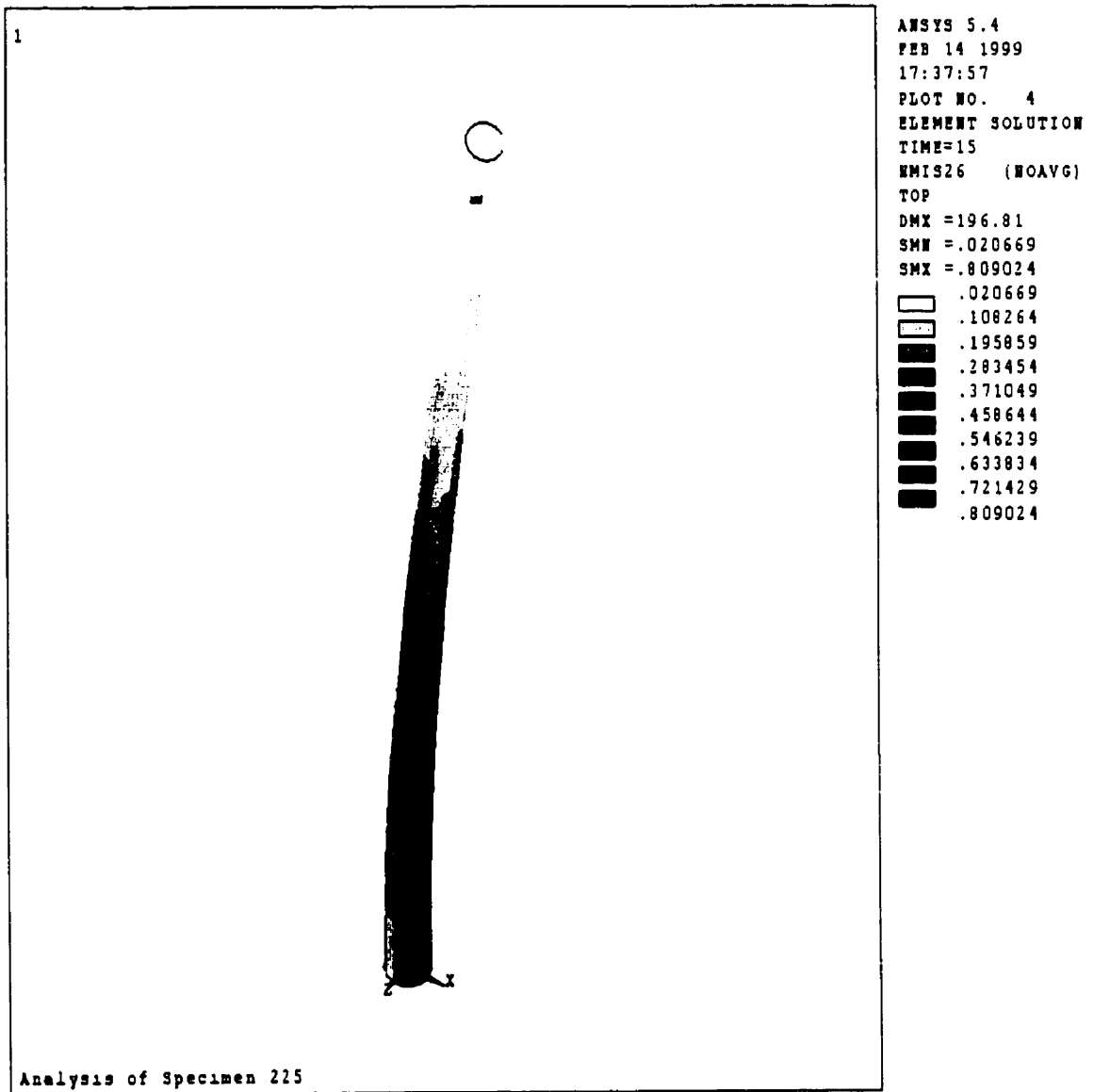


Figure (6-9): Values of the Tsai-Wu failure criterion along specimen A25

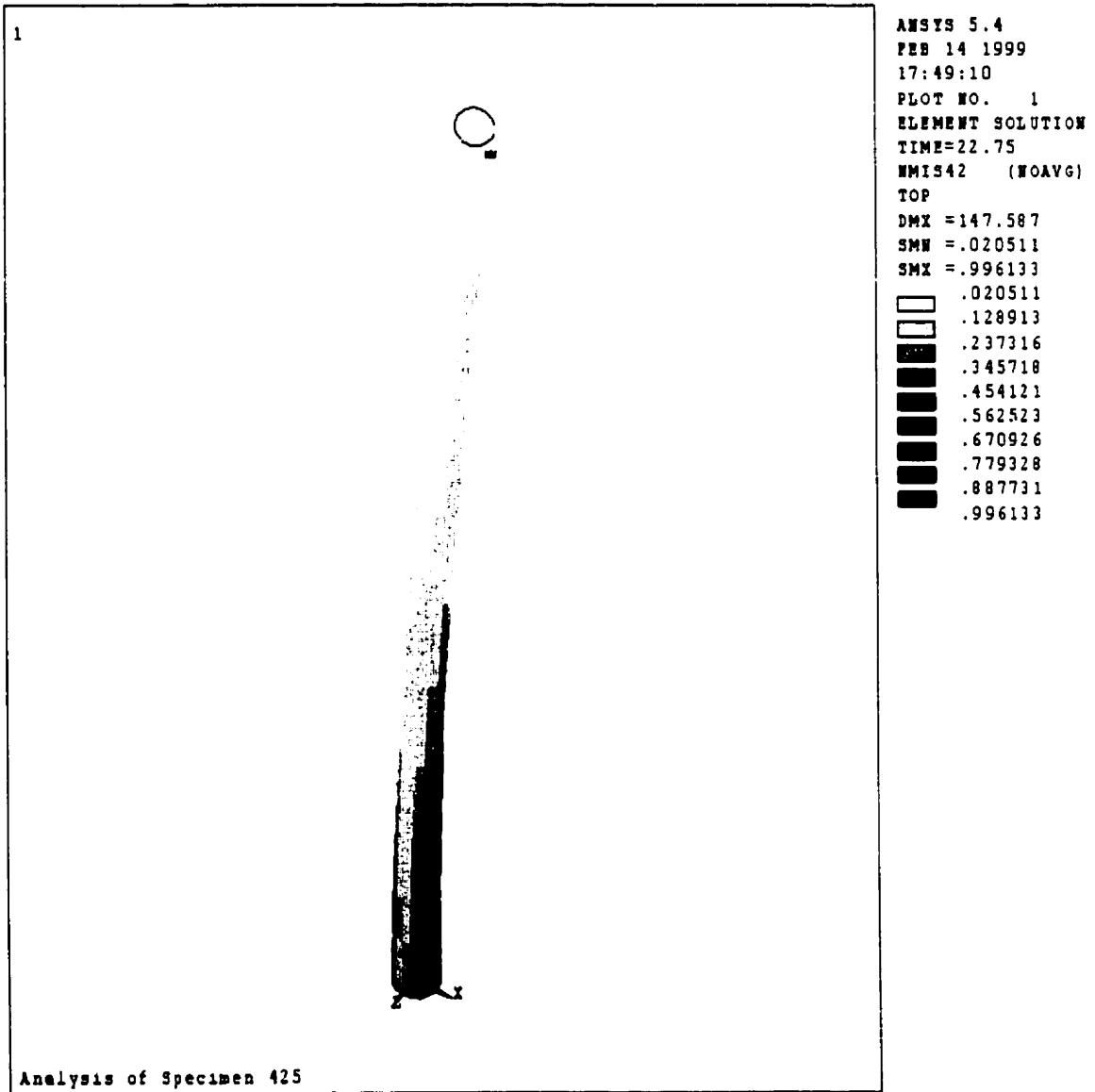


Figure (6-10): Values of the Tsai-Wu failure criterion along specimen C25

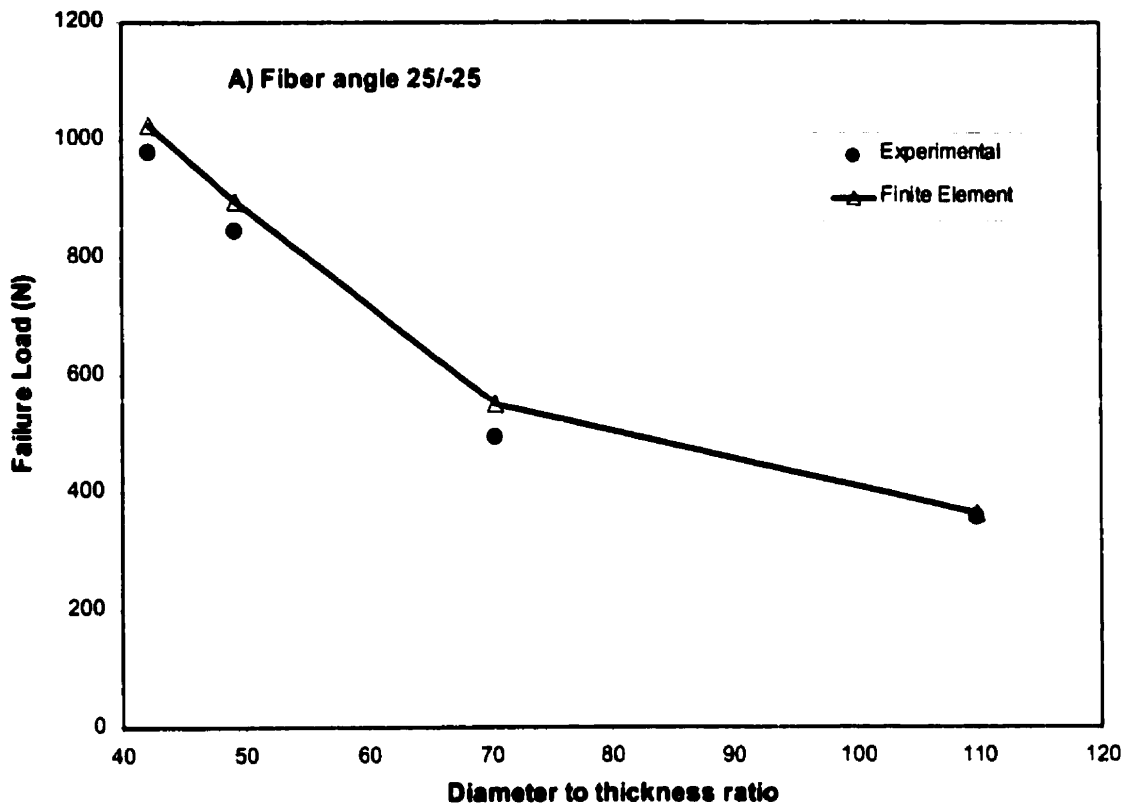


Figure (6-11): Comparison between finite element model and experimental failure load

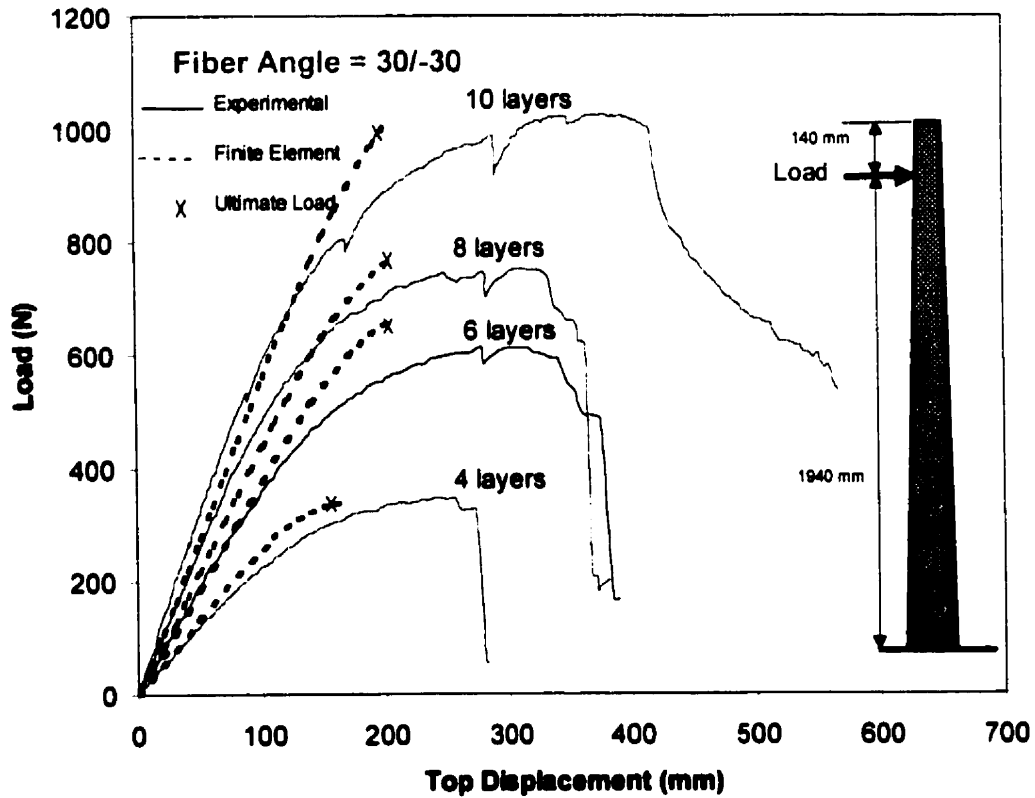


Figure (6-12): Comparison of load-deflection curves between experimental and finite element method

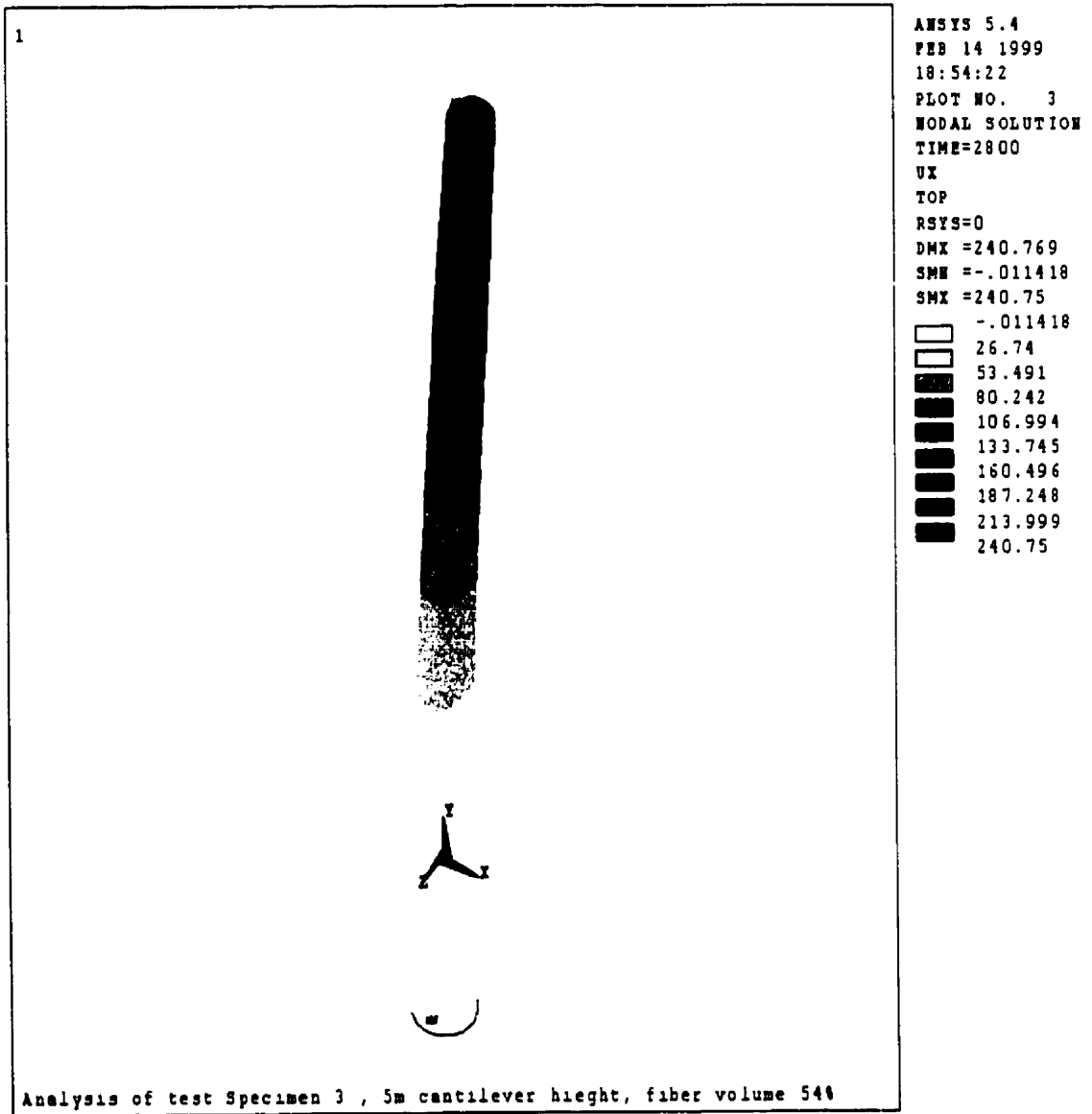


Figure (6-13): Deformed shape for full-scale Specimen 5

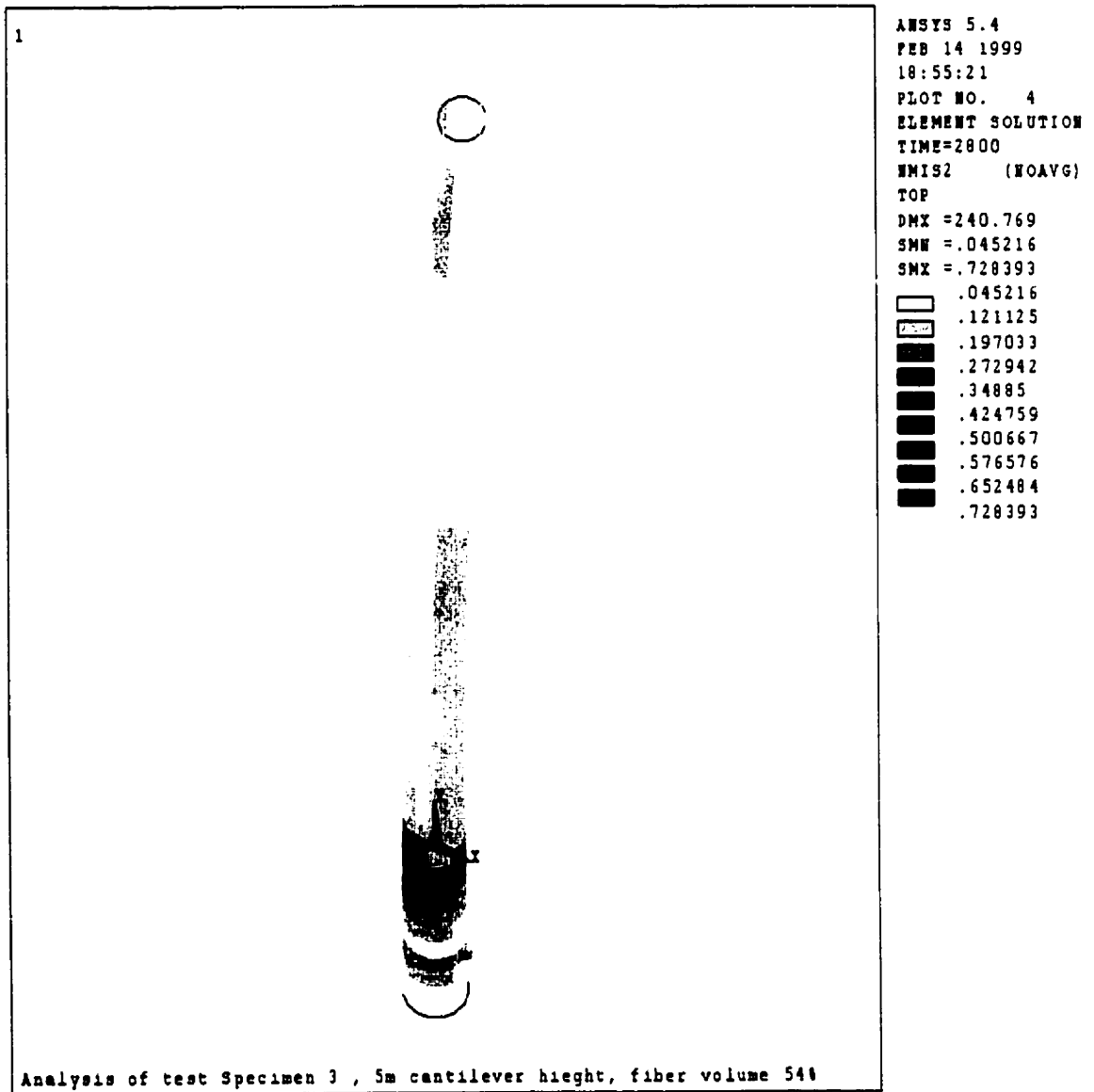


Figure (6-14): Values of the Tsai-Wu failure criterion along full-scale Specimen 5

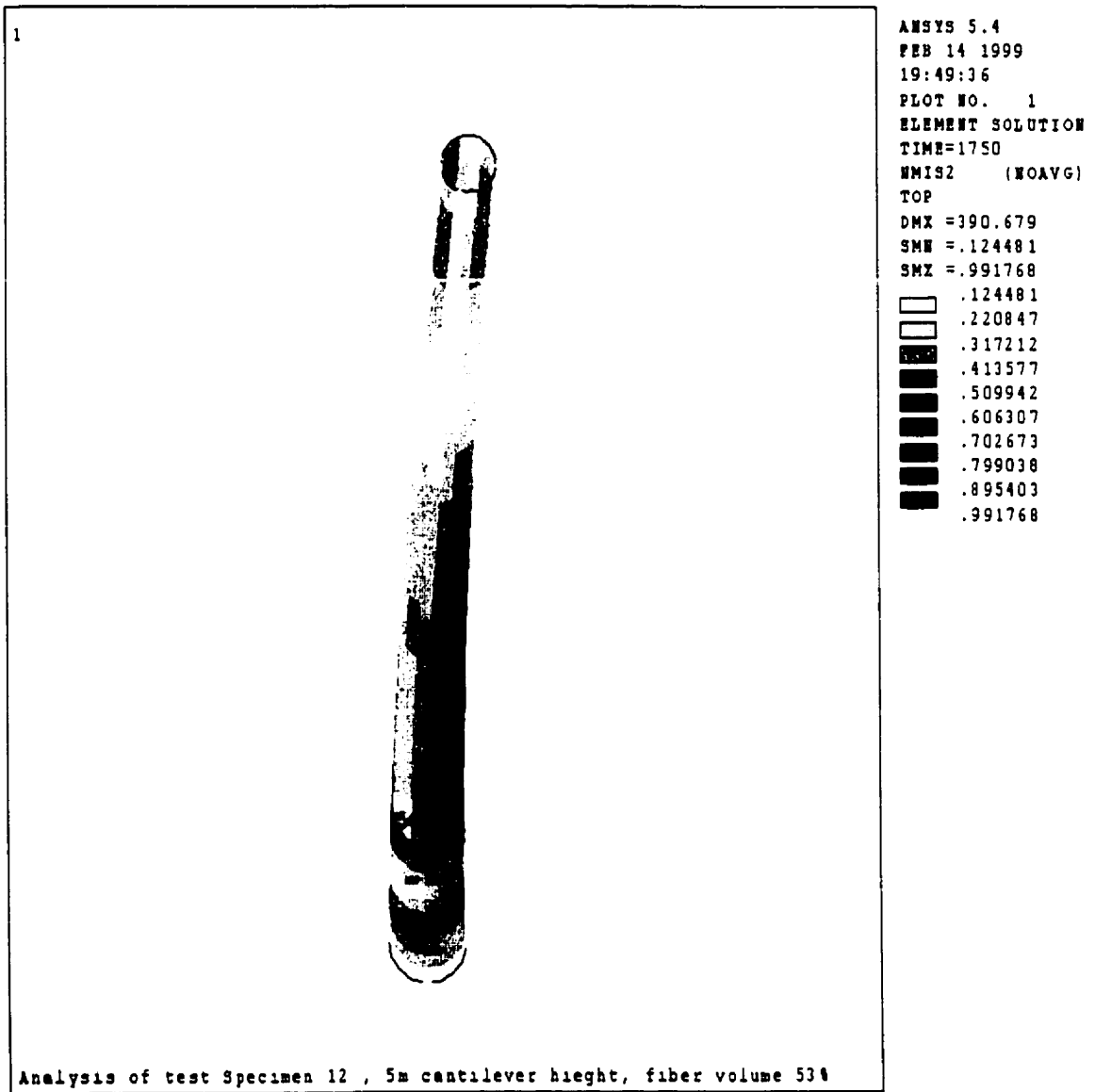


Figure (6-15): Values of the Tsai-Wu failure criterion value full-scale specimen 6

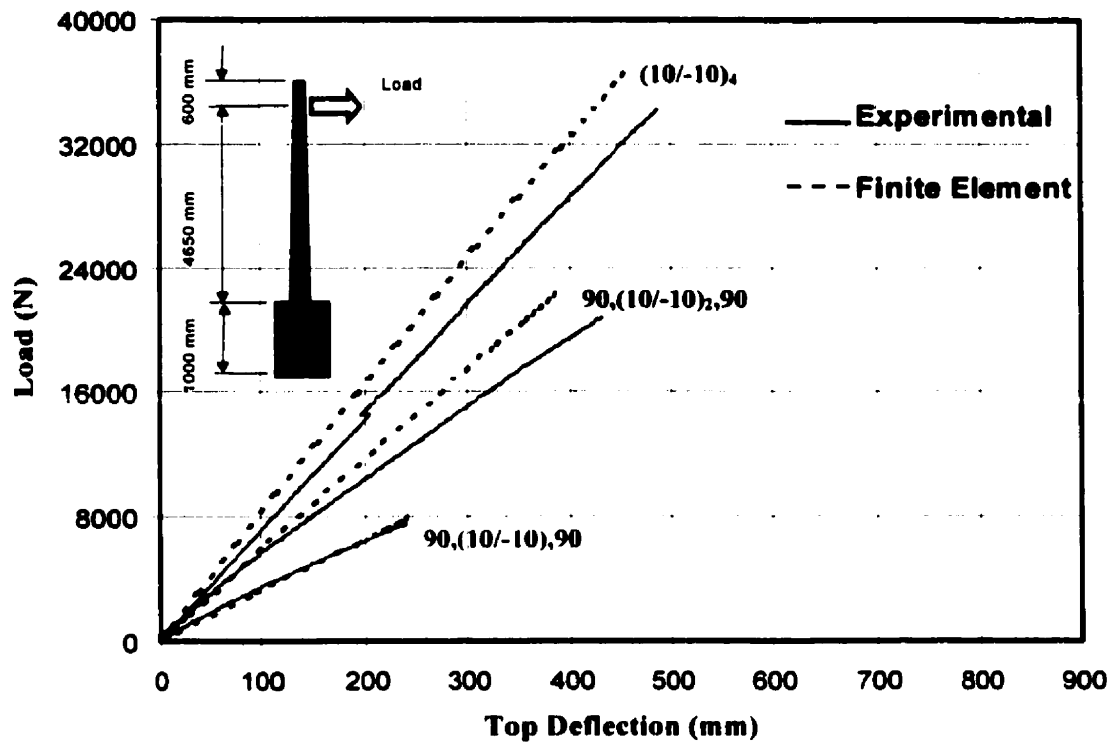


Figure (6-16): Comparison between experimental and finite element load-deflection relationship for 10° full-scale specimens

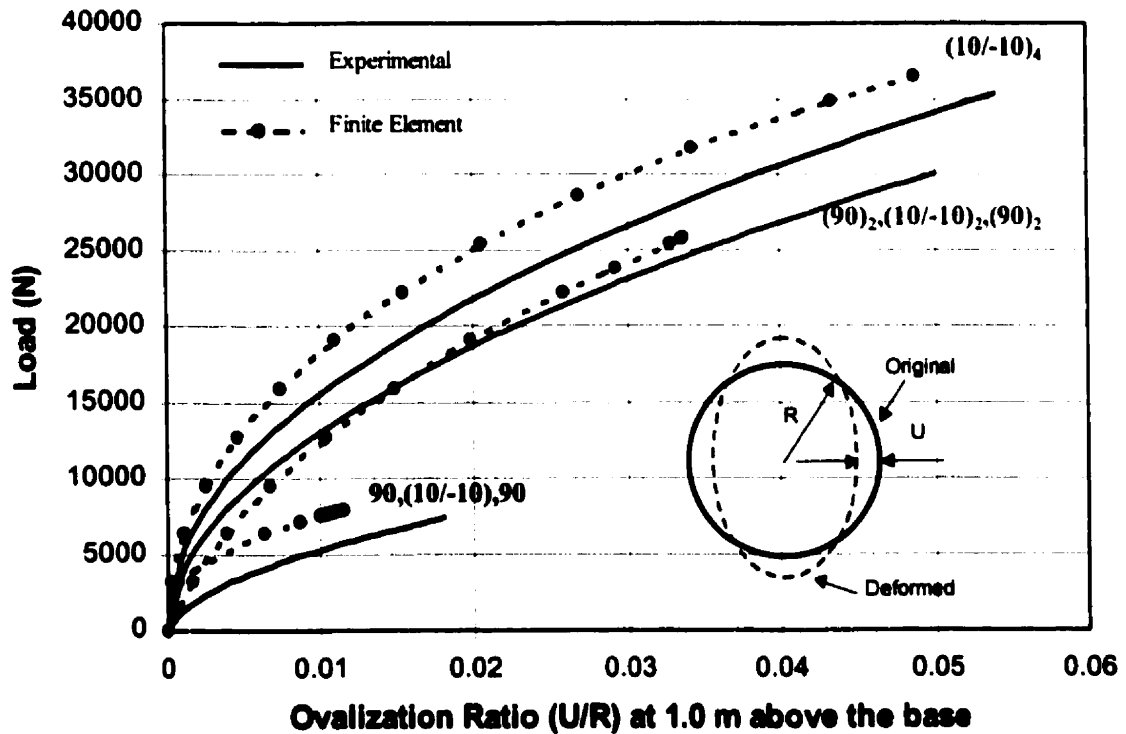


Figure (6-17): Comparison between experimental and finite element load-ovalization relationship for 10° full-scale specimens

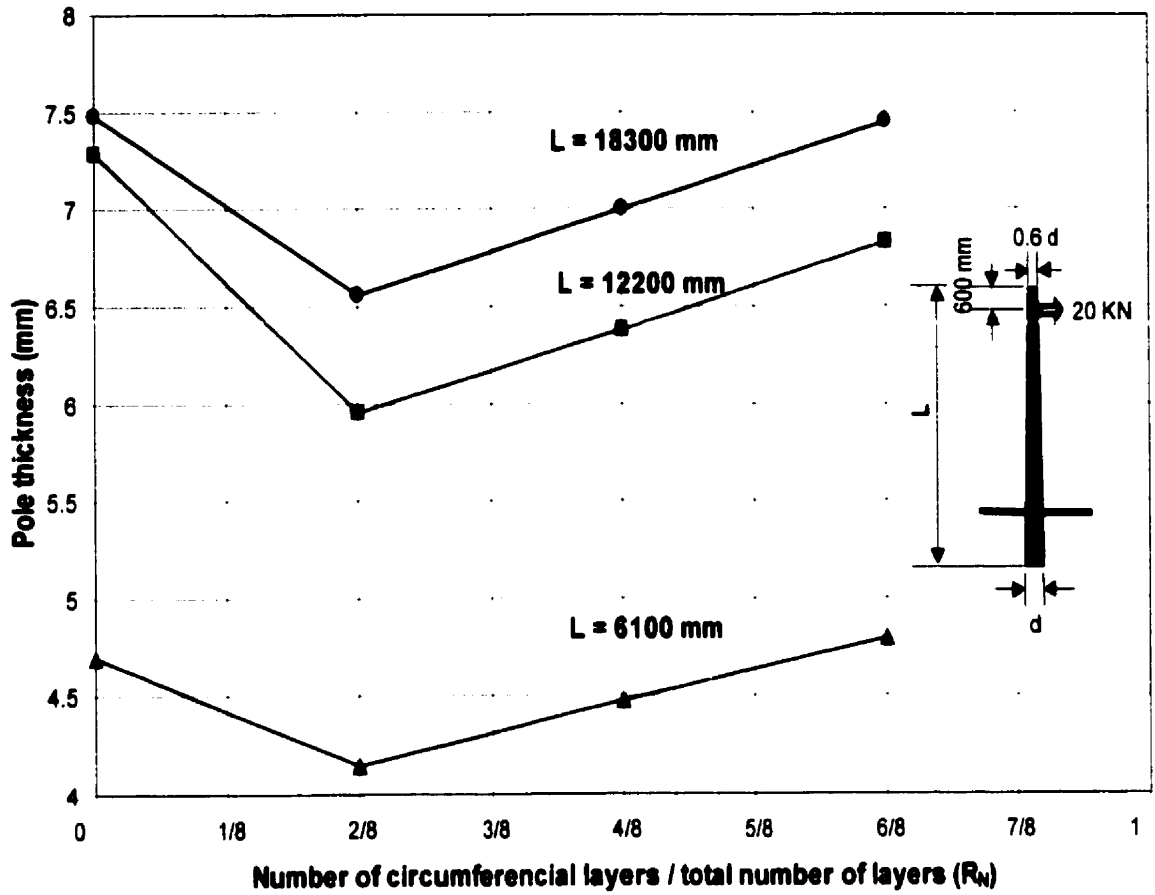


Figure (6-18): Effect of circumferential layers on the thickness of GFRP poles

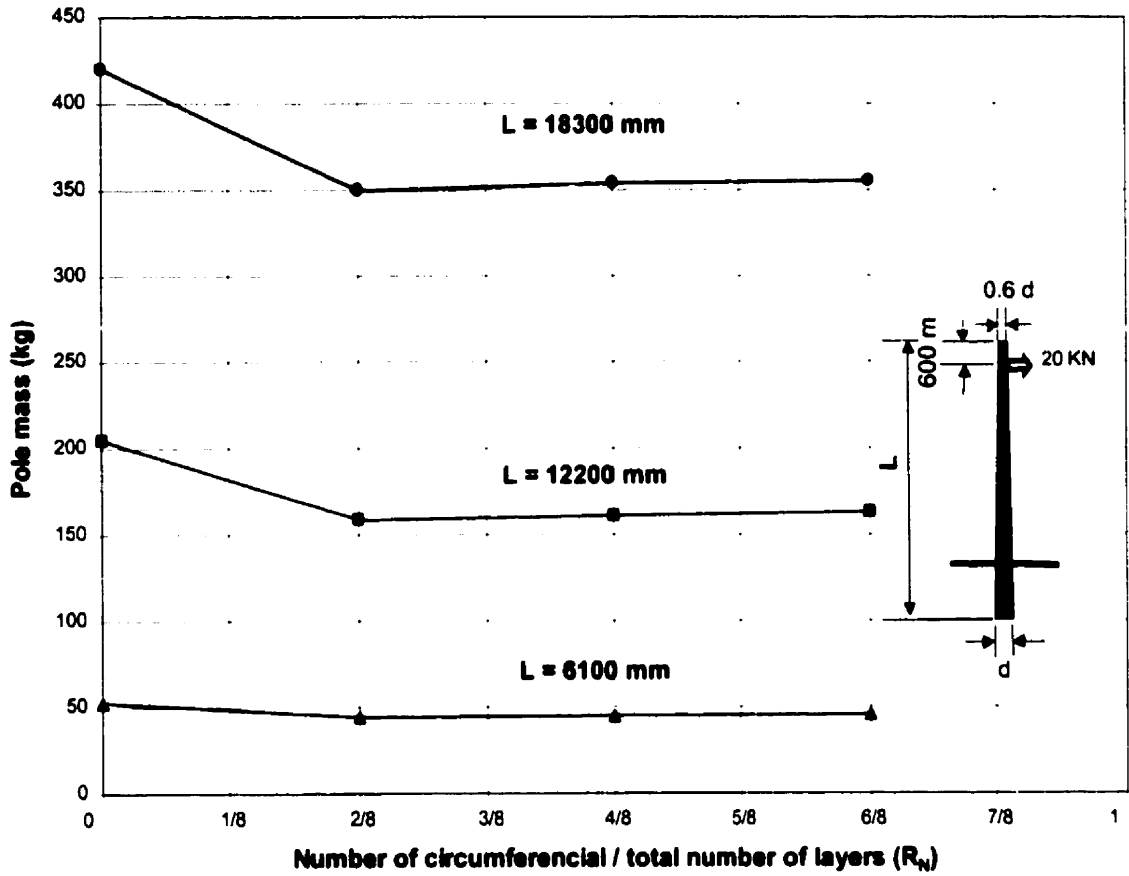


Figure (6-19): Effect of circumferencial layers on the mass of GFRP poles

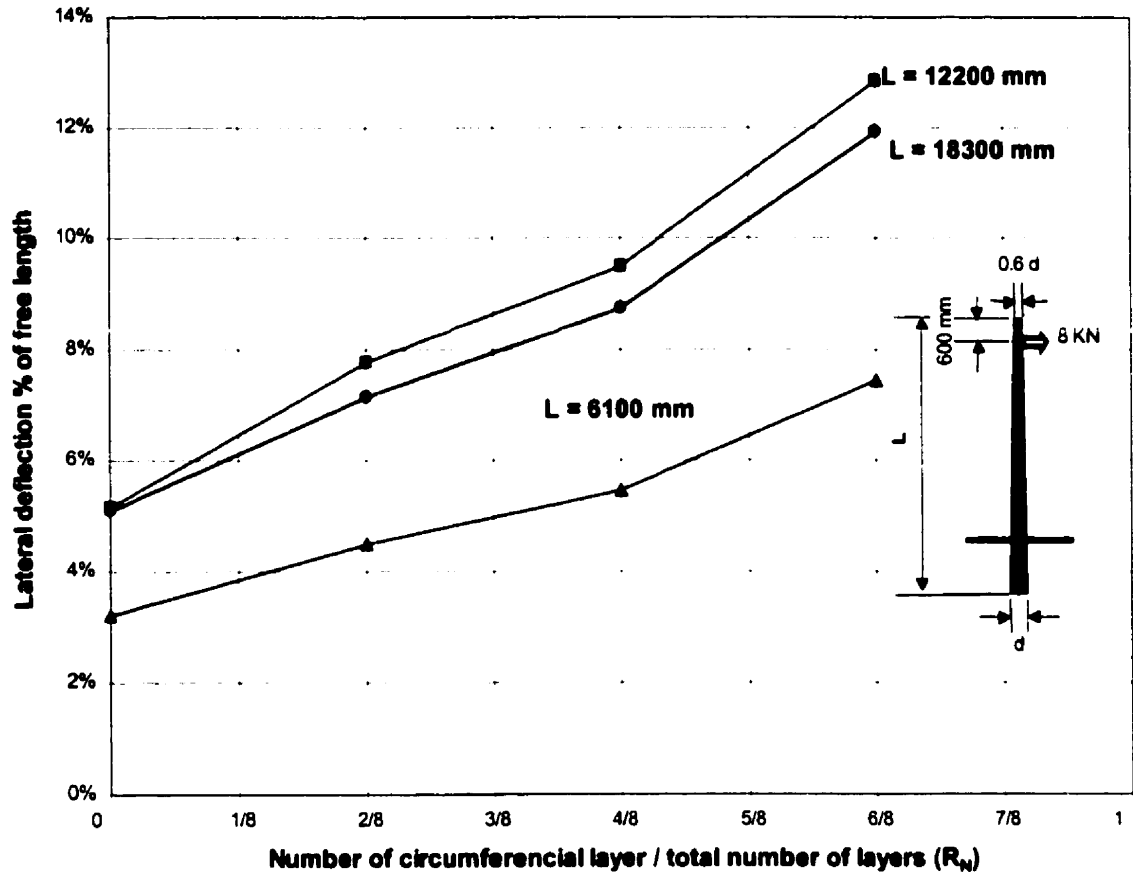


Figure (6-20): Effect of circumferential layers on the lateral deflection of GFRP poles

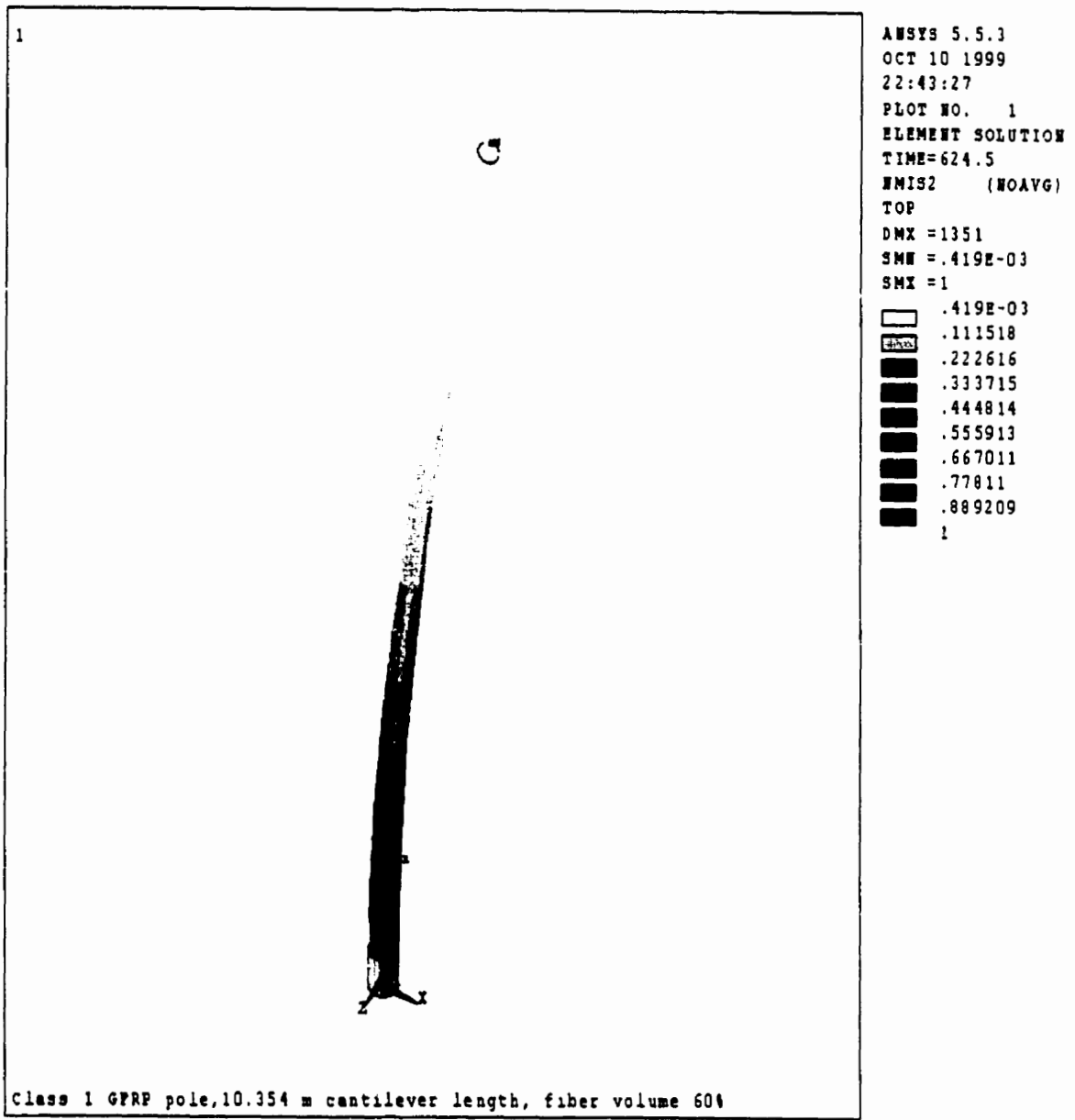


Figure (6-21): Values of the Tsai–Wu failure criterion for a 12.2 m class1 GFRP poles without circumferencial fibers

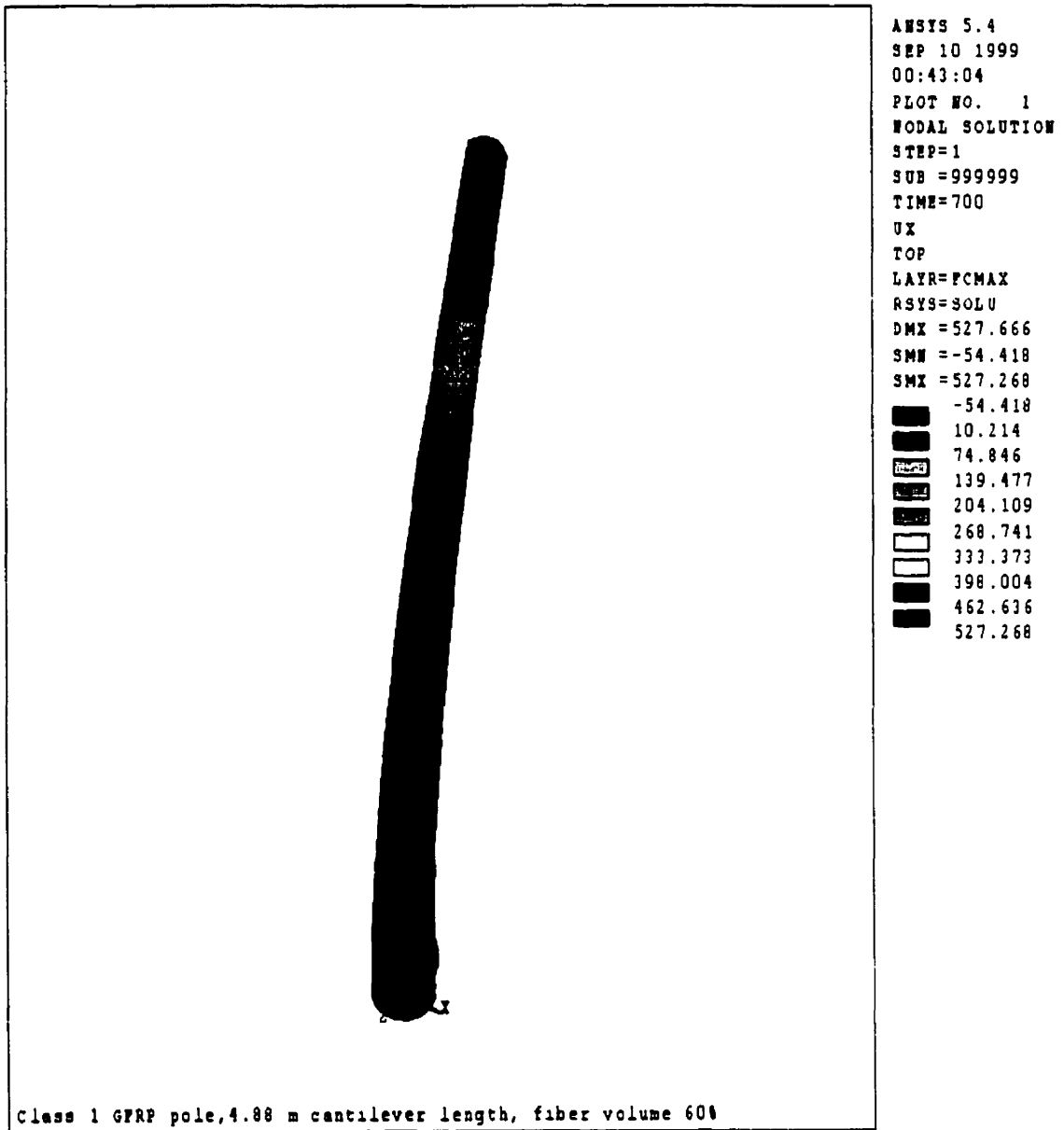


Figure (6-22): Local buckling a 6.1 m class 1 GFRP pole with circumferential fibers

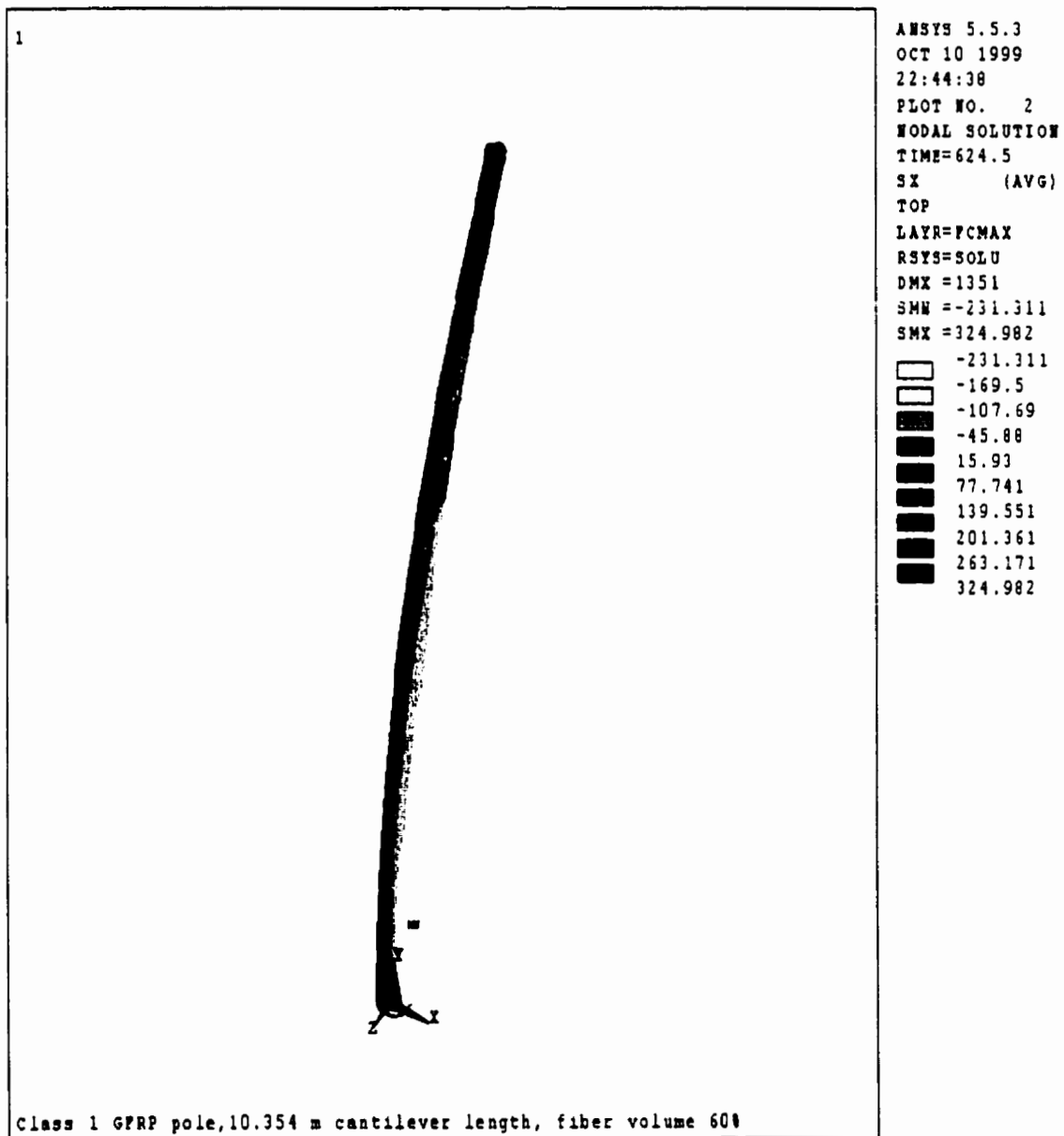


Figure (6-23): Distribution of stresses in the fiber direction for a 12.2 m class 1 GFRP pole without circumferencial fibers

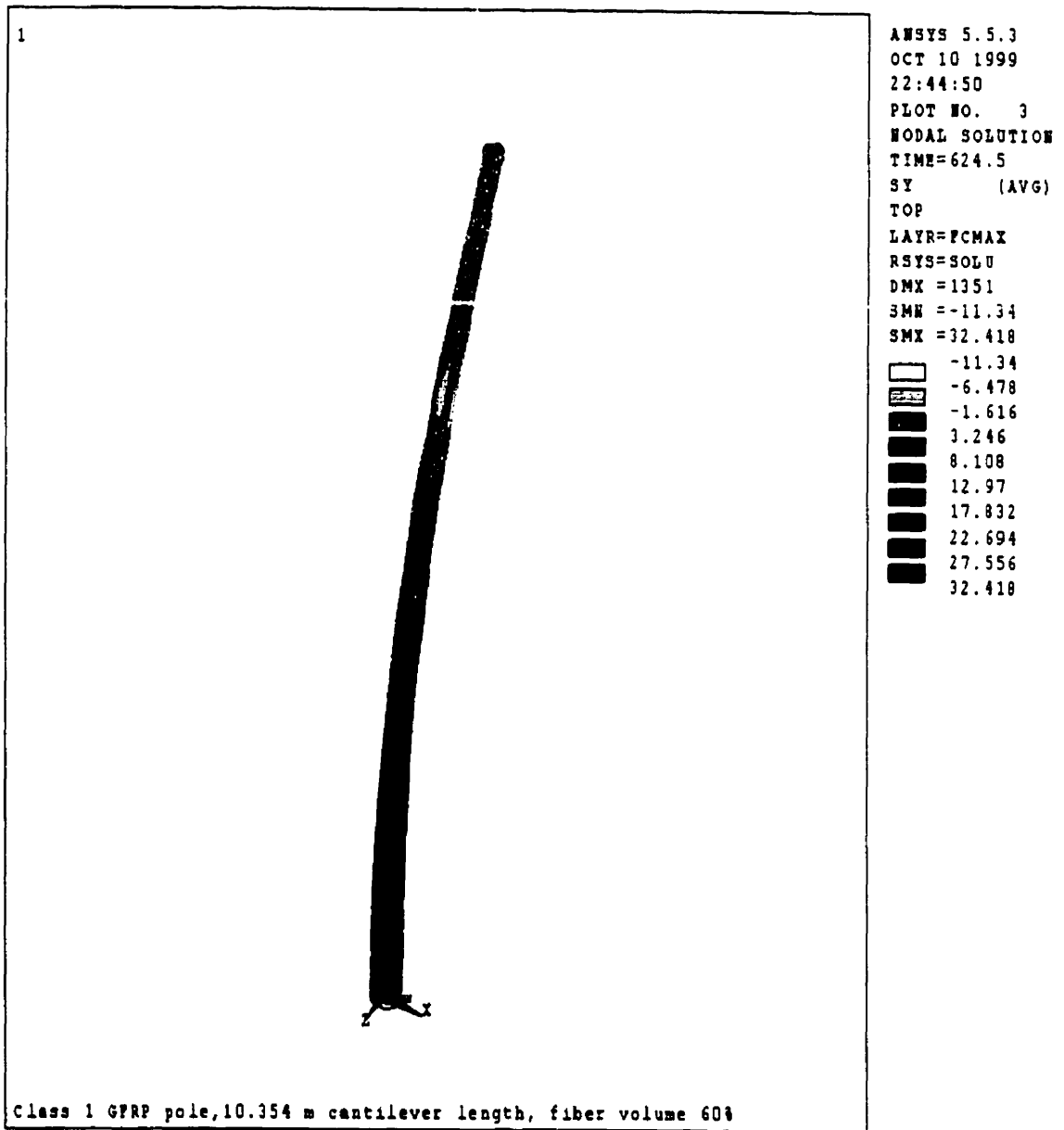


Figure (6-24): Distribution of stresses in the transverse to fiber direction for a 12.2 m class I GFRP pole without circumferential fibers

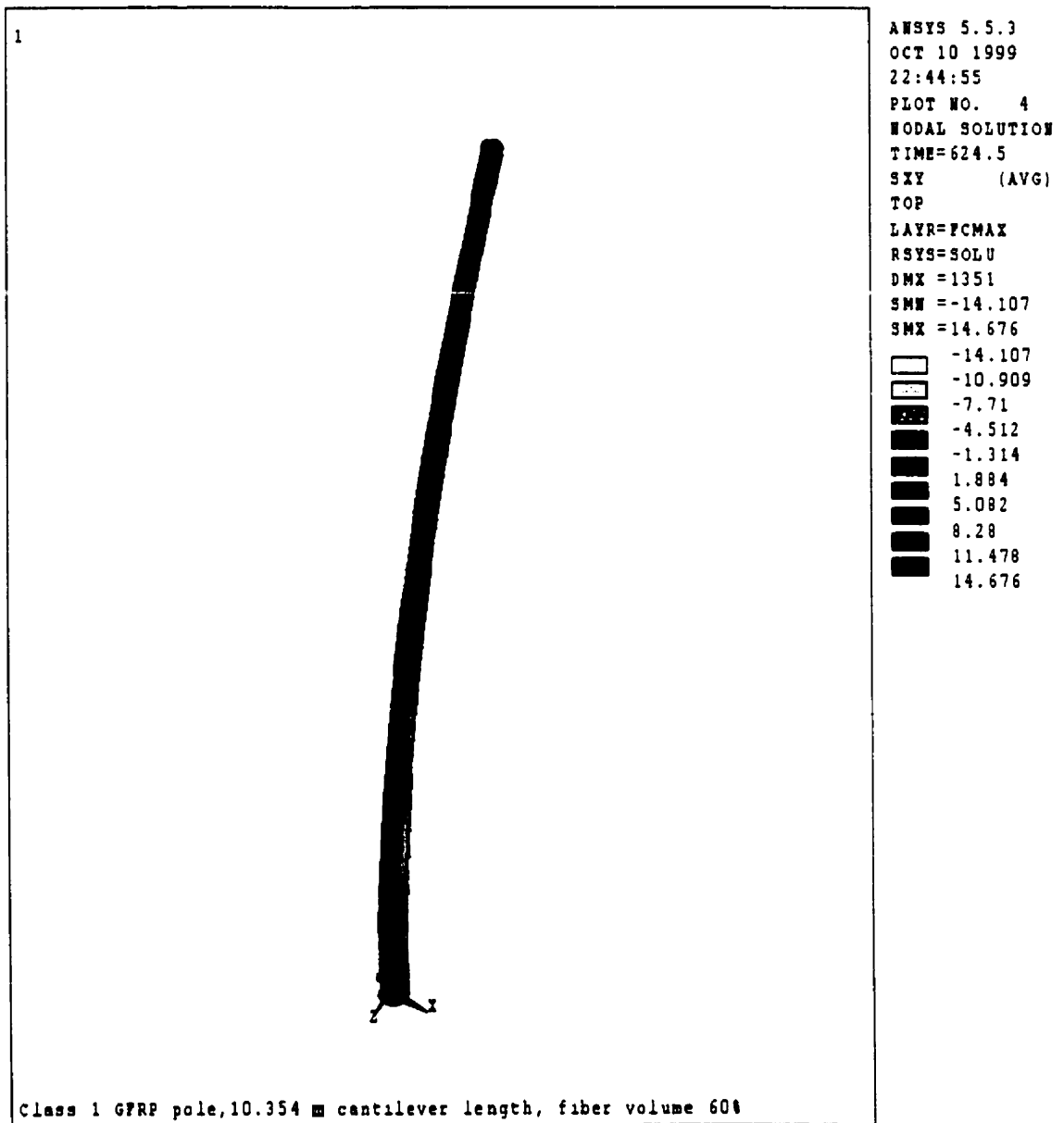


Figure (6-25): Distribution of shear stresses in the fiber direction and transverse to fiber direction for a 12.2 m class 1 GFRP pole without circumferential fibers

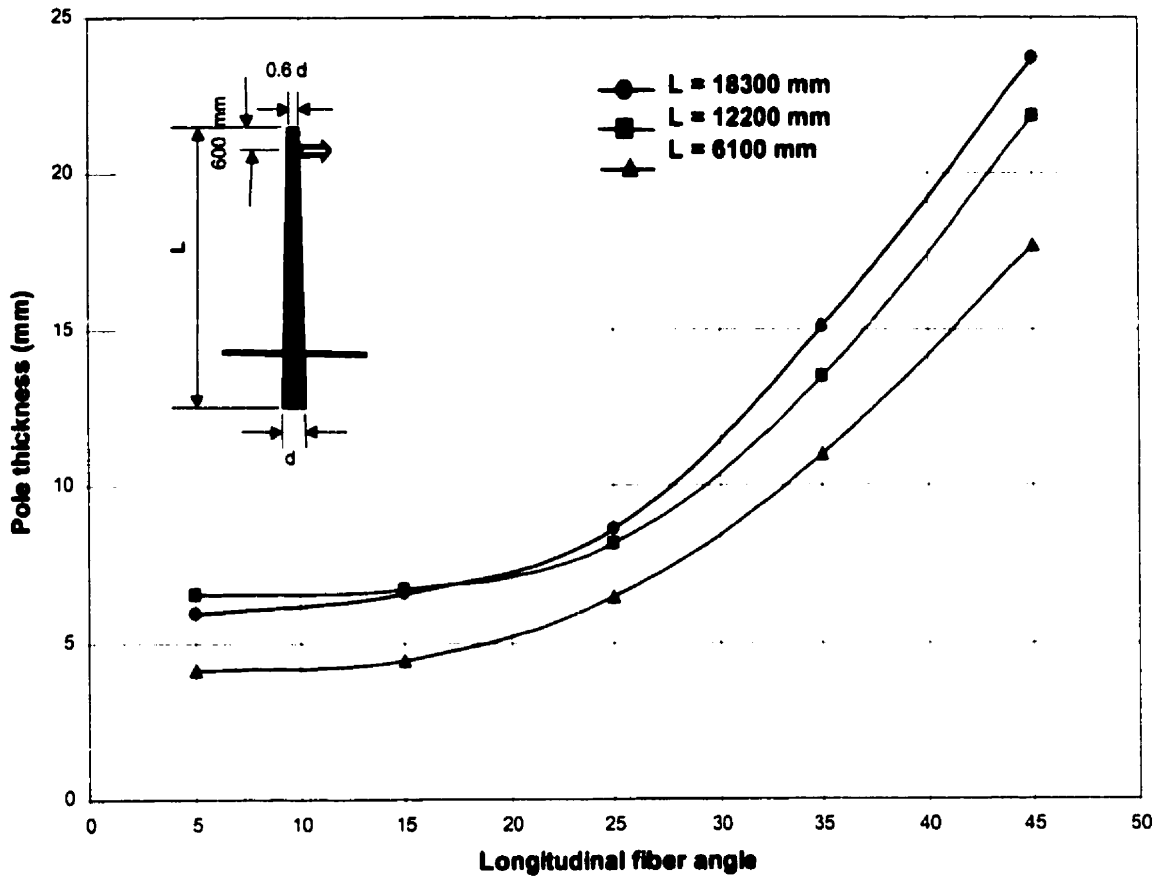


Figure (6-26): Effect of longitudinal fiber angle on the thickness of GFRP poles

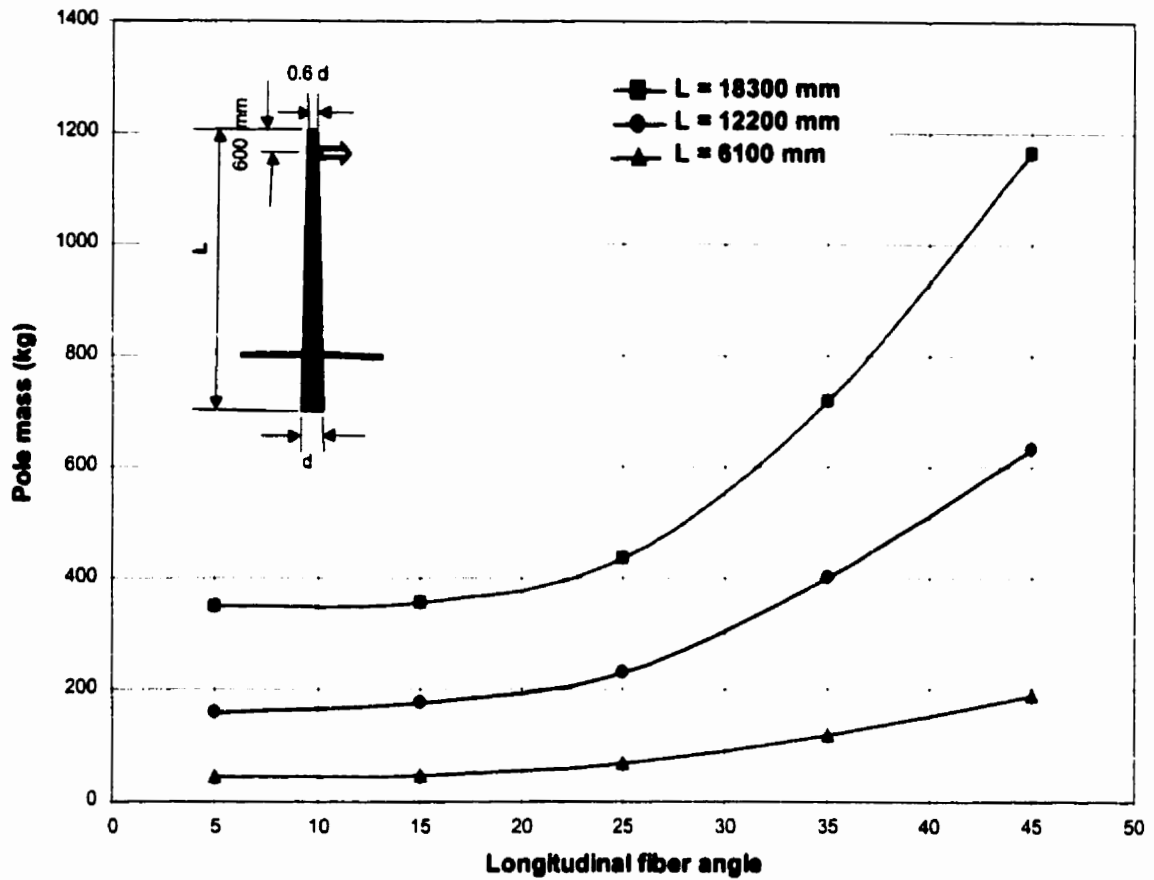


Figure (6-27): Effect of longitudinal fiber angle on the mass of GFRP poles

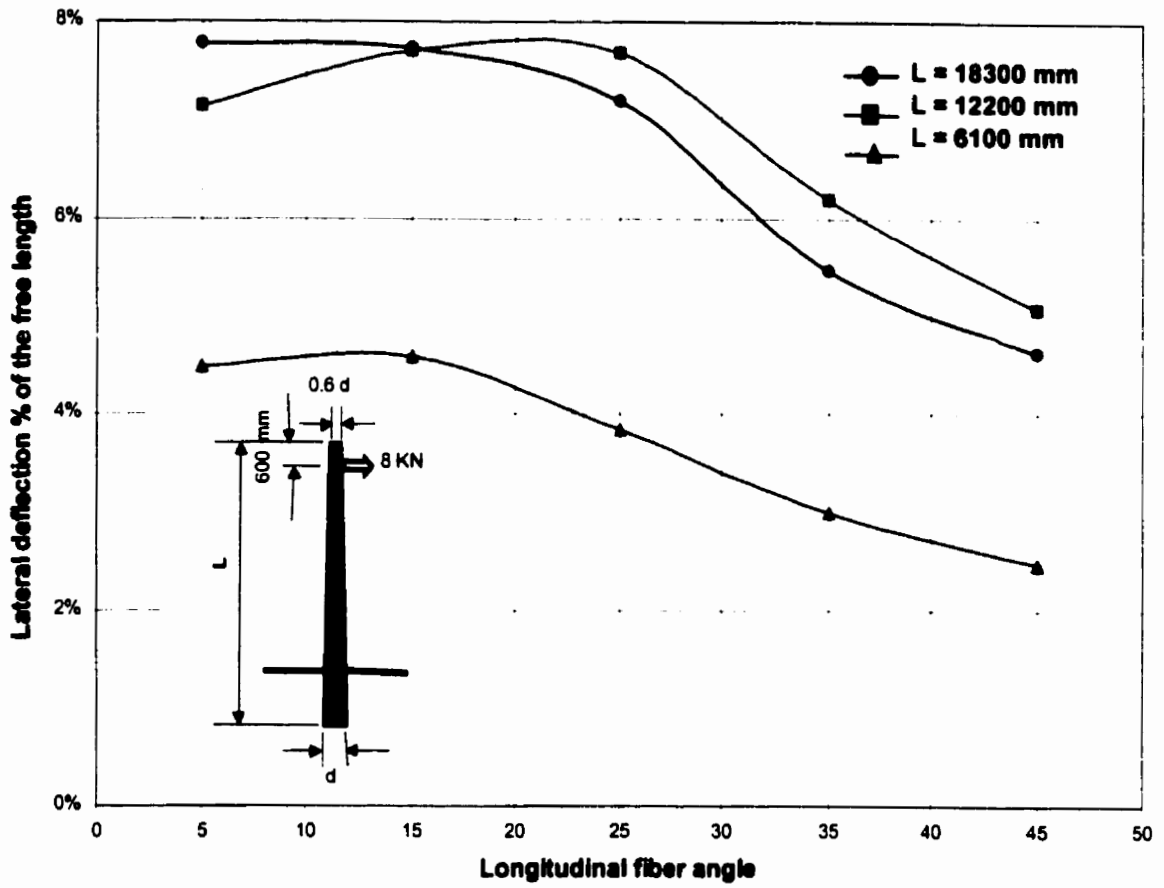


Figure (6-28): Effect of longitudinal fiber angle on the lateral deflection of GFRP poles

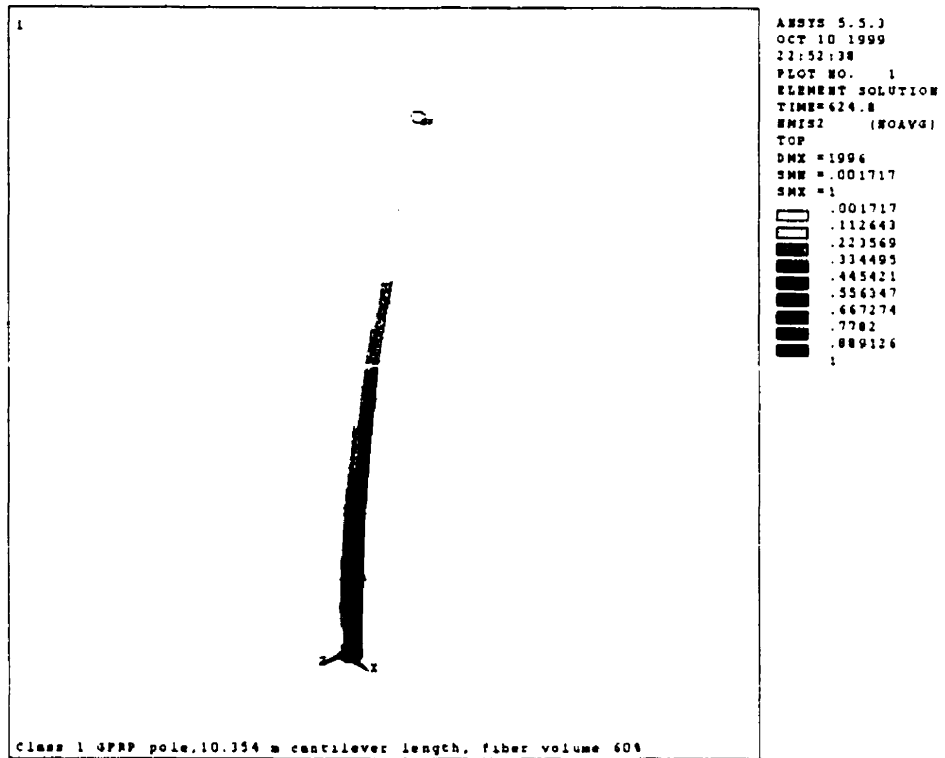


Figure (6-29): Compression side failure mode of a 12.2 m class I GFRP poles with 15° longitudinal fiber angle

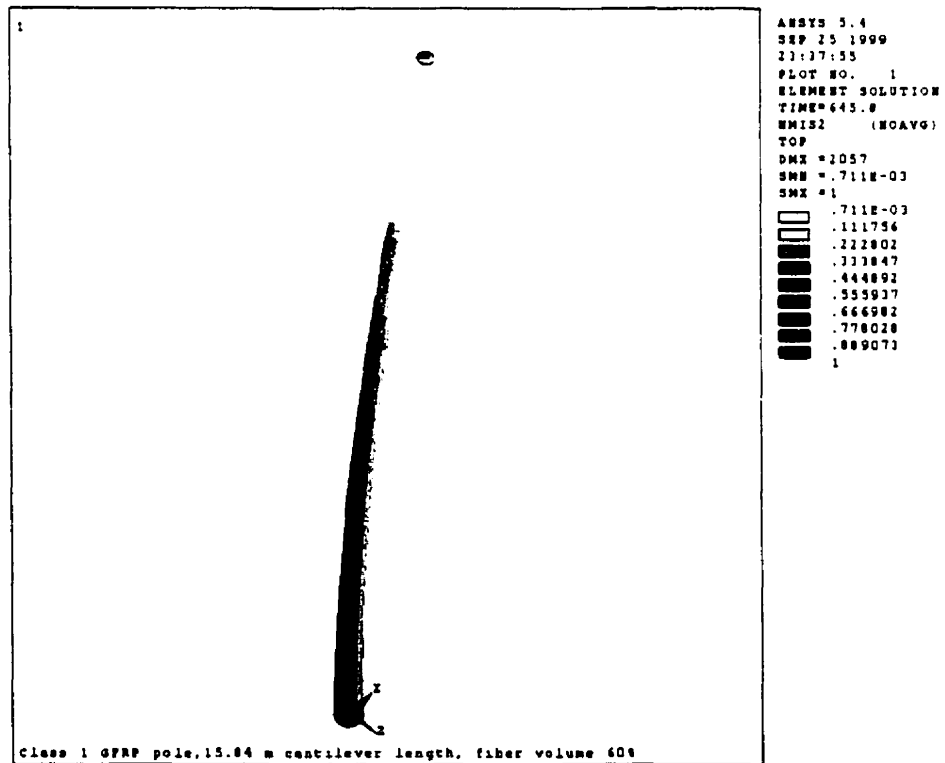


Figure (6-30): Tension side failure mode of a 18.3 m GFRP pole with 45° longitudinal fiber angle

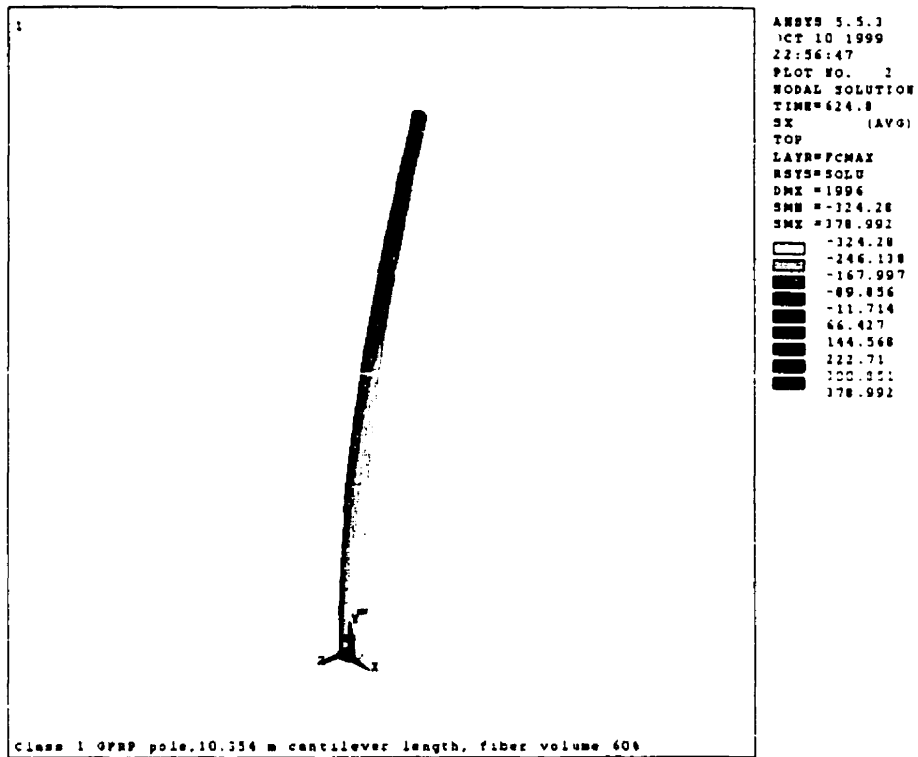


Figure (6-31): Distribution of stresses in the fiber direction for a 12.2 m class 1 GFRP pole with 15° longitudinal fiber angle

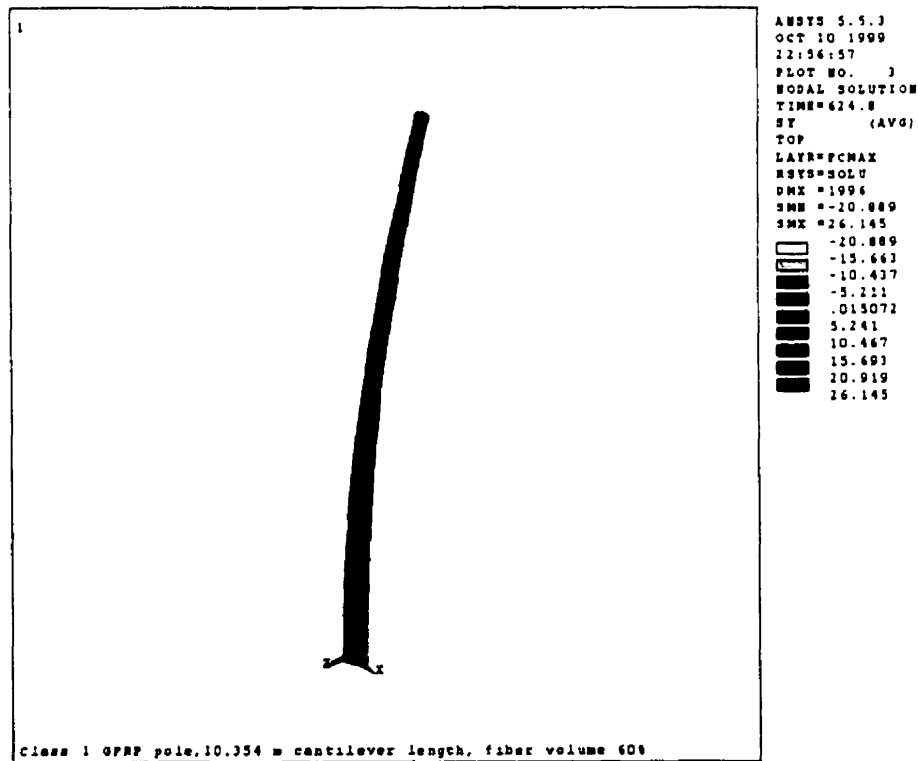


Figure (6-32): Distribution of stresses in the transverse to fiber direction for a 12.2 m class 1 GFRP pole with 15° longitudinal fiber angle

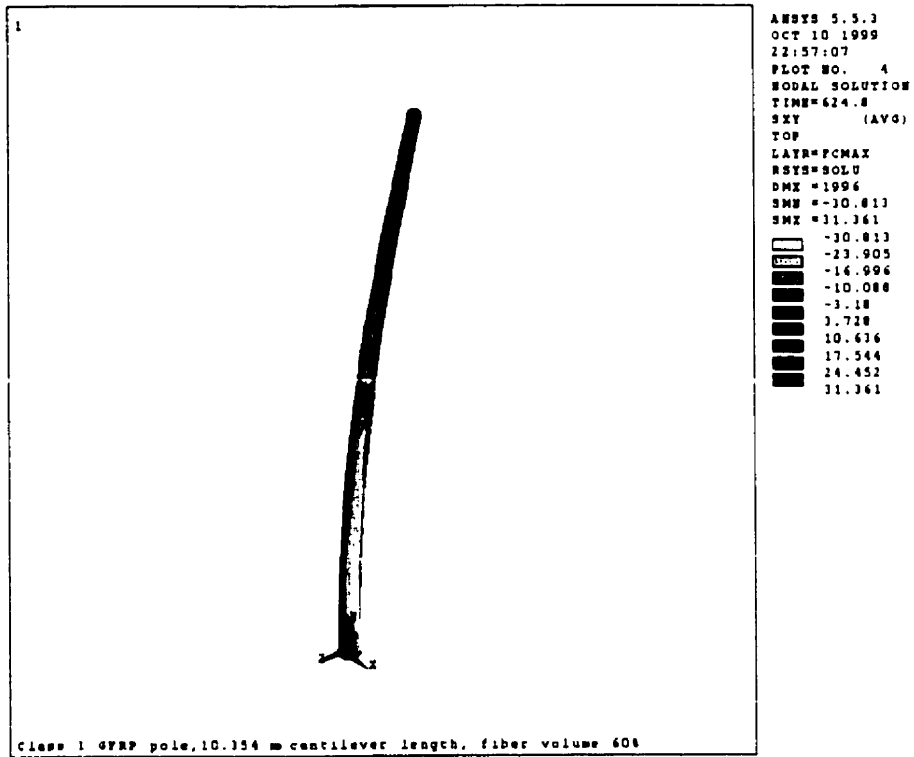


Figure (6-33): Distribution of shear stresses in the fiber and transverse to fiber plane for a 12.2 m class1 GFRP pole with 15° longitudinal fiber angle

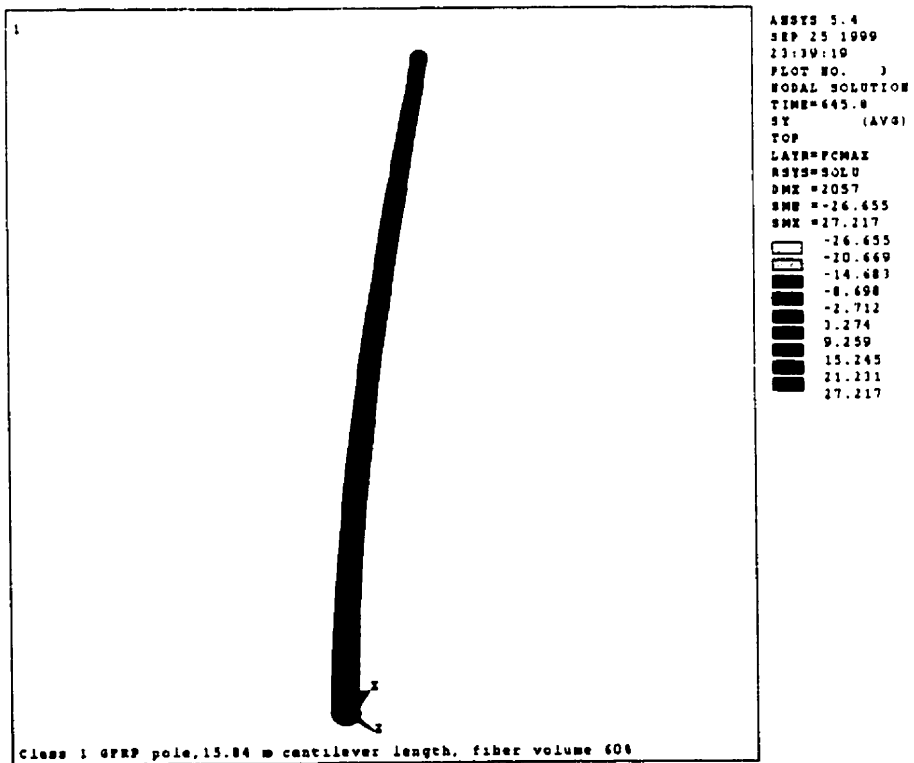


Figure (6-34): Distribution of stresses in the transverse to fiber direction for a 18.3 m class1 GFRP pole with 45° longitudinal fiber angle

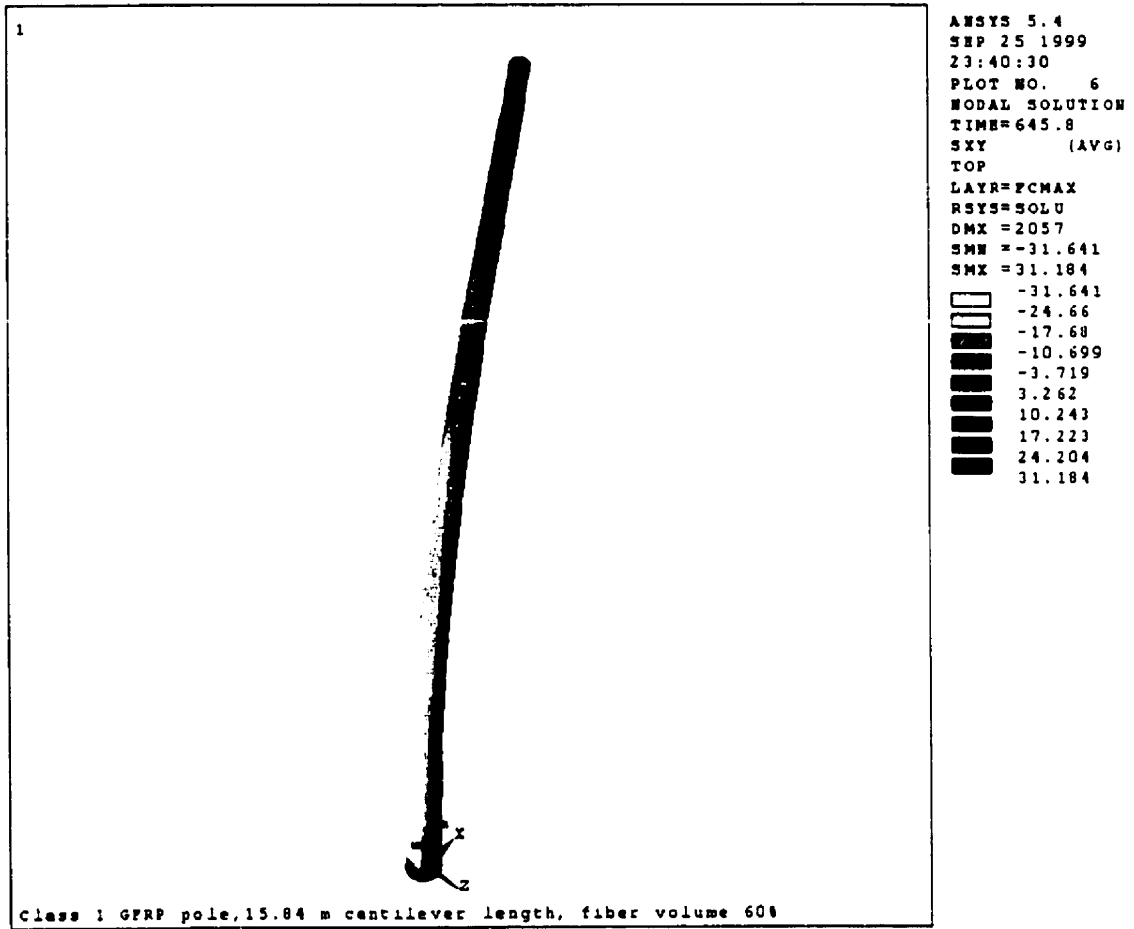


Figure (6-35): Distribution of shear stresses in the fiber direction and transverse to fiber direction for a 18.3 m class 1 GFRP pole with 45° longitudinal fiber angle

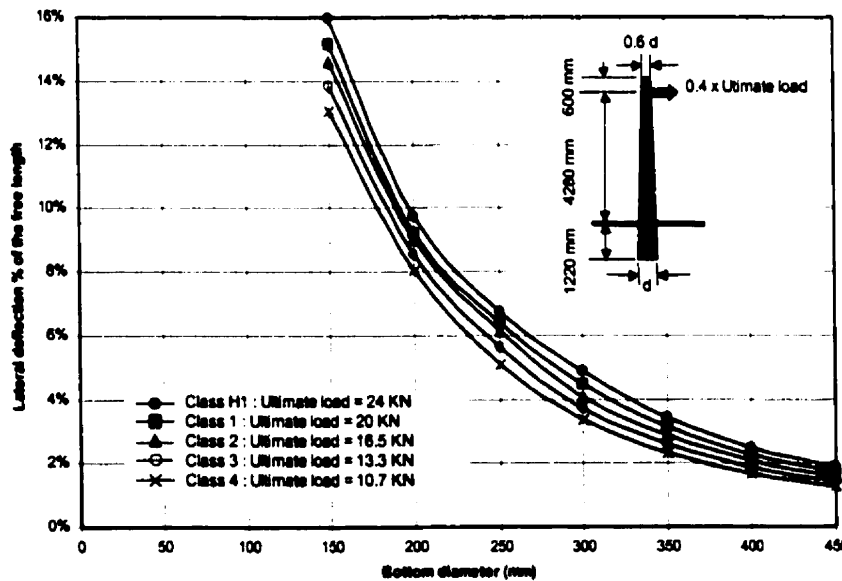
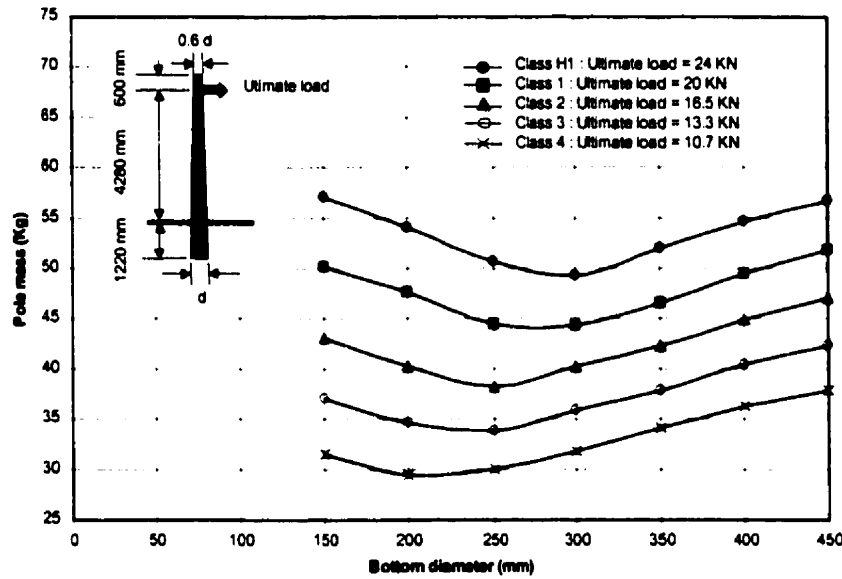
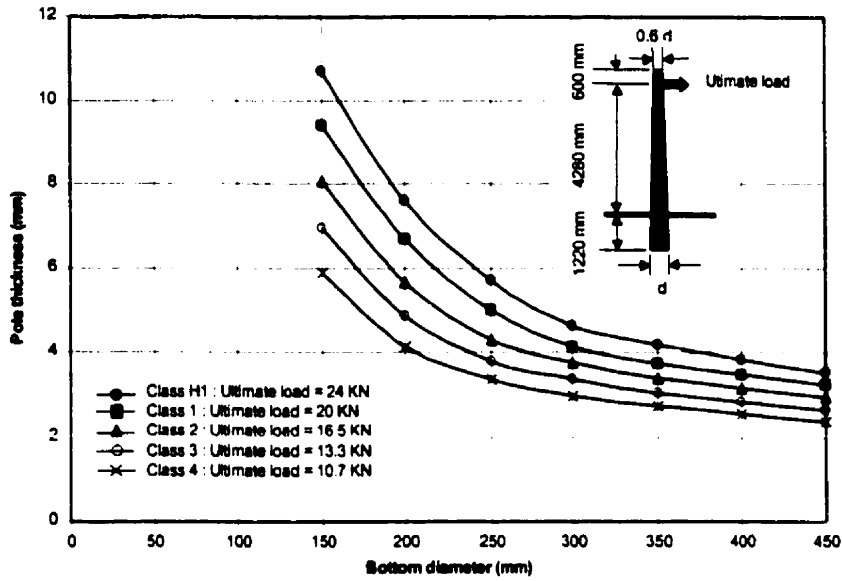


Figure (6-36): Design charts for 6.1 m GFRP poles (strength criterion)

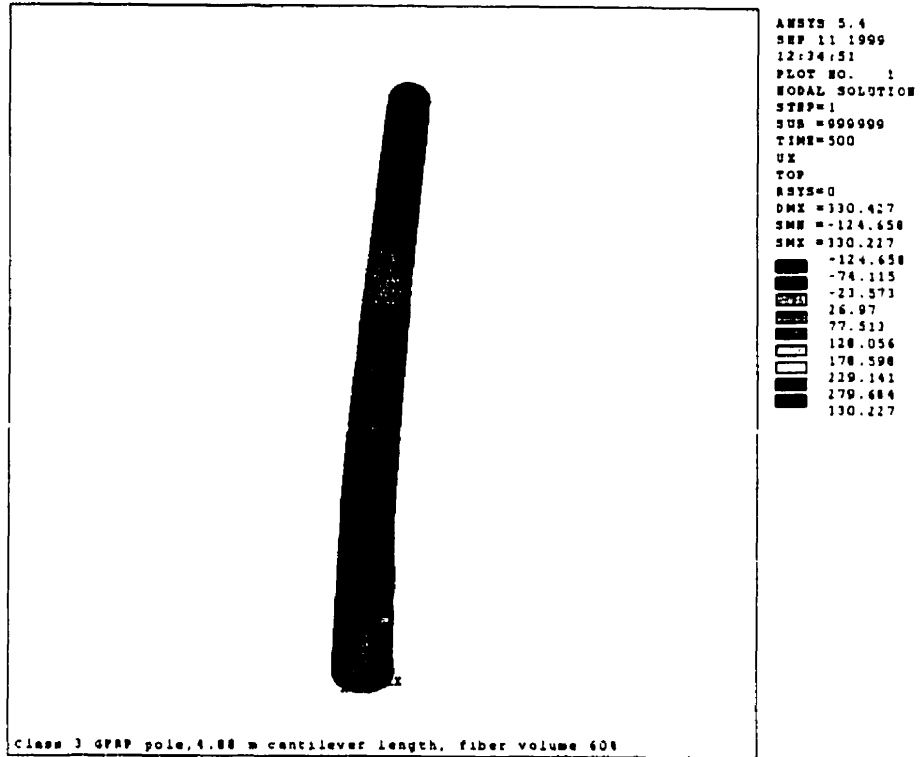


Figure (6-37): Local buckling of a 6.1 m class 3 GFRP pole

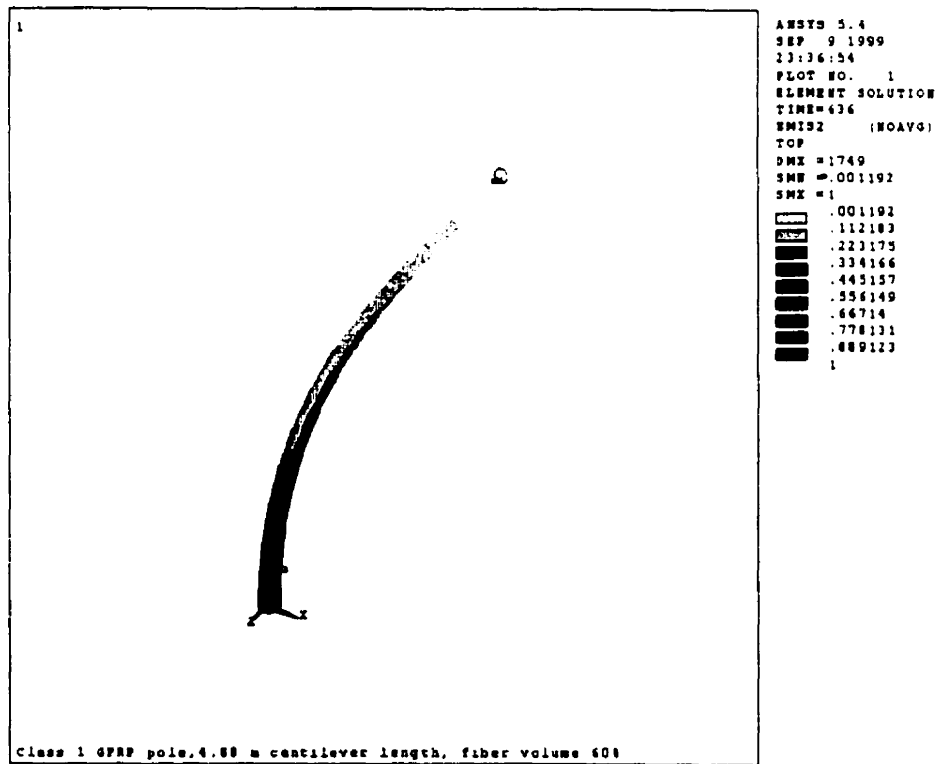


Figure (6-38): Compression side failure mode for a 6.1 m class 1 GFRP pole

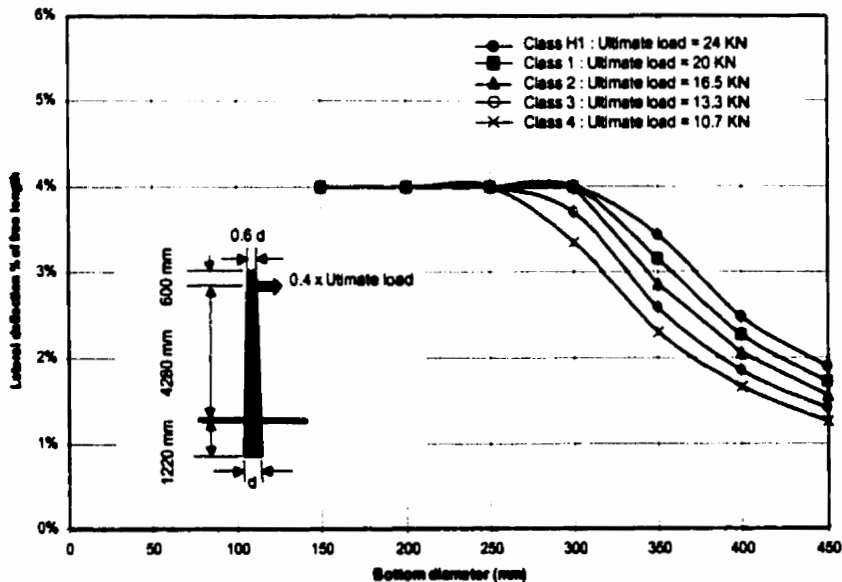
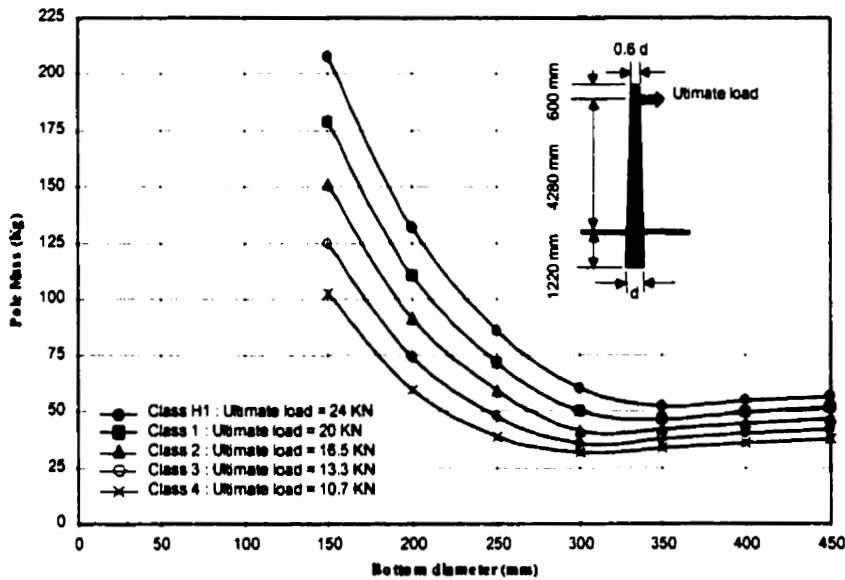
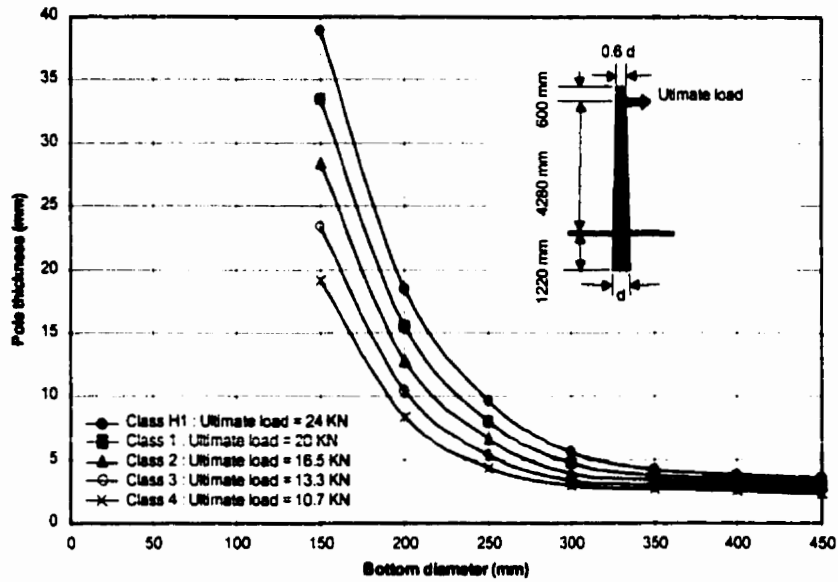


Figure (6-39): Design charts for 6.1 m GFRP poles (strength and deflection criteria)

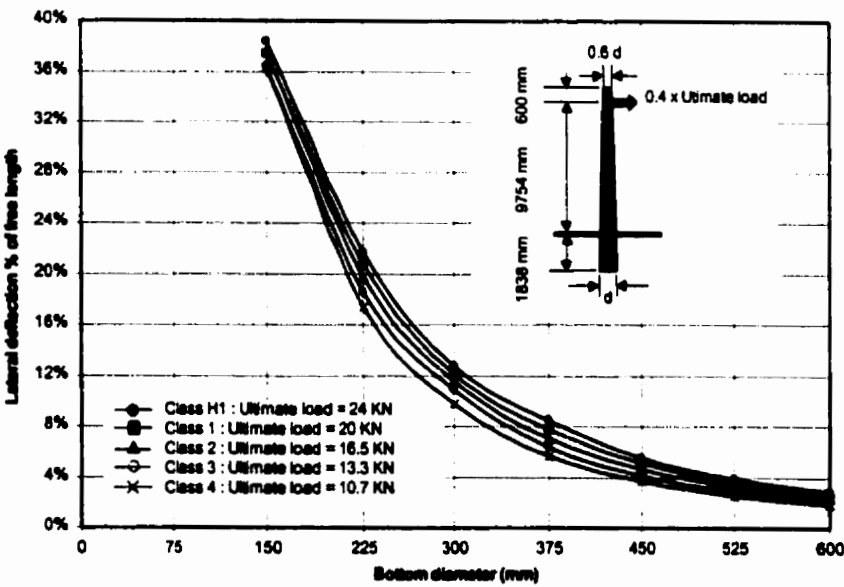
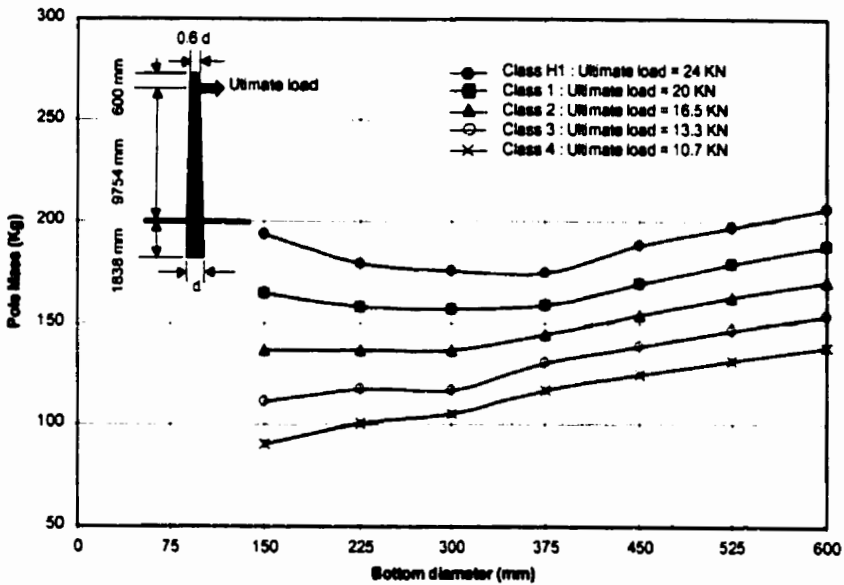
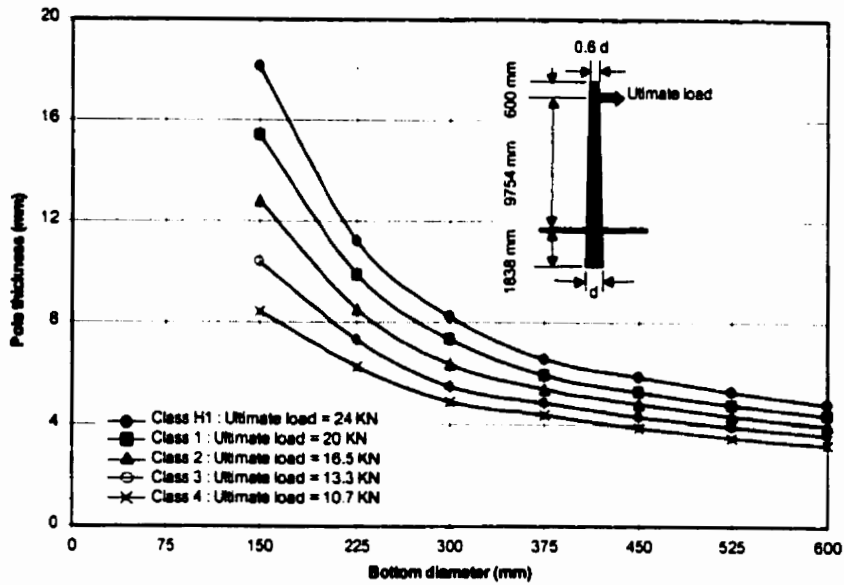


Figure (6-40): Design charts for 12.2 m GFRP poles (strength criterion)

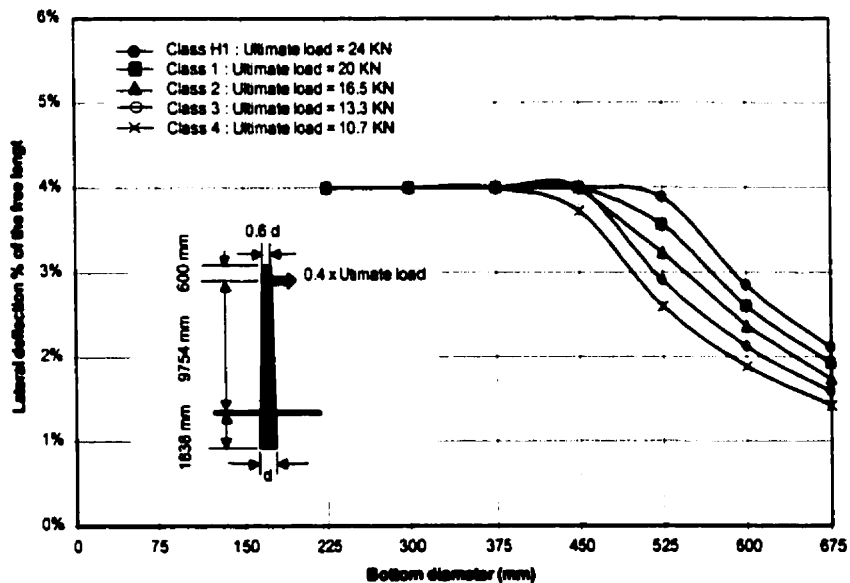
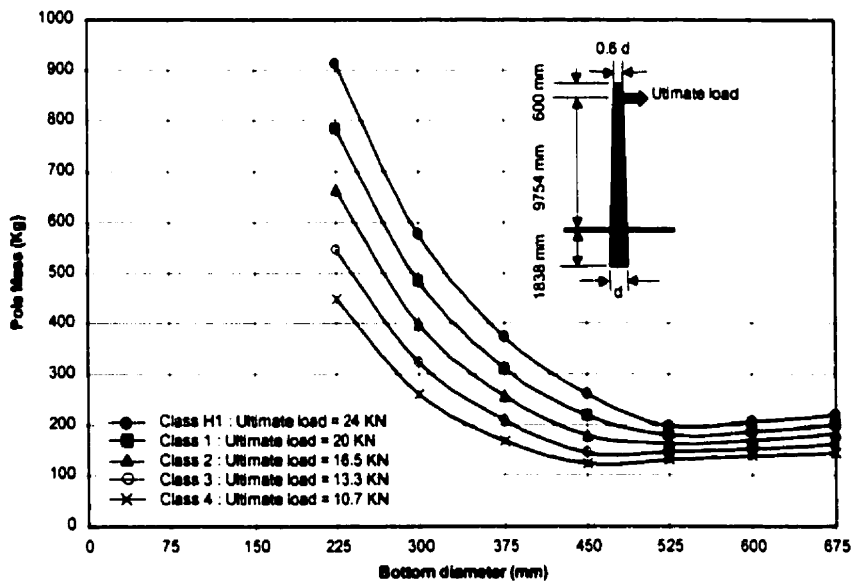
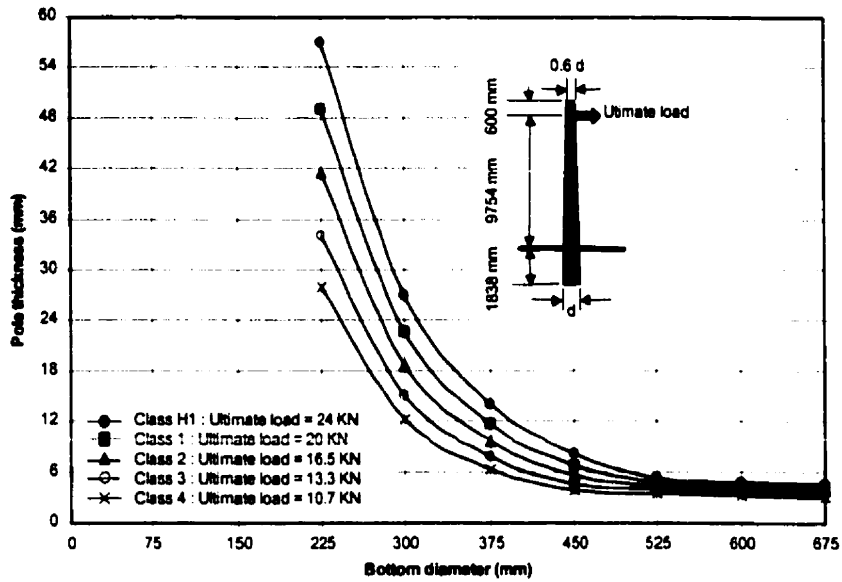


Figure (6-41): Design charts for 12.2 m GFRP poles (strength and deflection criteria)

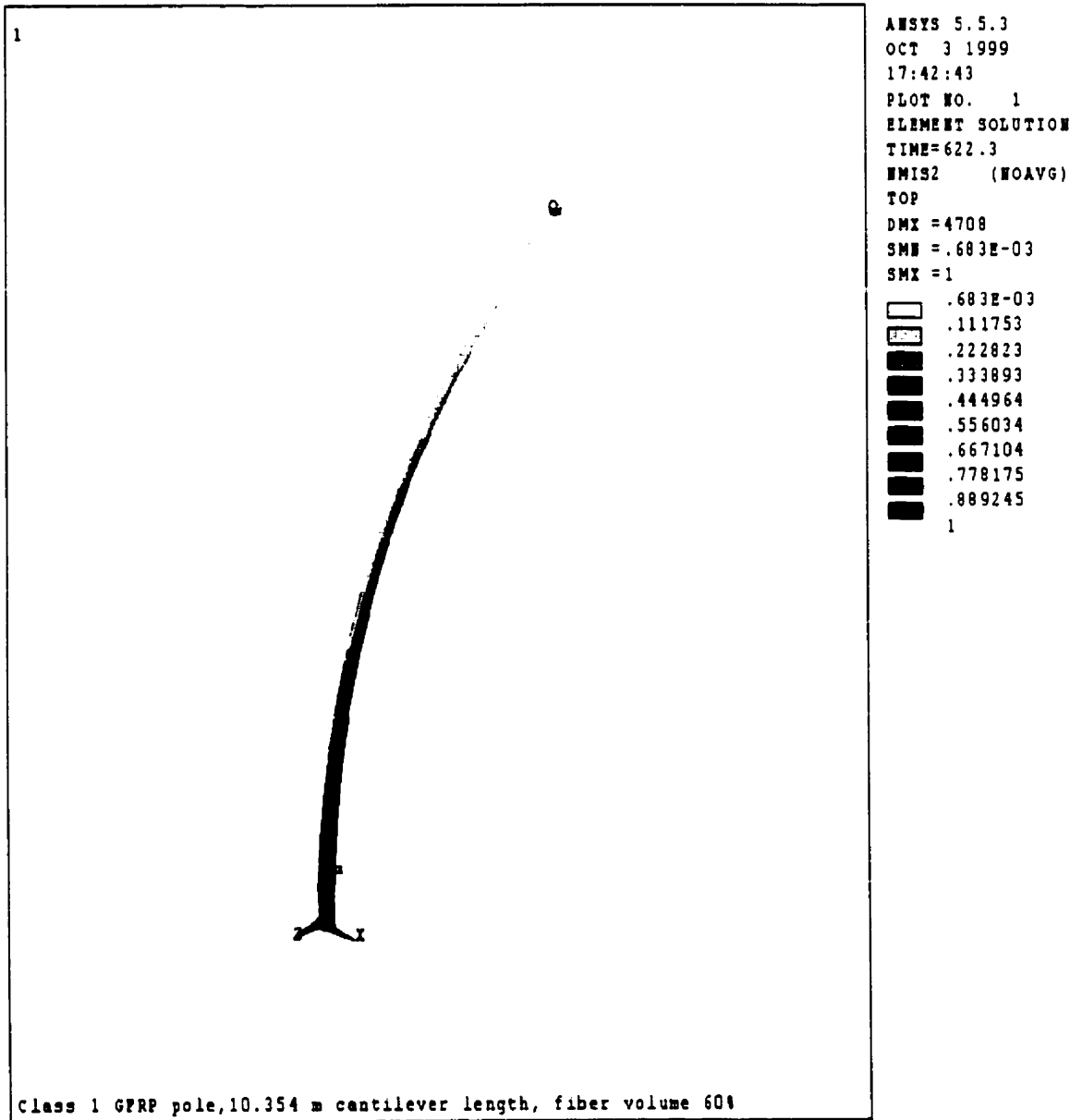


Figure (6-42): Compression side failure mode for a 12.2 m class 1 GFRP pole with bottom diameter 225 mm

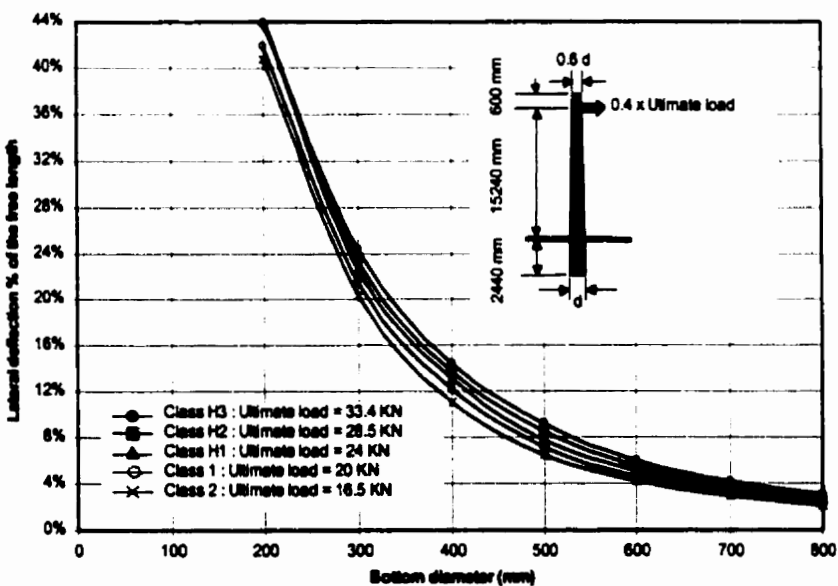
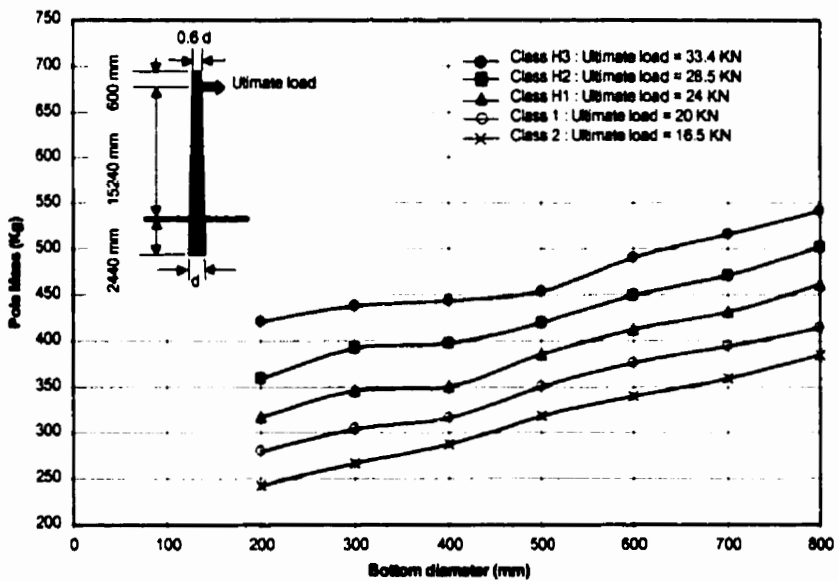
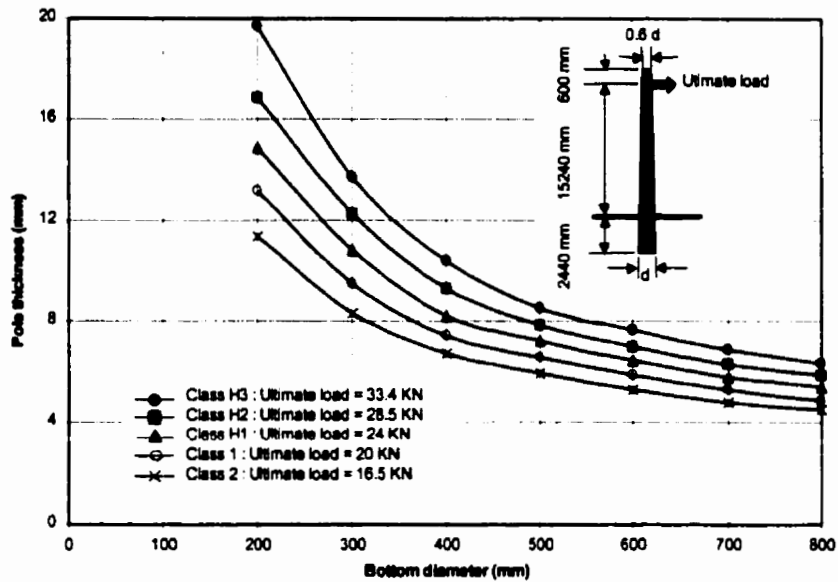


Figure (6-43): Design charts for 18.3 m GFRP poles (strength criterion)

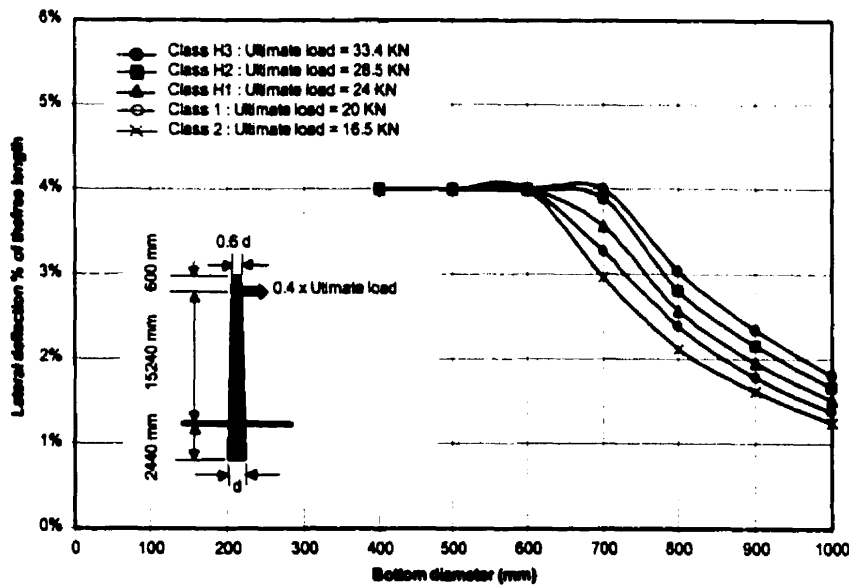
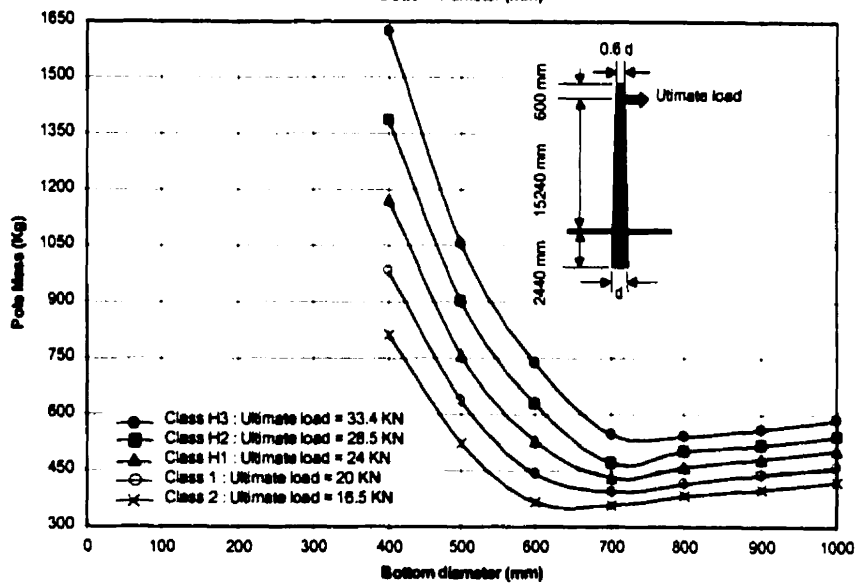
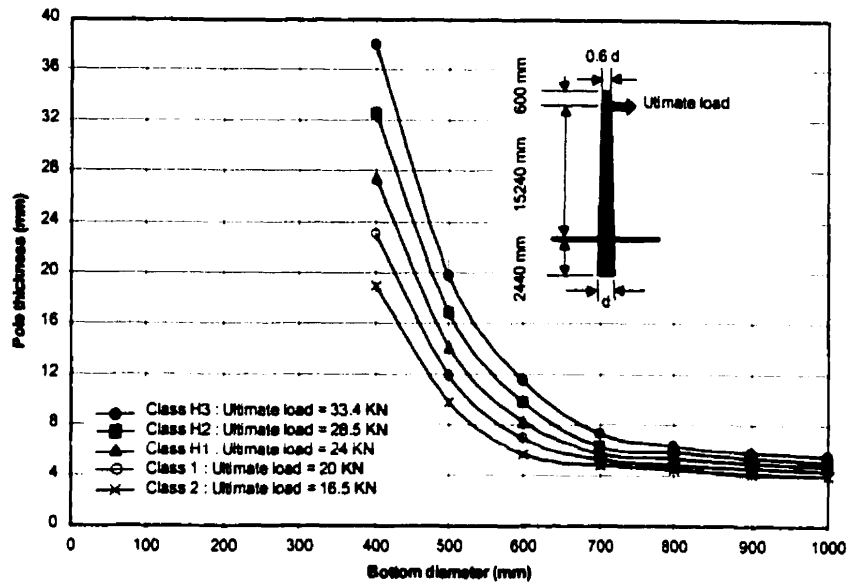


Figure (6-44): Design charts for 18.3 m GFRP poles (strength and deflection criteria)

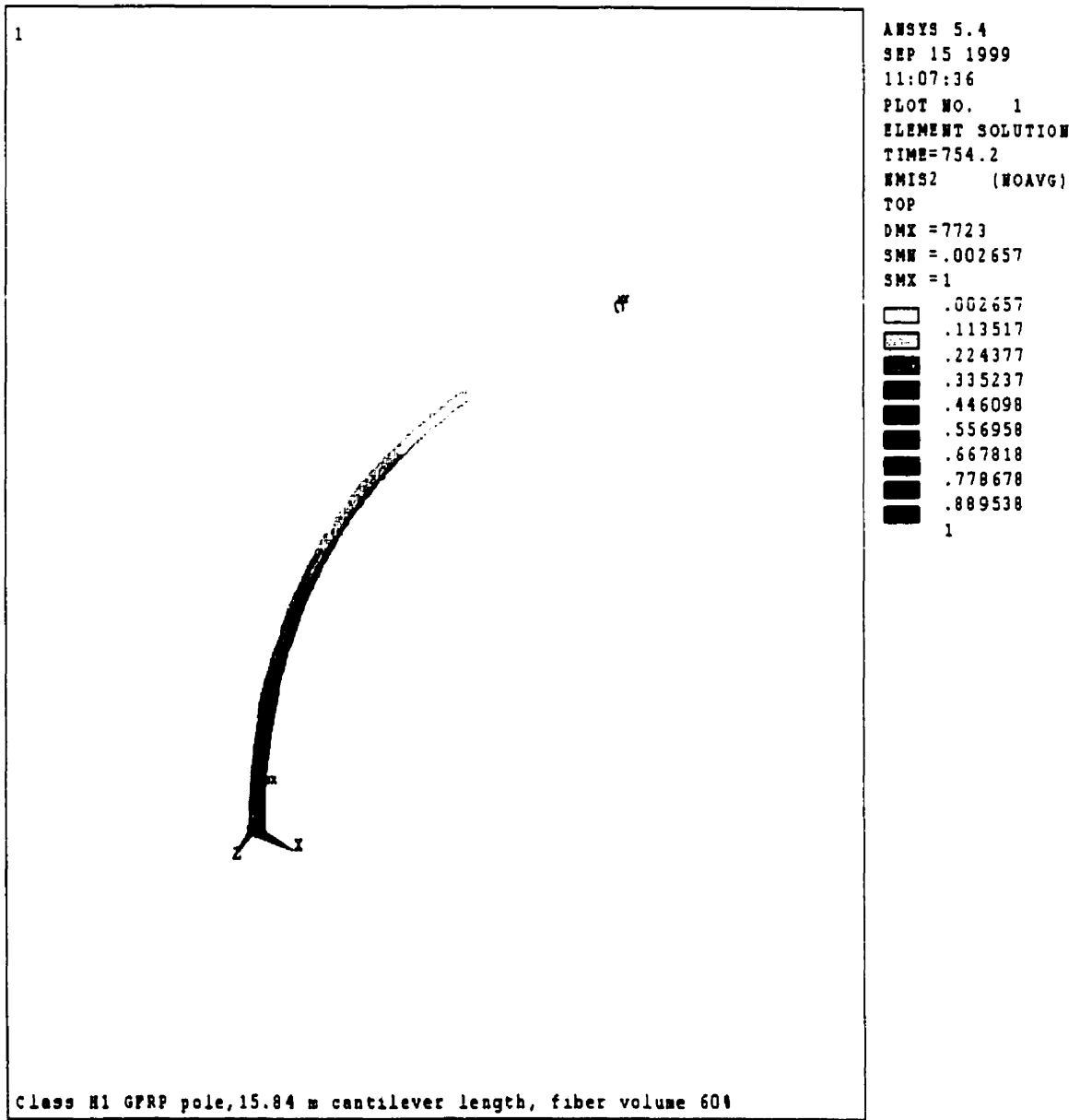


Figure (6-45): Compression side failure mode for a 18.3 m class H1 GFRP pole with bottom diameter 300 mm

CHAPTER 7

SIMPLIFIED FINITE ELEMENT METHOD FOR DYNAMIC ANALYSIS OF TAPERED GFRP POLES

7.1 INTRODUCTION

This chapter presents a simple finite element formulation for the dynamic analysis of tapered GFRP poles with hollow circular cross-section. Many studies have been conducted on the dynamic behavior of thin-walled sections made from steel as well as composite materials, but only a few on tapered sections (Polyzois et al. 1998). In fact, the vast majority of studies are concerned with the dynamic behavior of steel members (homogeneous and isotropic material). Composite cross-sections are usually thin-walled and the wall is treated in this study as a laminated plate that can be orthotropic or generally orthotropic. Transmission poles are mainly subjected to cantilever bending since loading due to the wires and wind gusts is applied laterally. In the present analysis, the poles were modeled with tapered beam elements. It was assumed that the behavior was linearly elastic and the material was orthotropic or anisotropic. Shear effects were accounted for in the analysis because of their significant role. Modal analysis was performed to obtain the natural frequency and period of poles with various lengths and geometry, and the results are compared to commercially available finite element codes. The analytical results presented herein were based on typical GFRP poles produced by filament winding.

7.2 EQUIVALENT MATERIAL PROPERTIES

Composite cross-sections are usually thin-walled and are produced with various cross-sectional dimensions. In the present case, the filament winding technique was employed to produce a tapered pole with circular hollow cross-section. A typical geometry of such a pole is shown in Figure (7-1a). The wall consists of an even number of layers with $[\pm\theta/-\theta]$ orientation angle with respect to the longitudinal direction forming an antisymmetric angle-ply laminate. Each layer had a thickness 0.22 mm and a constant volume fraction $v_f=65\%$ was assumed. The stacking sequence of a 4-layered laminate is shown in Figure (7-1b). The properties of the material under study, as computed from information provided by the material suppliers, were $E_1= 48$ GPa, $E_2=13.30$ GPa, $\nu_{12}=0.235$ and $G_{12} = 5.17$ GPa, where 1 denotes the fiber direction and 2 the transverse direction. Using the classical lamination theory (Tsai, 1989), the stiffness components of a generally orthotropic plate can be determined. The constitutive equation for the laminate is

$$\begin{Bmatrix} N \\ M \end{Bmatrix} = \begin{bmatrix} A & B \\ B & D \end{bmatrix} \begin{Bmatrix} \varepsilon \\ \kappa \end{Bmatrix} \quad (7-1)$$

where, N and M are the stress resultants and stress couples; $\{\varepsilon\}$ and $\{\kappa\}$ are the strains and the curvatures; and, the stiffness coefficients A_{ij} , B_{ij} , and D_{ij} correspond to membrane, coupling, and bending stiffness coefficient and are defined as follows:

$$A_{ij} = \int_{-t/2}^{t/2} \bar{Q}_{ij} dz \quad (7-2)$$

$$B_{ij} = \int_{-t/2}^{t/2} z \bar{Q}_{ij} dz \quad (7-3)$$

$$D_{ij} = \int_{-t/2}^{t/2} z^2 \bar{Q}_{ij} dz \quad (7-4)$$

where, t is the laminate thickness and \bar{Q}_{ij} are the transformed layer stiffness components.

The terms \bar{Q}_{ij} for various values of lamination angle θ are listed in Table (7- 1).

Table (7- 1): Stiffness components \bar{Q}_{ij} as function of $\pm\theta$.

| $\pm\theta$ (degrees) | \bar{Q}_{11} (GPa) | \bar{Q}_{22} (GPa) | \bar{Q}_{12} (GPa) | \bar{Q}_{66} (GPa) | \bar{Q}_{16} (GPa) | \bar{Q}_{26} (GPa) |
|--------------------------|-------------------------|-------------------------|-------------------------|-------------------------|-------------------------|-------------------------|
| 0 | 48.75 | 13.51 | 3.17 | 5.17 | 0 | 0 |
| 5 | 48.21 | 13.51 | 3.44 | 5.44 | ± 3.04 | ± 0.02 |
| 10 | 46.65 | 13.54 | 4.20 | 6.20 | ± 5.84 | ± 0.18 |
| 15 | 44.18 | 13.67 | 5.38 | 7.37 | ± 8.22 | ± 0.59 |
| 20 | 40.98 | 13.99 | 6.81 | 8.81 | ± 10.00 | ± 1.33 |
| 25 | 37.28 | 14.63 | 8.34 | 10.34 | ± 11.09 | ± 2.41 |
| 30 | 33.33 | 15.71 | 9.78 | 11.78 | ± 11.44 | ± 3.82 |

In case of angle ply laminate ($\pm\theta$), all the terms B_{ij} will be equal to zero except B_{16} , and B_{26} .

Inverting Equation (7-1) we obtain

$$\begin{Bmatrix} \epsilon_x \\ \epsilon_y \\ \gamma_{xy} \\ \kappa_x \\ \kappa_y \\ \kappa_{xy} \end{Bmatrix} = \begin{bmatrix} a_{11} & a_{12} & a_{13} & b_{11} & b_{12} & b_{13} \\ a_{21} & a_{22} & a_{23} & b_{21} & b_{22} & b_{23} \\ a_{31} & a_{32} & a_{33} & b_{31} & b_{32} & b_{33} \\ b_{11} & b_{12} & b_{13} & d_{11} & d_{12} & d_{13} \\ b_{21} & b_{22} & b_{23} & d_{21} & d_{22} & d_{23} \\ b_{31} & b_{32} & b_{33} & d_{31} & d_{32} & d_{33} \end{bmatrix} \begin{Bmatrix} N_x \\ N_y \\ N_{xy} \\ M_x \\ M_y \\ M_{xy} \end{Bmatrix} \quad (7-5)$$

Although the shear-extension coupling terms A_{16} and A_{26} in Equation (7-2) vanish in antisymmetric laminates, the term a_{11} in Equation (7-5) includes the shear effect due to layer stiffness transformation. The terms a_{13} and a_{23} are also zero in this case. The effective longitudinal modulus $E_{x\text{eff}}$ can be calculated from Equation (7-5) as:

$$E_{x\text{eff}} = \frac{1}{a_{11}t} \quad (7-6)$$

Since the cross-section is thin-walled, the effective longitudinal modulus $E_{x\text{eff}}$ can be used for the axial as well as the flexural problem without loss of material characteristics that affect the structural behavior of the member. The effective longitudinal modulus $E_{x\text{eff}}$ for various cases of lamination angle $\pm\theta$ and total thickness t is listed in Table (7- 2).

**Table (7- 2): Effective longitudinal modulus E_{eff} (GPa) for various number of layers
(N)**

| $\pm\theta$ | E_{eff} (GPa) | | | | |
|-------------|------------------------|-------|-------|-------|-------|
| | N=2 | N= 4 | N=10 | N=20 | N=50 |
| 0 | 48.00 | 48.00 | 48.00 | 48.00 | 48.00 |
| 5 | 46.07 | 47.02 | 47.29 | 47.32 | 47.33 |
| 10 | 41.29 | 44.34 | 45.19 | 45.31 | 45.34 |
| 15 | 35.56 | 40.45 | 41.81 | 42.00 | 42.06 |
| 20 | 30.14 | 35.80 | 37.37 | 37.59 | 37.66 |
| 25 | 25.48 | 30.81 | 32.26 | 32.46 | 32.52 |
| 30 | 21.68 | 25.92 | 27.04 | 27.19 | 27.24 |
| 35 | 18.67 | 21.58 | 22.32 | 22.42 | 22.45 |
| 40 | 16.41 | 18.13 | 18.54 | 18.60 | 18.61 |
| 45 | 14.79 | 15.66 | 15.85 | 15.88 | 15.89 |

7.3 FINITE ELEMENT FORMULATION

In order to approximate the static and dynamic behavior of the tapered column, a beam finite element was developed for analyzing tapered sections. The tapered beam with a length L and a circular hollow cross-section of uniform thickness t shown in

Figure (7-2) was assumed. The radii at the small and the large end were R_1 and R_2 , respectively. Since the cross-section was thin-walled, the cross-sectional area and moment of inertia were computed as $A=2\pi R t$ and $I=\pi R^3 t$, respectively. The radius R was assumed to vary linearly over the length. This implied a linear variation of the area A and a cubic variation of the moment of inertia I with respect to the length L . Thus, it was convenient to adopt a coordinate system x - y , shown in Figure (7-2a), in which the area and moment of inertia were expressed as follows:

$$A = A_0 x \quad (7-7)$$

$$I = I_0 x^3 \quad (7-8)$$

The shift α of the origin of the coordinate system was defined geometrically, since $R_2/R_1=(L+\alpha)/\alpha$, as follows:

$$\alpha = \frac{L}{R_2/R_1 - 1} \quad (7-9)$$

where, A_0 and I_0 are coefficients defined below:

$$A_0 = 2\pi \left(\frac{R_1}{\alpha} \right) t \quad (7-10)$$

and,

$$I_0 = \pi \left(\frac{R_1}{\alpha} \right)^3 t \quad (7-11)$$

The equation of motion for flexural free vibrations of the tapered beam was expressed as (Warburton, 1976)

$$\rho A \frac{\partial^2 v}{\partial t^2} + \frac{\partial^2}{\partial x^2} \left(E_{\text{eff}} I \frac{\partial^2 v}{\partial x^2} \right) = 0 \quad (7-12)$$

where, ρ is the mass density of the composite material, and E_{eff} is the effective longitudinal modulus. In view of Equations (7-7) and (7-8), Equation (7-12) are

$$\rho A_0 x \frac{\partial^2 v}{\partial t^2} + \frac{\partial^2}{\partial x^2} \left(E_{\text{eff}} I_0 x^3 \frac{\partial^2 v}{\partial x^2} \right) = 0 \quad (7-13)$$

The shape functions resulting from the solution of the static equilibrium equation was used; that is,

$$-\frac{\partial^2}{\partial x^2} \left[E_{\text{eff}} I_0 x^3 \frac{\partial v^2}{\partial x^2} \right] = 0 \quad (7-14)$$

The general solution of the above equation is

$$v(x) = c_1 x + c_2 \ln x + c_3 \frac{1}{x} + c_4 \quad (7-15)$$

or in a matrix form,

$$v(x) = \left\{ x \quad \ln x \quad \frac{1}{x} \quad 1 \right\} \begin{Bmatrix} c_1 \\ c_2 \\ c_3 \\ c_4 \end{Bmatrix} = \{ \mathbf{g}_r \}^T \{ \mathbf{c}_r \} \quad (7-16)$$

where, subscript f is related to flexure. The coefficients $c_{r,i}$ ($i=1,2,3,4$) are related to the nodal displacements as follows:

$$\begin{Bmatrix} v_1 \\ \theta_1 \\ v_2 \\ \theta_2 \end{Bmatrix} = \begin{bmatrix} \alpha & \ln \alpha & \frac{1}{\alpha} & 1 \\ 1 & \frac{1}{\alpha} & -\frac{1}{\alpha^2} & 0 \\ \alpha + L & \ln(\alpha + L) & \frac{1}{\alpha + L} & 1 \\ 1 & \frac{1}{\alpha + L} & -\frac{1}{(\alpha + L)^2} & 0 \end{bmatrix} \begin{Bmatrix} c_1 \\ c_2 \\ c_3 \\ c_4 \end{Bmatrix}_r \quad (7-17a)$$

or in a concise form

$$\{v\} = [N_r] \{c_r\} \quad (7-17b)$$

Inverting Equation (7-17) and using Equation (7-16), the deflection $v(x)$ was expressed with respect to the nodal displacements as follows:

$$v(x) = \{g_r\}^T [N_r]^{-1} \{v\} = \{g_r\}^T [B_r] \{v\} \quad (7-18)$$

From Equation (7-13),

$$v'' = \{g_r^*\}^T \{c_r\} = \{g_r^*\}^T [B_r] \{v\} \quad (7-19)$$

where,

$$\{g_r^*\}^T = \left\{ 0 \quad -\frac{1}{x^2} \quad \frac{2}{x^3} \quad 0 \right\}^T \quad (7-20)$$

The strain energy W of the element was expressed as,

$$\begin{aligned}
W &= \frac{1}{2} \int_{\alpha}^{\alpha+L} E_{\text{eff}} I \left(\frac{\partial^2 v}{\partial x^2} \right)^2 dx \\
&= \frac{1}{2} \{v\}^T [B_r]^T \left[\int_{\alpha}^{\alpha+L} \{g_r^*\}^T (E_{\text{eff}} I_0 x^3) \{g_r^*\} dx \right] [B_r] \{v\}
\end{aligned} \tag{7-21}$$

Thus, the element stiffness matrix $[k_r]$ is

$$[k_r] = [B_r]^T \left[\int_{\alpha}^{\alpha+L} \{g_r^*\}^T (E_{\text{eff}} I_0 x^3) \{g_r^*\} dx \right] [B_r] = [B_r]^T [\bar{k}_r] [B_r] \tag{7-22}$$

where $[\bar{k}_r]$ is given by

$$[\bar{k}_r] = EI_0 \begin{bmatrix} 0 & 0 & 0 & 0 \\ 0 & \ln(\alpha+L) - \ln \alpha & \frac{2}{\alpha+L} - \frac{2}{\alpha} & 0 \\ 0 & \frac{2}{\alpha+L} - \frac{2}{\alpha} & \frac{2}{\alpha^2} - \frac{2}{(\alpha+L)^2} & 0 \\ 0 & 0 & 0 & 0 \end{bmatrix} \tag{7-23}$$

The kinetic energy T of the element is

$$T = \frac{1}{2} \int_{\alpha}^{\alpha+L} \rho A \left(\frac{\partial v}{\partial t} \right)^2 dx = \frac{1}{2} \{\dot{v}\}^T [B_r]^T \left[\int_{\alpha}^{\alpha+L} \{g_r^*\}^T (\rho A_0 x) \{g_r^*\} dx \right] [B_r] \{\dot{v}\} \tag{7-24}$$

and the mass matrix $[m_r]$ is

$$[m_r] = [B_r]^T \left[\int_{\alpha}^{\alpha+L} \{g_r^*\}^T (\rho A_0 x) \{g_r^*\} dx \right] [B_r] = [B_r]^T [\bar{m}_r] [B_r] \tag{7-25}$$

where, the terms of $[\bar{m}_r]$ are given in explicit form as

$$\bar{m}_{r,11} = \frac{1}{4} \rho A_0 \{(\alpha+L)^4 - \alpha^4\} \tag{7-26a}$$

$$\bar{m}_{r,12} = \frac{1}{9} \rho A_0 \{(\alpha + L)^3 (3 \ln(\alpha + L) - 1) - \alpha^3 (3 \ln \alpha - 1)\} \quad (7-26b)$$

$$\bar{m}_{r,13} = \frac{1}{2} \rho A_0 \{(\alpha + L)^2 - \alpha^2\} \quad (7-26c)$$

$$\bar{m}_{r,14} = \frac{1}{3} \rho A_0 \{(\alpha + L)^3 - \alpha^3\} \quad (7-26d)$$

$$\bar{m}_{r,22} = \frac{1}{4} \rho A_0 \{(\alpha + L)^2 (2 \ln^2(\alpha + L) - 2 \ln(\alpha + L) + 1) - \alpha^2 (2 \ln^2 \alpha - 2 \ln \alpha + 1)\} \quad (7-26e)$$

$$\bar{m}_{r,23} = \rho A_0 \{(\alpha + L)(\ln(\alpha + L) - 1) - \alpha(\ln \alpha - 1)\} \quad (7-26f)$$

$$\bar{m}_{r,24} = \frac{1}{4} \rho A_0 \{(\alpha + L)^2 (2 \ln(\alpha + L) - 1) - \alpha^2 (2 \ln \alpha - 1)\} \quad (7-26g)$$

$$\bar{m}_{r,33} = \rho A_0 \{\ln(\alpha + L) - \ln \alpha\} \quad (7-26h)$$

$$\bar{m}_{r,34} = \rho A_0 L \quad (7-26i)$$

$$\bar{m}_{r,33} = \frac{1}{2} \rho A_0 \{(\alpha + L)^2 - \alpha^2\} \quad (7-26j)$$

A similar procedure can be followed for the case of axial vibration of the tapered beam.

The equation of motion for axial free vibrations is (Timoshenko et al., 1974)

$$\rho A \frac{\partial^2 u}{\partial t^2} - \frac{\partial}{\partial x} \left(E_{\text{eff}} A \frac{\partial u}{\partial x} \right) = 0 \quad (7-27)$$

where, u is the axial displacement. In view of Equation (7-7), Equation (7-27) becomes

$$\rho A_0 x \frac{\partial^2 u}{\partial t^2} - \frac{\partial}{\partial x} \left(E_{\text{eff}} A_0 x \frac{\partial u}{\partial x} \right) = 0 \quad (7-28)$$

For the axial case, we will use the shape functions resulting from the solution of the static equilibrium equation, that is

$$\frac{\partial}{\partial x} \left[E_{\text{eff}} A_0 x \frac{\partial u}{\partial x} \right] = 0 \quad (7-29)$$

The general solution of Equation (7-29) is

$$u(x) = c_1 + c_2 \ln x \quad (7-30)$$

or in a matrix form

$$u(x) = \{1 \quad \ln x\} \begin{Bmatrix} c_1 \\ c_2 \end{Bmatrix} = \{\mathbf{g}_a\}^T \{\mathbf{c}_a\} \quad (7-31)$$

where, subscript a now stands for axial deformation. The coefficients $c_{a,i}$ ($i=1,2$) are in this case related to the nodal displacements as follows:

$$\begin{Bmatrix} u_1 \\ u_2 \end{Bmatrix} = \begin{bmatrix} 1 & \ln \alpha \\ 1 & \ln(\alpha + L) \end{bmatrix} \begin{Bmatrix} c_1 \\ c_2 \end{Bmatrix}_a \quad (7-32a)$$

that is

$$\{\mathbf{u}\} = [\mathbf{N}_a] \{\mathbf{c}_a\} \quad (7-32b)$$

Inverting Equation (7-32) and using Equation (7-31), the axial deflection $u(x)$ with respect to the nodal displacements can be expressed as follows:

$$\mathbf{u}(x) = \{\mathbf{g}_s\}^T [\mathbf{N}_s]^{-1} \{\mathbf{u}\} = \{\mathbf{g}_s\}^T [\mathbf{B}_s] \{\mathbf{u}\} \quad (7-33)$$

From Equation (7-33) we obtain

$$\mathbf{u}' = \{\mathbf{g}'_s\}^T \{\mathbf{c}_s\} = \{\mathbf{g}'_s\}^T [\mathbf{B}_s] \{\mathbf{u}\} \quad (7-34)$$

where,

$$\{\mathbf{g}'_s\}^T = \left\{ 0 \quad \frac{1}{x} \right\} \quad (7-35)$$

The strain energy W of the element is

$$\begin{aligned} W &= \frac{1}{2} \int_{\alpha}^{\alpha+L} E_{\text{eff}} A \left(\frac{\partial u}{\partial x} \right)^2 dx \\ &= \frac{1}{2} \{\mathbf{u}\}^T [\mathbf{B}_s]^T \left[\int_{\alpha}^{\alpha+L} \{\mathbf{g}'_s\}^T (E_{\text{eff}} A_0 x) \{\mathbf{g}'_s\} dx \right] [\mathbf{B}_s] \{\mathbf{u}\} \end{aligned} \quad (7-36)$$

Thus, the element stiffness matrix $[\mathbf{k}_s]$ is

$$[\mathbf{k}_s] = [\mathbf{B}_s]^T \left[\int_{\alpha}^{\alpha+L} \{\mathbf{g}'_s\}^T (E_{\text{eff}} A_0 x) \{\mathbf{g}'_s\} dx \right] [\mathbf{B}_s] = [\mathbf{B}_s]^T [\bar{\mathbf{k}}_s] [\mathbf{B}_s] \quad (7-37)$$

where, $[\bar{\mathbf{k}}_s]$ is given by

$$[\bar{\mathbf{k}}_s] = E_{\text{eff}} A_0 \begin{bmatrix} 0 & 0 \\ 0 & \ln(\alpha + L) - \ln \alpha \end{bmatrix} \quad (7-38)$$

The kinetic energy T of the element is

$$\mathbf{T} = \frac{1}{2} \int_{\alpha}^{\alpha+L} \rho A(x) \left(\frac{\partial \mathbf{u}}{\partial t} \right)^2 dx = \frac{1}{2} \{\dot{\mathbf{u}}\}^T [\mathbf{B}_s]^T \left[\int_{\alpha}^{\alpha+L} \{\mathbf{g}_s\}^T (\rho A_0 x) \{\mathbf{g}_s\} dx \right] [\mathbf{B}_s] \{\dot{\mathbf{u}}\} \quad (7-39)$$

and the mass matrix $[\mathbf{m}_s]$ is

$$[\mathbf{m}_s] = [\mathbf{B}_s]^T \left[\int_{\alpha}^{\alpha+L} \{\mathbf{g}_s\}^T (\rho A_0 x) \{\mathbf{g}_s\} dx \right] [\mathbf{B}_s] = [\mathbf{B}_s]^T [\bar{\mathbf{m}}_s] [\mathbf{B}_s] \quad (7-40)$$

where the terms of $[\bar{\mathbf{m}}_s]$ are given in explicit form as

$$\bar{m}_{s,11} = \frac{1}{2} \rho A_0 \{(\alpha + L)^2 - \alpha^2\} \quad (7-41a)$$

$$\bar{m}_{s,12} = \frac{1}{4} \rho A_0 \{(\alpha + L)^2 (2 \ln(\alpha + L) - 1) - \alpha^2 (2 \ln \alpha - 1)\} \quad (7-41b)$$

$$\bar{m}_{s,22} = \frac{1}{4} \rho A_0 \{(\alpha + L)^2 (2 \ln^2(\alpha + L) - 2 \ln(\alpha + L) + 1) - \alpha^2 (2 \ln^2 \alpha - 2 \ln \alpha + 1)\} \quad (7-41c)$$

Thus, the equilibrium equation for the tapered element in matrix terms can be written as follows:

$$[\mathbf{m}] \{\ddot{\delta}\} + [\mathbf{k}] \{\delta\} = \{\mathbf{f}\} \quad (7-42)$$

where, $\{\mathbf{f}\}$ is the nodal force vector and $\{\delta\}$ is the nodal displacement vector, that is

$$\{\delta\}^T = \{u_1 \quad v_1 \quad \phi_1 \quad u_2 \quad v_2 \quad \phi_2\}^T \quad (7-43)$$

It should be pointed out that the axial vibrations are uncoupled from flexural vibrations. This is true only for the present case because the cross-section is thin-walled and doubly symmetric and hence bending-extension coupling vanishes.

7.4 NUMERICAL RESULTS AND DISCUSSION

The tapered beam element developed herein was employed to perform modal analysis of poles with various geometric characteristics. For the cases considered in the analysis, a material density $\gamma = 1.94 \text{ gm/cm}^3$ and $N=50$ layers were used. The total thickness of the pole was assumed to be $t=11 \text{ mm}$. The numerical results were first validated through a convergence study. A pole with lamination angle $\theta = \pm 15^\circ$ and ratio $d_2/d_1 = 0.5$ was modeled with the tapered element developed in this study and the prismatic hollow beam element given in Appendix B. Moreover, a detailed model of the pole was analyzed with 3-D shell elements using the ANSYS finite element program (ANSYS, 1995). The natural frequency ω of the fundamental flexural vibration mode was plotted as a function of the number of elements used in the discretization for both tapered and prismatic elements in Figure (7-3). The numerical values for both models are listed in Table (7- 3).

Table (7-3): Convergence study for tapered and prismatic element models

| Number of elements | Tapered element | | | Prismatic element | | |
|--------------------|-----------------------|------------|------------|-----------------------|------------|------------|
| | ω (rad/sec) | T (sec) | Error % | ω (rad/sec) | T (sec) | Error % |
| 2 | 11.583 | 0.542 | 0.16 | 10.467 | 0.600 | 10.49 |
| 3 | 11.569 | 0.543 | 0.03 | 11.052 | 0.569 | 4.64 |
| 4 | 11.566 | 0.543 | 0 | 11.270 | 0.569 | 2.62 |
| 5 | 11.565 | 0.543 | 0 | 11.374 | 0.558 | 1.68 |
| 6 | 11.565 | 0.543 | 0 | 11.432 | 0.552 | 1.16 |
| 7 | 11.565 | 0.543 | 0 | 11.467 | 0.550 | 0.85 |
| 8 | 11.565 | 0.543 | 0 | 11.490 | 0.548 | 0.65 |
| 9 | 11.565 | 0.543 | 0 | 11.505 | 0.547 | 0.52 |
| 10 | 11.565 | 0.543 | 0 | 11.517 | 0.546 | 0.41 |

A rapid convergence was observed when a model with tapered elements was used, where the fundamental frequency $\omega=11.565$ rad/sec was obtained using only three elements with an error 0.03%, while the convergence was relatively slower when prismatic elements were employed. The rate of convergence was not affected by the ratio d_2/d_1 when the pole was modeled with tapered elements and this provides a significant advantage when using the proposed element. The fundamental frequency ω of the pole

modeled with 2400 shell element was obtained using ANSYS code and it was found to be equal to 11.654 rad/sec. The difference in the frequency ω between the beam and shell models was 0.77%, and was very negligible. The natural frequency and period of the fundamental model was computed for various values of the lamination angle $\pm\theta$ and the ratio d_2/d_1 . The results are listed in Table (7- 4).

Table (7-4): Natural frequency and period for various values of lamination angle

| Lamination angle $\pm\theta$ | $d_2/d_1 = 1$ | | $d_2/d_1 = 0.75$ | | $d_2/d_1 = 0.5$ | |
|---------------------------------|-----------------------|------------|-----------------------|------------|-----------------------|------------|
| | ω (rad/sec) | T (sec) | ω (rad/sec) | T (sec) | ω (rad/sec) | T (sec) |
| 0 | 11.359 | 0.553 | 11.748 | 0.535 | 12.354 | 0.508 |
| 5 | 11.280 | 0.557 | 11.666 | 0.538 | 12.268 | 0.512 |
| 10 | 11.041 | 0.569 | 11.418 | 0.550 | 12.008 | 0.523 |
| 15 | 10.634 | 0.591 | 10.998 | 0.571 | 11.565 | 0.543 |
| 20 | 10.063 | 0.624 | 10.407 | 0.604 | 10.944 | 0.574 |
| 25 | 9.351 | 0.672 | 9.671 | 0.650 | 10.170 | 0.618 |
| 30 | 8.558 | 0.734 | 8.851 | 0.710 | 9.308 | 0.675 |
| 35 | 7.769 | 0.809 | 8.035 | 0.782 | 8.450 | 0.743 |
| 40 | 7.074 | 0.888 | 7.316 | 0.859 | 7.694 | 0.817 |
| 45 | 6.535 | 0.961 | 6.759 | 0.929 | 7.108 | 0.884 |

The laminate used had total thickness $t = 11$ mm. The results showed that the lower the ratio d_2/d_1 , the higher the fundamental frequency ω is, as indicated in Figure (7-4). In addition, the fundamental frequency is directly proportional to the effective modulus E_{eff} and, hence, there is a significant drop in the natural frequency when the lamination angle θ , exceeds 10° . The fundamental period T is expected to be in the range of 0.5 to 0.6 sec for GFRP poles with a lamination angle $\pm\theta = 10^\circ$. The fundamental frequency of thin wall sections is not affected by the thickness t because the area and the moment of inertia vary linearly with respect to thickness, as indicated in Equations (7-10) and (7-11). A significant parameter that affects the dynamic behavior of transmission poles is the presence of cross-arms that are installed at the top to hold the wires and any possible transformer equipment. These devices were modeled as a concentrated mass M placed at the free end of the pole. A parametric study was performed to examine the effect of a mass M located at the tip of the pole. The mass of the pole M_p was assumed to be 541 kg. The natural frequency and the period of the fundamental model of the pole were computed for various values of the lamination angle $\pm\theta$ and the mass ratio M/M_p . The results are plotted in Figure (7-5). The results showed that the higher the mass ratio M/M_p , the lower the fundamental frequency ω is. Also, the fundamental frequency of the pole increased as the mass ratio M/M_p decreased. This effect is shown in Figure (7-6), where the natural frequency of a pole with $\pm\theta = 10^\circ$ and $d_2/d_1 = 0.5$ was plotted as a function of the mass ratio M/M_p . The results showed a significant reduction of the natural frequency ω in the presence of the mass M at the top of the pole.

7.5 CONCLUSIONS

A simple finite element formulation for the dynamic analysis of tapered composite poles with hollow circular cross-section is presented. The tapered beam presented herein is employed to perform modal analysis of tapered composite poles used in transmission lines. High degree of accuracy is obtained with small number elements in the mesh. The natural frequency and period of the fundamental flexural vibration mode of the column are computed for various cases of lamination angle, taper ratio, and mass at the top. The tapered element presented in this study is valid for cross section with any taper ratio as well as cross-section made from conventional materials. It can be easily extended to perform time-history analysis using numerical integration schemes, e.g. Newmark's- β method.

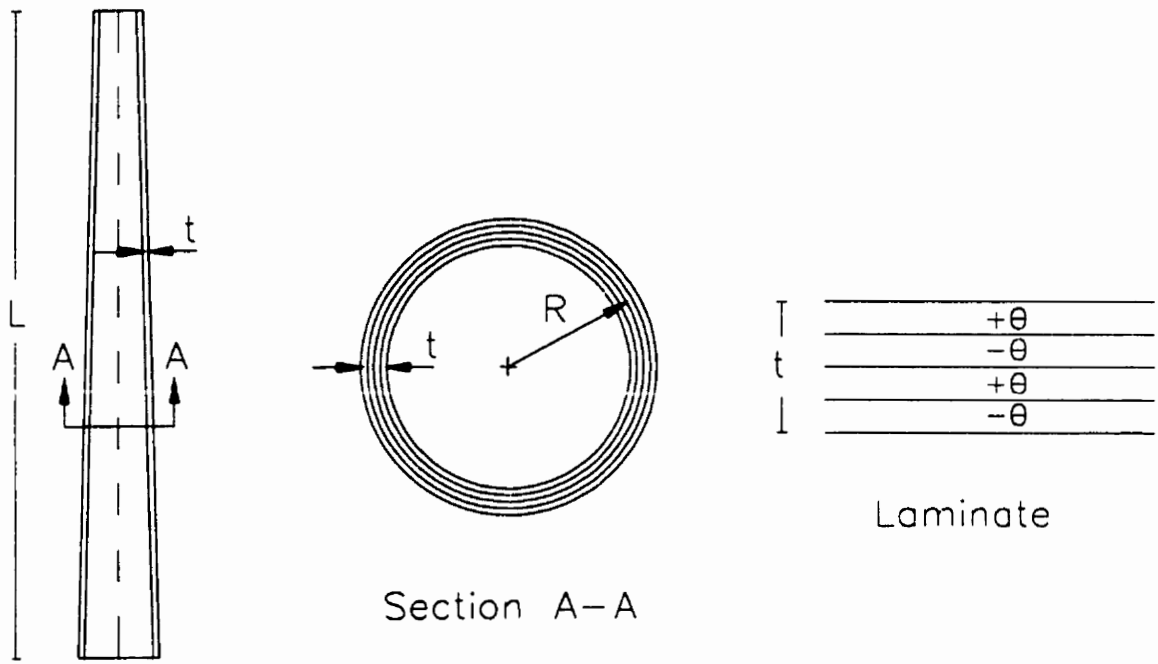


Figure (7-1): Geometry and lay-up of composite tapered pole

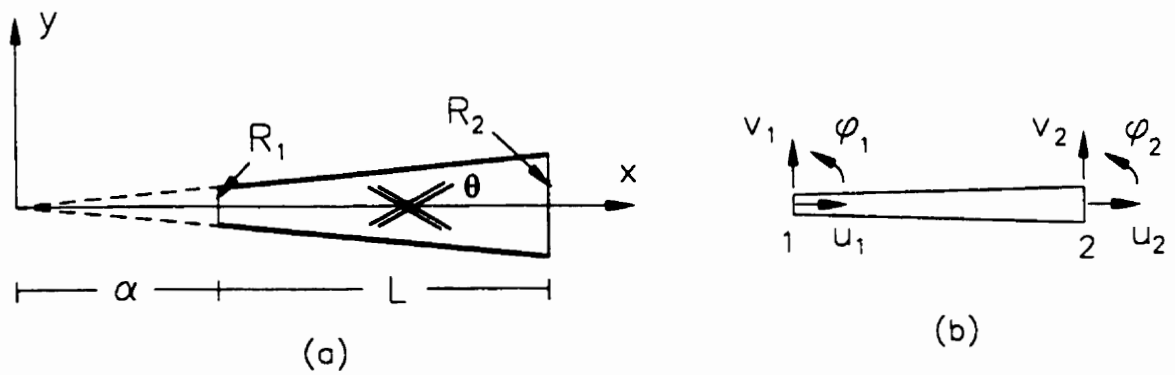


Figure (7-2): (a) Coordinate system, (b) Tapered element and degrees-of-freedom

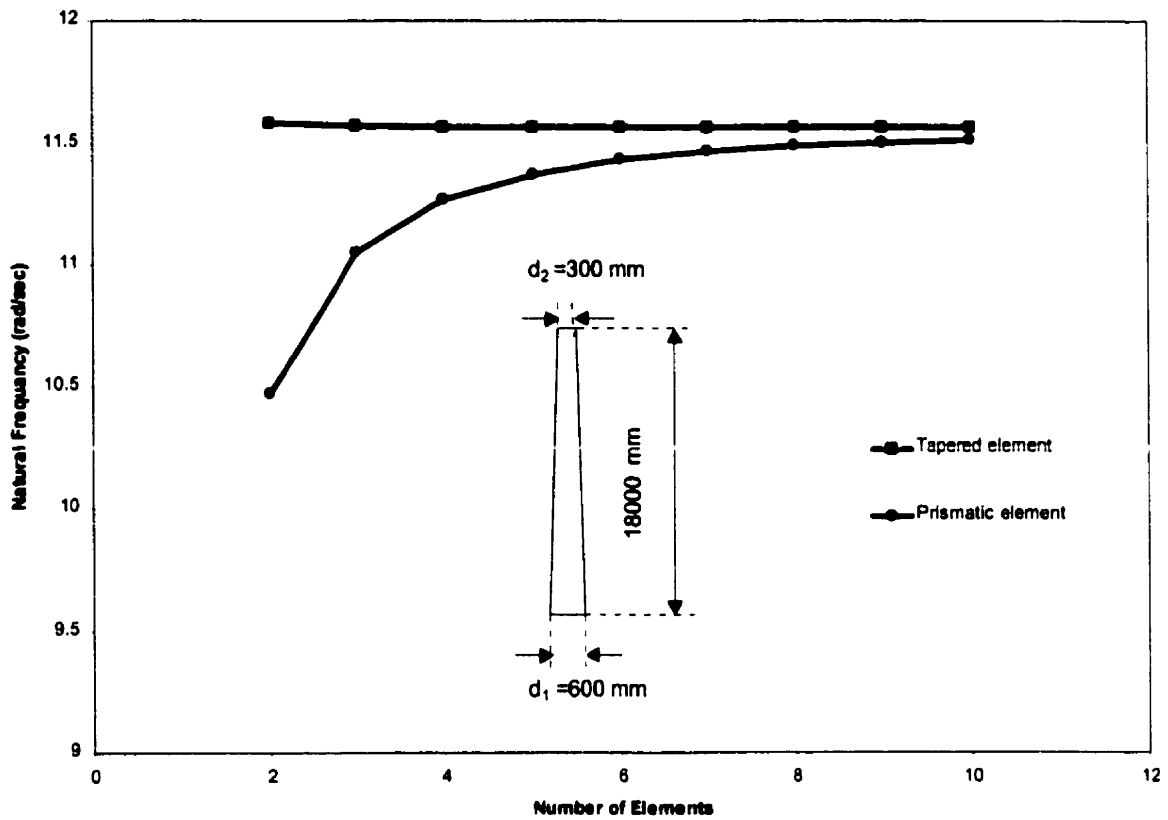


Figure (7-3): Convergence study for the tapered and prismatic beam elements

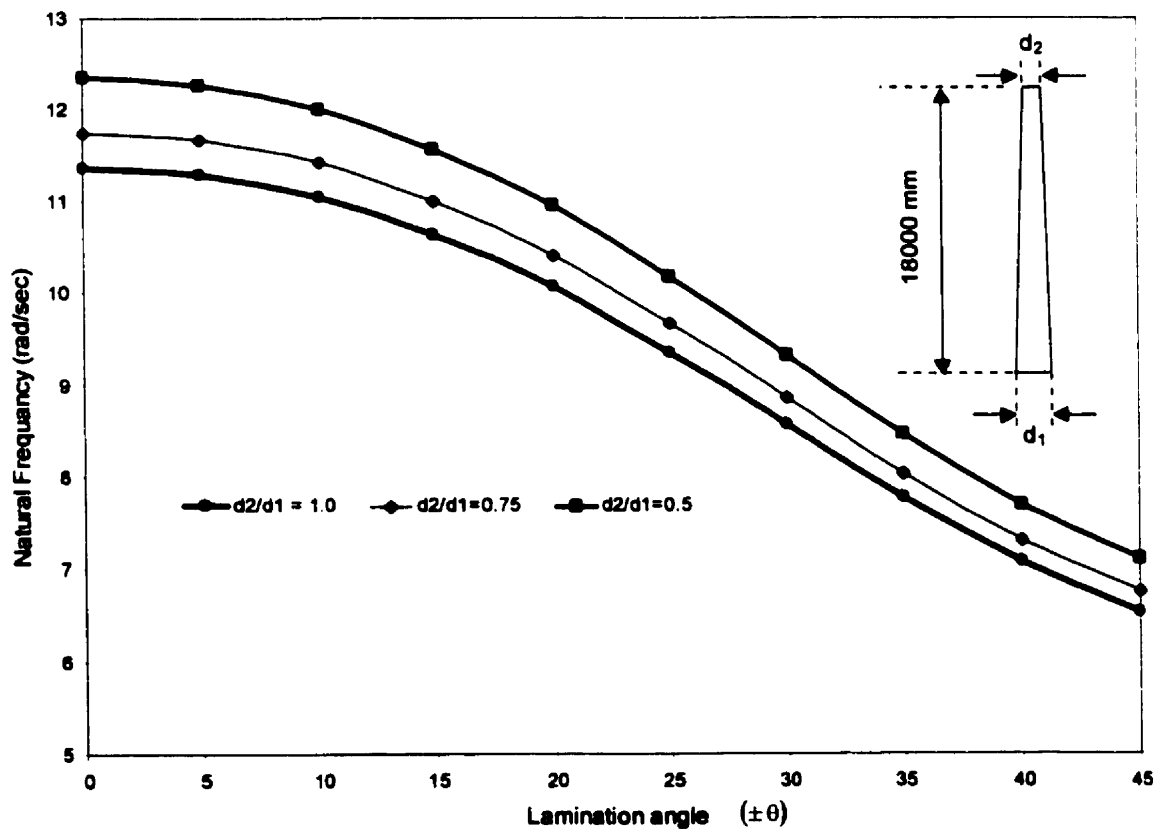


Figure (7-4): Natural frequency for various taper ratios and lamination angles

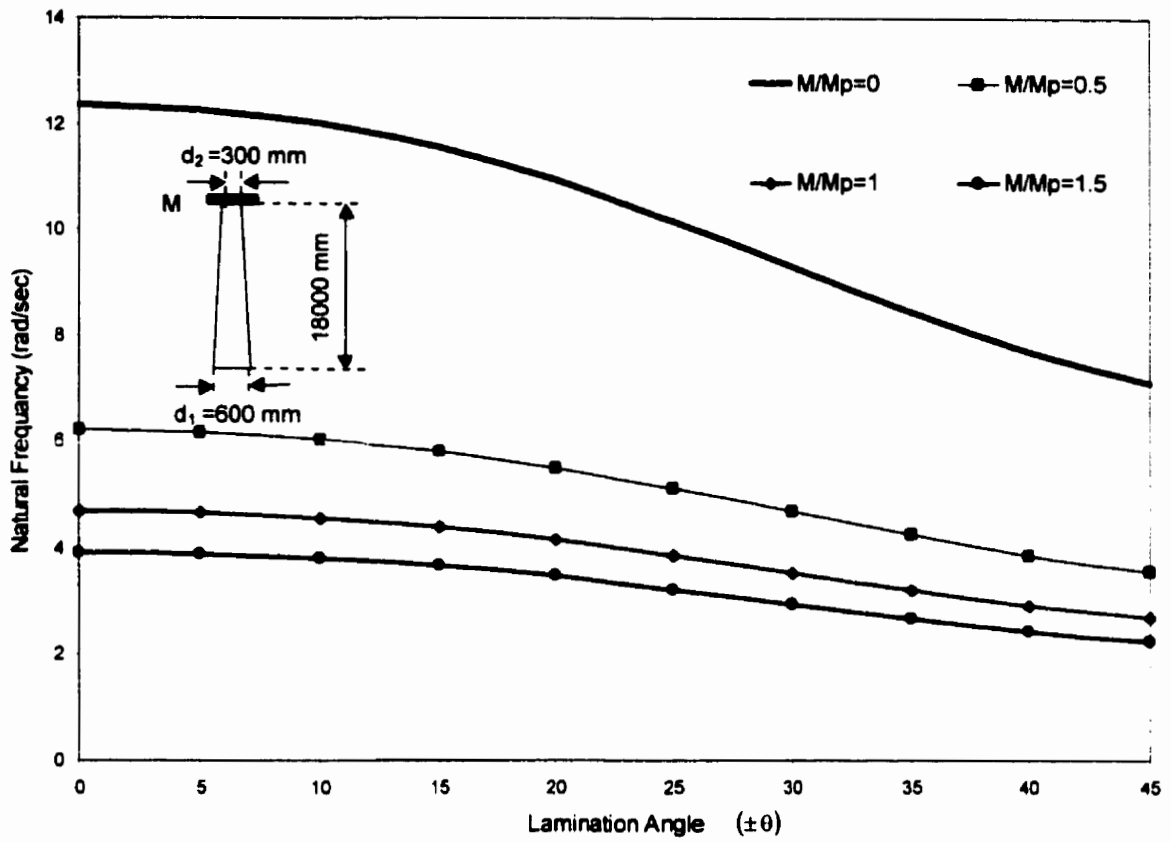


Figure (7-5): Natural frequency for various mass ratios and lamination angles

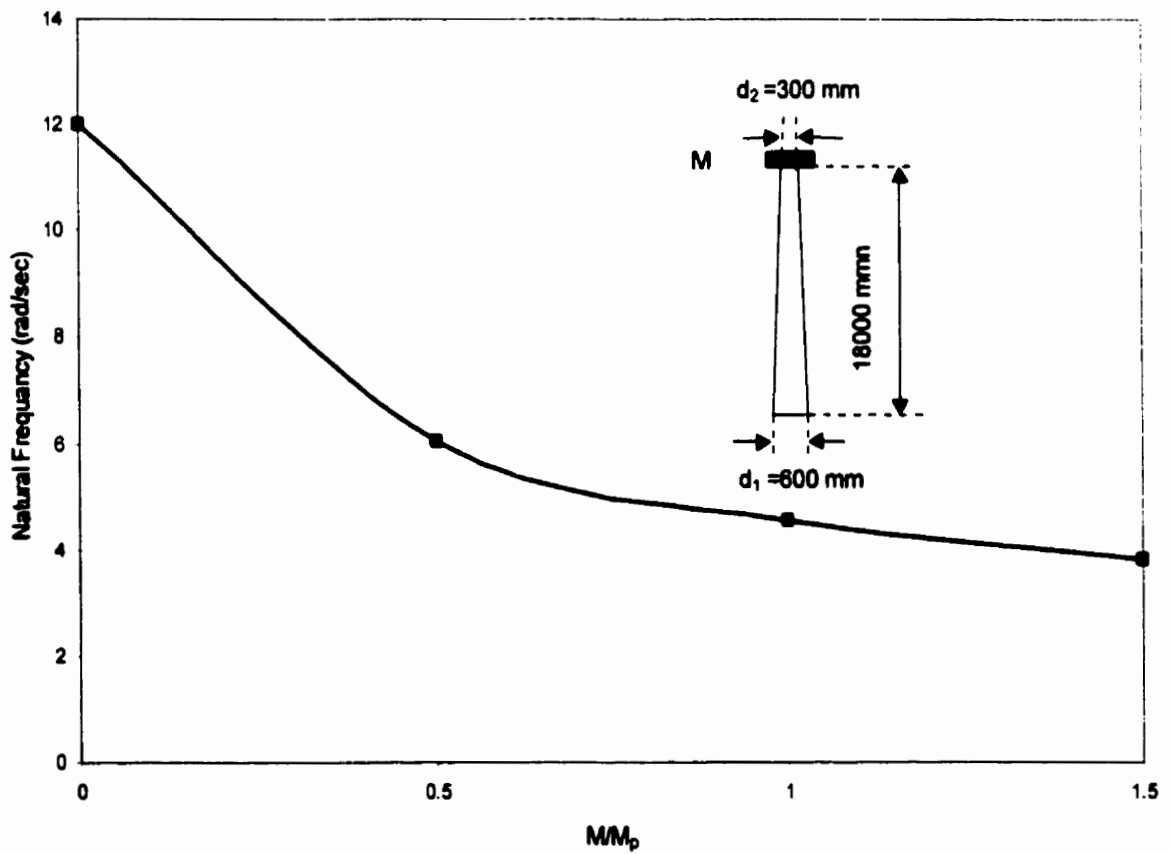


Figure (7-6): Natural frequency as a function of the mass ratio for $d_2/d_1 = 0.5$

CHAPTER 8

SUMMARY, CONCLUSIONS, AND RECOMMENDATIONS FOR FUTURE WORK

Experimental and theoretical studies were conducted to evaluate the structural performance of GFRP poles for use in transmission lines. The poles were fabricated at the ISIS–Faroex Filament Winding Facility in Gimli, Manitoba, using the filament winding process. Glass fibers (1100 TEX) and polyester resin were utilized to wind the all the GFRP pole specimens. The experimental program included testing of twelve scaled (2.5 m) and twelve full-scale specimens (6.1 m). The parametric variations used in this program included the wind angle, number of layers, wall–thickness, and fiber lay–up sequence. The specimens were tested to failure according to current standard governing the use of wooden poles. The experimental data included failure loads, displacements, changes in cross–section, and strains at various locations along the span. In the theoretical component of the study involved both rational and numerical methods were employed to analyze and simulate the behavior of the tested specimens. The theory of minimum strain energy along with the classical lamination theory were adopted to develop a nonlinear analytical model capable of predicting failure of GFRP poles by local buckling. In addition, the ANSYS finite element program was used to obtain a more accurate description of the behavior of GFRP poles. Layered composite shell elements were in this finite element analysis. The effect of large deformations and cross–section distortion were also included in a nonlinear geometric analysis. The ultimate capacity of

the specimens tested was determined using both the analytical model and the finite element analysis. Both methods yielded results that were in very good correlation with the experimental results. Once the finite element analysis was verified through comparison with the experimental results, it was used to conduct an extensive parametric study to determine the influence of other parameters, such as fiber lay-up and cross-section dimensions, on the behavior of a series of GFRP poles. Through this parametric study a complete set of design charts was produced for various lengths of GFRP poles and a wide range of classes of distribution and transmission line poles. A simplified finite element formulation for the dynamic analysis of GFRP poles was also presented in this study. Modal analysis was performed to calculate the natural frequency of GFRP with various geometry. Comparison between results from this dynamic analysis and results from the ANSYS finite element program showed an excellent correlation. Although the results from dynamic analysis were not verified through testing, it is hoped that such testing may be the focus of future work on GFRP poles.

Based on the results of both the experimental and the theoretical investigations performed in this study a number of conclusion are drawn. These are listed below in point form.

- 1) **Glass Fiber-Reinforced Plastic (GFRP) poles are excellent candidates as replacement of traditional poles in transmission lines. GFRP poles can be designed for the same load carrying capacity as wooden, concrete, or steel poles but weighing considerably less.**

- 2) The load carrying capacity-to-mass ratio of scaled poles was 0.145 kN/kg, 52% higher than wooden poles with equivalent strength. The lateral displacement of those specimens at ultimate loads varied from 11% to 18% of the free height.
- 3) The load carrying capacity-to-mass ratio of the full-scale specimens was 0.47 kN/kg. This was as much as 500% higher than wooden poles with equivalent strength. The lateral displacement of full-scale specimens at ultimate load did not exceed 13% of the free length of the specimen.
- 4) The highest load carrying capacity-to-mass ratio was achieved in specimens that incorporated circumferential fibers along with longitudinal fibers.
- 5) The stiffness of GFRP poles wound with both circumferential fibers and longitudinal fibers was, approximately, 20% smaller than that of poles having longitudinal fibers only, although both types of poles had the same number of layers. Moreover, the load carrying capacity of GFRP poles having circumferential fibers was 22% higher than similar GFRP poles with longitudinal fibers only.
- 6) Three different failure modes were observed in the scaled specimens. The first failure mode was characterized by local buckling of the specimen on the compression side. Specimens with a radius-to-thickness ratio (R/t) equal to 57 failed in this manner. The second failure mode involved a diagonal fracture parallel to the fiber direction on the compression side due to in-plane shear stress and transversely to the fiber stress. Specimens with R/t ratio equal to 40 failed this way. The third failure mode involved fractured fibers on the tension side of the poles due to transverse fiber pull-out. Specimens with R/t ratio equal to 23 failed this way.

- 7) Ten of the full-scale specimens failed by local buckling as the R/t ratio for those specimens varied from 42 to 75. One specimen failed prematurely and one that had only longitudinal fibers and no circumferencial fibers failed on the compression side with the formation of diagonal crack parallel to the fiber direction.
- 8) The linear load–deflection relationship of the scaled specimens was linear up to 70% of the ultimate load. At higher load levels a nonlinear behavior was observed due to progressive failure of the matrix.
- 9) Ovalization, or sectional distortion was evident in both scaled and the full-scale specimens. The load–ovalization relationship was high non–linear. It, thus, became important to include this s nonlinear behavior in the analysis of GFRP poles.
- 10) A nonlinear analytical model which accounts for the ovalization of the cross section was developed to predict the critical local buckling load of GFRP poles. The results obtained from this model were in very good agreement with the experimental results. The average ratio of the experimental–to–theoretical failure load was 0.85 with a standard deviation less than 10%.
- 11) The finite element program ANSYS was used to perform a nonlinear numerical analysis of GFRP poles. This program accounts for the nonlinear behavior of the poles and includes a strength failure check by applying the Tsai-Wu failure criterion. Both scaled and full-scale specimens were analyzed by the finite element method. The results were in an excellent agreement with the experimental results. The average ratio of the experimental–totheoretical failure load was 0.99 with a standard deviation of 12%.

- 12) The parametric study showed that an optimum mass of GFRP poles is achieved when the ratio of circumferential-to-total number of layers is 2/8 and the longitudinal fibers are as close to 0^0 as possible.
- 13) The parametric study also showed that the optimum diameter for 6.1 m GFRP poles when both strength and serviceability criteria are included in the analysis varies from 300 mm to 350 mm depending on the pole class. For 12.2 m and 18.3 m GFRP poles the optimum diameter varies from 450 mm to 525 mm and from 600 mm to 700 mm, respectively, again depending on the class of the pole.
- 14) The simplified finite element model which was also developed for the dynamic analysis of GFRP poles produced results for the natural frequency which were in excellent agreement with the results obtained from the ANSYS finite element program.
- 15) The dynamic analysis showed that the fundamental frequency of GFRP poles is not affected by the variation in the wall thickness. but is affected by the longitudinal fiber angle. The natural frequency is inversely proportional to the longitudinal fiber angle. For an 18 m GFRP pole with a 600 mm bottom diameter, the natural frequency was 11 rad/sec.
- 16) The dynamic analysis also showed that the fundamental frequency of GFRP poles decreased as the concentrated mass mounted on the top of the poles was increased.

The research work for the development of GFRP poles at the University of Manitoba was the most extensive of kind ever conducted. A number of major achievements were accomplished towards the development of GFRP for transmission poles. More work in related areas, however, must still be conducted in order to make this product commercially viable. A number of research areas are suggested here to broaden the understanding of the behavior of GFRP poles. Areas which need further study include:

- 1) Investigation of the behavior of GFRP poles under the combined effect of axial and lateral loads.
- 2) Investigation of various types of joints between pole segments; between cross-arms and poles; and between poles and concrete foundations.
- 3) Experimental investigation of the effect of cyclic loading on the strength of GFRP poles.
- 4) Evaluation of various foundation designs including, in the case of direct burial, the optimum embedment length.
- 5) Evaluation of serviceability factors, such as climbability, repair, replacement; etc.
- 6) Evaluation of the effect of ultraviolet light and fire on the long term performance of GFRP poles.

A number of these areas are already being investigated by colleagues at the University of Manitoba.

REFERENCES

- Adams, R. D. (1987). "Damping Properties Analysis of Composites" in T. J. Reinhart et al. (Editors), *ASM International, Materials Park, OH, Engineering Materials Handbook, Volume 1, Composites*, pp. 206-217.
- Agarwal, B. D., and Broutman, L. J. (1990). *Analysis and Performance of Fiber Composites*, 2nd Edition, John Wiley & Sons, Inc., New York.
- Ahmad, S., Irons, B. M., and Zienkiewicz, O. C. (1970). "Analysis of Thick and Thin Structures by Curved Finite Elements" *International Journal of Numerical Methods in Engineering*, Vol. 2, pp. 419-451.
- ANSI O5.1 (1992). *American National Standard for Wood Poles – Specifications and Dimension*, American National Standard Institute, New York, U.S.A.
- Azzi, V. D., and Tsai, S. W. (1965). "Anisotropic Strength of Composites" *Proceeding of the Society for Experimental Stress Analysis*, XXII (2), pp.283-288.
- Brazier, L. G. (1927). "On the Flexure of Thin Cylindrical Shells and other Thin Sections" *proceedings of the Royal Society, Series A*, Vol. CXVI, pp. 104-114.
- Calladine, C. R. (1983). *Theory of Shell Structures*, Cambridge Univ. Press, Cambridge, England, UK.
- CAN/CSA-O15-90 (1990). *Wood Utility Poles and Reinforcing Stubs Forest Products*, Canadian Standards Association, Ontario, Canada.
- Chao, W., and Reddy, J. N. (1984). "Analysis of Laminated Composite Shells Using a Degenerated Three Dimensional Element" *International Journal of Numerical Methods in Engineering*, Vol. 20, pp. 1991-2007.

- Cheng, S., and Ho, B. P. C. (1963). "Stability of Heterogeneous Anisotropic Cylindrical Shells under Combined Loading" *AIAA Journal*, Vol. 1, No. 4 pp. 893-898.
- D 3039-76 (1990). *Standard Test Method for Tensile Properties of Fiber-Resin Composites*, ASTM Standards and Literature References for Composite Materials, 2nd edition, American Society for Testing and Materials, Philadelphia, PA.
- Derrick, G. L. (1996). "Fiberglass Composite Distribution and Transmission Poles" *Manufactured Distribution and Transmission Pole Structures Workshop Proceeding*, July 25-26, Electric Power Research Institute, pp. 55-61.
- Design of Steel Transmission Pole Structures (1990). *ASCE Manual and Reports on Engineering Practice No. 72*, American Society of Civil Engineering, New York, U.S.A.
- Dong, S. B., Pister, K. S., and Taylor, R. L. (1962). "On the Theory of Laminated Anisotropic Shells and Plates" *Journal of Aerospace Science*, Vol.29, No. 8, pp. 969-975.
- Escher, G. A. (1982). "Design and Testing of an Optimum Fiberglass Reinforced Pole and Market Study on the Demand for Utility Poles in Canada" *Project 77-52A* prepared for ABCO Plastics, Nova Scotia, Canada, July 12, 65 pp.
- Fabian, O. (1977) "Collapse of Cylindrical Elastic Tubes under Combined Bending, Pressure and Axial Loads" *International Journal of Solids and Structures*, Vol. 13, pp. 1257-1270.
- Fried, I. (1973). "Shear in C^0 and C^1 bending finite elements" *International Journal of Solid Structures*, Vol. 9, pp. 449-460.
- Gibson, R. F. (1995). *Principle of Composite Materials Mechanics*, McGraw-Hill, Inc.

- Gould, P. L., and Basu, P. K (1977). "Geometric Stiffness Matrices for the Finite Element Analysis of Rotation; Shells" *Journal of Structures Mechanics*, Vol. 5, No. 2, pp. 87-105.
- Hashin, Z. (1980). "Failure Criteria for Unidirectional Fiber Composites" *Journal of Applied Mechanics*, Vol 47, pp. 329-334.
- Hill, R. (1948). "A Theory of the Yielding and Plastic Flow of Anisotropic Metals" *Proceeding of the Royal Society of London, Series A*, 193, pp. 281-297.
- Hoffman, O. (1967). "The Brittle Strength of Orthotropic Materials" *Journal of Composite Materials*, Vol. 1, pp.200-206.
- Holston, A. (1968). "Buckling of Filament Wound Cylinders by Axial Compression" *AIAA Journal*, Vol. 6, No. 5, pp. 935-936.
- Hutchinson, J. W. (1968). "Buckling and initial Postbuckling Behavior of Oval Cylindrical Shells" *Journal of Applied Mechanics*, Vol. 35, pp. 66-72.
- Ibrahim, S., and Polyzois, D. (1999). "Ovalization Analysis of Fiber-Reinforced Plastics Poles" *Composite Structures* Vol. 45, No. 1, pp. 7-12.
- Ibrahim, S., Hassan, S. K., and Polyzois, D. (1999a) "Experimental Investigation of Full-Scale Fiber-Reinforced Plastic Tapered Poles under Lateral Loading" *Proceedings of the Sixth International Conference on Composites Engineering (ICCE/6)*, pp. 345-346, June 27- July 3, Orlando, Florida
- Ibrahim, S., Polyzois, D., and Hassan, S. K. (1999b). "Development of Glass Fiber-Reinforced Plastic Poles for Transmission and Distribution Lines" *The Canadian Journal of Civil Engineering*, accepted for publication on October 18, 1999, number of pages submitted: 25.

- Irons, B. M. (1970). "A frontal Solution Program for Finite Element Analysis" International journal of Numerical Methods in Engineering, Vol. 2, No. 1, pp. 5-23.**
- Jenkins, C. F. (1920). "Report on Materials of Construction Used in Aircraft and Aircraft Engines" Great Britain Aeronautical Research Committee.**
- Jeusette, J. P., and Laschet, G. (1990). "Pre- and Postbuckling Finite Element Analysis of Curved Composite and Sandwich Panels" AIAA Journal, Vol. 28, No. 7, pp. 1233-1239.**
- Jones, R. M., and Morgan, H. S. (1975). "Buckling and Vibration of Cross ply Laminated Circular Cylindrical Shells" AIAA Journal, Vol. 13, No. 5, pp. 664-671.**
- Jun, S. M. and Hong, C. S. (1988). "Buckling Behavior of Laminated Composite Cylindrical Panels under Axial Compression" Computers & Structures, Vol.29, No. 3 pp. 479-490.**
- Keward, K. T. (1978). "Nonlinear Collapse of Thin-Walled Composite Cylinders under Flexural Loading" Proceedings of the Second International Conference on Composite Materials (ICCM2), Toronto, Canada, pp. 353-365.**
- Labossiere, P., and Turkkan, N. (1992). "Optimization of composite materials with genetic algorithms and neural networks" Advanced composite materials in bridges and structures, Canadian Society of Civil Engineering, , pp.659-668.**
- Li, L. Y. (1995). "Bending Instability of Composite Tubes" Journal of Aerospace Engineering, Vol. 9, No. 9, pp. 58-61.**
- Libai, A., and Bert, C. W. (1994). "A Mixed Variational Principal and Its Application to the Nonlinear Bending Problem of Orthotropic Tubes-I. Development of General Theory and Reduction to Cylindrical Shells" International Journal of Solids and Structures, Vol. 31, No. 7, pp. 1003-1018.**

- Lin, Z. M. (1995). "Analysis of Pole-Type Structures of Fibre-Reinforced Plastics by Finite Element Method" Ph.D. Thesis, University of Manitoba, Canada.**
- Martin, J. D., and Richter, C. S. (1974). "A Marketing Approach to the Development of the RP/C lighting Pole Market" 29th Annual Technical Conference, 1974, Reinforced Plastics/Composite Institute, The Society of the Plastics Industry, Inc., section 3-A, pp. 1-5.**
- McClure, G., Boire, L., and Carriere, J. C. (1992). "Applications of Advanced Composite Materials in Overhead Power Lines and Telecommunications Structures" Advanced Composite in Bridges and Structures, K.W. Neale and P. Labossiere, editors, Canadian Society of Civil Engineering, pp.543-549.**
- Miller, M. F. (1994). "Fiberglass Distribution Poles: A Case of Study" IEEE 13th Annual PES T&D conference and Expo 8 pp.**
- Mufti, A. A., Erki, M. A., and Jaeger, L. G. (1991). "Advanced Composite Materials With Application to Bridges", State of the Art Report, Canadian Society of Civil Engineering, CSCE, pp. 350-361.**
- Mufti, A. A., Erki, M. A., and Jaeger, L. G. (1992). "Advanced Composite Materials With Application in Bridges and Structures In Japan", Task Force Report, Canadian Society of Civil Engineering, CSCE, pp. 171-182.**
- Munro, M. (1988). "Review of Manufacturing of Fiber Composite Components by Filament Winding" Polymer Composites, Vol. 9, No. 5.**
- Murphy, J. (1998) *Reinforced Plastics Handbook*, Second Edition, Elsevier Advanced Technolgy.**
- National Electrical Safety Code (NESC) (1997). The Institute of Electric and Electronics Engineering, Inc., New York, U.S.A.**

- Navaratna, D. R., Pian, T. H. H., and Wittmer, E. A. (1968). "Stability Analysis of Shell of Revolution by the Finite Element Method" *AIAA Journal*, Vol. 6, No. 2, pp. 355-360.
- Neilsen, L. E. (1974). *Mechanical Properties of Polymers and Composites*, Vol. 2, Marcel Dekker, New York.
- Noor, A. K., and Mathers, M. D. (1974). "Nonlinear Finite Element Analysis of Laminated Composite Shells" *Computational Methods in Nonlinear Mechanics*, J.T. Oden, E.B. Becker, R.R. Craig, R.S. Dunham, C.P. Jonshon and W.L. Oberkampf, editors, Proceeding of International Conference on Computational Methods in Nonlinear Mechanics, Austin, Texas.
- Noor, A. K., burton, W. S., and Peters, J. M. (1991). "Assessment of Computational Models for Multilayered Composite Cylinders" *International Journal of Solids Structures*, Vol. 27, No. 10 pp.1269-1286.
- Panda, S., and Natarajan, R. (1981). "Analysis of Laminated Composite Shell Structures by Finite Element Method" *Composite Structures*, Vol. 14, pp. 225-230.
- Polyzois, D., Ibrahim, S., and Raftoyiannis, I. G. (1999) "Performance of Fiber-Reinforced Plastic Tapered Poles under Lateral Loading" *Journal of Composite Materials*, Vol. 33, No. 10, pp.941-960.
- Polyzois, D., Raftoyiannis, I. G., and Ibrahim, S. (1998). " Finite Element Method for the Dynamic Analysis of Tapered Composite Poles" *Composite Structures*, Vol. 43, No. 1, pp. 25-34.
- Reddy, J. N. (1981). "A Finite Element Analysis of Large Deflection Bending of Laminated Anisotropic Shells" *Nonlinear Finite Element Analysis of Plates and Shells*, T.J.R. Hughes, A. Pifko, and A. Jay, editors, AMD-48, ASME, pp. 249-263.

- Reddy, J. N. (1984). "Exact Solutions of Moderately Thick Laminated Shells" Journal of Engineering Mechanics, Vol. 110, No. 5, pp.794-809.**
- Reissner, E. (1959). "On Finite Bending of Pressurized Tubes" Journal of Applied Mechanics, Vol. 26, pp.386-392.**
- Saadatmanesh, L. J., and Ehsani, M. R. (1994). "Seismic Retrofit of Existing Reinforced Concrete Column by Glass-Fiber Composites", Proceeding of the Third material Engineering Conference ASCE, pp. 758-763.**
- Saigal, S., Kapania, R. K., and Yang, T. Y. (1986). "Geometrically Nonlinear Finite Element Analysis of Imperfect Laminated Shells" Journal of Composite Materials, Vol. 20, March, pp. 197-214.**
- Seide, P., and Weingarten, V. I. (1961). "On the buckling of Circular Cylindrical Shells under Pure Bending" Journal of Applied mechanics, Vol. 28, pp. 112-116.**
- Stephens, W., Starnes, Jr, J. H., and Almroth, B. O. (1975). "Collapse of Long Cylindrical Shells under Combined bending and pressure Loads" AIAA Journal Vol. 13, pp. 20-25.**
- Tatting, B. F., Gurdal, Z., and Vasiliev, V. (1996). "Nonlinear Response of Long Orthotropic Tubes under Bending Including Brazier Effect" AIAA Journal, Vol. 34, No. 9, pp. 1934-1940.**
- Tatting, B.F., Gurdal, Z., and Vasiliev, V. (1997). "The Brazier Effect for Finite length Composite Cylinders under Bending" International Journal of Solids and Structures, Vol. 34, No. 12, pp. 1419-1440.**
- Tennyon, R. C., MacDonald, D., and Nanyaro, A. P. (1978). "Evaluation of the Tensor polynomial Failure Criterion for Composite Materials" Journal of Composite Materials, Vol. 12, pp. 63-75.**

- Timoshenko, S. P., Young, D. H., and Weaver, W. (1974). *Vibration Problems in Engineering*, 4th ed., McGraw-Hill, New York, NY.
- Tsai, S. W. (1989). *Composites Design*, 4th ed., Think Composites, OH.
- Tsai, S. W., and Hahn, H. T. (1980). *Introduction to Composite Materials* Technomic Publishing Co., Lancaster, PA.
- Tsai, S. W., and Wu, E. M. (1971) "A General Theory of Strength for Anisotropic Materials" *Journal of Composites materials*, Vol. 5, pp. 58-80.
- Ugural, A. C., and Cheng, S. (1968). "Buckling of Composite Cylindrical Shells under Pure Bending" *AIAA Journal*, Vol. 6, No. 2, pp. 349-354.
- Vanderbuilt, M. D., and Criswell, M. E. (1988). "Reliability Analysis of Pole-Type Transmission Structures" *Computer and Structures*, Vol. 6, No. 2, pp. 335-343.
- Vinson, J. R., and Sierakowski, R. L. (1987). *The Behavior of Structures Composed of Composite Materials*, Martinus Nijhoff, The Netherlands: Martinus Nijhoff.
- Waddoups, R. M. (1967). "Advanced Composite Materials Mechanics for the Design and Stress Analyst" General Dynamics, Fort Worth Division Report FZM-4763, Fort Worth, TX.
- Waltz, T. L., and Vinson, J. R. (1976). "Interlaminar Stresses in Laminated Cylindrical Shells of Composite Materials" *AIAA Journal* Vol. 14, No. 9, pp.1213-1218.
- Warburton, G. B. (1976). "The Dynamical Behaviour of Structures", Pergamon Press, London.
- Whitney, J. M., and Sun, C. T. (1973). "A Refined Theory for Laminated Anisotropic Cylindrical Shells" *Journal of Applied Mechanics*, Vol. 41, pp. 471-476.

- Wu, E. M. (1974). "Phenomenological Anisotropic Failure Criterion" Composite Materials, G.P. Sendeckyj, editor, Vol.2, pp.353-431, Mechanics of Composite Materials Academic Press, New York.**
- Yuan, R. L., Hasen, Z., Green, A., and Bisarnsin, T. (1991). "Fiber-Reinforced Plastic Composite Columns", Advanced Composite Material in Civil Engineering Structures, Proceedings ASCE Specialty Conference, S.L.Iyer editor, ASCE, pp. 205-211.**
- Yunus, S., Kohnke, P.C., and Saigal, S. (1989). "An Efficient Through-Thickness Integration Scheme in Unlimited Layered Doubly Curved Isoparametric Composite Shell Element" International Journal for Numerical Methods In Engineering, Vol. 28, pp. 2777-2793.**

APPENDIX A

ANSYS INPUT FILES

A.1 INPUT FILE FOR SCALED SPECIMEN A25:

```
/BATCH
!-----
!ts225.inp
!Specimen 225, 2 m pole, 4 layers (25,-25,.....) , using shell99
!t=0.84 mm
! using fixed base and SI units
!-----
/COM,ANSYS REVISION 5.4      12:00:00  Nov. 2, 1998
/prep7
/show,x11
/pbc,f,1
/pbc,u,1
/nerr,5,50000
/pnum,kp,1
/pnum,line,1
/pnum,area,1
/view,1,3500,6000,5000
k,1,0,0,0
k,2,0,2000,0
k,3,47.32,0,0
k,4,46.45,200,0
k,5,45.15,500,0
k,6,41.675,1300,0
k,7,40.81,1500,0
k,8,39.94,1700,0
k,9,38.94,1930,0
l,1,2
l,3,4
l,4,5
l,5,6
l,6,7
l,7,8
l,8,9
arotat,2,3,4,5,6,7,1,2,360,4
et,1,99,,0,0,0,2,2,,0
r,1,4,0 !# of layers is the number after (1).
rmore,
```

rmore,1,47.5,0.2875,1,-47.5,0.2875
rmore,1,47.5,0.2875,1,-47.5,0.2875
!
r,2,4,0
rmore,
rmore,1,56.5,0.22,1,-56.5,0.22
rmore,1,56.5,0.22,1,-56.5,0.22
!
r,3,4,0
rmore
rmore,1,65,0.2035,1,-65,0.2035
rmore,1,65,0.2035,1,-65,0.2035
!
r,4,4,0
rmore
rmore,1,62.5,0.2175,1,-62.5,0.2175
rmore,1,62.5,0.2175,1,-62.5,0.2175
!
r,5,4,0
rmore
rmore,1,57.5,0.23625,1,-57.5,0.23625
rmore,1,57.5,0.23625,1,-57.5,0.23625
!
r,6,4,0
rmore
rmore,1,50,0.2825,1,-50,0.2825
rmore,1,50,0.2825,1,-50,0.2825
!
mp,ex,1,43265
mp,ey,1,11856
mp,ez,1,11856
mp,gxy,1,4603
mp,gyz,1,4603
mp,gxz,1,4603
mp,prxy,1,0.242
mp,pryz,1,0.3
mp,prxz,1,0.242
tb,fail,1,1
tbtemp,,crit
tbdata,1,0,1,1
tbtemp,0
tbdata,10,1020,-620,40,-140,40,-140
tbdata,16,60,60,60,-1,-1,-1
eshape,3,0
esize,,4
asel,s,loc,y,100

```
aatt,1,1,1
lsel,s,loc,y,100
lesize,all,25
amesh,all
allsel,all
asel,s,loc,y,350
aatt,1,2,1
lsel,s,loc,y,350
lesize,all,30
amesh,all
allsel,all
asel,s,loc,y,900
aatt,1,3,1
lsel,s,loc,y,900
lesize,all,35
amesh,all
allsel,all
asel,s,loc,y,1400
aatt,1,4,1
lsel,s,loc,y,1400
lesize,all,40
amesh,all
allsel,all
asel,s,loc,y,1600
aatt,1,5,1
lsel,s,loc,y,1600
lesize,all,40
amesh,all
allsel,all
asel,s,loc,y,1815
aatt,1,6,1
lsel,s,loc,y,1815
lesize,all,50
amesh,all
allsel,all
nset,s,loc,y,0
d,all,ux,0,0,,uy,uz,rotx,roty,rotz
allsel,all
save
finish
/solu
/title,Analysis of Specimen 225
antype,static
nlgeom,on
autots,on
nsubst,10,500,10,on
```

```
nropt,full
neqit,20
nset,s,loc,y,1930
f,all,fx,15 ! TOTAL LOAD = 32 * fx
time,15
allsel,all
outres,,all
lswrite,1
lssolve,1
save
FINISH
```

A.2 INPUT FILE FOR FULL-SCALE SPECIMEN 3:

BATCH

```
!-----  
!ts4.inp  
!Specimen 3 , 6 m pole, 8 layers (2*90,10,-10,.....,2*90) , using shell99  
!t= 4.94 mm at base, 6.4 mm at top  
!8 layers finite element  
!using fixed base and SI units  
!-----  
/COM,ANSYS REVISION 5.4      12:00:00 june 30, 1999  
/prep7  
/show,x11  
/pbc,f,1  
/pbc,u,1  
/nerr,5,50000  
/pnum,kp,1  
/pnum,line,1  
/pnum,area,1  
/view,1,3500,6000,5000  
! Geometry  
k,1,0,0,0  
k,2,0,2000,0  
k,3,208,-1000,0  
k,4,198.9,0,0  
k,5,189.8,1000  
k,6,180.65,2000,0  
k,7,171.54,3000,0  
k,8,158,4486,0  
k,9,152.4,5100,0  
l,1,2  
l,3,4  
l,4,5  
l,5,6  
l,6,7  
l,7,8  
l,8,9  
arotat,2,3,4,5,6,7,1,2,360,4  
! element  
et,1,99,,0,0,0,1,3,  
! Real constant for 1 st zone  
r,1,8,0 !# of layers is the number after (1)  
rmore,  
rmore,2,0,0.5,2,0,0.5  
rmore,1,-80,0.66,1,80,0.66  
rmore,1,-80,0.66,1,80,0.66
```

```

rmore,2,0,0.5,2,0,0.5
!
r,2,8,0 !# of layers is the number after (1)
rmore,
rmore,2,0,0.5,2,0,0.5
rmore,1,-80,0.7,1,80,0.7
rmore,1,-80,0.7,1,80,0.7
rmore,2,0,0.5,2,0,0.5
!
r,3,8,0 !# of layers is the number after (1)
rmore,
rmore,2,0,0.5,2,0,0.5
rmore,1,-80,0.74,1,80,0.74
rmore,1,-80,0.74,1,80,0.74
rmore,2,0,0.5,2,0,0.5
!
r,4,8,0 !# of layers is the number after (1)
rmore,
rmore,2,0,0.5,2,0,0.5
rmore,1,-80,0.78,1,80,0.78
rmore,1,-80,0.78,1,80,0.78
rmore,2,0,0.5,2,0,0.5
!
r,5,8,0 !# of layers is the number after (1)
rmore,
rmore,2,0,0.5,2,0,0.5
rmore,1,-80,0.85,1,80,0.85
rmore,1,-80,0.85,1,80,0.85
rmore,2,0,0.5,2,0,0.5
!
r,6,8,0 !# of layers is the number after (1)
rmore,
rmore,2,0,0.5,2,0,0.5
rmore,1,-80,0.89,1,80,0.89
rmore,1,-80,0.89,1,80,0.89
rmore,2,0,0.5,2,0,0.5
!
mp,ex,1,44632
mp,ey,1,12461.2
mp,ez,1,12461.2
mp,gxy,1,4850.6
mp,gyz,1,4850.6
mp,gxz,1,4850.6
mp,prxy,1,0.24
mp,pryz,1,0.3
mp,prxz,1,0.24

```

```

!
mp,ex,2,44632
mp,ey,2,12461.2
mp,ez,2,12461.2
mp,gxy,2,4850.6
mp,gyz,2,4850.6
mp,gxz,2,4850.6
mp,prxy,2,0.24
mp,pryz,2,0.3
mp,prxz,2,0.24
!
tb,fail,1,1
tbtemp,,crit
tbdata,1,0,1,1
tbtemp,0
tbdata,10,1300,-691,46,-130,1000,-1000 ! don't check z direction (normal to the shell)
tbdata,16,50,50,50,-1,-1,-1
!
tb,fail,2,1
tbtemp,,crit
tbdata,1,0,1,1 ! check maximum stress and Tsai-Wu failure criteria
tbtemp,0
tbdata,10,1300,-691,1000,-1000,1000,-1000 ! ignore check lateral stresses for circum.
layers
tbdata,16,500,500,500,-1,-1,-1 ! ignore check of circum layer
!
!
eshape,3,0
esize,,4
!
asel,s,loc,y,-500
aatt,1,1,1
lsel,s,loc,y,-500
lesize,all,,,10,
amesh,all
allsel,all
!
asel,s,loc,y,500
aatt,1,2,1
lsel,s,loc,y,500
lesize,all,,,10
amesh,all
allsel,all
!
asel,s,loc,y,1500
aatt,1,3,1

```



```

lsel,s,loc,y,1500
lesize,all,,,10
amesh,all
allsel,all
!
asel,s,loc,y,2500
aatt,1,4,1
lsel,s,loc,y,2500
lesize,all,,,8
amesh,all
allsel,all
!
asel,s,loc,y,3743
aatt,1,5,1
lsel,s,loc,y,3743
lesize,all,,,8
amesh,all
allsel,all
!
asel,s,loc,y,4793
aatt,1,6,1
lsel,s,loc,y,4793
lesize,all,,,3
amesh,all
allsel,all
! Boundary conditions
nset,s,loc,y,0
d,all,uz,0,0,,,rotx,roty,rotz
d,all,ux,11.3508,0,,,
nset,all
nset,s,loc,y,-1000
d,all,uy,0,0
nset,all
!
nset,s,loc,y,-100
d,all,uz,0,0,,,rotx,roty,rotz
d,all,ux,9.459,0,,,
nset,all
!
nset,s,loc,y,-200
d,all,uz,0,0,,,rotx,roty,rotz
d,all,ux,7.5672,0,,,
nset,all
!
nset,s,loc,y,-300
d,all,uz,0,0,,,rotx,roty,rotz

```

```

d,all,ux,5.6754,0,,
nset,all
!
nset,s,loc,y,-400
d,all,uz,0,0,,,rotx,roty,rotz
d,all,ux,3.7836,0,,
nset,all
!
nset,s,loc,y,-500
d,all,uz,0,0,,,rotx,roty,rotz
d,all,ux,1.8918,0,,
nset,all
!
nset,s,loc,y,-900,-600
d,all,uz,0,0,,,rotx,roty,rotz
d,all,ux,0,0,,
nset,all
!
nset,s,loc,y,-1000
d,all,uz,0,0,,,ux,uy,rotx,roty,rotz
nset,all
!
nset,s,loc,y,100
nset,r,loc,x,-200,0
d,all,ux,13.24,0,
nset,all
!
save
finish
/solu
/title,Analysis of test Specimen 4 , 5m cantilever hieght, fiber volume 60%
antype,static
nlgeom,on
autots,on
sstif,on
nsubst,15,500,15,on
nropt,full
neqit,20
cnvtol,f,,0.0002,,1
cnvtol,m,,0.0005,,1
cnvtol,u,,0.04,,0
nset,s,loc,y,4486
nset,r,loc,x,-160,0 ! 17 node selected
f,all,fx,2800! TOTAL LOAD = 17 * fx = 47600 N = 48 KN = 10,700 lb
nset,all
time,2800

```

**allsel,all
outres,,all
lswrite,l
lssolve,l
save
FINISH**

APPENDIX B

STIFFNESS AND MASS MATRIX FOR PRISMATIC ELEMENTS

$$[K] = \frac{E}{L^3} \begin{bmatrix} AL^2 & 0 & 0 & -AL^2 & 0 & 0 \\ 0 & 12I & 6IL & 0 & -12I & 6IL \\ 0 & 6IL & 4IL^2 & 0 & -6IL & 2IL^2 \\ -AL^2 & 0 & 0 & AL^2 & 0 & 0 \\ 0 & 12I & -6IL & 0 & 12I & -6IL \\ 0 & 6IL & 2IL^2 & 0 & -6IL & 4IL^2 \end{bmatrix} \quad (B-1)$$

$$[m] = \frac{\rho AL}{420} \begin{bmatrix} 140 & 0 & 0 & 70 & 0 & 0 \\ 0 & 156 & 22L & 0 & 54 & -13L \\ 0 & 22L & 4L^2 & 0 & 13L & -3L^2 \\ 70 & 0 & 0 & 140 & 0 & 0 \\ 0 & 54 & 13L & 0 & 156 & -22L \\ 0 & -13L & -3L^2 & 0 & -22L & 4L^2 \end{bmatrix} \quad (B-2)$$